

Air Force Institute of Technology

AFIT Scholar

Theses and Dissertations

Student Graduate Works

10-18-1996

Optical Detection Properties of Silicon-Germanium Quantum Well Structures

Michael R. Gregg

Follow this and additional works at: <https://scholar.afit.edu/etd>



Part of the [Semiconductor and Optical Materials Commons](#)

Recommended Citation

Gregg, Michael R., "Optical Detection Properties of Silicon-Germanium Quantum Well Structures" (1996). *Theses and Dissertations*. 5823.
<https://scholar.afit.edu/etd/5823>

This Dissertation is brought to you for free and open access by the Student Graduate Works at AFIT Scholar. It has been accepted for inclusion in Theses and Dissertations by an authorized administrator of AFIT Scholar. For more information, please contact AFIT.ENWL.Repository@us.af.mil.

AFIT/DS/ENP/96-07

OPTICAL DETECTION PROPERTIES
OF
SILICON-GERMANIUM QUANTUM WELL STRUCTURES

DISSERTATION

Michael R. Gregg, Captain, USAF

AFIT/DS/ENP/96

19970521 018

Approved for public release; distribution unlimited

DTIC QUALITY INSPECTED 1

AFIT/DS/ENP/96-07

**Optical Detection Properties
of
Silicon-Germanium Quantum Well Structures**

DISSERTATION

Presented to the Faculty of the Graduate School of Engineering
of the Air Force Institute of Technology
Air University
In Partial Fulfillment of the
Requirements for the Degree of
Doctor of Philosophy

Michael R. Gregg, B.A., M.S.
Captain, USAF

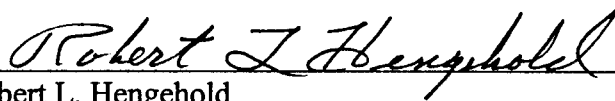
October 1996

Approved for public release; distribution unlimited

Optical Detection Properties
of
Silicon-Germanium Quantum Well Structures

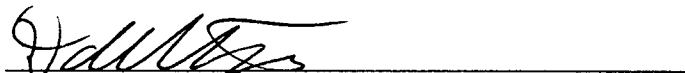
Michael R. Gregg, BA, MS
Captain, USAF

Approved:



Robert L. Hengehold
Professor and Head, Department of Engineering Physics
Chairman, Advisory Committee

18 Oct '96



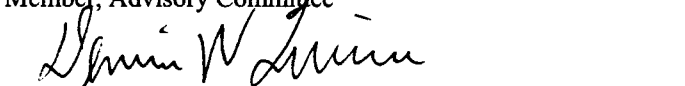
David E. Weeks
Assistant Professor of Engineering Physics
Member, Advisory Committee

18 Oct 96



Yung Kee Yeo
Professor of Engineering Physics
Member, Advisory Committee

18 Oct 96



Dennis W. Quinn
Professor of Mathematics and Statistics
Member, Advisory Committee

18 OCT 96



George K. Haritos, Col, USAF
Associate Dean, Graduate School of Engineering

18 Oct 96

Accepted:



Robert A. Calico
Dean, Graduate School of Engineering

Preface

All things must end, and alas after almost five years, my time at AFIT has ended. This project has progressed in ways I never could have imagined in the beginning. The original conception of the project was an experimental characterization of the optical properties of silicon-germanium multiple quantum wells. The difficulty of making absorption measurements on material grown on the non-conventional substrates forced me to obtain a deeper theoretical understanding of the structures, and to develop the photoresponse technique. Hopefully we have now put together a unified and coherent package that can be put to good use.

I must give thanks to the many folks who have helped me along the way. A special thanks goes to my advisor, Dr. Robert Hengehold, who has helped me on matters great and small. I appreciate that he was willing to let me barge into his office almost any time. I owe a great debt to Dr. David Weeks, without whom I could not have tackled the theory. Even though his voice impersonations are quite pathetic, he has been a great friend and sounding board. I also thank Dr. Phil Thompson, a.k.a. "Homer the catman" of the Naval Research Laboratory who has provided the samples used in the experiment. He has been a constant source of encouragement. I thank Dr. Yung Kee Yeo for his critical reading of the manuscript and his good suggestions. I appreciate the patience with which Dr. Frank Szmulowicz answered my questions on the EFA and his willingness to help. The technical staff has been absolutely superb. Greg Smith has worked tirelessly to obtain the necessary equipment and to keep it operational. Belinda

Johnson has been a great help, especially in the making devices. I must thank my wife Teresa and my daughter Amy. They have been a blessing to my life. They have endured with grace and have provided the support and stability I needed to complete the job. Finally, I must thank God for proving his faithfulness again. -mrg

Table of Contents

PREFACE	iii
TABLE OF CONTENTS	v
LIST OF FIGURES	viii
LIST OF TABLES	xvii
LIST OF SYMBOLS	xviii
ABSTRACT	xx
1. INTRODUCTION	1-1
2. BACKGROUND	2-1
A. INFRARED PHOTODETECTORS.....	2-1
B. SILICON/GERMANIUM ALLOYS.....	2-14
C. PREVIOUS WORK.....	2-17
3. THEORETICAL MODEL FOR VALENCE BANDS IN Si/Si _{1-x} Ge _x QUANTUM WELLS.....	3-1
A. INTRODUCTION.....	3-1
B. Si _{1-x} Ge _x UNSTRAINED, BULK BAND STRUCTURE	3-7
C. THE EFFECTS OF STRAIN ON BULK ENERGY LEVELS.....	3-22
D. A SIMPLE QUANTUM WELL ANALYSIS	3-33
E. ENVELOPE FUNCTION APPROXIMATION.....	3-40
1. Background.....	3-40
2. Bound-state solutions ³⁹	3-46
3. Band Decomposition.....	3-52
F. TRANSITION STRENGTHS	3-56
G. FERMI LEVEL APPROXIMATION.....	3-64
H. COMPARISON BETWEEN Si/SiGe AND GAAS/ALGAAS.....	3-71
I. CALCULATED ENERGY VALUES.....	3-78
4. EXPERIMENTAL TECHNIQUES.....	4-1

A. INTRODUCTION.....	4-1
B. PHOTOLUMINESCENCE	4-4
1. Diagnostic Tool.....	4-4
2. PL Experimental Procedures and Apparatus	4-7
C. FOURIER TRANSFORM INFRARED SPECTROSCOPY (FTS).....	4-11
1. Introduction to FTS Techniques	4-11
2. FTS Experimental Apparatus.....	4-18
D. ABSORPTION MEASUREMENTS.....	4-22
1. Absorption measurements on Si/Si _{1-x} Ge _x waveguides	4-22
2. Reference Techniques	4-29
3. Sample Preparation and Mounting.....	4-40
E. PHOTORESPONSE MEASUREMENTS	4-45
1. Signal Generation and Data Acquisition Procedures.....	4-45
2. Sample Preparation and Experimental Setup.....	4-47
5. RESULTS AND DISCUSSION.....	5-1
A. INTRODUCTION.....	5-1
B. PHOTOLUMINESCENCE	5-4
C. ABSORPTION	5-22
1. Introduction.....	5-22
2. [001] Absorption Data.	5-24
3. [110] Absorption Data	5-31
D. PHOTORESPONSE.....	5-40
1. Shifting the responsivity range	5-40
2. Phenomenological Effects	5-57
3. SiGe Alloys used in QWIPs.....	5-68
6. CONCLUSIONS AND RECOMMENDATIONS	6-1
A. CONCLUSIONS.....	6-1
B. RECOMMENDATIONS	6-5

APPENDIX A. PROPERTIES OF INTRINSIC SILICON AND GERMANIUM.....	A-1
APPENDIX B. CHRONOLOGICAL REVIEW OF THE DEVELOPMENT OF SI/SI _{1-x} GE _x HETEROSTRUCTURES	B-1
APPENDIX C. ZONE CENTER ENERGIES.....	C-1
APPENDIX D. P'S AND Q'S FOR MOMENTUM MATRIX ELEMENTS	D-1
APPENDIX E. SAMPLE LIST	E-1
APPENDIX F. MULTI-PHONON TRANSITION PEAKS FOR BULK SI ¹⁶	F-1
APPENDIX G. ENERGIES OF SI PL LINES	G-1
BIBLIOGRAPHY	Bib1
VITA	V-1

List of Figures

FIGURE 2-1. DETECTIVITY, D^* , AS A FUNCTION OF WAVELENGTH FOR VARIOUS PHOTOCONDUCTORS AND PHOTODIODES (INDICATED WITH PD).....	2-2
FIGURE 2-2. PROCESSES OF INTRINSIC (BAND-TO-BAND) AND EXTRINSIC PHOTOEXCITATIONS. ²	2-3
FIGURE 2-3. ROOM TEMPERATURE BANDGAPS, LATTICE CONSTANTS, AND WAVELENGTH CUTOFFS FOR GROUP III-V, II-VI, AND GROUP IV ALLOY SYSTEMS.	2-3
FIGURE 2-4. THE PHOTOCONDUCTOR DETECTOR. PHOTOGENERATED CARRIERS MOVE IN RESPONSE TO THE APPLIED VOLTAGE V , GENERATING A PHOTOCURRENT I_p PROPORTIONAL TO THE INCIDENT PHOTON FLUX. ¹	2-5
FIGURE 2-5. STRUCTURE AND ENERGY BAND DIAGRAM OF A SCHOTTKY BARRIER PHOTODIODE FORMED BY DEPOSITION A METAL ON AN N-TYPE SEMICONDUCTOR. ¹	2-6
FIGURE 2-6. (A) ENERGY -BAND DIAGRAM OF THE $P^+ \setminus Si_{1-x} Ge_x / P-Si$ HIP DETECTOR (B) STRUCTURE OF THE TEST DEVICE. ⁹	2-7
FIGURE 2-7. DISCONTINUITIES OF BANDEDGE ENERGIES AT FOUR KINDS OF INTERFACES: BAND OFFSETS (LEFT), BAND BENDING AND CARRIER CONFINEMENT (MIDDLE), AND SUPERLATTICES (RIGHT).....	2-10
FIGURE 2-8. MODULATION-DOPED Si-Ge SUPERLATTICE.....	2-10
FIGURE 2-9. (A) BOUND-TO-CONTINUUM TRANSITION AND (B) BOUND-TO-BOUND TRANSITION IN A QUANTUM WELL STRUCTURE UNDER AN APPLIED ELECTRIC FIELD. ³	2-11
FIGURE 2-10. DIAMOND LATTICE CRYSTAL STRUCTURE. ²	2-14

FIGURE 3-1. THE (A) [001], (B) [110], AND (C) [111] COORDINATES RELATIVE TO THE [001] COORDINATE SYSTEM.....	3-17
FIGURE 3-2. SCHEMATIC DIAGRAM REPRESENTING STRAINED LAYER EPITAXY	3-23
FIGURE 3-3. VALENCE BANDS ($J=3/2$, $M_j=\pm 3/2, \pm 1/2$, AND $J=1/2$, $M_j=\pm 1/2$) AND THE LOWEST CONDUCTION BAND IN DIAMOND AND ZINCBLLENDE-TYPE SEMICONDUCTORS FOR UNSTRAINED (LEFT) AND STRAINED (RIGHT) CRYSTALS.....	3-24
FIGURE 3-4. STRAIN INDUCED ENERGY SHIFT FOR ALL THREE VALENCE BANDS AS A FUNCTION OF GERMANIUM COMPOSITION	3-27
FIGURE 3-5. THE STRAIN INDUCED EFFECTIVE MASS SHIFT ALONG THE GROWTH DIRECTION AS A FUNCTION OF GERMANIUM COMPOSITION. HH, LH AND SO DENOTE HEAVY HOLE, LIGHT HOLE AND SPLIT-OFF HOLE RESPECTIVELY.....	3-29
FIGURE 3-6. ENERGY BANDS DERIVED FROM DIAGONALIZING THE HAMILTONIAN WHERE (A) $H_{TOTAL} = H_0 + H_{K,P}$, (B) $H_{TOTAL} = H_0 + H_{K,P} + H_{SO}$, (C) $H_{TOTAL} = H_0 + H_{K,P} + H_{SO} + H_{STRAIN}$ FOR Si[110], $x=0.30$ AND $\pi/A \approx 0.57$	3-31
FIGURE 3-7. BAND OFFSETS FOR ANY GROWTH DIRECTION AT A Si/SiGe INTERFACE FOR STRAINED AND UNSTRAINED CASE. V_{OFFSET} REPRESENTS THE QUANTUM WELL DEPTH FOR THE HEAVY HOLE BAND.	3-34
FIGURE 3-8. GRAPHICAL REPRESENTATION OF SOLUTIONS TO THE 1-D SCHRÖDINGER EQUATION FOR THE HEAVY HOLE BAND OF A Si[001]/Si _{0.70} Ge _{0.30} MQW WITH A WELL WIDTH OF 30 Å.....	3-38
FIGURE 3-9. SCHEMATIC DIAGRAM OF BOUND STATE ENERGY LEVELS IN A Si[001]/Si _{0.70} Ge _{0.30} MQW WITH A WELL WIDTH OF 30 Å. ENERGIES ARE DETERMINED USING A SIMPLE QUANTUM WELL MODEL.	3-39
FIGURE 3-10. SCHEMATIC DIAGRAM SHOWING THE DEGENERACY POINTS IN EACH BAND AS A FUNCTION OF ENERGY AND OF K_z	3-42
FIGURE 3-11. DISPERSION CURVES FOR A Si[001]/Si _{0.70} Ge _{0.30} MQW WHERE $L=30$ Å. DASHED LINES REPRESENT ZONE CENTER ENERGIES FROM THE SIMPLE WELL MODEL. $\pi/A \approx 0.51$	3-51
FIGURE 3-12. DISPERSION CURVES FOR A Si[110]/Si _{0.70} Ge _{0.30} MQW WHERE $L=30$ Å. DASHED LINES REPRESENT ZONE CENTER ENERGIES FROM THE SIMPLE WELL MODEL. $\pi/A \approx 0.51$	3-51

FIGURE 3-13. BAND WEIGHTS VS. $k_{\parallel}[110]$ FOR A $\text{Si}[001]/\text{Si}_{0.70}\text{Ge}_{0.30}$ MQW WITH $L=30 \text{ \AA}$. $\pi/A \approx 0.51$	3-54
FIGURE 3-14. BAND WEIGHTS VS. $k_{\parallel}[00-1]$ FOR A $\text{Si}[110]/\text{Si}_{0.70}\text{Ge}_{0.30}$ MQW WITH $L=30 \text{ \AA}$. $\pi/A \approx 0.51$	3-55
FIGURE 3-15. ENVELOPE FUNCTION IN EACH SUBBAND FOR A $\text{Si}[001]$ MQW STRUCTURE WHERE $x=0.30$, $L=30 \text{ \AA}$. $k_{\parallel}[110]=0.04 \text{ \AA}^{-1}$	3-56
FIGURE 3-16. ENVELOPE FUNCTION DECOMPOSITION FOR HH2 IN A $\text{Si}[001]/\text{Si}_{1-x}\text{Ge}_x$ MQW WITH $x=0.30$, $L=30 \text{ \AA}$, FOR TWO k_{\parallel} VALUES.	3-58
FIGURE 3-17. SQUARED MOMENTUM MATRIX ELEMENTS FOR TWO POLARIZATION OF INCIDENT LIGHT FOR A $\text{Si}[001]/\text{Si}_{0.70}\text{Ge}_{0.30}$ MQW WITH $L=30 \text{ \AA}$	3-61
FIGURE 3-18. SQUARED MOMENTUM MATRIX ELEMENTS FOR A $\text{Si}[110]$ MQW WITH $x=0.30$ AND $L=30 \text{ \AA}$ AT THREE DIFFERENT POLARIZATIONS.	3-62
FIGURE 3-19. CONSTANT ENERGY CONTOURS FOR IDENTICAL $\text{Si}[110]$ (TOP) AND $\text{Si}[001]$ (BOTTOM) MQW STRUCTURES.	3-65
FIGURE 3-20. AVERAGE ENERGY BANDS AND FERMI LEVELS FOR DIFFERENT DOPING LEVELS FOR MQWS GROWN ON $\text{Si}[110]$ (TOP) AND $\text{Si}[001]$ (BOTTOM).	3-67
FIGURE 3-21. DENSITY OF STATES AND INTEGRATED DENSITY OF STATES FOR AVERAGED ENERGY BANDS IN A $\text{Si}[110]$ MQW WHERE $x=0.18$ AND $L=45 \text{ \AA}$	3-68
FIGURE 3-22. DENSITY OF STATES AND INTEGRATED DENSITY OF STATES FOR AVERAGED ENERGY BANDS IN A $\text{Si}[001]$ MQW WHERE $x=0.18$ AND $L=45 \text{ \AA}$	3-69
FIGURE 3-23. DISPERSION RELATIONS FOR $\text{Si}[110]/\text{Si}_{0.82}\text{Ge}_{0.18}$ MQW WITH WELL WIDTH OF 45 \AA . SOLID LINES ARE FOR THE $[00-1]$ DIRECTION AND THE DASHED LINES ARE FOR THE $[-110]$ DIRECTION.	3-72
FIGURE 3-24. DISPERSION RELATIONS FOR $\text{Si}[001]/\text{Si}_{0.82}\text{Ge}_{0.18}$ MQW WITH WELL WIDTH OF 45 \AA . SOLID LINES ARE FOR THE $[110]$ DIRECTION AND THE DASHED LINES ARE FOR THE $[010]$ DIRECTION.	3-72

FIGURE 3-25. DISPERSION RELATIONS FOR GAAS[001]/AL _{0.30} GA _{0.70} AS MQW WITH WELL WIDTH OF 50 Å. SOLID LINES ARE FOR THE [110] DIRECTION AND THE DASHED LINES ARE FOR THE [010] DIRECTION.	3-73
FIGURE 3-26. SQUARED MOMENTUM MATRIX ELEMENTS FOR THREE POLARIZATIONS OF INCIDENT LIGHT FOR A SI[110]/SI _{0.82} GE _{0.18} MQW WITH L=45 Å.	3-74
FIGURE 3-27. SQUARED MOMENTUM MATRIX ELEMENTS FOR TWO POLARIZATIONS OF INCIDENT LIGHT FOR A SI[001]/SI _{0.82} GE _{0.18} MQW WITH L=45 Å.	3-75
FIGURE 3-28. SQUARED MOMENTUM MATRIX ELEMENTS FOR TWO POLARIZATIONS OF INCIDENT LIGHT FOR A GAAS(001)/AL _{0.30} GA _{0.70} AS MQW WITH L=50 Å.	3-76
FIGURE 4-1. RECOMBINATION PROCESSES OF EXCITED ELECTRONS IN SEMICONDUCTORS. (A) BAND-TO- BAND; (B) FREE EXCITON; (C) BOUND EXCITON; (D) DONOR-TO-VALENCE BAND; (E) CONDUCTION BAND-TO-ACCEPTOR; (F) DONOR-ACCEPTOR PAIR; (G) PHONON-ASSISTED OR INDIRECT.	4-5
FIGURE 4-2. SCHEMATIC DIAGRAM OF PHOTOLUMINESCENCE EXPERIMENTAL APPARATUS.	4-8
FIGURE 4-3. MICHELSON INTERFEROMETER.	4-12
FIGURE 4-4. DIAGRAM OF THE BIORAD FTS 60A FOURIER TRANSFORM SPECTROSCOPY SYSTEM. ⁶²	4-19
FIGURE 4-5. SPECTRAL RESPONSE PRODUCED BY THE COMBINATION OF THE GLOWBAR SOURCE, KBR BEAMSPLITTER, AND DTGS DETECTOR THROUGH VARIOUS WINDOW MATERIALS.	4-21
FIGURE 4-6. DIAGRAM OF THE QUANTUM WELL STRUCTURE, THE PLANE OF INCIDENCE FORMED BY THE INCIDENT RAY AND THE SURFACE NORMAL, THE POYNTING VECTOR, AND THE ELECTRIC FIELD VECTORS.	4-23
FIGURE 4-7. ILLUSTRATION OF THE CRITICAL AND COMPLEMENTARY CRITICAL ANGLES.	4-24
FIGURE 4-8. SCHEMATIC OF SAMPLE FASHIONED INTO AN OPTICAL WAVEGUIDE AND THE LIGHT PATH THROUGH THE SAMPLE.	4-24

FIGURE 4-9. TRANSMISSION OF PARALLEL AND NORMAL COMPONENTS AS A FUNCTION OF BEVEL ANGLE.	4-25
FIGURE 4-10. THE POWER CONFINEMENT FACTOR FOR AN AIR/SILICON INTERFACE.....	4-26
FIGURE 4-11. PLOT SHOWING THE COS(X) DEPENDENCE OF THE PARTIAL POLARIZED INPUT BEAM THROUGH THE POLARIZER.	4-29
FIGURE 4-12. SELF-REFERENCE CORRECTION FACTORS TAKEN FROM AN UNDOPED SI (110) SUBSTRATE GENERATED BY DIVIDING SPECTRA AT 0,22,45,67 POLARIZER SETTINGS BY 90 DEGREE SETTING.	4-30
FIGURE 4-13. RAW SINGLE BEAM DATA. S00 AND S90 REPRESENT THE SIGNAL INTENSITY, I_{SAMPLE} , TAKEN AT POLARIZER SETTINGS OF 0 AND 90 DEGREES. B00 AND B90 REPRESENT $I_{\text{BACKGROUND}}$ TAKEN AT 0 AND 90 DEGREES.	4-32
FIGURE 4-14. ABSORBANCE SPECTRA TAKEN IN SUBSTRATE REFERENCE MODE. DATA FOR 0 AND 90 DEGREE POLARIZATIONS SHOWN.....	4-34
FIGURE 4-15. ABSORBANCE SPECTRUM A Si(110) SUBSTRATE MEASURED IN THE WAVEGUIDE CONFIGURATION. NUMBERED LINES INDICATE MULTI-PHONON TRANSITIONS ASSOCIATED WITH IMPURITIES IN SILICON.	4-35
FIGURE 4-16. ABSORBANCE SPECTRA SHOWING THE ELIMINATION OF ABSORPTION PEAKS ASSOCIATED WITH MULTI-PHONON TRANSITIONS IN SI AND THE FREE CARRIER CORRECTION FACTORS.....	4-37
FIGURE 4-17. FINAL FORM OF ABSORBANCE SPECTRA CORRECTED FOR SI BACKGROUND PEAKS AND FREE CARRIER BACKGROUND ABSORPTION.....	4-38
FIGURE 4-18. SCHEMATIC DRAWING OF WAVEGUIDE POLISHING JIG.....	4-41
FIGURE 4-19. SCHEMATIC DIAGRAM OF WAVEGUIDE MOUNT.....	4-43
FIGURE 4-20. PHOTORESPONSE SPECTRA TAKEN AT 77 K UNDER NORMAL INCIDENCE ILLUMINATION. RAW DATA AND CURVE FIT ARE SHOWN.	4-46
FIGURE 4-21. CUT-AWAY DIAGRAM OF MESA STRUCTURE USED IN PR MEASUREMENTS.	4-48

FIGURE 4-22. SCHEMATIC DIAGRAM FOR PHOTORESPONSE MEASUREMENTS.	4-49
FIGURE 5-1. PL SPECTRA OF A Si[110] SUBSTRATE AND AN UNDOPED STANDARD SAMPLE 30528.2.	5-5
FIGURE 5-2. PL SPECTRA OF SAMPLE 50117.1 TAKEN AT DIFFERENT TEMPERATURES SHOWING BROADBAND AND CARBON RELATED FEATURES	5-8
FIGURE 5-3. PL SPECTRA SHOWING LUMINESCENCE INTENSITY AS A FUNCTION OF BORON DOPING.	5-10
FIGURE 5-4. PL SPECTRA SHOWING CHANGE IN PEAK POSITION WITH VARIATION IN QUANTUM WELL WIDTH AND CONSTANT GE COMPOSITION.....	5-12
FIGURE 5-5. PL SPECTRA SHOWING BROADBAND SHIFT WITH DIFFERENT GE COMPOSITIONS AND A CONSTANT WELL WIDTH.....	5-13
FIGURE 5-6. PL SPECTRA OF AN UNDOPED SAMPLE SHOWING THE PENETRATION DEPTH DEPENDENCE OF THE BROADBAND AND CARBON RELATED FEATURES.	5-14
FIGURE 5-7. PL SPECTRA OF A DOPED SAMPLE SHOWING THE PENETRATION DEPTH DEPENDENCE OF THE BROADBAND AND CARBON RELATED FEATURES	5-15
FIGURE 5-8. PL SPECTRA SHOWING A COMPARISON BETWEEN IDENTICAL MQW STRUCTURES GROWN ON (100) AND (110) SUBSTRATES. PORTIONS OF THE PLOTS HAVE MULTIPLIED BY A FACTOR OF 10.	5-17
FIGURE 5-9. PL SPECTRA SHOWING A COMPARISON BETWEEN IDENTICAL MQW STRUCTURES GROWN AT TEMPERATURES OF 550 °C AND 710 °C. PORTIONS OF THE PLOTS HAVE MULTIPLIED BY A FACTOR OF 10.....	5-18
FIGURE 5-10. PL SPECTRA SHOWING THE EFFECTS OF ANNEALING ON THE CARBON RELATED DEFECTS AND THE BROADBAND LUMINESCENCE.	5-19
FIGURE 5-11. ABSORBANCE SPECTRA OF NRL SAMPLE 50406.1 USING SUBSTRATE REFERENCING BACKGROUND SUBTRACTION.	5-25

FIGURE 5-12. SCHEMATIC DRAWING SHOWING THE EFA ZONE CENTER ENERGIES AND POSSIBLE TRANSITIONS FOR A Si[001]/Si _{0.70} Ge _{0.30} , 30 Å WELL MQW STRUCTURE. THE SHIFTED POSITION OF HH1 DUE TO THE EXCHANGE INTERACTION EFFECT IS INDICATED BY THE DASHED LINE.....	5-26
FIGURE 5-13. ABSORBANCE SPECTRA OF NRL SAMPLE 50406.1 SHOWING THE EFFECTS OF ROTATING THE POYNTING VECTOR PERPENDICULAR AND PARALLEL TO THE QUANTUM WELL PLANES. DATA HAS BEEN NORMALIZED.	5-28
FIGURE 5-14. ABSORBANCE SPECTRA OF NRL SAMPLE 50728.1 USING SUBSTRATE REFERENCING BACKGROUND SUBTRACTION.	5-30
FIGURE 5-15. SCHEMATIC DRAWING SHOWING THE EFA ZONE CENTER ENERGIES AND POSSIBLE TRANSITIONS FOR A Si[001]/Si _{0.60} Ge _{0.40} , 40 Å WELL MQW STRUCTURE. THE SHIFTED POSITION OF HH1 DUE TO THE EXCHANGE INTERACTION EFFECT IS INDICATED BY THE DASHED LINE.....	5-31
FIGURE 5-16. ABSORBANCE SPECTRA FOR A Si[110]/Si _{0.70} Ge _{0.30} , 30 Å WELL MQW STRUCTURE WITH 15 PERIODS. SAMPLE GROWN VIA MBE AT 550 °C.....	5-33
FIGURE 5-17. SCHEMATIC DRAWING SHOWING THE ZONE CENTER BAND ENERGIES AND POSSIBLE TRANSITIONS FOR A Si[110]/Si _{0.70} Ge _{0.30} , 30 Å WELL MQW STRUCTURE. THE SHIFTED POSITION OF HH1 DUE TO THE EXCHANGE INTERACTION EFFECT IS INDICATED BY THE DASHED LINE.....	5-34
FIGURE 5-18. ABSORBANCE SPECTRA FOR A Si[110]/Si _{0.70} Ge _{0.70} , 20 Å WELL MQW STRUCTURE WITH 20 PERIODS. SAMPLE GROWN VIA MBE AT 550 °C.....	5-36
FIGURE 5-19. SCHEMATIC DRAWING SHOWING THE BAND STRUCTURE AND POSSIBLE TRANSITIONS FOR A Si[110]/Si _{0.70} Ge _{0.70} , 20 Å WELL MQW STRUCTURE. THE SHIFTED POSITION OF HH1 DUE TO THE EXCHANGE INTERACTION EFFECT IS INDICATED BY THE DASHED LINE.....	5-37
FIGURE 5-20 NORMALIZED ABSORBANCE SPECTRA FOR TWO SAMPLES WITH A CONSTANT GERMANIUM COMPOSITION OF 30 PERCENT AND WELL WIDTHS OF 20 Å AND 30 Å.....	5-38
FIGURE 5-21. PHOTORESPONSE SPECTRUM OF A GaAs/Al _{0.30} Ga _{0.70} As MQW WITH A WELL WIDTH OF 40 Å TAKEN AT 50 K. USED TO VERIFY EXPERIMENTAL TECHNIQUE.....	5-42
FIGURE 5-22. TYPICAL PHOTORESPONSE SPECTRUM OF A Si[001]Si _{0.70} Ge _{0.30} MQW WITH A WELL WIDTH OF 30 Å TAKEN AT 77 K UNDER NORMAL INCIDENCE ILLUMINATION.	5-42

FIGURE 5-23. SCHEMATIC DIAGRAM FOR POSITION OF ZONE CENTER ENERGY LEVELS IN A Si[110]/SiGe QW WITH A CONSTANT WELL WIDTH OF 40 Å AND Ge CONCENTRATION OF 20 AND 30 PERCENT.....	5-44
FIGURE 5-24. COMBINED ABSORBANCE AND PHOTORESPONSE SPECTRA FOR A Si[110]/Si _{0.80} Ge _{0.20} MQW WITH 40 Å WELL WIDTH. THE PHOTORESPONSE HAS BEEN ENLARGED TO SHOW DETAIL.....	5-45
FIGURE 5-25. COMBINED ABSORBANCE AND PHOTORESPONSE SPECTRA FOR A Si[110]/Si _{0.70} Ge _{0.30} MQW WITH 40 Å WELL WIDTH. THE PHOTORESPONSE HAS BEEN ENLARGED TO SHOW DETAIL.	5-47
FIGURE 5-26. PHOTORESPONSE SPECTRA (NORMALIZED) OF 2 (110) Si/SiGe MQW SAMPLES WITH CONSTANT WELL WIDTH OF 40 Å AND Ge COMPOSITIONS OF 0.20, AND 0.30. DATA WAS TAKEN AT NORMAL INCIDENCE AT 77 K, 1 V BIAS.	5-49
FIGURE 5-27. SCHEMATIC DIAGRAM FOR POSITION OF THE EFA ZONE CENTER ENERGY LEVELS IN A Si[110]/SiGe QW WITH A CONSTANT Ge PERCENTAGE OF 30 PERCENT AND WELL WIDTHS OF 20 Å, 30 Å AND 40 Å.	5-50
FIGURE 5-28. COMBINED ABSORBANCE AND PHOTORESPONSE SPECTRA FOR A Si[110]/Si _{0.70} Ge _{0.30} MQW WITH 20 Å WELL WIDTH. THE PHOTORESPONSE HAS BEEN ENLARGED TO SHOW DETAIL.	5-51
FIGURE 5-29. COMBINED ABSORBANCE AND PHOTORESPONSE SPECTRA FOR A Si[110]/Si _{0.70} Ge _{0.30} MQW WITH 30 Å WELL WIDTH. THE PHOTORESPONSE HAS BEEN ENLARGED TO SHOW DETAIL.	5-52
FIGURE 5-30. COMBINED ABSORBANCE AND PHOTORESPONSE SPECTRA FOR A Si[110]/Si _{0.70} Ge _{0.30} MQW WITH 40 Å WELL WIDTH. THE PHOTORESPONSE HAS BEEN ENLARGED TO SHOW DETAIL.	5-53
FIGURE 5-31. ABSORBANCE SPECTRA OF 3(110) Si/SiGe MQW SAMPLES WITH A CONSTANT WELL DEPTH AND WELL WIDTHS OF 20, 30, & 40 Å. DATA TAKEN IN WAVEGUIDE CONFIGURATION, SUBSTRATE REFERENCED.	5-54
FIGURE 5-32. PHOTORESPONSE SPECTRA (NORMALIZED) OF 3(110) Si/SiGe MQW SAMPLES WITH A CONSTANT WELL DEPTH AND WELL WIDTHS OF 20, 30, & 40 Å. DATA TAKEN AT NORMAL INCIDENCE AT 77 K AND 1 V BIAS.	5-56
FIGURE 5-33. SCHEMATIC DRAWING SHOW EFFECT OF DOPING LEVEL ON ENERGY RANGE OF HOLES.	5-57

FIGURE 5-34. PHOTORESPONSE SPECTRA (NORMALIZED) OF 3(110) Si/SiGe MQW SAMPLES WITH $x=0.20$ AND $L=40 \text{ \AA}$ AND 3 DOPING LEVELS. DATA TAKEN AT NORMAL INCIDENCE AT 77 K.	5-58
FIGURE 5-35. PHOTORESPONSE SPECTRA OF A (110) Si/SiGe MQW SAMPLES WITH $x=0.30$ AND $L=20 \text{ \AA}$ AT 4 DIFFERENT TEMPERATURES. DATA TAKEN AT NORMAL INCIDENCE.	5-60
FIGURE 5-36. PHOTORESPONSE SPECTRA OF A (110) Si/SiGe MQW SAMPLES WITH $x=0.10$ AND $L=30 \text{ \AA}$ AT 2 DIFFERENT TEMPERATURES. DATA TAKEN AT NORMAL INCIDENCE.	5-61
FIGURE 5-37. PHOTORESPONSE SPECTRA OF A Si[110]/SiGe MQW SAMPLES WITH $x=0.30$ AND $L=20 \text{ \AA}$ AT 5 DIFFERENT VOLTAGES. DATA TAKEN AT NORMAL INCIDENCE. INSET SHOWS DEPENDENCE OF +PEAK INTENSITY ON BIAS VOLTAGE.	5-64
FIGURE 5-38. (A) PHOTORESPONSE SPECTRA OF A Si[001]/SiGe MQW SAMPLE WITH $x=0.30$ AND $L=30 \text{ \AA}$ AT 2 DIFFERENT GROWTH TEMPERATURES. DATA TAKEN AT NORMAL INCIDENCE. (B) NORMALIZED SPECTRA.	5-66
FIGURE 5-39. PHOTORESPONSE SPECTRA OF A [001] AND [110] Si/SiGe MQW SAMPLE WITH $x=0.30$ AND $L=30 \text{ \AA}$. DATA TAKEN AT NORMAL INCIDENCE AT 77 K. GROWTH TEMPERATURE = 710 °C.	5-67
FIGURE 5-40. SPECTRA THAT SHOW THE PHOTORESPONSE CAN BE TUNED TO COVER THE 3 TO 12 μm WAVELENGTH RANGE. THE TOP CURVE IS PLOTTED VS. ENERGY AND SHOWS THE PREDICTED VALUES FOR THE LONG WAVELENGTH CUTOFF AND PEAK POSITION. THE BOTTOM CURVE IS PLOTTED VS. WAVELENGTH AND SHOWS THE TUNING EFFECT WITH CHANGE IN Ge COMPOSITION.	5-69
FIGURE 5-41. PHOTORESPONSE SPECTRA OF MULTI-COLOR DETECTOR #1 TAKEN AT THREE DIFFERENT TEMPERATURES UNDER NORMAL INCIDENCE AND 1 V BIAS.	5-70
FIGURE 5-42. PHOTORESPONSE SPECTRA OF MULTI-COLOR DETECTOR #2 TAKEN AT THREE DIFFERENT TEMPERATURES UNDER NORMAL INCIDENCE AND 1 V BIAS.	5-71

List of Tables

TABLE 3-1. CALCULATED ZONE CENTER ENERGIES FOR Si[001]	3-79
TABLE 3-2. CALCULATED ZONE CENTER ENERGIES FOR Si[110]	3-80
TABLE 4-1. ABSORPTION COEFFICIENTS AND PENETRATION DEPTHS OF AVAILABLE LASER LINES.....	4-7
TABLE 5-1. PL EMISSION PEAKS ASSOCIATED WITH BORON IMPURITIES.	5-6
TABLE 5-2. IDENTIFIED PHONONS AND THEIR ENERGY VALUES.	5-7
TABLE 5-3. PHOTOLUMINESCENCE PEAKS DUE TO CARBON RELATED DEFECTS.	5-9

List of Symbols

AB	absorption
A-D	analog to digital
AFIT	Air Force Institute of Technology
BLIP	background limited performance
BZ	Brillouin zone
CCD	charge coupled device
CG	Clebsch-Gordan
CVD	chemical vapor deposition
DTGS	deuterated triglycine sulfate
EFA	envelope function approximation
eV	electron volt
FPA	focal plane array
FTIR	Fourier transform infrared spectroscopy
FTS	Fourier transform spectroscopy
FWHM	full width half maximum
H	Hamiltonian
$H_{\mathbf{k} \cdot \mathbf{p}}$	$\mathbf{k} \cdot \mathbf{p}$ Hamiltonian
H_{so}	spin-orbit Hamiltonian
H_{strain}	strain Hamiltonian
V_{offset}	barrier potential
HBT	heterojunction bipolar transistors
HH	heavy hole
HIP	heterojunction internal photoemitter
IP	internal photoemission
IR	infrared
LEED	low energy electron diffraction
LH	light hole

LHe	liquid helium
LN	liquid nitrogen
LK	Luttinger-Kohn
LWIR	long wavelength infrared detector
MBE	molecular beam epitaxy
MCT	mercury cadmium telluride
MOSFET	metal oxide field effect transistor
MQW	multiple quantum well
NRL	Naval Research Laboratory
PL	photoluminescence
PR	photoresponse
QW	quantum well
QWIP	quantum well infrared photodetector
SiGe	silicon germanium
SO	split-off
TEM	tunneling electron microscopy
VLSI	very large scale integration
Å	Angstrom (10^{-10} m)
μm	micron (10^{-6} m)

Abstract

A study has been carried out on Si/SiGe multi-quantum well structures to determine their applicability as normal incidence infrared detectors in the spectral range of 2-12 μm . The research effort was primarily experimental, however, extensive calculations were performed to initially explain the experimental data and then used to design subsequent structures. Multiple quantum well structures grown on both Si[001] and Si[110] substrates via molecular beam epitaxy were studied by photoluminescence, absorption, and photoresponse measurements over a wide parameter space. Variables included quantum well depth and width, well doping, number of wells and growth temperature. Well widths were varied from 20Å to 50Å, Ge composition from 10% to 60%, boron doping from $1 \times 10^{18} \text{ cm}^{-3}$ to $8 \times 10^{19} \text{ cm}^{-3}$, number of wells from 5 to 30 and growth temperature from 550°C to 710°C.

Calculations using $\mathbf{k} \cdot \mathbf{p}$ theory and the envelope function approximation were performed to determine the position of the bound states in the wells, the amount of band mixing and the transition strengths for bound-to-bound transitions for Si[001]/Si_{1-x}Ge_x, Si[110]/Si_{1-x}Ge_x and GaAs/AlGaAs quantum well structures. The Si[110] structures have more allowed energy bands which are significantly mixed. A comparison was made between Si[001]/Si_{1-x}Ge_x, Si[110]/Si_{1-x}Ge_x and GaAs/AlGaAs quantum well structures designed to operate in the 8-12 μm region, and all three showed comparable momentum matrix elements.

OPTICAL DETECTION PROPERTIES OF SILICON-GERMANIUM QUANTUM WELL STRUCTURES

1. Introduction

The Air Force is interested in the development of an infrared (IR) photodetector that is (a) usable in the 3-5 μm or 8-12 μm atmospheric transmission windows; (b) operable at temperatures greater than the 20-30 K currently required by bulk material detectors; and (c), affordable. Bulk mercury cadmium telluride (HgCdTe) is currently the material of choice to cover this particular wavelength range. Unfortunately, even though both the government and industry have spent millions of research dollars trying to improve this material, HgCdTe is still not the optimum solution, because it not only suffers from poor uniformity and reproducibility, but it contains toxic constituents as well. The most mature semiconductor material is of course silicon, but bulk silicon is not conducive to making detectors in the previously mentioned wavelength ranges. However, quantum well structures made from silicon-germanium (SiGe) alloys may be used to produce a detector which is responsive in these wavelength regions. Researchers have exhaustively studied bulk silicon and germanium materials over the last forty years, and naturally, the silicon-germanium alloy system has also been investigated for possibilities of novel heterostructures. However, an inability to grow high-quality,

lattice-mismatched layers, such as Si/Si_{1-x}Ge_x (i.e. Si_{0.70}, Ge_{0.30} represents 70% Si and 30% Ge in the alloy), has hindered the development of practical devices. Not until the evolution of molecular beam epitaxy (MBE) in the late 1970s were strained-layer SiGe alloys grown that could be used in practical devices. In recent years, however, advances in MBE and chemical vapor deposition (CVD) techniques have led to growth of high quality Si/Si_{1-x}Ge_x layers. These layers are currently used on a small scale to fabricate heterojunction bipolar transistors (HBTs) and metal oxide semiconductor field effect transistors (MOSFETs). Some work has been done on the development of photodetectors using MBE grown epitaxial layers, but it has not progressed beyond the research level.

There are four primary reasons for considering a quantum well infrared photodetector (QWIP) made from SiGe alloys. First of all, using quantum wells with varying alloy compositions and well widths provides great flexibility in tuning the response of the detector to the desired wavelength range. QWIPs can also be fabricated to respond in multiple wavelength bands simultaneously by using multiple well width and well depth combinations on a single device. In addition, QWIPs will operate at 77 K. Secondly, normal incidence detection, which is desirable in any detection scheme, may be enhanced in SiGe QWIPs. Normal incidence detection eliminates the need for waveguides or gratings to couple the incident light into the device region, thus reducing processing steps and cost. Thirdly, the potential for cost reduction in the production of the detector itself and its associated signal processing circuitry is very large. Most of the signal processing electronics in use today is based on silicon technology, and silicon devices will most likely dominate the electronics market in the future because there is no

other material that can match it in performance and cost. As a result, industry is interested in matching new technology to silicon very-large-scale-integration (VLSI) circuits. Monolithic integration of Si/Si_{1-x}Ge_x electro-optic devices with silicon signal-processing circuitry would eliminate the need for multi-material process lines and hybrid circuits, both of which significantly increase processing complexity and cost. Finally, a Si/SiGe QWIP should provide superior uniformity to make IR focal plane arrays (FPAs). FPAs based on other materials, notably HgCdTe, are currently used for thermal imaging, guidance, reconnaissance, surveillance, ranging and communication systems, but they suffer from uniformity and reproducibility problems.

The broad goal of this research was to theoretically and experimentally characterize Si/Si_{1-x}Ge_x quantum well heterostructures, grown on Si[110] substrates, to determine the validity of their use in QWIPs and suitability to Air Force needs. The non-conventional substrate orientation, Si[110], was chosen with the belief that normal incidence absorption properties would be enhanced, thus leading to a better and less expensive photodetector. More specifically, the objective was to determine if Si[110]/SiGe MQWs could be tuned to respond in the 3-12 μm wavelength region and operate under normal incidence illumination at 77 K.

To obtain those objectives, a wide parameter space of multiple quantum well material was selected for growth via MBE, with variables in well depth, well width, doping level, repeat periods, growth temperature and substrate orientation to determine the usefulness of the SiGe alloy system for QWIPs. Doped and undoped MQWs were examined with the photoluminescence (PL) technique to determine crystal quality and the

effects of doping. The doped materials were measured for their infrared absorption (AB) properties as a function of electric field polarization via Fourier transform spectroscopy (FTS). After initial attempts at interpreting the absorption data, it became apparent that a much deeper theoretical understanding of the materials and structures was necessary, and so appropriate models were developed to predict the dispersion relations in the planes perpendicular to the growth direction, wave functions, effective masses, oscillator strengths and Fermi energies. The samples were then reassessed as to their absorption properties and then photoresponse (PR) measurements were made on the same samples as a function of sample temperature, and applied bias. Using the extended theoretical models developed in this dissertation, the experimental data can be qualitatively explained, with the result that Si/Si_{1-x}Ge_x quantum well structures can be shown to be viable IR detectors which can be grown to elicit the desired response in the desired wavelength range.

A detailed description of the work performed is found in the following chapters. Chapter 2 provides background material and contains a discussion of various detector schemes and the advantages of SiGe QWIPs in particular. An explanation of the theoretical calculations used to predict the performance of QWIP structures is developed in Chapter 3 along with a theoretical comparison of a GaAs/AlGaAs structure and a Si/SiGe structure designed for photodetection at 10 μm . Experimental procedures and equipment used in making photoluminescence, absorbance, and photoresponse measurements are described in Chapter 4. Experimental data obtained is presented and discussed in Chapter 5. Conclusions and recommendations for further work are found in

Chapter 6 followed by the Appendices and the Bibliography. A separate supplement to the dissertation, which contains computer programs developed in the theoretical sections, has also been prepared, and is available on request.

There are several contributions made to the current body of knowledge by this dissertation. First of all; it presents a computational model which is now available to treat MQW structures grown on non-conventional orientation substrates, Si[110] substrates in particular. Before this study, only MQWs grown on [001] substrates could be fully treated by established theory while [111] oriented MQWs were treated to a lesser extent in the literature. However, the [110] oriented MQWs were not treated in the literature and thus required one to return to the fundamental Luttinger-Kohn theory and develop the entire computational scheme for pertinent calculations on such structures. The model includes the capability to obtain the dispersion relations, transition strengths for bound-to-bound transitions and an estimate of the Fermi energy. Secondly, credible FTIR absorption spectra have been obtained for the first time on [110] SiGe MQWs. Careful absorption measurements which correlate well with the theoretical predictions were obtained on a wide range of samples. Thirdly, photoresponse spectra have been obtained for the first time on [110] SiGe MQWs. The parameter space explored is much greater than the data presented in the literature on [001] SiGe MQWs. These spectra also correlate well with theoretical predictions. Finally, Si[110]/SiGe and Si[001]/SiGe MQWs are shown experimentally to be viable IR detectors. They can be effectively tuned to cover the 3-12 μm wavelength region, and they operate at 77 K under normal incidence conditions. It is also shown theoretically that the SiGe QWIPs should have

performance greater than or equal to GaAs/AlGaAs QWIPs which is the current state-of-the-art QWIP material.

2. Background

A. Infrared Photodetectors

Infrared detectors are usually classified as thermal or photon devices. Thermal detectors operate on the principle that absorption of infrared energy will raise the temperature in the device causing a change in some material property such as electrical conductivity. Photon detectors operate on the principle that absorption of a photon will cause a specific quantum event, such as an interband transition in a semiconductor.¹ Photon detectors can be further divided into the following classes: photoconductors, which generate a current; photovoltaics, which generate a voltage; or photodiodes which can be operated in either a photoconductive or photovoltaic mode. These devices are intrinsically faster than thermal detectors and are desirable for processes that require rapid detection such as imaging, tracking, and surveillance. Infrared (IR) photon detectors are generally divided into four groups, each with distinct advantages and disadvantages: intrinsic (non-doped), extrinsic (doped), free-carrier (metal silicide-Schottky barrier), and quantum well detectors. Figure 2-1 shows the detectivity for various intrinsic and extrinsic photodiodes and photoconductors. Infrared detectors made from the group II-VI ternary alloy, mercury-cadmium-telluride ($\text{Hg}_{1-x}\text{Cd}_x\text{Te}$ or MCT), an intrinsic material, currently dominate the market much like silicon dominates signal processing applications. Other intrinsic detectors, not as technologically advanced, have been fabricated from $\text{InAs}_{1-x}\text{Sb}_x$ (InAsSb), $\text{Hg}_{1-x}\text{Zn}_x\text{Te}$ (HgZnTe) and $\text{Hg}_{1-x}\text{Mn}_x\text{Te}$ (HgMnTe).

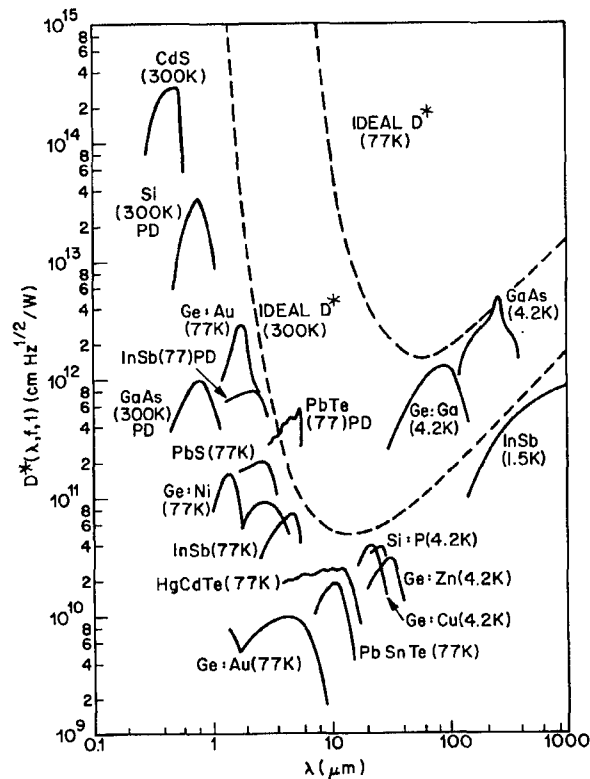


Figure 2-1. Detectivity, D^* , as a function of wavelength for various photoconductors and photodiodes (indicated with PD).²

HgCdTe is a direct band gap semiconductor and absorption occurs via interband (valence band to conduction band) transitions in the bulk material as shown in Figure 2-2. By varying the Hg to Cd ratio, the band gap of HgCdTe can be tailored to absorb IR radiation at wavelengths of interest from 1 to 25 μm . (see Figure 2-3) Intrinsic photon detectors like HgCdTe are characterized by high optical absorption coefficients and large quantum efficiencies and have the added advantage of relatively low thermal generation rates compared to extrinsic or free-carrier devices. As a result, the operating temperature for

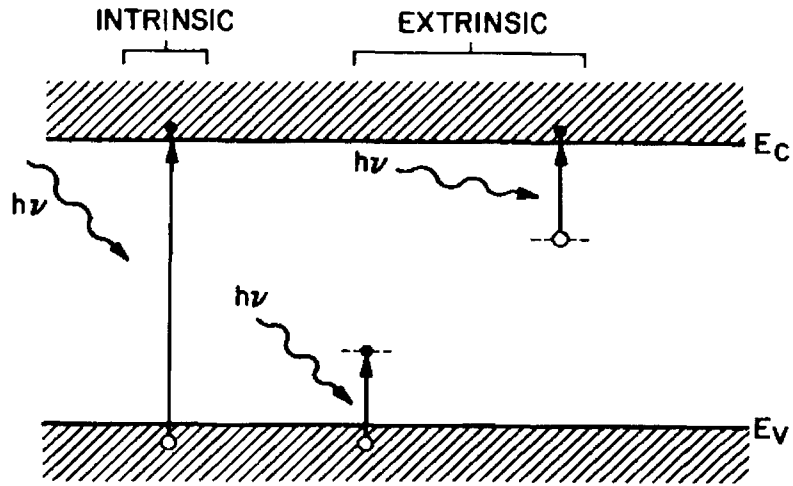


Figure 2-2. Processes of intrinsic (band-to-band) and extrinsic photoexcitations.²

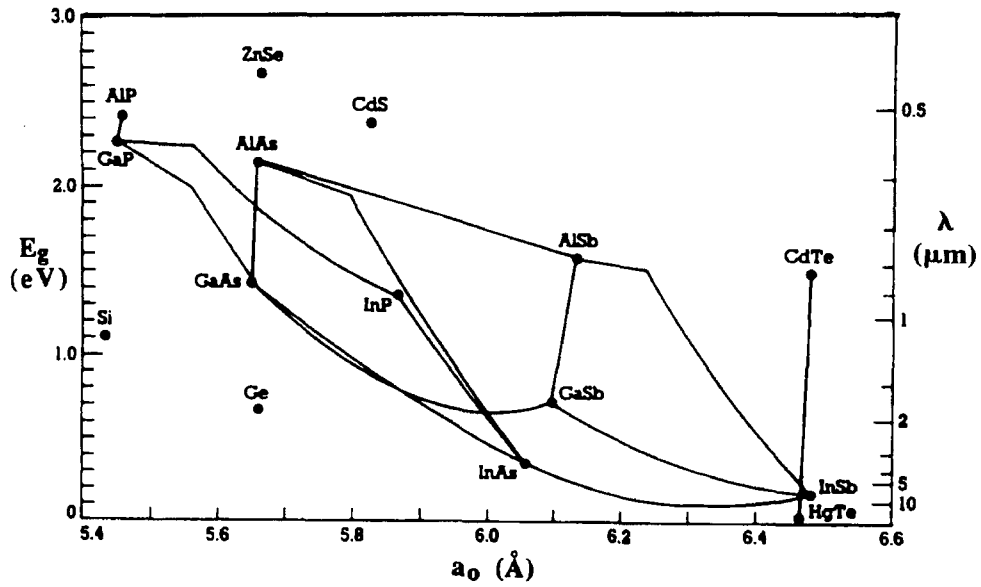


Figure 2-3. Room temperature bandgaps, lattice constants, and wavelength cutoffs for group III-V, II-VI, and group IV alloy systems.³

intrinsic detectors is higher than for other types of photon detectors. These desirable attributes translate to a flexibility in design and the capability to produce IR detectors with background-limited performance (BLIP) at temperatures greater than 77K.⁴

HgCdTe does however have significant disadvantages. Millions of research dollars have been used to fund research on this alloy system over the past thirty years to improve crystal uniformity of bulk materials and epitaxial layers. Such research has led to improvements, but the uniformity remains a problem for large array applications at the longer wavelengths. In addition the materials used in this alloy are highly toxic.

In contrast to the HgCdTe system, extrinsic Si detectors have the advantages of uniformity, reliability and easy integration with low noise Si readout circuitry, but they are very limited in flexibility of design. Extrinsic photoconductivity operates on transitions between bound and free states as shown in Figure 2-2. A photon interacts with a bound electron at a donor site to produce a free electron and bound hole, or a photon interacts with a bound hole at a acceptor site to produce a free hole and a bound electron. The limited flexibility is derived from the small spread in activation energies associated with dopant impurities. Boron is a commonly used acceptor in silicon with an activation energy of 44 meV which corresponds to a long-wavelength cutoff of 28 μm . Since extrinsic Si detectors contain no heterojunctions they can be fabricated with superior uniformity over the wide area which is necessary to fabricate large FPAs. However, they must be cooled to liquid helium temperatures to minimize thermal excitation. Such cooling requirements are a significant disadvantage for space based applications where weight is a primary factor. For both intrinsic HgCdTe and extrinsic Si

detectors, photoabsorption and carrier transport take place in the bulk semiconductor.

(see Figure 2-4)

Internal photoemission (IP) detectors offer an alternative approach in which photon absorption takes place in the contact or electrode region, and the resulting hot carrier is emitted over a potential barrier into a semiconductor depletion region as shown in Figure 2-5. The resulting charge in the contact is then injected into a charge coupled device (CCD). These free carrier detectors have generated great interest in the past decade. $\text{Pd}_2\text{Si}/\text{p-Si}$ Schottky photodiodes have been developed for the 1 to 3.5 μm region while $\text{PtSi}/\text{p-Si}$ Schottky photodiodes, the most advanced IP detector at this time, have been demonstrated for use in the 3 to 5 μm wavelength region.⁵ While these detectors have the uniformity and reproducibility necessary for fabrication of 1024 by 1024 element arrays,⁶ they are limited in their spectral range of response. In addition, the

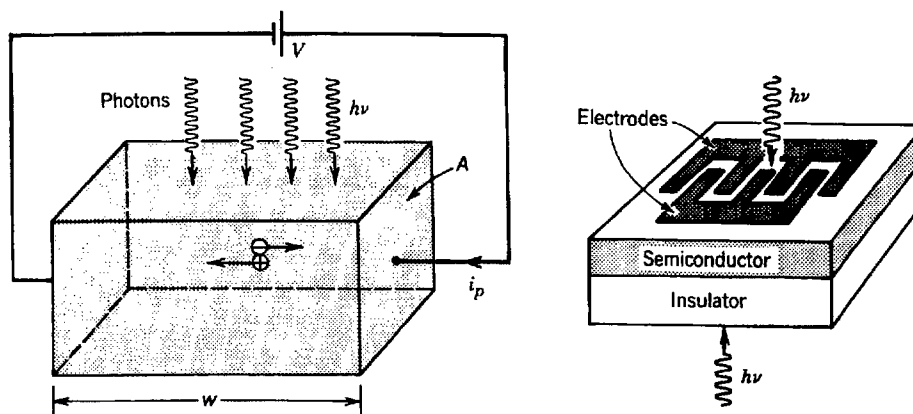


Figure 2-4. The photoconductor detector. Photogenerated carriers move in response to the applied voltage V , generating a photocurrent i_p proportional to the incident photon flux.¹

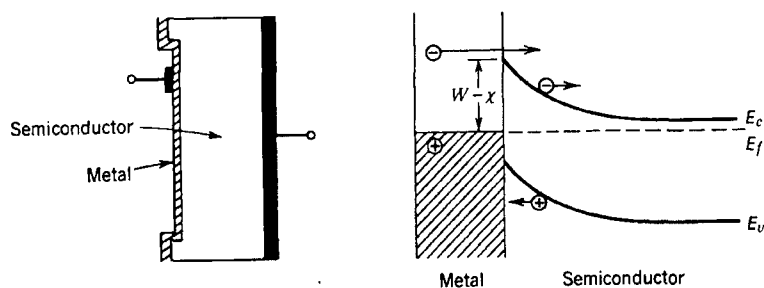


Figure 2-5. Structure and energy band diagram of a Schottky barrier photodiode formed by deposition a metal on an n-type semiconductor.¹

effective quantum efficiency in the 3 to 5 μm range is on the order of 1%. Dark current is dominated by thermionic emission in internal photoemitters, and so a tradeoff exists between lower potential barriers, which allow longer wavelength response, and lower operating temperatures. Attempts have been made to push the response out to 8 μm with iridium silicides, but these efforts have not been entirely successful. With the advent of silicon MBE epitaxial growth, Si/SiGe heterojunction internal photoemission (HIP) IR detectors have been fabricated and demonstrated to exhibit tailored response from 2 to 10 μm with a quantum efficiency on the order of 4%.⁷ The idea for HIP detectors, or free carrier detectors, was first proposed by Shepherd *et al.* in 1973⁸ but, due to lack of growth technology, was not demonstrated until 1990 by Lin *et al.*⁹ The detection mechanism involves infrared absorption in the SiGe region followed by internal photoemission of the excited holes over the effective barrier height. The infrared absorption occurs primarily through free carrier absorption due to the heavy doping in the alloy. The HIP structure consists of a degenerately doped p^+ -SiGe layer as the emitter

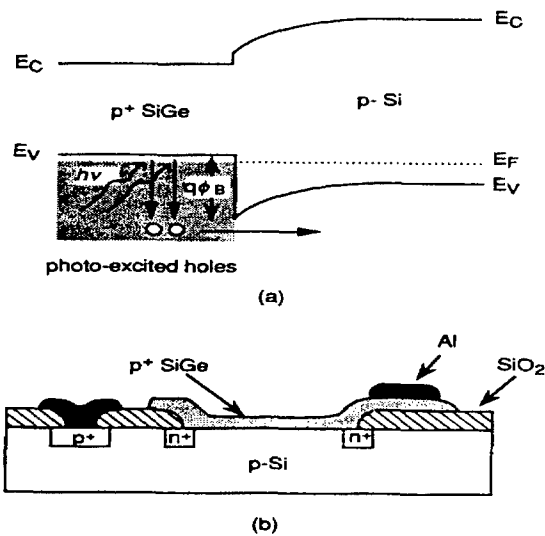


Figure 2-6. (a) Energy band diagram of the $p^+ \text{Si}_{1-x}\text{Ge}_x/\text{p-Si}$ HIP detector (b) Structure of the test device.⁹

(vs. the metal silicide in the IP) and a p-type Si substrate as the collector. (see Figure 2-6)

Holes are the majority carrier because the band offset between Si and SiGe is almost entirely in the valence band. The long wavelength cutoff is determined by the effective barrier height which is in turn determined by the energy difference between the Fermi level in the SiGe layer and the valence band offset. The valence band offset varies with Ge concentration in the SiGe layers. In Schottky detectors, photons can excite carriers from states far below the Fermi energy which do not gain sufficient energy to overcome the barrier. Only those carriers excited from states near the Fermi energy can exceed the barrier energy. The quantum efficiency, Y , for internal photoemission is given by

$$Y = C_f (h\nu - \Psi_0) / h\nu, \text{ where } C_f \text{ is the Fowler emission coefficient that depends}$$

inversely on the Fermi level, and Ψ_0 is the Schottky barrier potential.⁵ In contrast, the narrow band of absorbing states in the $p^+ \text{Si}_{1-x}\text{Ge}_x$ layer of the HIP leads to a sharper turn-on. According to Lin, “this property avoids a serious weakness of Schottky detectors where the Fowler’s dependence provides reasonable quantum efficiency only at photon energies well above the energy barrier, in which a device must be designed with a significantly lower barrier than the desired energy response, requiring a correspondingly lower operating temperature to reduce the dark current to acceptable values.”⁹ These devices are attractive because the strong free carrier absorption obtained is not restricted by the photon polarization field.

There has been interest in using free carrier absorption as the primary absorption mechanism for infrared detectors.¹⁰ The merit of this approach is that free carrier absorption is not constrained by selection rules and should therefore be sensitive to normally incident light. However, there is sufficient evidence both theoretically and experimentally (presented in Chapters 3 and 5) to show that quantum well infrared photodetectors are sensitive to normally incident light. The argument is also made that free carrier absorption is stronger than intersubband or intrasubband absorption. While this is undoubtedly true for long wavelengths because the free carrier absorption scales as the wavelength squared, this is not true for the 3-12 μm region as will be shown later in Chapter 5. Because free carrier absorption depends on phonon interaction to conserve momentum, the quantum efficiency of a detector based on this approach is intrinsically lower than that of a detector based on direct transitions such as a quantum well infrared photodetector.

Like the HIPs, quantum well infrared photodetectors (QWIPs) also employ heterojunctions of semiconductor alloys. If the individual wells are placed in close proximity so that the wave functions of neighboring wells overlap, the structure is called a superlattice. Conversely, if the wells are spaced far enough apart to minimize wavefunction overlap, the structure is called a multiple quantum well. Since their conception by Esaki and Tsu in 1970,¹¹ a wealth of applications for quantum wells and superlattices have intrigued researchers. However, development of MBE growth techniques was necessary before high-quality, quantum well structures could be fabricated. Semiconductor hetero-interfaces exhibit abrupt discontinuities in the local band structure and thus quantum wells can be made by growing alternating layers of differing materials. There are four types of quantum well structures as shown in Figure 2-7. The allowed energies in the well are quantized and their exact values depend on the well width and the barrier height. In addition, strain induced by lattice mismatch of the epitaxial growth will shift the energy levels. Quantum well features are also produced by δ -doping (see Figure 2-8) in which the growth of highly doped well regions is followed by growth of intrinsic regions.

Absorption in QWIPs takes place between the ground state in the well and a bound excited state or an excited state in the continuum above the barrier. A photocurrent is produced when the device is biased to sweep excited carriers out of the well region as

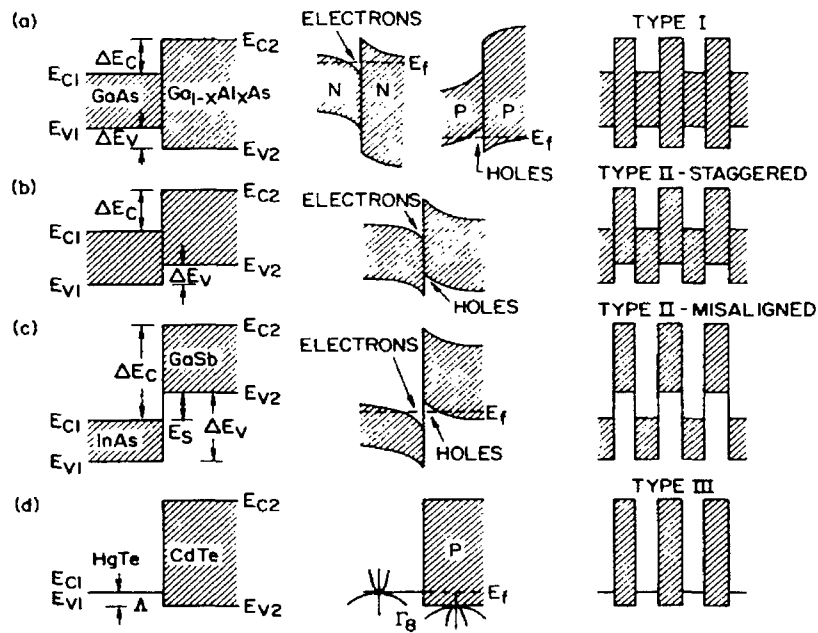


Figure 2-7. Discontinuities of bandedge energies at four kinds of interfaces: band offsets (left), band bending and carrier confinement (middle), and superlattices (right).¹²

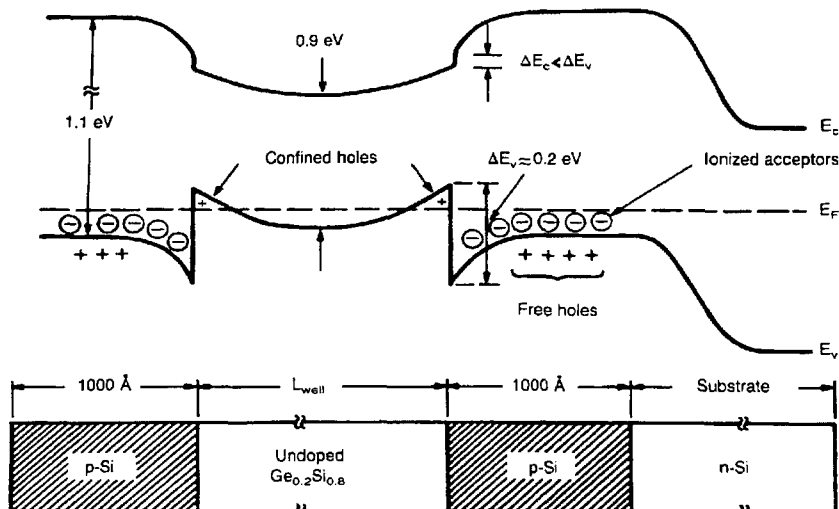


Figure 2-8. Modulation-doped Si-Ge superlattice.¹³

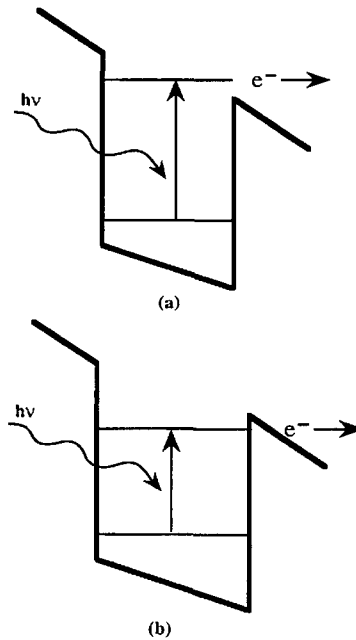


Figure 2-9. (a) Bound-to-continuum transition and (b) bound-to-bound transition in a quantum well structure under an applied electric field.³

shown in Figure 2-9. According to Manasreh and Brown,³ QWIPs are expected to have the following advantages over other detector types:

1. A higher degree of uniformity than MCT detectors, which is especially important for FPAs;
2. Smaller leakage currents due to suppression of tunneling available in superlattices;
3. Lower Auger recombination rates due to substantial splitting of the light- and heavy-hole bands;
4. Technologically mature device fabrication and materials processing techniques (especially true for Si and GaAs based structures);
5. Tunability of upper cutoff wavelengths;
6. Radiation hardness due to a very small active region;

7. Ease of crystal growth;
8. Detectivity (D^*) comparable to that of HgCdTe at temperatures as high as 80 K;
9. Lower cost due to compatibility with existing signal processing circuitry.

The GaAs/AlGaAs ternary system has been the most extensively studied for IR detector applications, but other material systems including InGaAs/InAlAs, InAs/GaInSb and Si/SiGe have been used to achieve wavelength response from 3 to 19 μm .⁴ The great advantage of using a silicon based detector is that it could be readily matched to silicon signal processing circuitry. As an added benefit, theoreticians have argued that the performance of Si/Si_{1-x}Ge_x MQWs should surpass the performance of GaAs/AlGaAs MQWs and should display enhanced photoabsorption.^{14,15} SiGe structures can be doped to a higher level than GaAs/AlGaAs structures due to a greater density of states which is, in turn, determined by larger effective masses and valley degeneracy. Greater doping will cause the Fermi level to drop in the well due to electron-electron exchange interactions thus inhibiting thermal generation. Larger effective masses will inhibit tunneling of electrons and holes through barriers, a problem which has proven significant for GaAs/AlGaAs structures. However, carriers with higher effective masses have poorer transport properties. Si/Si_{1-x}Ge_x devices should prove superior for normal incidence applications in n-type devices. The lowest conduction band minima of n-type superlattices or quantum wells of indirect materials are not oriented along the growth direction. Thus, n-type QWIPs exhibit an effective mass anisotropy especially on (110) oriented growth and show promise of having large optical matrix elements for

intersubband transitions at normal incidence. An alternative to n-type MQWs are the p-type MQWs for which the intersubband selection rules intrinsically allow normal incidence absorption. Szmulowicz and Brown¹⁶ argue that in p-type MQWs, a strong mixing of the valence bands and the conduction band occurs which imposes an s-like wave function symmetry on the normally p-like valence band wave functions. Transitions between a pair of bands with s-like and p-like symmetry components are allowed by selection rules thus creating the possibility of normal incidence absorption. In addition, the strong mixing of the light and heavy hole valence band states leads to the non-parabolicity and anisotropy of these bands. Just as in the case of the n-type structures, where anisotropy leads to off-diagonal effective mass components which can lead to normal incidence absorption, a similar effect is present in p-type structures. The exact nature of the optical transitions in p-type materials has proven difficult to model and is the focus of continued research at this time.

B. Silicon/Germanium Alloys

Even though the optical and electrical properties of Si/SiGe heterostructures are not well understood, the individual bulk properties of silicon and germanium are well understood and are tabulated in many sources. (see Appendix A) Silicon and germanium are both Column IV elements exhibiting tetrahedral bonding. They both have a diamond lattice structure which can be viewed as two interpenetrating, face-centered, cubic (FCC) sublattices with one sublattice displaced from the other by one quarter of the distance along a diagonal of the cube. (see Figure 2-10) The disadvantage of these materials individually is that they have indirect bandgaps and therefore are extremely poor optical emitters with low carrier mobilities compared to GaAs or InP. In addition, their tetrahedral bonding symmetry causes negligible change in index of refraction over a

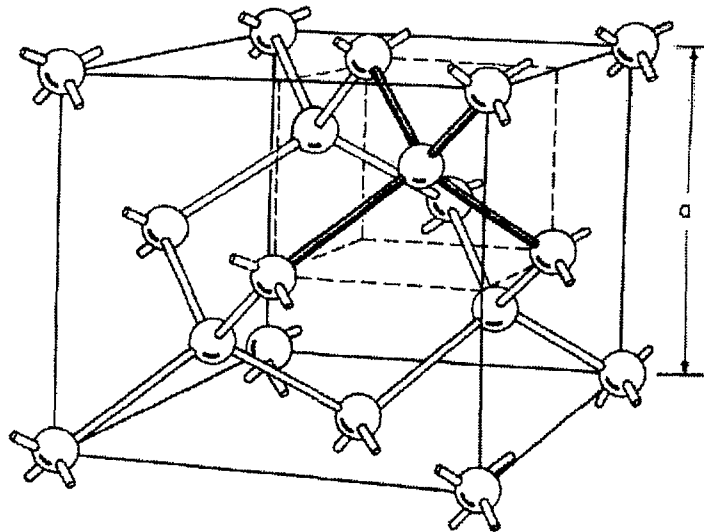


Figure 2-10. Diamond lattice crystal structure.²

relatively wide range of wavelengths, and as a result, they are not likely candidates for electro-optic modulators. One of the driving forces behind the development of the SiGe alloy system came from a desire to push the response of detectors out into the near IR since optical telecommunication systems use fused-silica-glass fibers with attenuation minima in the 1.3 to 1.5 μm range. Silicon photodiodes work extremely well in the visible and out to the Si absorption edge near 1.1 μm . The 1.12 eV band gap is sufficiently large to inhibit thermal generation yet small enough to remain sensitive. Germanium, however, with a bandgap of 0.7 eV is responsive out to 1.5 μm , but thermal generation becomes a problem. Researchers have known for many years that the fundamental indirect bandgap of bulk $\text{Si}_{1-x}\text{Ge}_x$ alloys spans this wavelength region, and extensive studies have determined the functional relationship between the alloy band gap and material composition. Study of the optical properties of $\text{Si}_{1-x}\text{Ge}_x$ alloys began in the 1950s with the work of Johnson and Christian¹⁷ and Levitas et al.¹⁸ Braunstein et al.¹⁹ performed a comprehensive investigation of the absorption edge in $\text{Si}_{1-x}\text{Ge}_x$ alloys in 1958. Paul and Warschauer²⁰ reported in 1959 the optical properties of $\text{Si}_{1-x}\text{Ge}_x$ alloys under hydrostatic pressure, thus determining the hydrostatic deformation potential. In 1963 Hensel and Feher²¹ performed cyclotron resonance measurements on silicon to determine the deformation potential under uniaxial strain while Murase et al.,²² performed similar experiments on germanium in 1970. These deformation potentials were used to determine the band gap in the $\text{Si}_{1-x}\text{Ge}_x$ alloys. Several attempts to produce high quality $\text{Si}_{1-x}\text{Ge}_x$ epilayers on single crystal silicon or germanium substrates in the early 1970s were not successful. In most cases the growth was three dimensional with large numbers

of threading dislocations, stacking faults and cracks in the layers. Unfortunately no purposeful work was achieved on the heterostructures until the advent of MBE and CVD growth techniques. The following paragraphs provide a brief historical sketch on the development of $\text{Si}_{1-x}\text{Ge}_x$ heterostructures in general, and significant advances in the development of QWIP structures in particular.

C. Previous Work

A thorough review of the historical development of Si/Si_{1-x}Ge_x heterostructures is placed in Appendix B, but a short summary is presented here. Kasper and co-workers at Bell Labs grew the first coherently strained Si_{1-x}Ge_x epilayers on silicon in 1975. Over the next ten years, the growth process was improved and fundamental studies on issues such as critical thickness were performed. An intense flurry of activity in the Si_{1-x}Ge_x field occurred between 1985 and 1992, beginning with the first functioning devices using the alloy in 1985. In 1989, Chang and James proposed that intersubband transitions in p-type quantum well structures could lead to normal incidence detection. Researchers at AT&T Bell Labs, including Bean, Bevk, Luryi, Pearsall, People, Temkin and others pushed the work in the mid to late eighties, while in the early nineties the work was been pushed principally by Lin at the Jet Propulsion Lab, Cal Tech and Karunasiri, Lee, Park, Wang and others at UCLA. Most of the work from the group at UCLA centered on absorption and photoresponse measurements for MQWs grown on Si[001] substrates. Although they published a large number of articles, much of the experimental data was repeated in subsequent papers. The effort has now broken down into smaller efforts with no single prolific group. The field has not exhaustively or even sufficiently been mined to consider the wide variation of parameters available to explore. A few groups are still exploring QWIPs while others are looking at HIPs. No group, other than the group at AFIT, is currently exploring QWIP devices on the non-conventional Si substrates, and to date, no one has published any experimental results on p-type Si[110] QWIPs. In general,

development of theoretical models is far behind the development of MQW structures. The difficulty in exploring the theory is that the calculations necessary to model the quantum well structures are very extensive and don't lend themselves to adequate and concise representation in the literature. It appears that the growth technology of Si/Si_{1-x}Ge_x heterostructures has sufficiently matured to where any conceivable quantum well structure can be grown, though growth of short period superlattices has not quite reached the same level. A deeper understanding of the band offsets, positions of energy levels, effects of high doping levels, valence band mixing and transport properties is necessary to achieve optimum performance from the Si_{1-x}Ge_x alloy system. For detector applications in particular, the drive for *normal* incidence detection necessitates a better theoretical understanding of device structures grown on (110) oriented substrates and experimental validation of the theoretical predictions.

This current research effort has placed an emphasis on developing MQWs on Si[110] substrates. To date, relatively little theoretical work has been done on the bulk properties of SiGe grown on Si substrates for this orientation,²³ and no work has been developed for the p-type MQWs. In addition, no experimental data on p-type structures exists. In this research, band structures and transition strengths have been developed from the **k•p** formalism with an extension into envelope function approximation theory. Furthermore, a wide parameter space of MQWs grown on Si(110) substrates has been explored using photoluminescence, absorption, and photoresponse measurements.

3. Theoretical Model For Valence Bands In Si/Si_{1-x}Ge_x Quantum Wells

A. Introduction

A theoretical understanding of the Si/Si_{1-x}Ge_x quantum well systems under investigation is an essential requirement for guiding and interpreting experimental observations. Values calculated from theoretical models can help explain experimental data and can facilitate the design of new structures. In this chapter, existing theoretical models are adapted to describe strained quantum wells grown along the crystalline [110] direction. Most of the theory for quantum well structures presented in the literature has been developed for the GaAs/AlGaAs system with the growth axis in the [001] direction, using $\mathbf{k}\cdot\mathbf{p}$ theory. This theory is applicable to any material system with a growth axis in the [001] direction provided the necessary constants are available. For example, the model used for GaAs/AlGaAs is easily extended to include strain effects and then adapted to describe a SiGe alloy system with the growth axis along the [001] direction. However, the model for quantum well structures with the growth axis in the [110] direction is *not* in the literature for either GaAs/AlGaAs or Si/SiGe. Furthermore, the model for [001] material *cannot* be modified by simply changing constants to obtain a [110] model. The [110] model must be completely derived using the basic elements of $\mathbf{k}\cdot\mathbf{p}$ theory. One of the primary contributions of this work is the detailed development of the expressions for the total 6 x 6 Hamiltonian describing strained Si_{1-x}Ge_x in the [110] direction. These expressions for strained bulk material are then used in the envelope

function approximation to obtain dispersion relations for [110] quantum well structures. Dispersion relations and band decompositions for Si[110] /SiGe quantum well structures are *not* in the literature and are presented here for the first time. The [110] dispersion relations differ both quantitatively and qualitatively from the dispersion relations for [001] material.

For historical perspective it is necessary to mention a few of the seminal papers in the development of band theory, particular as they apply to SiGe alloys. The roots of $\mathbf{k} \cdot \mathbf{p}$ theory, the primary method found in the literature for determining quantum well band structures, are found in the work performed in the mid 1950's by Luttinger and Kohn, Kane, and Dresselhaus, Kip and Kittel using degenerate perturbation theory.^{24, 25, 26} In 1963, Hasegawa authored a paper discussing the valence band structure in silicon single crystals subjected to a uniaxial stress.²⁷ In the paper he wrote out explicit equations for the 6×6 $\mathbf{k} \cdot \mathbf{p}$ and strain Hamiltonians for the [001] direction in terms of the orbital angular momentum operators. Hensel and Feher also published a paper in 1963 in which they gave a general form of a 4×4 Hamiltonian, in terms of the total angular momentum operator, for the three primary directions in the cubic crystal [001], [110], and [111].²⁸ However, since they used the $|j m_j\rangle$ representation of the total angular momentum operator, J , instead of the orbital angular momentum operator, L , the coupling between the split-off band and the heavy hole and light hole bands are not properly accounted for. (Note that hereafter for simplicity of notation, m_j will be written as m). In 1966 Cardona and Pollak published the band structure for Si and Ge calculated via a 15 band, $\mathbf{k} \cdot \mathbf{p}$ model along the [001] and [111] directions.²⁹ Ma, Wang and

Schulman calculated the band structure of coherently grown $\text{Si}_{1-x}\text{Ge}_x$ alloys on different orientation substrates in 1993 using a semi-empirical tight-binding method.³⁰

The modeling of the band structure of quantum well materials did not begin to develop until the early 1980's or about the time that quantum well structures could be grown via MBE and MOCVD. Since [100] substrates are the most common material to grow on, a very large majority of the models were developed with the [001] growth direction in mind. Two methods for modeling the quantum well energy levels which are microscopic in nature are the empirical tight-binding approach and the pseudopotential approach. The empirical tight-binding approach begins with a series of energies characteristic of the atomic sp^3 bonds which connect one atom to another. The wavefunction is determined by considering the consecutive addition of atoms. In 1985, Schulman and Chang used tight-binding equations to point out that valence band mixing is significant in GaAs/AlGaAs quantum wells, and that dipole-allowed transitions are allowed between all pairs of valence and conduction subbands.³¹ In the pseudopotential formalism, consecutive layers of material which form the quantum well are treated as perturbations to the bulk. In 1986, Smith and Mailhot used an empirical pseudopotential to calculate quantum well band structures.³² The advantage of these approaches is that they describe the band structure throughout the entire zone. However, they are somewhat computationally intensive.

A third approach to modeling the energy levels, called the envelope function approximation (EFA), was adapted from effective mass theory which had been used for more than 30 years to calculate the energy levels of impurities in a crystal. A detailed

discussion of the EFA is presented in Section E of this chapter. In this adaptation, the quantum wells, rather than impurities, break the translational symmetry of the lattice. In the absence of translational symmetry, the electronic wavefunction in the growth direction is given by the product of the periodic part of the Bloch function at zone center together with an envelope function. Early applications of the EFA for analyzing QW structures are found in the work of White and Sham,³³ Altarelli,³⁴ Schuurmans and t'Hooft,³⁵ and Bastard.^{36,37} The envelope function approximation is versatile and readily adaptable to include strain effects. Furthermore, the energy levels of interest for actual devices are near high symmetry points, such as zone center, for which the EFA compares favorably with the tight-binding method.³⁸ Chang and James,³⁹ were the first to use envelope function theory on GaAs/AlGaAs quantum wells to show that normal incidence absorption could be obtained in p-type MQWs using a 4 x 4 representation of the quantum well Hamiltonian. Their approach was later refined and expanded to an 8 x 8 representation of the quantum well Hamiltonian for an unstrained GaAs/AlGaAs system by Szmulowicz.⁴⁰ These models use momentum matrix elements to determine the strength of the quantum well transitions. However, as in the case of the bulk Hamiltonian, these momentum matrix elements used by Chang and James and Szmulowicz for [001] material cannot be simply modified to describe material grown along different crystallographic directions. Thus the momentum matrix elements for [110] material are also derived and presented here for the first time.

Once the machinery for deriving the [110] bulk Hamiltonian and momentum matrix elements is developed, it may be used to rederive the [001] Hamiltonian and

momentum matrix elements to verify the procedure, as well as to analyze QW systems grown along any direction. Although the steps needed to derive the bulk Hamiltonian for arbitrary growth directions are scattered throughout the literature they are not collected in a single paper or book. Therefore, it seems pertinent to outline all the steps in this document, and so the remainder of this chapter is organized as follows. Unstrained bulk energy band structures are discussed in Section B. These structures are obtained by considering the Luttinger-Kohn form of the $\mathbf{k}\cdot\mathbf{p}$ Hamiltonian, $H_{\mathbf{k},\mathbf{p}}$, where $E=E(\mathbf{k})$ is given by the eigenvalues of a 6×6 matrix representation of the Hamiltonian. The effects of strain are discussed in Section C where a separate Hamiltonian, H_{strain} , is formulated. In addition, a Hamiltonian to account for spin-orbit effects, H_{so} , and a potential energy term, V_{offset} are also considered. In Section D, a rough approximation to the bound energy levels is determined by considering the heavy hole, light hole and split-off bands independently. This simple calculation assumes that the valence bands are decoupled and that the wave function can be approximated by a simple plane wave. In fact, the bands *are* coupled and the wave function is not adequately approximated by a plane wave. These deficiencies are corrected by using envelope function approximation theory (EFA) which is developed in Section E. The EFA formalism shows that although the uncoupled band approach provides an elementary description of Si[001] MQWs, it is not adequate for Si[110] MQWs. A discussion of the transition strengths is presented in Section F, and a discussion of the approximations used to find the Fermi energy is in Section G. The computational models are used in Section H to make comparisons between [110] and [001] Si/SiGe and [001] GaAs/AlGaAs quantum well structures that

will operate in the 10 μm region. Finally in Section I, values for the zone center energy levels are tabulated using the simple analysis and the more sophisticated EFA analysis.

B. $\text{Si}_{1-x}\text{Ge}_x$ Unstrained, Bulk Band Structure

As in most solid state problems, the analysis of the electronic and optical properties of quantum well structures begins with a determination of the energy band structure, $E=E(\mathbf{k})$, also called the dispersion relations. Dispersion relations for the thin, epitaxial $\text{Si}_{1-x}\text{Ge}_x$ layers used in QWIP structures are difficult to obtain for several reasons. First, most theoretical models require empirically determined data as input. Unfortunately, little experimental determination of the bulk properties of $\text{Si}_{1-x}\text{Ge}_x$ alloys has been made even though the bulk properties are well known for Si and Ge individually. As a result, most parameters for bulk $\text{Si}_{1-x}\text{Ge}_x$ are obtained by linear interpolation between the Si and Ge values. Second, theoretical characterization of lattice mismatched, Si/ $\text{Si}_{1-x}\text{Ge}_x$ heterostructures is further complicated because epitaxial growth can proceed as strained, relaxed, or partially relaxed. Strained growth occurs because silicon and germanium have lattice constants which differ by 4.2 %, ($a_{\text{Si}} = 5.431 \text{ \AA}$, $a_{\text{Ge}} = 5.657 \text{ \AA}$) which is very large for epitaxial growth. As more germanium is introduced into the alloy, the lattice becomes more distorted thus causing more strain. The introduction of strain reduces symmetry in the crystal, partially lifting the degeneracy in the valence bands at the center of the Brillouin zone (BZ). In addition, the energy bands become nonparabolic and anisotropic, thereby inducing a change in the effective masses. Once bulk Si and strained bulk $\text{Si}_{1-x}\text{Ge}_x$ properties are understood, the bulk pictures for the barrier region and well region can be combined to model a quantum well.

The $\mathbf{k}\cdot\mathbf{p}$ method for obtaining band structures was chosen for this research primarily for its ease of implementation. In the $\mathbf{k}\cdot\mathbf{p}$ method, the band structure in the vicinity of a high symmetry point in \mathbf{k} space, such as the gamma point, Γ , depends on a small number of parameters (band gap, effective masses, and spin-orbit splitting) which may be determined by experiment. It is particularly well suited to include external perturbations like strain and can be readily adapted to heterostructures. This method has proven to be an effective tool for the study of energy bands and wave functions for over 40 years.^{26,41,42} The accuracy of the approach may also be determined by comparison with methods that provide a more global description of the band structure such as the tight binding method. Eppenga has shown that the confined energies and transition strengths derived from $\mathbf{k}\cdot\mathbf{p}$ theory applied to quantum wells, are in excellent agreement with results obtained from tight-binding theory.³⁸

The following section is a brief derivation of the matrix representation of the bulk Hamiltonian. The reader is referred to Luttinger and Kohn²⁴ for more details. They developed a simple matrix expression for the Hamiltonian of bulk semiconductors from which the band structure close to the Brillouin zone center can be obtained. For systems with cubic (O_h) symmetry, the matrix may be further simplified and expressed as a function of angular momentum matrices, the wavevector \mathbf{k} , and empirically determined parameters referred to as Luttinger coefficients. The Luttinger coefficients, or effective mass parameters, are determined through cyclotron resonance measurements.

The analysis of the bulk dispersion relations begins with Schrodinger's equation for an electron moving in a three dimensional lattice,

$$H\Psi_{\mathbf{n}\mathbf{k}}(\mathbf{r}) = \left\{ \frac{\mathbf{p}^2}{2m} + V(\mathbf{r}) \right\} \Psi_{\mathbf{n}\mathbf{k}}(\mathbf{r}) = E_n(\mathbf{k})\Psi_{\mathbf{n}\mathbf{k}}(\mathbf{r}), \quad (3-1)$$

where $\mathbf{p} = -i\hbar\nabla$, and $V(\mathbf{r})$ is an effective potential with the periodicity of the lattice. Using Bloch's theorem, the eigenstates, $\Psi_{\mathbf{n}\mathbf{k}}(\mathbf{r})$, of the Hamiltonian may be expressed as

$$\Psi_{\mathbf{n}\mathbf{k}}(\mathbf{r}) \equiv \langle \mathbf{r} | \Psi_{\mathbf{n}\mathbf{k}} \rangle = \exp\{i\mathbf{k} \cdot \mathbf{r}\} u_{\mathbf{n}\mathbf{k}}(\mathbf{r}), \quad (3-2)$$

where $u_{\mathbf{n}\mathbf{k}}(\mathbf{r})$ has the periodicity of the lattice, \mathbf{k} lies in the first BZ, and n is a band index. The $\Psi_{\mathbf{n}\mathbf{k}}(\mathbf{r})$ are a complete set of basis vectors within which any function of position may be expanded. Luttinger and Kohn (LK) have proven that for any fixed value of $\mathbf{k} = \mathbf{k}_0$, the states

$$X_{\mathbf{n}\mathbf{k}}(\mathbf{r}) = \langle \mathbf{r} | \mathbf{n}\mathbf{k} \rangle = \exp\{i\mathbf{k} \cdot \mathbf{r}\} u_{\mathbf{n}\mathbf{k}_0}(\mathbf{r}) \quad (3-3)$$

also form a complete set of basis vectors. As a matter of convenience and without loss of generality, \mathbf{k}_0 is set to zero. Matrix elements of the Hamiltonian in the $X_{\mathbf{n}\mathbf{k}}(\mathbf{r}) \rightarrow |\mathbf{n}\mathbf{k}\rangle$ representation are given by

$$\begin{aligned} H_{n'n} \delta(\mathbf{k}' - \mathbf{k}) &= \langle n'\mathbf{k}' | \hat{H} | n\mathbf{k} \rangle \\ &= \int d\mathbf{r} X_{n'\mathbf{k}'}^*(\mathbf{r}) H X_{n\mathbf{k}}(\mathbf{r}) \\ &= \int d\mathbf{r} \exp\{i(\mathbf{k} - \mathbf{k}') \cdot \mathbf{r}\} u_{n'\mathbf{k}'}^*(\mathbf{r}) \left\{ E_n(0) + \frac{\hbar\mathbf{k} \cdot \mathbf{p}}{m} + \frac{\hbar^2\mathbf{k}^2}{2m} \right\} u_{n\mathbf{k}}(\mathbf{r}) \quad (3-4) \\ &= \left\{ \left(E_n(0) + \frac{\hbar^2\mathbf{k}^2}{2m} \right) \delta_{n'n} + \sum_{\alpha=x,y,z} \frac{\hbar k_\alpha p_{n'n}^\alpha}{m} \right\} \delta(\mathbf{k}' - \mathbf{k}) \end{aligned}$$

where the $p_{n'n}^\alpha$ are momentum matrix elements given by,

$$p_{n'n}^\alpha = N \int d\mathbf{r} u_{n'0}^*(\mathbf{r}) p_\alpha u_{n0}(\mathbf{r}). \quad (3-5)$$

The integral in Eq 3-5 is over the unit cell and N is a normalization constant.

Eq 3-4 is exact for all values of \mathbf{k} . However, to determine the dispersion relations, $E_n(\mathbf{k})$, all of the $p_{n'n}$ matrix elements must be computed and the resulting matrix representation of the Hamiltonian diagonalized. To avoid this prohibitively difficult procedure, the $\mathbf{k}\cdot\mathbf{p}$ method assumes that $\mathbf{k}-\mathbf{k}_0$ is a small quantity and that the Hamiltonian in Eq 3-4 is diagonalized by neglecting terms of order $(\mathbf{k}-\mathbf{k}_0)^3$ and higher. This is accomplished by a similarity transformation of the Hamiltonian,

$$\begin{aligned} H' &= U^\dagger H U \\ &= \exp\{-S\} H \exp\{S\} \\ &= H + [H, S] + \frac{1}{2} [[H, S], S] + \dots \end{aligned} \quad (3-6)$$

where a Taylor's series expansion of $U = \exp\{S\}$ has been used to formulate an approximate Hamiltonian H' . For a suitable choice of S in the absence of degeneracy, LK show that to second order in $(\mathbf{k}-\mathbf{k}_0)$ the Hamiltonian H' is given by,

$$\begin{aligned} H_{n'n} \delta(\mathbf{k}'-\mathbf{k}) &= \langle n' \mathbf{k}' | \hat{H}' | n \mathbf{k} \rangle \\ &= \langle n' \mathbf{k}' | \exp\{S\} \hat{H} \exp\{S\} | n \mathbf{k} \rangle \\ &= \left\{ \left(E_n(0) + \frac{\hbar^2 \mathbf{k}^2}{2m} \right) + \sum_{\alpha\beta} \frac{\hbar^2 k_\alpha k_\beta p_{n'n}^\alpha}{m^2} \sum_{n'' \neq n} \frac{p_{nn''}^\alpha p_{n''n}^\beta}{E_n - E_{n''}} \right\} \delta_{nn'} \delta(\mathbf{k}'-\mathbf{k}) \end{aligned} \quad (3-7)$$

where diagonal terms of order $(k-k_0)^3$ and off diagonal terms of order $(k-k_0)^2$ have been neglected. For future reference, it is convenient to define $H' = H_0 + H_{k,p}$ where

$$\langle n'k' | \hat{H}_0 | nk \rangle = \left\{ E_n(0) + \frac{\hbar^2 k^2}{2m} \right\} \delta_{n'n} \delta(\mathbf{k}' - \mathbf{k}) \quad (3-8)$$

and

$$\langle n'k' | \hat{H}'_{k,p} | nk \rangle = \left\{ \sum_{\alpha\beta} \frac{\hbar^2 k_\alpha k_\beta}{m^2} \sum_{n'' \neq n} \frac{p_{nn''}^\alpha p_{n''n}^\beta}{E_n - E_{n''}} \right\} \delta_{n'n} \delta(\mathbf{k}' - \mathbf{k}). \quad (3-9)$$

It is useful to note that the $|nk\rangle$ representation of the Hamiltonian H' is diagonal and yields the dispersion relations for a non-degenerate system,

$$E_n(\mathbf{k}) = E_n(0) + \frac{\hbar^2 k^2}{2m} + \sum_{\alpha\beta} \frac{\hbar^2 k_\alpha k_\beta}{m^2} \sum_{n'' \neq n} \frac{p_{nn''}^\alpha p_{n''n}^\beta}{E_n - E_{n''}} \quad (3-10)$$

A derivation of the effective mass theorem is then obtained by comparing like powers of k in Eq 3-10 and in a Taylor's series expansion of $E_n(\mathbf{k})$ about $\mathbf{k}_0 = \mathbf{0}$.

For Si and Ge, the Γ point is at zone center and the choice of $\mathbf{k}_0 = \mathbf{0}$ applies.

However, at zone center in the absence of spin-orbit coupling and strain, the eigenvalues of H' are degenerate. In the presence of degeneracy, off diagonal elements of H' in the degenerate subspace cannot be neglected. As a result, the $|nk\rangle$ representation of the Hamiltonian, H' , becomes block diagonal where matrix elements of H_0 remain unchanged and matrix elements of $H_{k,p}$ are given by

$$\langle n' \mathbf{k}' | \hat{H}'_{k-p} | n \mathbf{k} \rangle = \left\{ \sum_{\alpha\beta} \frac{\hbar^2 k_\alpha k_\beta}{m^2} \sum_{n'' \neq n, n'} \frac{p_{m''}^\alpha p_{n''}^\beta}{E_n - E_{n''}} \right\} \delta(\mathbf{k}' - \mathbf{k}) \quad (3-11)$$

where n' and n label degenerate eigenstates, $E_n(k=0)$ is the degenerate eigenvalue, and the dimension of the block diagonal matrix is determined by the number of degenerate eigenvectors. Because the direct bandgaps of Si and Si_{1-x}Ge_x are relatively large and the spin-orbit energy is relatively small, the three doubly degenerate valence bands will be the focus of attention. In the absence of spin-orbit coupling, six degenerate basis vectors and a 6 x 6 representation of $H' = H_0 + H_{k-p}$ are obtained. Matrix elements of the 6 x 6 representation of the bulk Hamiltonian are given by the sum of Eq 3-8 and Eq 3-11,

$$\begin{aligned} H_{n'n} \delta(\mathbf{k}' - \mathbf{k}) &= \langle n' \mathbf{k}' | \hat{H}_0 + \hat{H}'_{k-p} | n \mathbf{k} \rangle \\ &= \left[\left\{ E_n(0) + \frac{\hbar^2 k^2}{2m} \right\} \delta_{nn'} + \left\{ \sum_{\alpha\beta} \frac{\hbar^2 k_\alpha k_\beta}{m^2} \sum_{n'' \neq n, n'} \frac{p_{m''}^\alpha p_{n''}^\beta}{E_n - E_{n''}} \right\} \delta(\mathbf{k}' - \mathbf{k}) \right] \end{aligned} \quad (3-12)$$

where the prime on H has been omitted to simplify the notation. Eq 3-12 provides the most general form for matrix elements of the bulk Hamiltonian, however H must also be invariant under rotations of the symmetric point group of the lattice. This constrains the Hamiltonian to be a linear combination of invariant operators, V_n^{Alg} , of the symmetric point group of the lattice,

$$\hat{H} = \sum_n h_n^{Alg} \hat{V}_n^{Alg}, \quad (3-13)$$

where the h_n^{Alg} are expansion coefficients. Using the face centered cubic symmetry of the Si and Ge lattice, LK and later Luttinger⁴³ show that: 1) there are three terms in the expansion of H given by Eq 3-13, 2) the three expansion coefficients, h_n^{Alg} , may be determined by computing momentum matrix elements given by Eq 3-5, or directly from the three empirically determined Luttinger parameters γ_n , and 3) the invariant operators, V_n^{Alg} , of the cubic group are expressed as the product of second order polynomials of the angular momentum operators L_x , L_y , and L_z together with second order polynomials of k_x , k_y , and k_z . The symmetry defined invariant Hamiltonian is then given by

$$\begin{aligned}\hat{H} &= \hat{H}_0 + \hat{H}_{k,p} \\ &= -\frac{\hbar^2}{2m} \left(2\gamma_1 (k_{xx} + k_{yy} + k_{zz}) \hat{1} \right) - 12\gamma_2 \left(\left(\hat{L}_x^2 - \frac{1}{3} \hat{L}^2 \right) k_{xx} + \text{c.p.} \right) - 24\gamma_3 \left(\left(\hat{L}_{xy} \right) k_{xy} + \text{c.p.} \right)\end{aligned}\tag{3-14}$$

where, L^2 , L_x , L_y , and L_z are the orbital angular momentum operators, γ_1 , γ_2 , γ_3 , are empirically determined Luttinger coefficients, $k_{xy} = (k_x \cdot k_y + k_y \cdot k_x)/2$ are quadratic polynomials of the components of the wave vector \mathbf{k} , $L_{xy} = (L_x \cdot L_y + L_y \cdot L_x)/2$ are anti-commutators of the angular momentum operators, and c.p. designates cyclic permutations with respect to the indices x,y,z. The beauty of this approach is that the bulk Hamiltonian in Eq 3-14 is expressed in terms of the Luttinger coefficients which are determined experimentally through cyclotron resonance experiments. With this method, computationally intensive calculations of the Bloch functions used to determine the momentum matrix elements are avoided.

The 6 x 6 matrix representation of the bulk Si or Si_{1-x}Ge_x Hamiltonian is obtained from the 6 x 6 representation of the angular momentum operators where each of the angular momentum operators are represented in the |nk> basis. It is convenient to replace the basis index n with the labels *l*, *m_l*, *s*, and *m_s* which are used to identify the six degenerate valence subbands. With this labeling scheme, |nk> = |*l m_l s m_s k*>, where *l* equals 1, *m_l* may equal 1,0, and -1, *s* equals ½, and *m_s* has the values ± ½. The 6 x 6 matrix representation of the angular momentum operators in the |nk> = |*l m_l s m_s k*> basis are given by the following.

$$\begin{aligned}
 L_x &= \frac{\hbar}{\sqrt{2}} \begin{bmatrix} 0 & 0 & 1 & 0 & 0 & 0 \\ 0 & 0 & 0 & 1 & 0 & 0 \\ 1 & 0 & 0 & 0 & 1 & 0 \\ 0 & 1 & 0 & 0 & 0 & 1 \\ 0 & 0 & 1 & 0 & 0 & 0 \\ 0 & 0 & 0 & 1 & 0 & 0 \end{bmatrix} &
 L_y &= \frac{i\hbar}{\sqrt{2}} \begin{bmatrix} 0 & 0 & -1 & 0 & 0 & 0 \\ 0 & 0 & 0 & -1 & 0 & 0 \\ 1 & 0 & 0 & 0 & -1 & 0 \\ 0 & 1 & 0 & 0 & 0 & -1 \\ 0 & 0 & 1 & 0 & 0 & 0 \\ 0 & 0 & 0 & 1 & 0 & 0 \end{bmatrix} \\
 L_z &= \hbar \begin{bmatrix} 1 & 0 & 0 & 0 & 0 & 0 \\ 0 & 1 & 0 & 0 & 0 & 0 \\ 0 & 0 & 0 & 0 & 0 & 0 \\ 0 & 0 & 0 & 0 & 0 & 0 \\ 0 & 0 & 0 & 0 & -1 & 0 \\ 0 & 0 & 0 & 0 & 0 & -1 \end{bmatrix} &
 L^2 &= 2\hbar^2 \begin{bmatrix} 1 & 0 & 0 & 0 & 0 & 0 \\ 0 & 1 & 0 & 0 & 0 & 0 \\ 0 & 0 & 1 & 0 & 0 & 0 \\ 0 & 0 & 0 & 1 & 0 & 0 \\ 0 & 0 & 0 & 0 & 1 & 0 \\ 0 & 0 & 0 & 0 & 0 & 1 \end{bmatrix} \quad (3-15)
 \end{aligned}$$

Replacing the angular momentum operators in Eq 3-14 by their corresponding representations in Eq 3-15 yields a 6 x 6 |nk> representation of the bulk Hamiltonian

$H = H_0 + H_{k,p}$. To incorporate the physically important effects of spin-orbit coupling into the $\mathbf{k} \cdot \mathbf{p}$ model, an additional Hamiltonian, H_{so} , added to $H = H_0 + H_{k,p}$. Since the spin-orbit energy is generally larger than other perturbation terms, it is useful to represent $H = H_0 + H_{k,p}$ in the eigenbasis of the spin-orbit Hamiltonian, H_{so} . Since H_{so} is diagonal in the $|j m \mathbf{k}\rangle$ basis, the matrix representation of $H = H_0 + H_{k,p}$ is transformed from the $|l m_l s m_s \mathbf{k}\rangle$ basis to the $|j m \mathbf{k}\rangle$ using

$$|j m \mathbf{k}\rangle = \sum_{m_l m_s} |l m_l s m_s \mathbf{k}\rangle \langle l m_l s m_s \mathbf{k} | j m \mathbf{k}\rangle = \sum_{m_l m_s} C_{m_l m_s m_j}^{l s j} |l m_l s m_s \mathbf{k}\rangle \quad (3-16)$$

where $C_{m_l m_s m_j}^{l s j}$ are the Clebsch-Gordan coefficients. The transformation matrix from the $|l m_l s m_s \mathbf{k}\rangle$ representation to the $|j m \mathbf{k}\rangle$ representation is given by

$$CG = \begin{bmatrix} 1 & 0 & 0 & 0 & 0 & 0 \\ 0 & \sqrt{1/3} & 0 & 0 & \sqrt{2/3} & 0 \\ 0 & \sqrt{2/3} & 0 & 0 & -\sqrt{1/3} & 0 \\ 0 & 0 & \sqrt{2/3} & 0 & 0 & \sqrt{1/3} \\ 0 & 0 & \sqrt{1/3} & 0 & 0 & -\sqrt{2/3} \\ 0 & 0 & 0 & 1 & 0 & 0 \end{bmatrix}. \quad (3-17)$$

An alternative phase convention was developed by Luttinger and Kohn (LK) and has become the standard in the literature. The LK transformation matrix has the following form.

$$LK = \begin{bmatrix} -1 & 0 & 0 & 0 & 0 & 0 \\ 0 & -i\sqrt{1/3} & 0 & 0 & -\sqrt{2/3} & 0 \\ 0 & -i\sqrt{2/3} & 0 & 0 & \sqrt{1/3} & 0 \\ 0 & 0 & \sqrt{2/3} & 0 & 0 & i\sqrt{1/3} \\ 0 & 0 & \sqrt{1/3} & 0 & 0 & -i\sqrt{2/3} \\ 0 & 0 & 0 & i & 0 & 0 \end{bmatrix} \quad (3-18)$$

To obtain $H = H_0 + H_{k,p}$ in the $|j m k\rangle$ representation, each of the matrices in Eq 3-15 are transformed to the $|j m k\rangle$ basis using

$$\begin{aligned} L_{x_t} &= LK^\dagger \cdot L_x \cdot LK \\ L_{y_t} &= LK^\dagger \cdot L_y \cdot LK \\ L_{z_t} &= LK^\dagger \cdot L_z \cdot LK \end{aligned} \quad (3-19)$$

and then substituted into Eq 3-14.

Eq 3-14 was derived using group theory arguments in a symmetry-adapted coordinate system. Therefore, to describe quantum well structures grown in a direction that is not aligned with the symmetry adapted coordinate system, the L operators must be rotated from the symmetry adapted coordinate system to a coordinate system with a z -axis aligned with the growth axis of interest. Primary growth directions of interest are designated by their Miller indices [001], [110], or [111], however any z -axis direction can be chosen. The three primary coordinate systems are shown in Figure 3-1. Using the cubic symmetry adapted coordinates as a reference system, the L and k operators are rotated using $R(\theta, \varphi)$ into the [001], [110] and [111] coordinates. (A Mathematica™ program has been written to perform these rotations and determine the $\mathbf{k} \cdot \mathbf{p}$ matrix elements for any orientation.)⁴⁴ The rotation operator, $R(\theta, \varphi)$, is given by

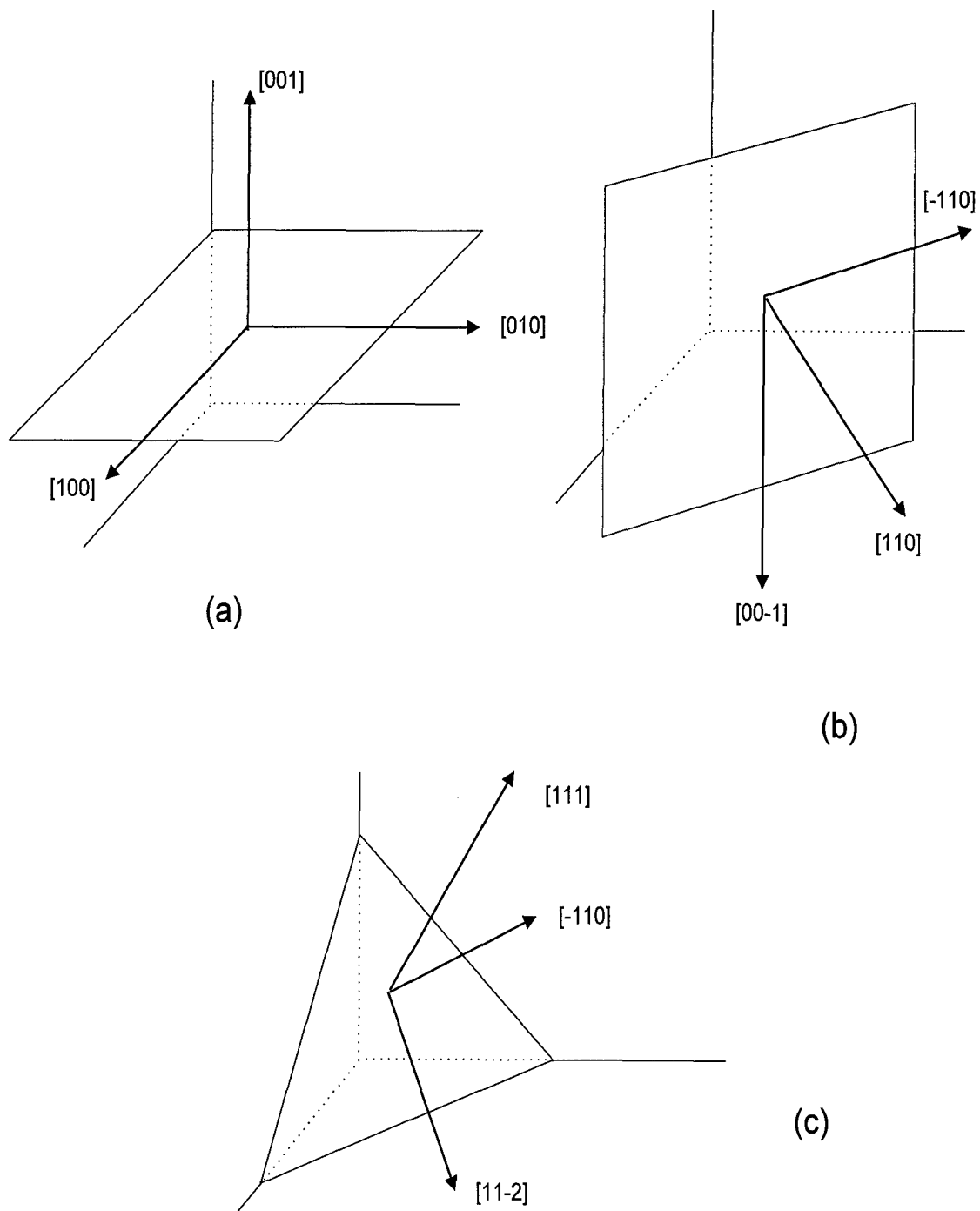


Figure 3-1. The (a) $[001]$, (b) $[110]$, and (c) $[111]$ coordinates relative to the $[001]$ coordinate system.

$$R(\theta, \varphi) = \begin{bmatrix} \cos\theta \cos\varphi & -\sin\varphi & \sin\theta \cos\varphi \\ \cos\theta \sin\varphi & \cos\varphi & \sin\theta \sin\varphi \\ -\sin\theta & 0 & \cos\theta \end{bmatrix} \quad (3-20)$$

where rotations to the [001], [110], and [111] coordinates are given by $\theta=0$, $\varphi=\pi/4$; $\theta=\pi/2$, $\varphi=\pi/4$; and $\theta=\arccos(1/\sqrt{3})$, $\varphi=\pi/4$ respectively. The rotated angular momentum operators are given by

$$\begin{bmatrix} L_{x'} \\ L_{y'} \\ L_{z'} \end{bmatrix} = R \cdot \begin{bmatrix} L_{yt} \\ L_{xt} \\ L_{zt} \end{bmatrix} = \begin{bmatrix} -L_{xt} \sin\varphi & +L_{yt} \cos\theta \cos\varphi & +L_{zt} \sin\theta \cos\varphi \\ L_{xt} \cos\varphi & +L_{yt} \cos\theta \sin\varphi & +L_{zt} \sin\theta \sin\varphi \\ -L_{yt} \sin\theta + L_{zt} \cos\theta \end{bmatrix}. \quad (3-21)$$

In a similar fashion, components of k are given by,

$$\begin{bmatrix} k_{x'} \\ k_{y'} \\ k_{z'} \end{bmatrix} = R \cdot \begin{bmatrix} k_{yt} \\ k_{xt} \\ k_{zt} \end{bmatrix} = \begin{bmatrix} -k_{xt} \sin\varphi & +k_{yt} \cos\theta \cos\varphi & +k_{zt} \sin\theta \cos\varphi \\ k_{xt} \cos\varphi & +k_{yt} \cos\theta \sin\varphi & +k_{zt} \sin\theta \sin\varphi \\ -k_{yt} \sin\theta + k_{zt} \cos\theta \end{bmatrix} \quad (3-22)$$

Substituting the 6 x 6 matrix representations of L_x , L_y , and L_z into Eq 3-14, yields the matrix representation of the Hamiltonian $H = H_0 + H_{k,p}$ in the $|j m \mathbf{k}\rangle$ basis for a particular value of $\mathbf{k}(k_x, k_y, k_z)$ as follows.

$$\begin{array}{cccccc}
m_j = & 3/2, & 1/2, & -1/2, & -3/2, & 1/2, & -1/2 \\
H = -\frac{\hbar^2}{2m_0} & \left(\begin{array}{cccccc}
H & \alpha & \beta & 0 & \frac{i}{\sqrt{2}}\alpha & -i\sqrt{2}\beta \\
\alpha^* & L & 0 & \beta & i\frac{D}{\sqrt{2}} & i\sqrt{\frac{3}{2}}\alpha \\
\beta^* & 0 & L & -\alpha & -i\sqrt{\frac{3}{2}}\alpha^* & i\frac{D}{\sqrt{2}} \\
0 & \beta^* & -\alpha^* & H & -i\sqrt{2}\beta^* & -\frac{i}{\sqrt{2}}\alpha^* \\
-\frac{i}{\sqrt{2}}\alpha^* & -i\frac{D}{\sqrt{2}} & i\sqrt{\frac{3}{2}}\alpha & i\sqrt{2}\beta & S & 0 \\
i\sqrt{2}\beta^* & -i\sqrt{\frac{3}{2}}\alpha^* & -i\frac{D}{\sqrt{2}} & \frac{i}{\sqrt{2}}\alpha & 0 & S
\end{array} \right) & & & & & & (3-23)
\end{array}$$

where for each orientation the matrix elements have the following values.

[001] growth direction

$$H = (k_x^2 + k_y^2 + k_z^2) \gamma_1 + (k_x^2 + k_y^2 - 2k_z^2) \gamma_2$$

$$L = (k_x^2 + k_y^2 + k_z^2) \gamma_1 - (k_x^2 + k_y^2 - 2k_z^2) \gamma_2$$

$$S = (k_x^2 + k_y^2 + k_z^2) \gamma_1$$

$$\alpha = -2i\sqrt{3}(k_x - ik_y)k_z\gamma_3$$

$$\beta = \sqrt{3}((k_x^2 - k_y^2)\gamma_2 - 2ik_x k_y \gamma_3)$$

$$D = L - H$$

[110] growth direction

$$H = (k_x^2 + k_y^2 + k_z^2) \gamma_1 - (k_x^2 - 2k_y^2 + k_z^2) \gamma_2 / 2 + 3(k_x^2 - k_z^2) \gamma_3 / 2$$

$$L=(k_x^2 + k_y^2 + k_z^2) \gamma_1 + (k_x^2 - 2 k_y^2 + k_z^2) \gamma_2 / 2 - 3(k_x^2 - k_z^2) \gamma_3 / 2$$

$$S=(k_x^2 + k_y^2 + k_z^2) \gamma_1$$

$$\alpha=-2 i \sqrt{[3]} (k_x \gamma_2 - i k_y \gamma_3) k_z$$

$$\beta=\sqrt{[3]} / 2 ((k_x^2 - 2 k_y^2 + k_z^2) \gamma_2 + (k_x^2 - 4 i k_x k_y - k_z^2) \gamma_3)$$

$$D=L-H$$

[111] growth direction

$$H=(k_x^2 + k_y^2 + k_z^2) \gamma_1 + (k_x^2 + k_y^2 - 2 k_z^2) \gamma_3$$

$$L=(k_x^2 + k_y^2 + k_z^2) \gamma_1 - (k_x^2 + k_y^2 - 2 k_z^2) \gamma_3$$

$$S=(k_x^2 + k_y^2 + k_z^2) \gamma_1$$

$$\alpha=\sqrt{[3]} / 3 (-\sqrt{[2]} k_x^2 - 2 i \sqrt{[2]} k_x k_y + \sqrt{[2]} k_y^2 - 4 i k_x k_z - 4 k_y k_z) \gamma_2 +$$

$$(\sqrt{[2]} k_x^2 + 2 i \sqrt{[2]} k_x k_y - \sqrt{[2]} k_y^2 - 2 i k_x k_z - 2 k_y k_z) \gamma_3)$$

$$\beta= \sqrt{[3]} / 3 ((k_x^2 - 2 i k_x k_y - k_y^2 - 2 i \sqrt{[2]} k_x k_z + 2 \sqrt{[2]} k_y k_z) \gamma_2 +$$

$$2(k_x^2 - 2 i k_x k_y - k_y^2 + 2 i \sqrt{[2]} k_x k_z - \sqrt{[2]} k_y k_z) \gamma_3)$$

$$D=L-H.$$

The matrix representation of $H = H_0 + H_{k,p}$ for the [001] and [111] growth directions were derived using the prescription outlined above and they agree exactly with other published results.^{45,46} However, the matrix elements of the $H=H_0 + H_{k,p}$ for growth along the [110] direction are new results. Ikonin⁴⁷ has previously published the matrix elements of a 4 x 4

$\mathbf{k}\cdot\mathbf{p}$ Hamiltonian for all three principle directions, however, he neglected the physically important matrix elements that couple the $j=3/2$ states with the $j=1/2$ states.

In the $|j\ m\ \mathbf{k}\rangle$ representation, the spin-orbit Hamiltonian, H_{so} , has a rather simple diagonal form for all growth directions,

$$H_{so} = \begin{bmatrix} 0 & 0 & 0 & 0 & 0 & 0 \\ 0 & 0 & 0 & 0 & 0 & 0 \\ 0 & 0 & 0 & 0 & 0 & 0 \\ 0 & 0 & 0 & 0 & 0 & 0 \\ 0 & 0 & 0 & 0 & -\Delta & 0 \\ 0 & 0 & 0 & 0 & 0 & -\Delta \end{bmatrix}, \quad (3-24)$$

where Δ is the empirically determined value of the spin-orbit energy. The total bulk Hamiltonian is then written in the following way.

$$H_{total} = H_0 + H_{\mathbf{k}\cdot\mathbf{p}} + H_{so} \quad (3-25)$$

The 6-fold degenerate energy eigenvalue of H_0 is the valence band-edge energy. By convention, this energy value is set to 0. By diagonalizing the total Hamiltonian, three doubly degenerate eigenvalues are obtained. $E_\lambda = E_\lambda(\mathbf{k})$ where E_{HH} denotes heavy hole energies, E_{LH} denotes light hole energies, and E_{SO} denotes split-off energies. The bulk dispersion relations are determined by evaluating the $E_\lambda(\mathbf{k})$ over a range of \mathbf{k} values.

C. The Effects of Strain on Bulk Energy Levels

Scientists have studied the effects of strain on semiconductors for over 40 years. The most notable studies were performed by Brooks,⁴⁸ Herring and Vogt,⁴⁹ Kleiner and Roth,⁵⁰ Hensel and Feher,²⁸ Hasegawa,²⁷ Kane,⁵¹ Balsev,⁵² Pollack,⁵³ and Bir and Pikus.⁵⁴ These experimentalists built on the band structure and effective mass theory developed by Kane, Kohn, and Luttinger in the 1950's. Pioneers in the growth of strained materials include Van der Merwe⁵⁵ and Jesser *et al.*⁵⁶ who determined the existence of a maximum or critical film thickness above which defects form to partially relieve the strain. Early work on $\text{Si}_{1-x}\text{Ge}_x$ multi-layer structures was performed by Bean *et al.*,⁵⁷ Chern *et al.*,⁵⁸ Matthews and Blakeslee,⁵⁹ People *et al.*,⁶⁰ and Van der Leur.⁶¹ Strained (also known as commensurate, coherent, or pseudomorphic) growth occurs when the lattice mismatch is accommodated by tetragonal distortion of the epilayers on the silicon substrate. In the minimum energy configuration the atoms maintain full bonding with the silicon by compressing together parallel to the growth interface and spreading apart perpendicular to the growth interface as illustrated in Figure 3-2. On the left side of the figure both materials are represented in their undistorted form. The bottom right shows strained layer growth typical of thin layers where the epitaxial layer compresses in the growth plane to match the substrate lattice atomic spacing which forces an extension in the growth direction. The top right shows misfit dislocation growth typical of thick mismatched layers where the epitaxial layer has returned to its bulk, undistorted form. All configurations of strain can be decomposed into two parts; (a) a hydrostatic component,

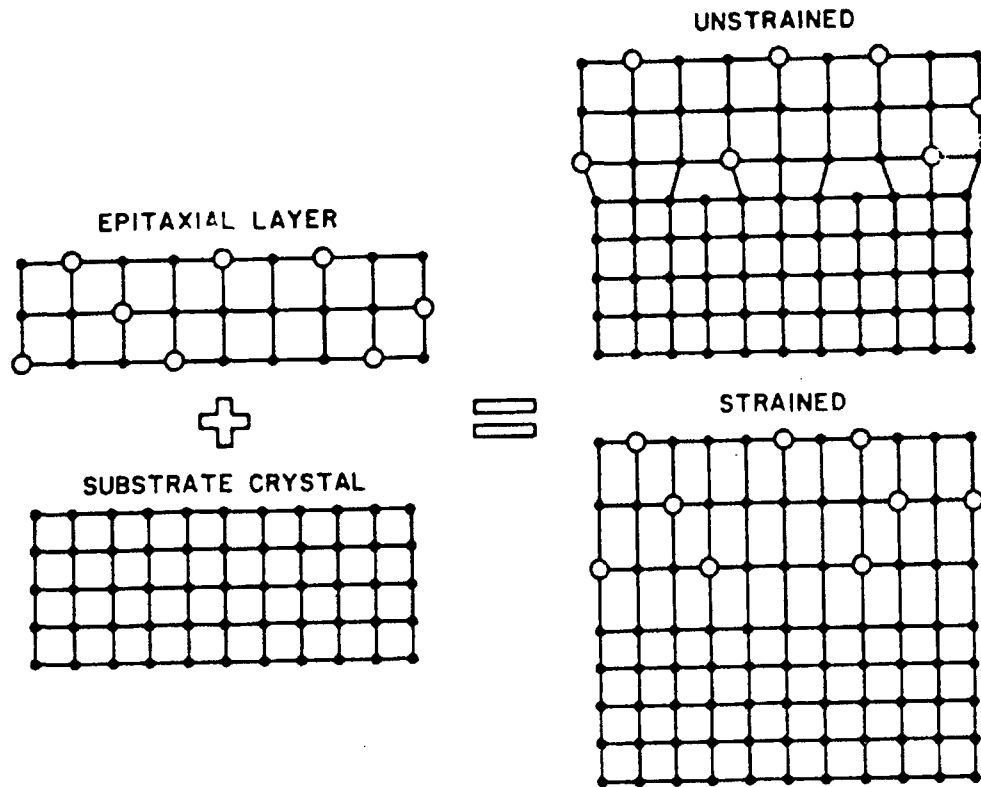


Figure 3-2. Schematic diagram representing strained layer epitaxy

which gives rise to a volume change without changing the crystal symmetry, and (b) the anisotropic component which reduces the symmetry of the strain free lattice. In the absence of spin-orbit coupling, diamond and zincblende semiconductors have a six-fold degenerate valence band dispersion relation at $k=0$, in the absence of spin. Spin-orbit interaction partially lifts the degeneracy into a four-fold degenerate $p_{3/2}$ multiplet (where $j=3/2$, $m_j = \pm 3/2, \pm 1/2$) and a two-fold degenerate $p_{1/2}$ doublet (where $j=1/2$, $m_j = \pm 1/2$). When uniaxial strain is applied to the crystal, the $j=3/2$ multiplet splits further into a pair of doublets. If the strain causes compression of the lattice then the light-hole band will

move closer in energy to the split-off band. If the strain causes extension, then the heavy-hole band will move closer in energy to the split-off band as shown in Figure 3-3. For the case of SiGe alloys grown on Si substrates, extension occurs in the growth direction and compression occurs in the plane perpendicular to the growth axis. The physical effects of strain in MQW structures are described by the strain Hamiltonian, H_{strain} . The strain Hamiltonian used to describe the strain effects on the band edges was developed independently in 1959 by Kleiner and Roth⁵⁰ and Pikus and Bir.⁵⁴ Unfortunately their notation for the deformation potentials differed and has remained a source of confusion and error for subsequent authors over the

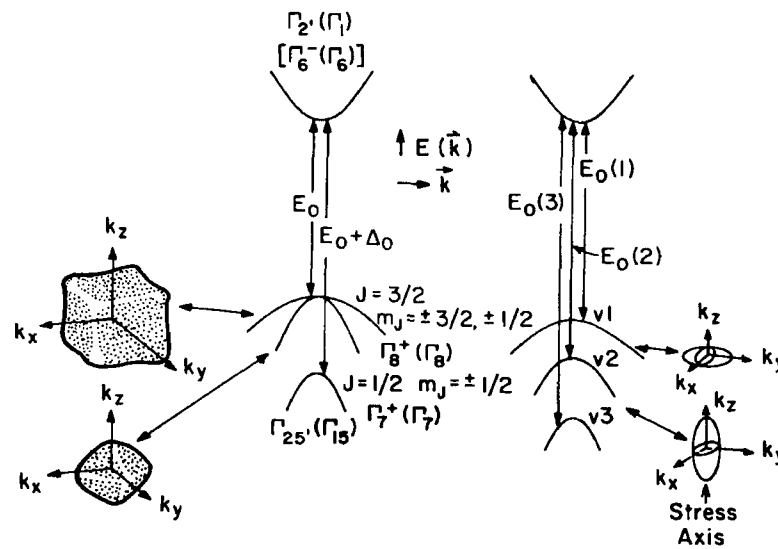


Figure 3-3. Valence bands ($j=3/2, m_j=\pm 3/2, \pm 1/2$, and $j=1/2, m_j=\pm 1/2$) and the lowest conduction band in diamond and zincblende-type semiconductors for unstrained (left) and strained (right) crystals.⁶²

years. This document will use only the Kleiner and Roth notation. Just as in the case of the $\mathbf{k}\cdot\mathbf{p}$ Hamiltonian, the strain Hamiltonian, H_{strain} , can be expanded in terms of the orbital angular momentum operators L^2 , L_x , L_y , and L_z .

$$H_{\text{strain}} = D_1(e_{xx} + e_{yy} + e_{zz})\hat{1} + 2D_2\left[\left(\hat{L}_x^2 - \frac{1}{3}\hat{L}^2\right)e_{xx} + \text{c.p.}\right] + 2D_3\left[\left(\hat{L}_{xy}\right)e_{xy} + \text{c.p.}\right] \quad (3-26)$$

where, L^2 , L_x , L_y , and L_z are the orbital angular momentum operators, D_1 , D_2 , and D_3 are the deformation potentials, e_{xx} , e_{yy} , etc. are the conventional strain components, and c.p. designates cyclic permutations with respect to the indices x,y,z. The valence band deformation potentials D_1 , D_2 , and D_3 are empirically obtained and a wide range of values are reported in the literature. D_1 gives the shift of the center of gravity of the entire valence band, D_2 represents the valence band splitting along the [001] direction and, D_3 represents the splitting along the [111] direction.⁵⁴ (Valence band deformation potentials are generally defined in terms of the conventional strain components, e_{ij} while the conduction band uniaxial splittings are generally defined in terms of strain tensor components $S_{ij} = 1/2 e_{ij}(1+\delta_{ij})$.) As the strained epitaxial growth proceeds along different directions in the crystal, the corresponding wave vectors, strain tensor, and angular operators must be rotated as was done in Section B for $H = H_o + H_{\mathbf{k}\cdot\mathbf{p}}$.⁴⁴ The 6×6 $|j m \mathbf{k}\rangle$ representation of the strain Hamiltonian, H_{strain} , is given by:

$$\begin{array}{cccccc}
m_j = 3/2, & 1/2, & -1/2, & -3/2, & 1/2, & -1/2 \\
H_{\text{strain}} = & \begin{bmatrix} e_1 + e_2 & 0 & e_3 & 0 & 0 & -i\sqrt{2}e_3 \\ 0 & e_1 - e_2 & 0 & e_3 & -i\sqrt{2}e_2 & 0 \\ e_3 & 0 & e_1 - e_2 & 0 & 0 & -i\sqrt{2}e_2 \\ 0 & e_3 & 0 & e_1 + e_2 & -i\sqrt{2}e_3 & 0 \\ 0 & i\sqrt{2}e_2 & 0 & i\sqrt{2}e_3 & e_1 & 0 \\ i\sqrt{2}e_3 & 0 & i\sqrt{2}e_2 & 0 & 0 & e_1 \end{bmatrix} & (3-27a)
\end{array}$$

where matrix elements e_1 , e_2 and e_3 for each of the primary growth directions are given as follows:

$$\begin{array}{l}
[001]; e_1 = D_1(2e_{xx} + e_{zz}), e_2 = 2/3 D_2(e_{zz} - e_{xx}), e_3 = 0, \\
[110]; e_1 = D_1(2e_{xx} + e_{zz}), e_2 = -D_2(e_{zz} - e_{xx})/3 + D_3 e_{xy}/2 \\
\quad e_3 = -D_2(e_{xx} - e_{zz})/\sqrt{3} + D_3(e_{xy})/(2\sqrt{3}), \\
[111]; e_1 = D_1 e_{xx}, e_2 = D_3 e_{xy}, e_3 = 0,
\end{array} \quad (3-27b)$$

where the values of e_{xx} , e_{zz} , and e_{xy} also depend on the orientation. Equations 3-27a and 3-27b have been independently derived and are in complete agreement with People.⁴⁵ To find the strain induced energy shifts of the valence band states, the eigenvalues of the strain Hamiltonian must be obtained where the deformation potentials and strain tensor components have been linearly interpolated between values for Si and Ge. The amount of strain induced shift depends on the crystal orientation, Ge composition, and particular band as illustrated in Figure 3-4. The strain shift data calculated for the [001] and [111] growth directions agrees well with strain shift data in the literature.^{63, 64} The strain shift data calculated for [110] growth direction has not been previously published and it falls between the [100] and [111] data for all three bands.

The total Hamiltonian including spin-orbit and strain terms can now be written as

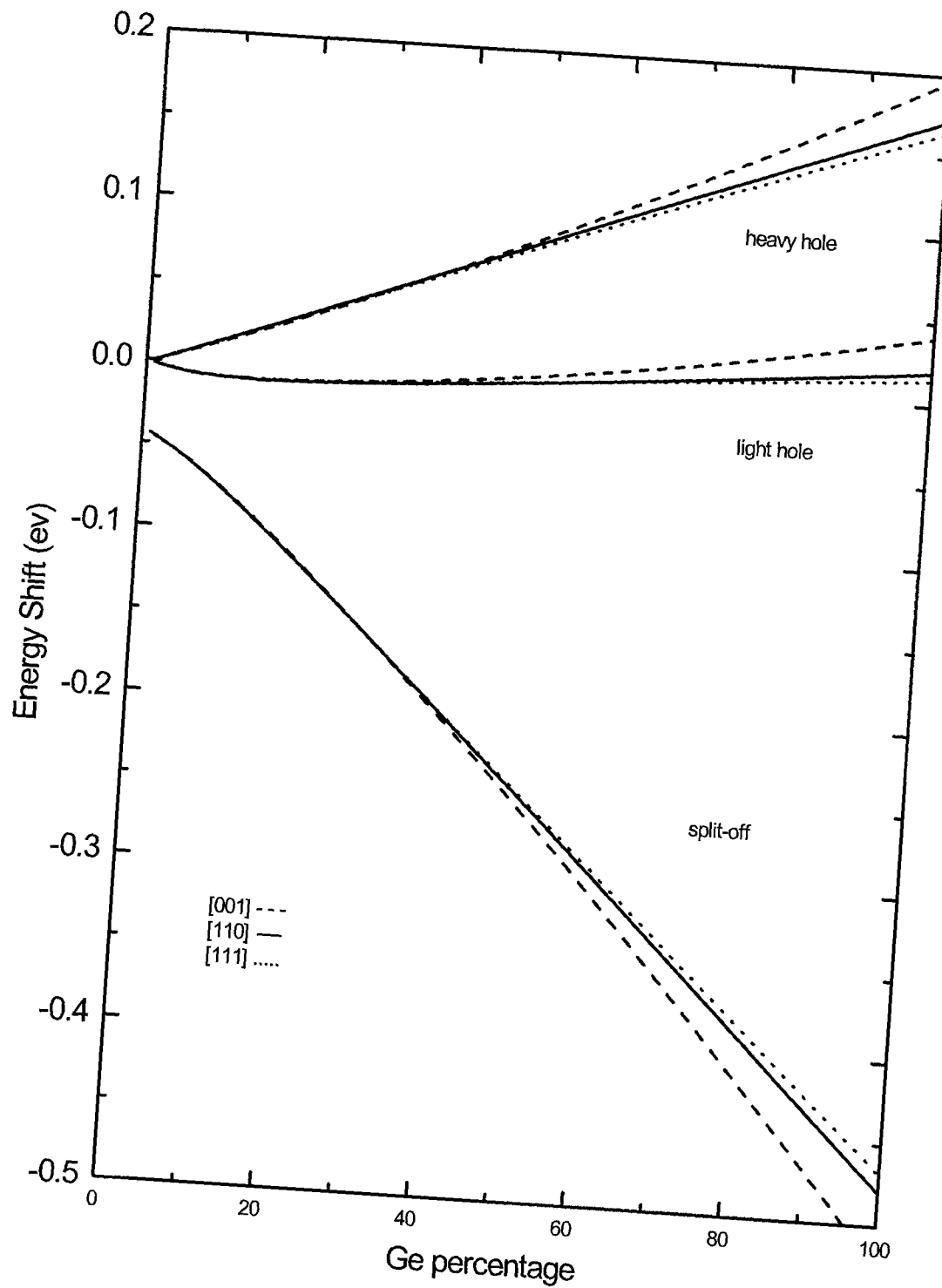


Figure 3-4. Strain induced energy shift for all three valence bands as a function of germanium composition

$$H_{\text{total}} = H_o + H_{k \cdot p} + H_{so} + H_{\text{strain}} \quad (3-28)$$

Dispersion relations, $E=E(\mathbf{k})$, that include the effects of spin-orbit coupling and strain are determined by diagonalizing the total Hamiltonian, H_{total} , given by Eq 3-28. Simple analytic expressions for $E_\lambda(\mathbf{k})$ (where $\lambda = \text{HH, LH and SO labels}$), are found for the [001] and [111] directions since the sixth order secular equation of H_{total} is easily factored into three quadratic equations. However, factorization of the secular equation for the [110] direction is more difficult and the resulting analytic expressions for the eigenvalues are prohibitively long.⁴⁴ As was previously noted, these expressions are *not* published in the literature. The experimentalist cannot simply look up eigenvalue expressions for strained [110] growth and plug in numbers to obtain dispersion relations. However, having derived the proper expression for H_{total} , dispersion relations, $E_\lambda(\mathbf{k})$, for the [110] direction are obtained. From the dispersion relations, the hole effective masses, m_λ^* , at $\mathbf{k}=0$ can be computed numerically as follows.

$$m_\lambda^* = \left. \frac{-\hbar^2}{\frac{\partial^2 E_{jm}(\mathbf{k})}{\partial k^2}} \right|_{\mathbf{k}=0} \quad (3-29)$$

The effective mass values along the growth direction for the different substrate orientations are presented graphically as a function of Ge composition in Figure 3-5. Calculation of m_λ^* in the [001] and [111] directions agree with the values calculated by Kahan,⁶³ however, the LH[001] curve varies slightly with Karunasiri.⁶⁴ It is difficult to

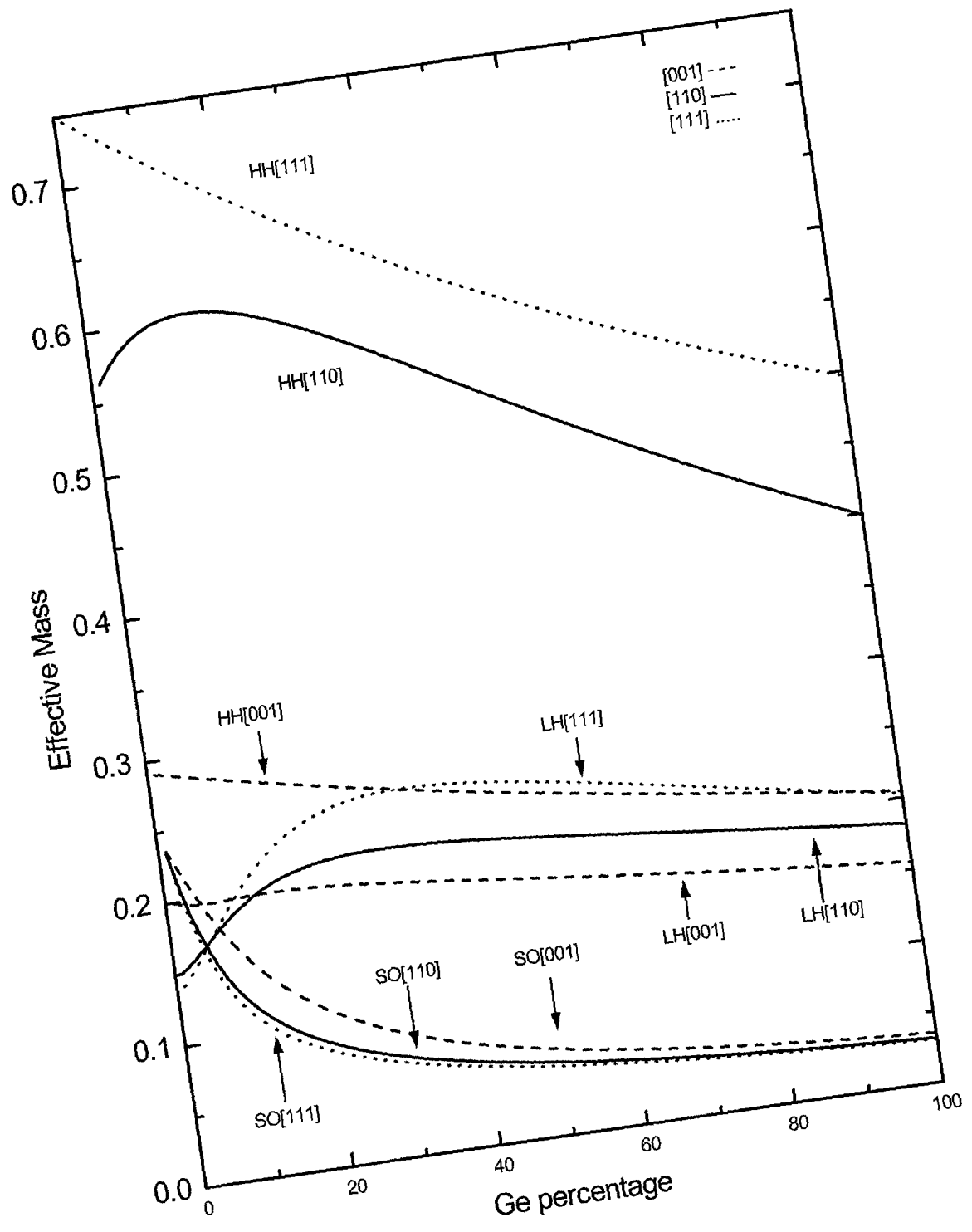


Figure 3-5. The strain induced effective mass shift along the growth direction as a function of germanium composition. HH, LH and SO denote heavy hole, light hole and split-off hole respectively.

ascertain the reason for the discrepancy because Karunasiri did not publish the details of his calculations. The [110] data presented in Figure 3-5 is a new contribution. Just as in the case of the strain shifted energies, this [110] data falls between the [001] and [111] data. A quantitative check of Figure 3-5 is available for 0.0 percent Ge. At zone center, the longitudinal, heavy hole effective mass m_{HH}^* , is expected to be inversely proportional to the sum of Luttinger parameters multiplying the k_z terms in the $\langle \frac{3}{2} \frac{3}{2} k | H | \frac{3}{2} \frac{3}{2} k \rangle$ matrix element in Eq 3-23. (i.e., $m_{(HH)}^* [001] \cong 1/(\gamma_1 - 2\gamma_2)$, $m_{(HH)}^* [110] \cong 1/(\gamma_1 - \gamma_2/2 - 3\gamma_3/2)$, $m_{(HH)}^* [111] \cong 1/(\gamma_1 - 2\gamma_3)$.) Using the Luttinger parameters of Si tabulated in Appendix A, specific values of the heavy hole masses are given by $m_{(HH)}^* [001] \cong 0.29$, $m_{(HH)}^* [110] \cong 0.53$, and $m_{(HH)}^* [111] \cong 0.75$. These numbers are in excellent agreement with the plots of Figure 3-5 for 0.0 percent Ge. These plots can also be compared with experimental data for 0.0 percent Ge. By taking the average of the values for the three orientations, it is determined that the heavy hole effective mass (m^*/m_0) is 0.53, and the light hole effective mass is 0.16. This is in excellent agreement with experimentally obtained values of 0.50 and 0.16 for heavy hole and light hole respectively.^{65,66}

Dispersion relations, $E_\lambda(\mathbf{k})$, given by the eigenvalues of the bulk Hamiltonian are shown in Figure 3-6. Part (a) shows the dispersion relations of $H_{total} = H_o + H_{k \cdot p}$ where spin-orbit and strain have been neglected. All three bands are degenerate at zone center where the zone center energy, $E_n(\mathbf{k}=0)$, is set to zero. Part (b) shows the effect of adding the spin-orbit perturbation ($H_{total} = H_o + H_{k \cdot p} + H_{so}$). At zone center the split-off band is

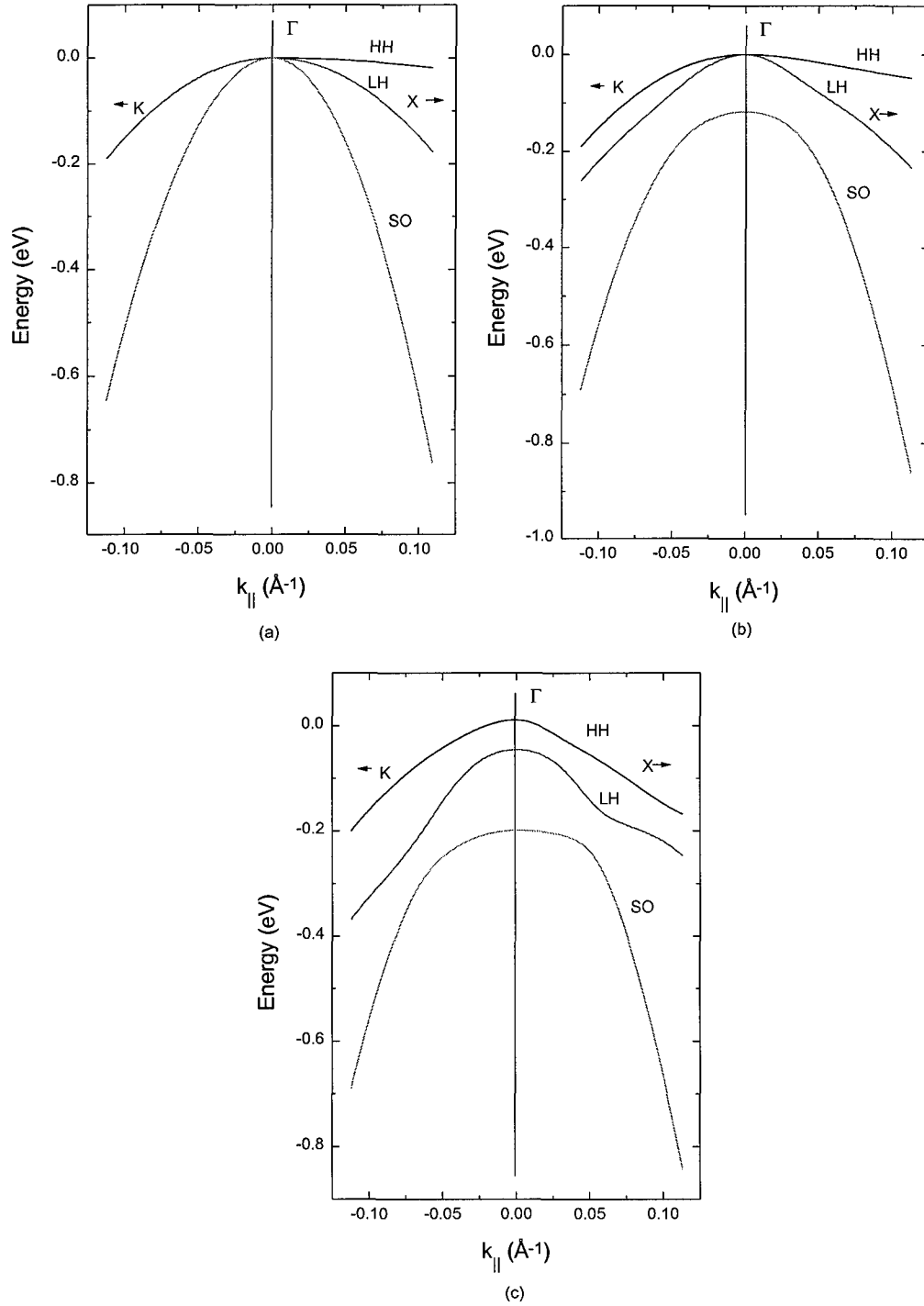
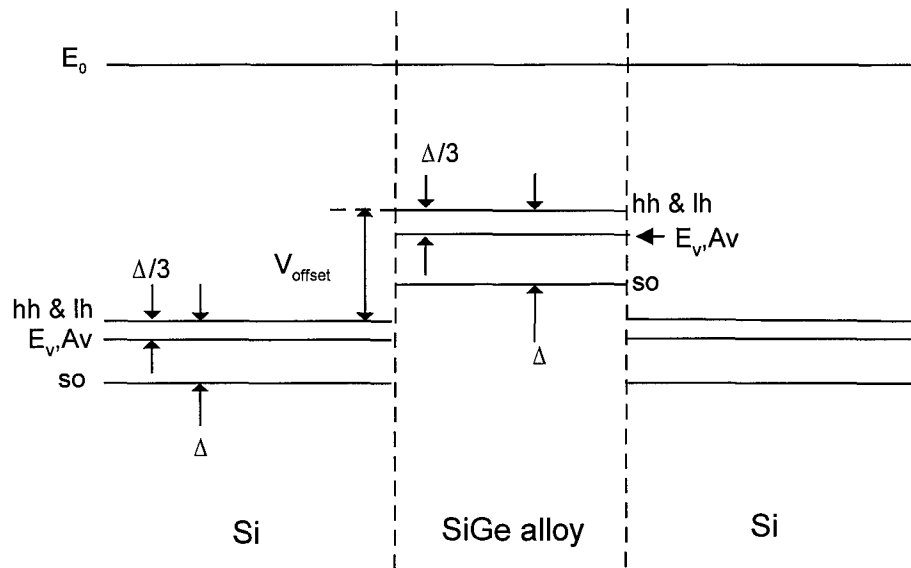


Figure 3-6. Energy bands derived from diagonalizing the Hamiltonian where (a) $H_{\text{total}} = H_0 + H_{k,p}$, (b) $H_{\text{total}} = H_0 + H_{k,p} + H_{so}$, (c) $H_{\text{total}} = H_0 + H_{k,p} + H_{so} + H_{\text{strain}}$ for Si[110], $x=0.30$ and $\pi/a \approx 0.57$.

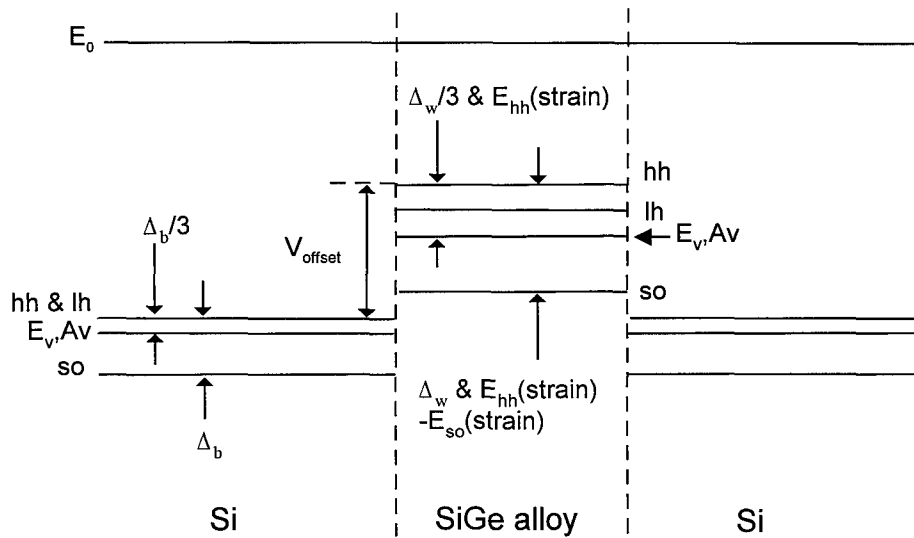
lowered by the spin-orbit energy, Δ , while the heavy hole and light hole bands are still degenerate. Part (c) shows the combined effect of spin-orbit and strain splitting ($H_{\text{total}} = H_0 + H_{\text{k-p}} + H_{\text{so}} + H_{\text{strain}}$). All three bands have distinct energies at zone center. The degree of separation and the amount of warping of the bands depends on the Ge concentration. Part (c) agrees well with bulk, strained band structures computed with the tight-binding method by Ma and Wang³⁰ which validates the approach used in this document.

D. A Simple Quantum Well Analysis

A single quantum well is made by sandwiching a planar well region of $\text{Si}_{1-x}\text{Ge}_x$ alloy between two barrier regions of pure Si. The resulting heterojunctions exhibit abrupt discontinuities, better known as band offsets, in the local band structure. The band offset, is determined by the local chemistry on an atomic scale and is generally determined experimentally. Holes moving in the well region parallel to the x,y plane are subject only to the periodic potential of the bulk $\text{Si}_{1-x}\text{Ge}_x$. Holes moving in the growth, or z direction encounter the abrupt band offset as they move from the well region to the barrier region. In a simple theoretical treatment of the optical and electronic properties of the heterostructure, the band offset at zone center ($\mathbf{k}=0$) is used to define the depth of a simple one dimensional square well. For strained SiGe alloys on Si substrates, approximately 80-90 percent of the offset occurs in the valence band, which indicates their usefulness as p-type devices. (A type I bandedge discontinuity is assumed for SiGe alloys grown on Si substrates of any orientation. Refer to Figure 2-7.)^{67,68,69} The valence band offset can be determined with what Van De Walle calls model solid theory⁷⁰ in which positions of the average energy (E_v , A_v) of the valence bands are found on an absolute scale. For unstrained materials, the valence band offset is determined by finding the energy difference between the heavy-hole levels of the well and barrier materials which are shifted up from the average band energy by $\Delta_w/3$ and $\Delta_b/3$ respectively as shown in Figure 3-7. In the strained case, the heavy-hole energy level in



Unstrained Case



Strained Case

Figure 3-7. Band offsets for any growth direction at a Si/SiGe interface for strained and unstrained case. V_{offset} represents the quantum well depth for the heavy hole band.

the alloy layer is shifted up by a mixture of both spin-orbit and strain effects. The amount of shift is determined by the zone center ($\mathbf{k}=0$) eigenvalues of the combined spin-orbit and strain Hamiltonians. The band offset is then determined as before, by the difference between the heavy-hole energies. The band offset is included in the total 6 x 6 Hamiltonian describing the heterostructure by adding a matrix of the form

$$H_{\text{offset}} = V \begin{bmatrix} 1 & 0 & 0 & 0 & 0 & 0 \\ 0 & 1 & 0 & 0 & 0 & 0 \\ 0 & 0 & 1 & 0 & 0 & 0 \\ 0 & 0 & 0 & 1 & 0 & 0 \\ 0 & 0 & 0 & 0 & 1 & 0 \\ 0 & 0 & 0 & 0 & 0 & 1 \end{bmatrix} \quad (3-30)$$

where the common convention is to set V equal to 0 in the barrier and V to V_{offset} in the well. The form of this term is identical for any growth direction. The total Hamiltonian is now expressed as follows.

$$H_{\text{total}} = H_0 + H_{\mathbf{k}\cdot\mathbf{p}} + H_{\text{so}} + H_{\text{strain}} + H_{\text{offset}} \quad (3-31)$$

If the kinetic energy of the holes in the z direction is less than V_{offset} then the holes become bound in the direction normal to the growth axis. However, their motion in the plane of the wells remains free. As a result, the energy eigenfunctions of the holes in the coordinate representation are given by a triple product which includes the following: (a)

the cell periodic Bloch part which describes the diffraction of the carriers by the periodic potential of the crystal, (b) a two-dimensional plane wave describing the motion in the x-y plane, and (c) a bound state wavefunction in the z direction normal to the MQWs.

Using envelope function theory, discussed more completely in Section E, eigenvalues and eigenfunctions of the total Hamiltonian, H_{total} , given by Eq 3-31 are determined by first computing the bulk eigenstates $|\lambda k\rangle_w$ and $|\lambda k\rangle_b$ in the well and barrier regions. The states $|\lambda k\rangle_w$ and $|\lambda k\rangle_b$ are six-fold degenerate zeroth order (zone center) eigenstates of the total Hamiltonian determined by diagonalizing H_{total} using parameters suitable for the barrier and well regions respectively. The label λ identifies the eigenstates as heavy hole, light hole and split-off. The coordinate representation of the barrier and well eigenstates together with their first derivatives are then matched at the heterojunction interface. The process of matching the zero order eigenfunctions and their derivatives mixes the corresponding heavy hole, light hole and split-off eigenfunctions. A successful match at the heterojunction occurs for discrete values of the total energy providing dispersion relations for each of these energies that are parameterized by k_{\parallel} .

A simpler approach that works well for the [001] and [111] direction (but not for the [110] direction) is to evaluate H_{total} at zone center ($\mathbf{k}=0$) to obtain the zone center energy levels of the barrier and well regions as illustrated by the strained case in Figure 3-7. This gives rise to a heavy hole, light hole, and split-off square well depth, V_{λ} , determined by the difference between the heavy hole, light hole, and split-off energy levels in the barrier and well regions. Using the dispersion relations of H_{total} in the well

region, the effective masses m_λ^* in the z direction are determined and used together with V_λ in the 1-D square well Schrödinger equation,

$$\frac{-\hbar^2}{2m_\lambda^*} \frac{\partial^2 \Psi(z)}{\partial z^2} + V_\lambda(z) \Psi(z) = E_\lambda \Psi(z) \quad (3-32)$$

to compute a zone center approximation to the dispersion relations determined by the EFA. To solve equation 3-32 a plane wave solution to Schrödinger's equation is assumed in the barrier and well region, and boundary conditions are satisfied using the standard approach outlined in many quantum mechanics texts.⁷¹ Discrete bound states in the well are obtained for hole energies less than V_λ , and hole energies greater than V_λ correspond to a continuum of unbound states. Eigenvalues, E_λ in Eq 3-32, are obtained by finding the roots of a transcendental equation. Graphical solutions for the heavy hole band of a Si/Si_{0.70}Ge_{0.30} quantum well structure where the well width, L, is 30 Å are illustrated in Figure 3-8. Energy eigenvalues correspond to points of intersection labeled with open circles and can be found numerically with a root finder routine.⁴⁴ The energy levels for the light hole band and split-off band are found in a similar fashion. Using the points of intersection as the zone center energies, a simple energy level diagram is shown in Figure 3-9 to illustrate the relative positions of the energies for each of the zone center bands. Extensive tables have been compiled for positions of the bound state energies for both Si[001] and Si[110] substrates and are presented in Appendix C. The results of this simple calculation for the [001] growth direction agrees very well with previously

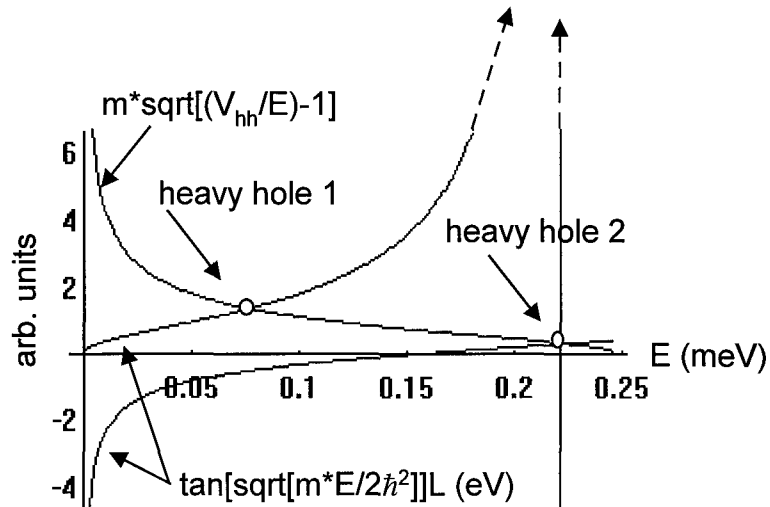


Figure 3-8. Graphical representation of solutions to the 1-D Schrödinger equation for the heavy hole band of a Si[001]/Si_{0.70}Ge_{0.30} MQW with a well width of 30 Å.

published results and with results obtained through the more sophisticated envelope function approximation in Section E.^{72,73} Calculations using a simple QW model for the [110] growth direction have not been previously published. However they do not compare well with the envelope function approximation calculation. The reason that the simple approximation works well at low Ge concentrations for the [001] material and does not work well for [110] material is explained by considering the matrix elements of the $\mathbf{k}\cdot\mathbf{p}$ Hamiltonian (Eq 3-23) for each structure. The α , β and D terms determine the amount of band coupling. When k_x and k_y are set to zero at the center of the BZ, α and β are zero for the [001] growth direction and D is a function of k_z . As a result, the heavy hole band is completely decoupled from light hole and split-off bands which are themselves only weakly coupled. Consequently, the simple approximation is relatively

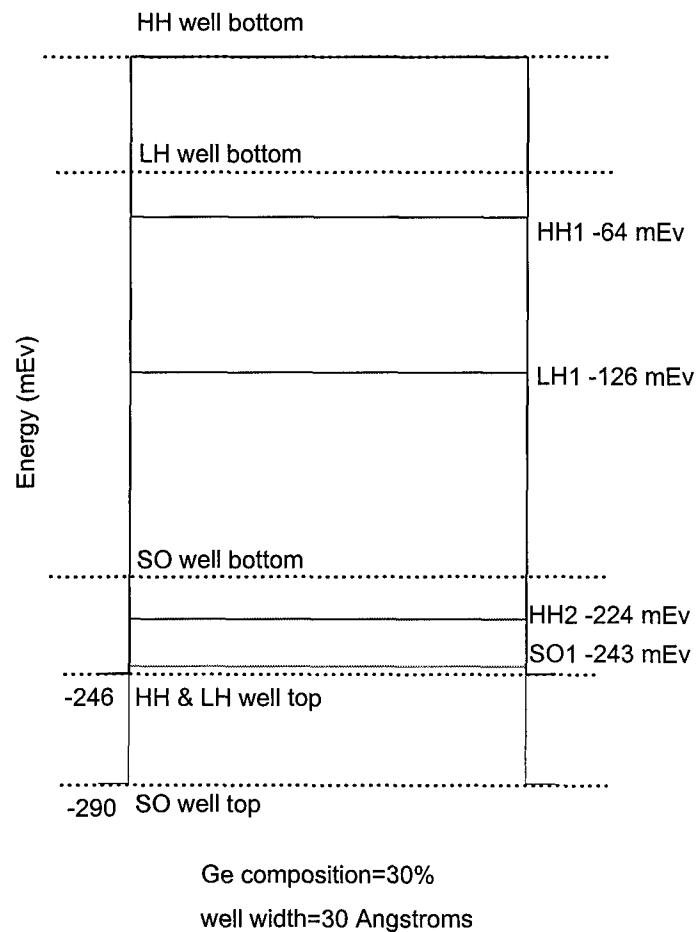


Figure 3-9. Schematic diagram of bound state energy levels in a Si[001]/Si_{0.70}Ge_{0.30} MQW with a well width of 30 Å. Energies are determined using a simple quantum well model.

good for [001] material until increasing strain forces a stronger coupling. Now consider the α and β terms for the [110] case. When k_x and k_y are set to zero at the center of the BZ, α still goes to zero but β does not. As a result, all the bands are coupled at zone center, and the simple approximation is a poor one. A comparison of the data for the uncoupled band and envelope function approximations will be given after the development of the envelope function approximation. (see Section G.)

E. Envelope Function Approximation

1. Background.

The envelope function approximation (EFA) provides a more sophisticated treatment of the zone center quantum well energies when compared with the simple quantum well analysis discussed in the previous section. Furthermore, the EFA may also be used to compute quantum well energies away from zone center. This give rise to a series of dispersion relations, $E = E_N(\mathbf{k}_{\parallel})$, where the continuous label \mathbf{k}_{\parallel} identifies the hole momentum in the plane of the quantum well, and the discrete index N labels energies that correspond to bound hole states in the growth direction.

The EFA proceeds by first determining the bulk eigenstates of the well and barrier regions using the approach outlined in the previous sections where

$$\begin{aligned} |\lambda \mathbf{k}\rangle &= \sum_{j,m} |j m \mathbf{k}\rangle \langle j m \mathbf{k} | \lambda \mathbf{k}\rangle \\ &= \sum_{j,m} A_{j,m}^{\lambda}(\mathbf{k}) |j m \mathbf{k}\rangle \end{aligned} \quad (3-33)$$

In Eq 3-33, heavy, light and split-off hole states are labeled by $\lambda = hh, lh$, and so, and the $|j m \mathbf{k}\rangle$ are the basis vectors used to obtain the initial 6×6 representation of the total Hamiltonian given by Eq 3-23. The expansion coefficients $A_{j,m}^{\lambda}(\mathbf{k})$ are determined by diagonalizing the bulk Hamiltonian given by Eq 3-23 using appropriate physical parameters for the barrier and well regions. A more complete notation for the bulk eigenstates in Eq 3-33 should include an extra label that distinguishes between the barrier

and well solutions, however, for notational clarity this label has been omitted. The coordinate representation of the $|\lambda \mathbf{k}\rangle$ is given by,

$$\begin{aligned}
 \chi_{\lambda \mathbf{k}}(\mathbf{r}) &= \langle \mathbf{r} | \lambda \mathbf{k} \rangle \\
 &= \sum_{j,m} A_{j,m}^{\lambda}(\mathbf{k}) \langle \mathbf{r} | j m \mathbf{k} \rangle \\
 &= \exp\{i \mathbf{k} \cdot \mathbf{r}\} \sum_{j,m} A_{j,m}^{\lambda}(\mathbf{k}) u_{jm0}(\mathbf{r}) \\
 &= \exp\{i \mathbf{k} \cdot \mathbf{r}\} u_{\lambda 0}(\mathbf{r})
 \end{aligned} \tag{3-34}$$

where the $u_{jm0}(\mathbf{r})$ are the cell periodic parts of the Bloch functions at zone center. Since the $u_{jm0}(\mathbf{r})$ are degenerate zone center eigenvectors of H_0 as defined by Eq 3-8, the $u_{\lambda 0}(\mathbf{r})$ given by the linear combination in Eq 3-33 are also degenerate zone center eigenvectors of H_0 .

Another degeneracy exhibited by the $|\lambda \mathbf{k}\rangle$ is illustrated in Figure 3-10 by drawing a horizontal line corresponding to a particular energy, E , and identifying its intercept with the hh, lh, and so bands. Vertical lines drawn through these intercepts will identify six values of $k_z = k_{\lambda z}$, each labeled by the band index λ . Thus, for a given value of energy E , there are six degenerate bulk eigenvectors, $|\lambda, \pm k_z \mathbf{k}_{\parallel}\rangle$ and where the momentum label \mathbf{k} has been explicitly separated into a component labeling momentum in the growth direction, $\pm k_z$, and components labeling momentum parallel to the quantum well, \mathbf{k}_{\parallel} . An essential point concerning this set of six-fold degenerate states is that for a fixed value of \mathbf{k}_{\parallel} , different values of $\pm k_z$ will yield different values of \mathbf{k} . It therefore follows that each of the six degenerate basis vectors, $|\lambda, \pm k_z \mathbf{k}_{\parallel}\rangle$, comes from a separate 6 x 6 Hamiltonian.

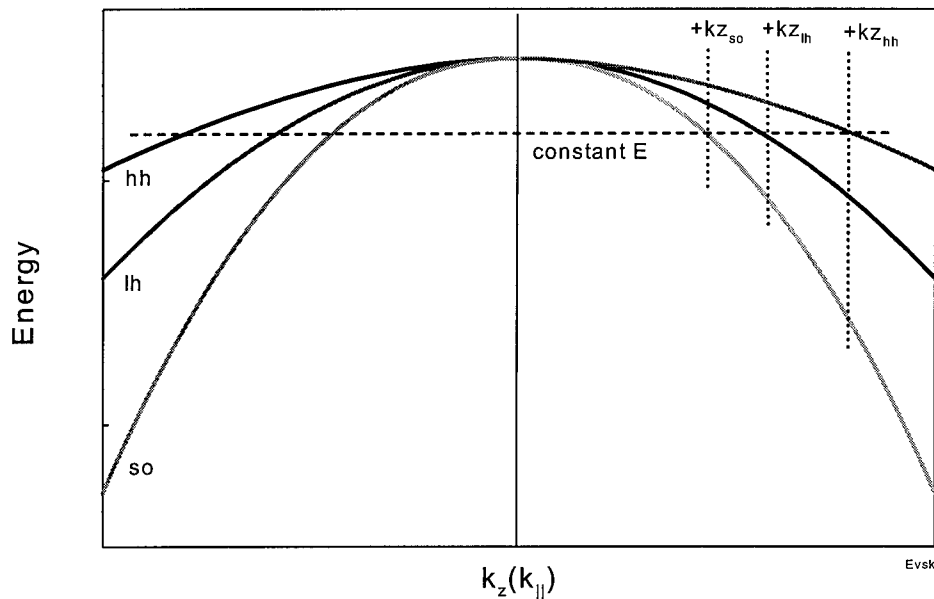


Figure 3-10. Schematic diagram showing the degeneracy points in each band as a function of energy and of k_z .

However, it is possible to show that these six basis vectors are linearly independent and therefore span a six dimensional degenerate eigenspace of the total Hamiltonian H given by Eq 3-31. It is worthwhile noting that this six dimensional space is the EFA analog to the two dimensional space spanned by plane waves, $\exp\{\pm k_z\}$ used for the simple analysis of the one dimensional quantum well mentioned in the previous section.

Quantum well eigenstates and eigenvalues are obtained in the EFA by determining which particular linear combinations of the bulk eigenstates $|\lambda, \pm k_z, k_{\parallel}\rangle$ in the barrier region and well region satisfy boundary conditions at the quantum well interface, The resulting eigenstates are formally given by

$$|\mathbf{Nk}_{\parallel}\rangle = \sum_{\lambda} f_N^{\lambda}(\mathbf{k}_z^{\lambda}, \mathbf{k}_{\parallel}) |\lambda, \mathbf{k}_z^{\lambda}, \mathbf{k}_{\parallel}\rangle \quad (3-35)$$

where N is a subband index identifying bound states in the growth direction, and the $f_N^{\lambda}(\mathbf{k}_z^{\lambda}, \mathbf{k}_{\parallel})$ are expansion coefficients of the λ^{th} bulk eigenstates that remain to be calculated. It is important to note that as in Eq 3-33, and additional index labeling the well and barrier regions has been omitted for notational clarity. Combining the sum over j and m in Eq 3-33 together with the sum over λ in Eq 3-35 yields,

$$\begin{aligned} |\mathbf{Nk}_{\parallel}\rangle &= \sum_{\lambda} f_N^{\lambda}(\mathbf{k}_z^{\lambda}, \mathbf{k}_{\parallel}) \sum_{j,m} A_{j,m}^{\lambda}(\mathbf{k}_z^{\lambda}, \mathbf{k}_{\parallel}) |jmk_z^{\lambda}, \mathbf{k}_{\parallel}\rangle \\ &= \sum_{\lambda} \sum_{j,m} F_{N,j,m}^{\lambda}(\mathbf{k}_z^{\lambda}, \mathbf{k}_{\parallel}) |jmk_z^{\lambda}, \mathbf{k}_{\parallel}\rangle \end{aligned} \quad (3-36)$$

The coordinate representation of Eq 3-36 is then given by,

$$\begin{aligned} \langle \mathbf{r} | \mathbf{Nk}_{\parallel} \rangle &= \sum_{\lambda} \sum_{j,m} F_{N,j,m}^{\lambda}(\mathbf{k}_z^{\lambda}, \mathbf{k}_{\parallel}) \langle \mathbf{r} | jmk_z^{\lambda}, \mathbf{k}_{\parallel} \rangle \\ &= \exp\{i\mathbf{k}_{\parallel} \cdot \mathbf{r}\} \sum_{j,m} \left(\sum_{\lambda} F_{N,j,m}^{\lambda}(\mathbf{k}_z^{\lambda}, \mathbf{k}_{\parallel}) \exp\{ik_z^{\lambda} z\} \right) u_{jm0}(\mathbf{r}) \end{aligned} \quad (3-37)$$

where,

$$F_{N,j,m}(\mathbf{k}_{\parallel}, z) = \sum_{\lambda} F_{N,j,m}^{\lambda}(\mathbf{k}_z^{\lambda}, \mathbf{k}_{\parallel}) \exp\{ik_z^{\lambda} z\} \quad (3-38)$$

is the jm^{th} component of the envelope function. The complete envelope function is then obtained by ignoring the rapidly oscillating cell periodic part of the Bloch function at zone center, $u_{jm0}(\mathbf{r})$, and summing over j and m,

$$F_N(\mathbf{k}_\parallel, z) = \sum_{\lambda, j, m} F_{N, j, m}^\lambda(k_z^\lambda, \mathbf{k}_\parallel) \exp\{ik_z^\lambda z\}. \quad (3-39)$$

Envelope function band weights, w_{Njm} are determined by normalizing the heterojunction eigenstates $|N\mathbf{k}_\parallel\rangle$, where,

$$\begin{aligned} \langle \mathbf{r} | N\mathbf{k}_\parallel \rangle &= \sum_{\substack{\lambda, j, m \\ \lambda', j', m'}} F_{N, j', m'}^{\lambda'*} F_{N, j, m}^\lambda \langle j' m' k_z^{\lambda'} \mathbf{k}_\parallel | j m k_z^\lambda, \mathbf{k}_\parallel \rangle \\ &= \sum_{\lambda, j, m} |F_{N, j, m}^\lambda(k_z^\lambda, \mathbf{k}_\parallel)|^2 \\ &= \sum_{j, m} w_{N, j, m} \end{aligned} \quad (3-40)$$

or

$$w_{N, j, m} = \sum_{\lambda} |F_{N, j, m}^\lambda(k_z^\lambda, \mathbf{k}_\parallel)|^2$$

The $|N, \mathbf{k}_\parallel\rangle$ are eigenstates of the full Hamiltonian given by Eq 3-31 where

$$H|N\mathbf{k}_\parallel\rangle = E_N(\mathbf{k}_\parallel)|N\mathbf{k}_\parallel\rangle. \quad (3-41)$$

The $|j m \pm k_z \mathbf{k}_\parallel\rangle$ representation of Eq 3-41 yields a set of equations that can be used to compute the $F_{Njm}^\lambda(k_z^\lambda, \mathbf{k}_\parallel)$,

$$\sum_{j, m} H_{j', m', j, m}(k_z^\lambda, \mathbf{k}_\parallel) F_{N, j, m}^\lambda(k_z^\lambda, \mathbf{k}_\parallel) = E_N(\mathbf{k}_\parallel) F_{N, j, m}^\lambda(k_z^\lambda, \mathbf{k}_\parallel) \quad (3-42)$$

where,

$$H_{j', m', j, m}(k_z^\lambda, \mathbf{k}_\parallel) = \langle j' m' k_z^{\lambda'} \mathbf{k}_\parallel | H | j, m, k_z^\lambda, \mathbf{k}_\parallel \rangle. \quad (3-43)$$

The j_m^{th} component of the envelope function $F_{N_{jm}}(\mathbf{k}_{\parallel}, z)$, may then be computed using Eq 3-38. It is important to note that the components of the envelope function, $F_{N_{jm}}(\mathbf{k}_{\parallel}, z)$, will satisfy boundary conditions only for the energies $E=E_N(\mathbf{k}_{\parallel})$. Thus for a particular choice of \mathbf{k}_{\parallel} in Eq 3-38, there exist a discrete set of values $k_z=k_z(E_N(\mathbf{k}_{\parallel}))$ which must be calculated. As a first step in this calculation, the relation between energy and momentum $E=E(\mathbf{k})$ must be inverted to compute $k_z=k_z(E, \mathbf{k}_{\parallel})$. To perform this inversion, the total Hamiltonian, $H=H_0 + H_{k \cdot p} + H_{so} + H_{\text{strain}} + H_{\text{offset}}$ is expanded in powers of k_z as follows:

$$H(\mathbf{k}_{\parallel}, k_z) = H_2(\mathbf{k}_{\parallel}) k_z^2 + H_1(\mathbf{k}_{\parallel}) k_z + H_0(\mathbf{k}_{\parallel}), \quad (3-44)$$

where $H_0(\mathbf{k}_{\parallel})$ in Eq 3-44 should not be confused with H_0 in Eq 3-31. Using this expansion, the associated k_z values and eigenvectors are obtained by solving the following complex, non-Hermitian, matrix eigenvalue problem where I_6 represents the 6 x 6 identity matrix.⁴⁰

$$\begin{bmatrix} -k_i I_6 & I_6 \\ -H_2^{-1}(H_0 - E) & -H_2^{-1}H_1 - k_i I_6 \end{bmatrix} \begin{bmatrix} C_i \\ k_i C_i \end{bmatrix} = 0 \quad (3-45)$$

This equation leads to 12 linearly independent eigenvectors $C_i \equiv C(\mathbf{k}_{\parallel}, k_i)$ which correspond to 6 doubly degenerate eigenvalues k_i which are indexed k_z values. It is important to re-emphasize that in the quantum well structures, the 3 doubly degenerate eigenvalues are associated with a particular energy, E , at a chosen value of \mathbf{k}_{\parallel} , whereas in the bulk, it is customary to obtain 6 doubly degenerate energy values for a chosen \mathbf{k} (k_x, k_y, k_z).

2. Bound-state solutions⁴⁰

It is determined that the center of the quantum well is at the origin of the z -axis, $z=0$. The well extends along the z -axis $\pm L/2$ where L is the well width. In the following equations, left or l , will designate the left-hand interface or $z=-L/2$ interface. Likewise, right or r , will designate the right-hand or $z=L/2$ interface. Having obtained the k_i and C_i for both the barrier and well regions, the envelope functions are easily constructed. For the left barrier, the envelope function is given by

$$F^{bl}(\mathbf{k}_{\parallel}, z) = \sum_{i=1}^6 b_i C^{bl}(\mathbf{k}_{\parallel}, k_i) \exp\{ik_i z\} \quad (3-46)$$

where the sum over i is restricted to values of k_i which are negative and pure imaginary to insure that the wavefunction decay to zero for large negative z , and the b_i are six unknown coefficients used to satisfy boundary conditions. The relationship between the $b_i C^{bl}$ and the j mth components of the envelope function is obtained by comparing Eq 3-46 with Eq 3-34. Using matrix notation, Eq 3-46 is given by

$$F^{bl}(\mathbf{k}_{\parallel}, z) = C^{bl} E^b(z) B, \quad (3-47)$$

where the superscripts b and l denote barrier and left-hand side respectively, and

$$\begin{aligned} (C^b)_{ij} &= C_j^b(\mathbf{k}_{\parallel}, k_i^b) \\ E^b(z)_{ij} &= \exp\{ik_i^b z\} \delta_{ij} \\ B_i &= b_i. \end{aligned}$$

To construct an envelope function for the other barrier requires the use of the other 6 k_i with positive imaginary parts and their companion C_i . However, Szmulowicz discusses

the use of symmetry operations which eliminates the need to obtain and keep track of these elements. For a symmetric well and flat-band condition⁷⁴, the total wave function can be chosen to be an eigenstate of parity with respect to reflection in the plane $z=0$. Because the total wave function is a direct product of the envelope function and the Bloch wave function, each component of the envelope function behaves differently. The reflection operator, $\Gamma(IC_{2z})$, (which consists of a 180° rotation about the z axis followed by an inversion) transforms the envelope function as

$$\Gamma(IC_{2z})F(\mathbf{k}_{\parallel}, z) = \pm F(\mathbf{k}_{\parallel}, -z). \quad (3-48)$$

So the envelope function in the other barrier can be obtained by

$$\begin{aligned} F^{\text{br}}(\mathbf{k}_{\parallel}, z) &= \sum_{i=7}^{12} b_i C^{\text{br}}(\mathbf{k}_{\parallel}, -\mathbf{k}_i) \exp\{-ik_i z\} \quad \text{or} \\ F^{\text{br}}(\mathbf{k}_{\parallel}, z) &\equiv \pm(\Gamma C^{\text{bl}}) E^{\text{b}}(-z)B \end{aligned} \quad (3-49)$$

where

$$\Gamma = \begin{bmatrix} 1 & 0 & 0 & 0 & 0 & 0 \\ 0 & -1 & 0 & 0 & 0 & 0 \\ 0 & 0 & 1 & 0 & 0 & 0 \\ 0 & 0 & 0 & -1 & 0 & 0 \\ 0 & 0 & 0 & 0 & -1 & 0 \\ 0 & 0 & 0 & 0 & 0 & 1 \end{bmatrix} \quad \text{and}$$

$$E^{\text{b}}(-z)_{ij} = \exp\{-ik_i^{\text{b}} z\} \delta_{ij}.$$

The \pm signs are used to form even and odd states respectively. All 12 k_i and C_i values are necessary to form the envelope function in the well region, but a similar symmetry operation can be used as in the barrier. For the even (+) or odd (-) state, the envelope function is given by

$$F^w(\mathbf{k}_{\parallel}, z) = \sum_{i=1}^6 w_i \left[C^w(\mathbf{k}_{\parallel}, k_i) \exp\{ik_i z\} \pm C^w(\mathbf{k}_{\parallel}, -k_i) \exp\{-ik_i z\} \right] \quad \text{or} \quad (3-50)$$

$$F^w(\mathbf{k}_{\parallel}, z) \equiv [C^w E^w(z) \pm \Gamma C^w E^w(-z)] W,$$

where the superscript w labels the well region of the quantum well and the w_i are six more unknown coefficients used to satisfy boundary conditions.

Since both Si and Ge are group IV materials, the approximation is made that the Bloch part of the wave function is the same in the barrier and well. As a result, the boundary conditions need only be applied to the envelope functions. A fortunate consequence of using eigenstates of parity is that boundary conditions have to be matched at one interface only. Boundary conditions are enforced by demanding continuity of the wave function $F^b = F^w$, at the barrier/well boundary. In matrix notation, this condition is expressed as,

$$[C^w E^w(z) \pm \Gamma C^w E^w(-z)] W = C^b E^b(z) B, \quad (3-51)$$

where all functions of z are evaluated at the boundary. The second boundary condition requires not that

$$\frac{\partial}{\partial z} F^b = \frac{\partial}{\partial z} F^w$$

but that (3-52)

$$H_2^b \frac{\partial}{\partial z} F^b + \frac{H_1^b}{-2i} F^b = H_2^w \frac{\partial}{\partial z} F^w + \frac{H_1^w}{-2i} F^w,$$

at the barrier/well boundary. Rewriting this equation in matrix form yields

$$\left\{ H_2^w [C^w K^w E^w(z) \mp \Gamma C^w K^w E^w(-z)] + \frac{H_1^w}{2} [C^w E^w(-z) \pm \Gamma C^w E^w(z)] \right\} W =$$

$$\left\{ H_2^b C^b E^b(z) K^b + \frac{H_1^b}{2} C^b E^b(z) \right\} B \quad (3-53)$$

where $K_{ij} = k_i \delta_{ij}$.⁷⁵ Thus the second boundary condition is an equality condition on the derivative of the envelope function for the well and the envelope function for the barrier multiplied by the ratio of the well effective mass to the barrier effective mass. It is interesting to note that this leads to a discontinuity in the derivative of the envelope functions at the interface. In some instances where the effective masses are of opposite signs, the discontinuity will cause a cusp at the interface. Combining the equations 3-44 and 3-46 produces a 12 x 12 homogeneous equation in the 12 unknown variables in B and W for the energy eigenvalues and associated eigenvectors.

$$\begin{bmatrix} M^w & -M^b \\ H_2^w N^w + \frac{H_1^w}{2} M^w & -\left(H_2^b N^b + \frac{H_1^b}{2} M^b \right) \end{bmatrix} \begin{bmatrix} W \\ B \end{bmatrix} = \begin{bmatrix} 0 \\ 0 \end{bmatrix} \quad \text{Eq (3-54)}$$

where

$$\begin{aligned} M^w &= [C^w E^w(z) \pm \Gamma C^w E^w(-z)], \\ M^b &= [C^b E^b(z)] \\ N^w &= [C^w K^w E^w(-z) \mp \Gamma C^w K^w E^w(z)] \\ N^b &= [C^b K^b E^b(z)]. \end{aligned}$$

A solution to the equation is found when the determinant of the matrix goes to zero, at which time the coefficients W and B are obtained. Back substitution into equations 3-40 and 3-43 produces the envelope function at the prescribed energy value and $k_{||}$ value.⁴⁴ Examples of the dispersion curves obtained with the EFA are shown in Figure 3-11 and Figure 3-12. The dashed lines in the figures indicate the zone center energies predicted by the simple model. Good agreement is obtained for Si[001] but dramatic differences are seen in the Si[110] predictions. The reason for the discrepancy is found by considering the $\mathbf{k} \cdot \mathbf{p}$ Hamiltonian (Eq 3-17). For the simple model, $\mathbf{k}(k_x, k_y, k_z)$ is set to zero, and so the $\mathbf{k} \cdot \mathbf{p}$ Hamiltonian goes to zero, which leads to isolated bands. In the EFA approach, boundary conditions determine that k_z is never zero. As a result, the $\mathbf{k} \cdot \mathbf{p}$ Hamiltonian has non-diagonal elements which assures partial band mixing even at zone center. For Si[001] material at $k_{||}=0$, the α and β terms go to zero but the D term

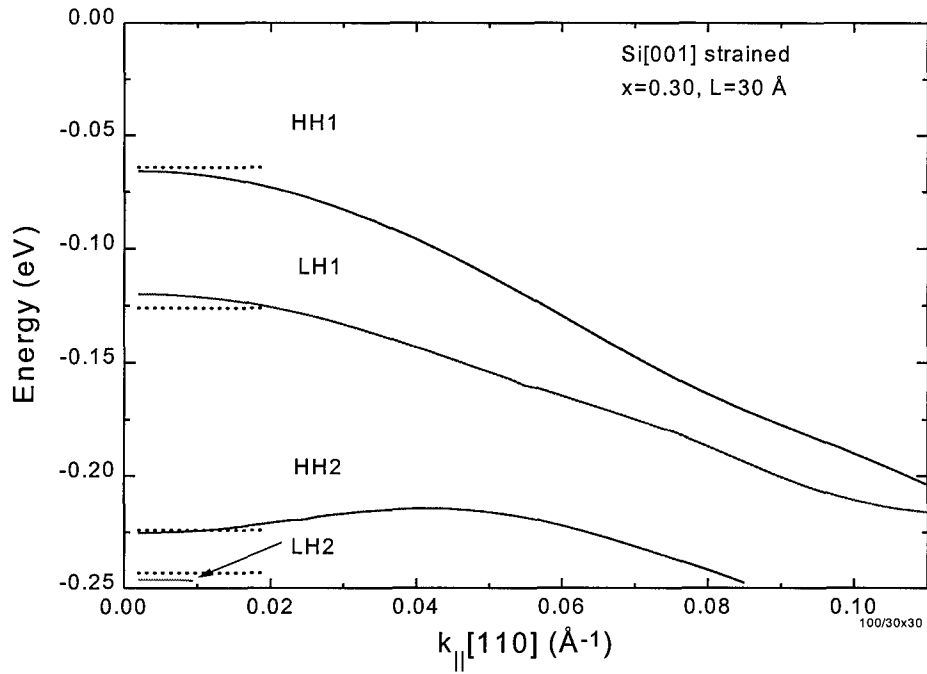


Figure 3-11. Dispersion curves for a Si[001]/Si_{0.70}Ge_{0.30} MQW where L= 30 Å. Dashed lines represent zone center energies from the simple well model. $\pi/a \approx 0.51$.

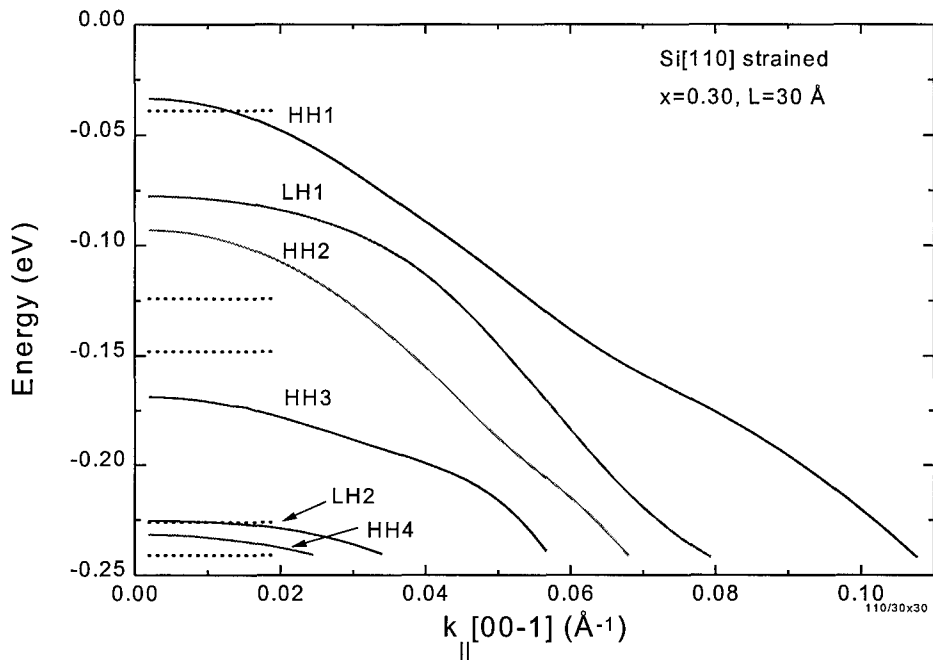


Figure 3-12. Dispersion curves for a Si[110]/Si_{0.70}Ge_{0.30} MQW where L= 30 Å. Dashed lines represent zone center energies from the simple well model. $\pi/a \approx 0.51$.

remains. The D terms mixes the $|j=3/2, m_j=\pm 1/2\rangle$ or light hole states with the $|j=1/2, m_j=\pm 1/2\rangle$ or split-off states. That is why a slightly larger discrepancy exists between light hole and split-off energies than for heavy hole energies in Figure 3-11. For Si[110] material at $k_{\parallel}=0$, only the α term goes to zero while the β and D term remain. The β terms insures that all three bands intermix which will create large discrepancies in the energies obtained from the simple model and the EFA approach as seen in Figure 3-12. What is also apparent when examining Figure 3-11 and Figure 3-12 is that the total number of heavy hole bands increases when going from the [001] to the [110] growth direction. This occurs because the heavy hole effective mass in the [110] direction is so much heavier than the heavy hole effective mass in the [001] direction. If the curves for the [111] direction were plotted, even more bands would be found in the well.

3. Band Decomposition

The envelope function used to obtain the dispersion relations are normalized where

$$1 = \sum_{\lambda, j, m} \left| F_{N, j, m}^{\lambda}(\mathbf{k}_z, \mathbf{k}_{\parallel}) \right|^2 = \sum_{j, m} w_{N, j, m}. \quad \text{Eq 3-55}$$

The bands weights $w_{N, j, m}$ give the contribution of $j m^{\text{th}}$ band, or $|j m_j\rangle$ state to the N^{th} envelope function. This is important to know because the selection rules depend on the band content of the initial and final states. Figure 3-13 and Figure 3-14 show the band decompositions of the envelope function as a function of k_{\parallel} for the first four bands shown in the previous figures. The band decomposition plots are obtained by adding like pairs

(i.e. coefficients for components of the envelope function derived from $|3/2,3/2\rangle$ and $|3/2,-3/2\rangle$ pair) of the normalized band weights calculated in Eq 3-48. Relatively little mixing occurs for the heavy hole states in the Si[001] material. At zone center, both heavy hole states are completely heavy-hole like, or have a band weight of 1.0. For a doping level of $1 \times 10^{19}/\text{cm}^3$, states will be occupied out to 0.04 \AA^{-1} . Over this range, even the light hole states are 70 percent light hole like. Since the degree of band mixing is minimal, the selection rules are not significantly different from a simple quantum well analysis.

Selection rules dictate that for the [001] sample that a HH1 to HH2 transition occurs more strongly for parallel incidence, or z-polarized, light. Z-polarized light indicates that the electric field of the incident light is polarized parallel to the growth direction. The selection rules also indicate that a LH1 to LH2 transition is more strongly allowed for normal incidence, or xy-polarized light. Xy-polarized light indicates that the electric field of the incident light is polarized perpendicular to the growth axis. In contrast to the band decomposition of the [001] material, all the bands of the [110] material are thoroughly mixed, even at zone center. These results have not been previously published and are potentially significant since band mixing will relax the selection rules, giving rise to allowed transitions for any polarization of incident light. It is worthwhile noting that the labels HH, LH, SO, used to identify the bands in Figure 3-13 and Figure 3-14 are selected by the predominant character of the band near zone center. This label rapidly loses its meaning as increased values of k_{\parallel} give rise to a more thorough mixing of the HH, LH, and SO bands.

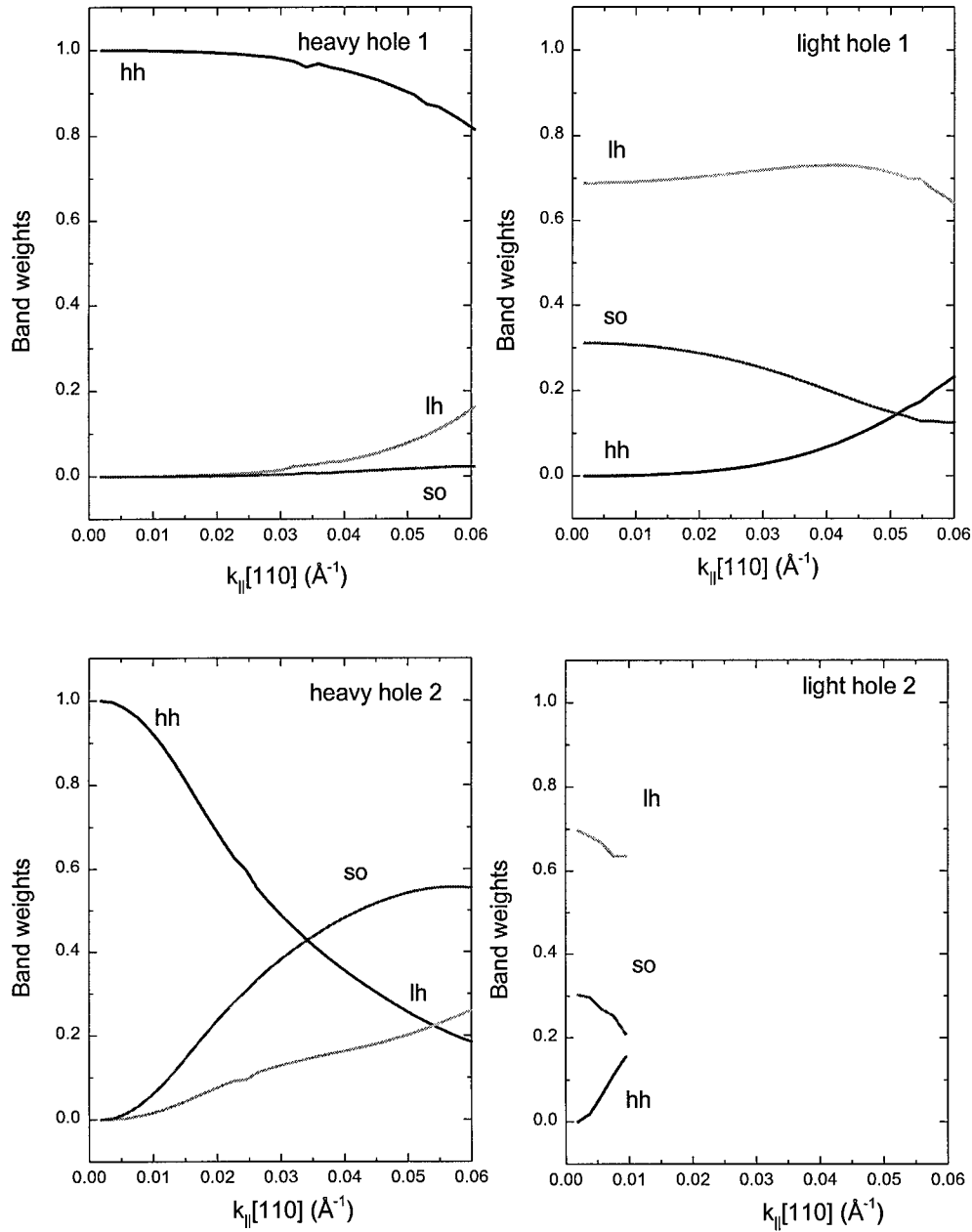


Figure 3-13. Band weights vs. $k_{\parallel}[110]$ for a Si[001]/Si_{0.70}Ge_{0.30} MQW with $L=30 \text{ \AA}$. $\pi/a \approx 0.51$.

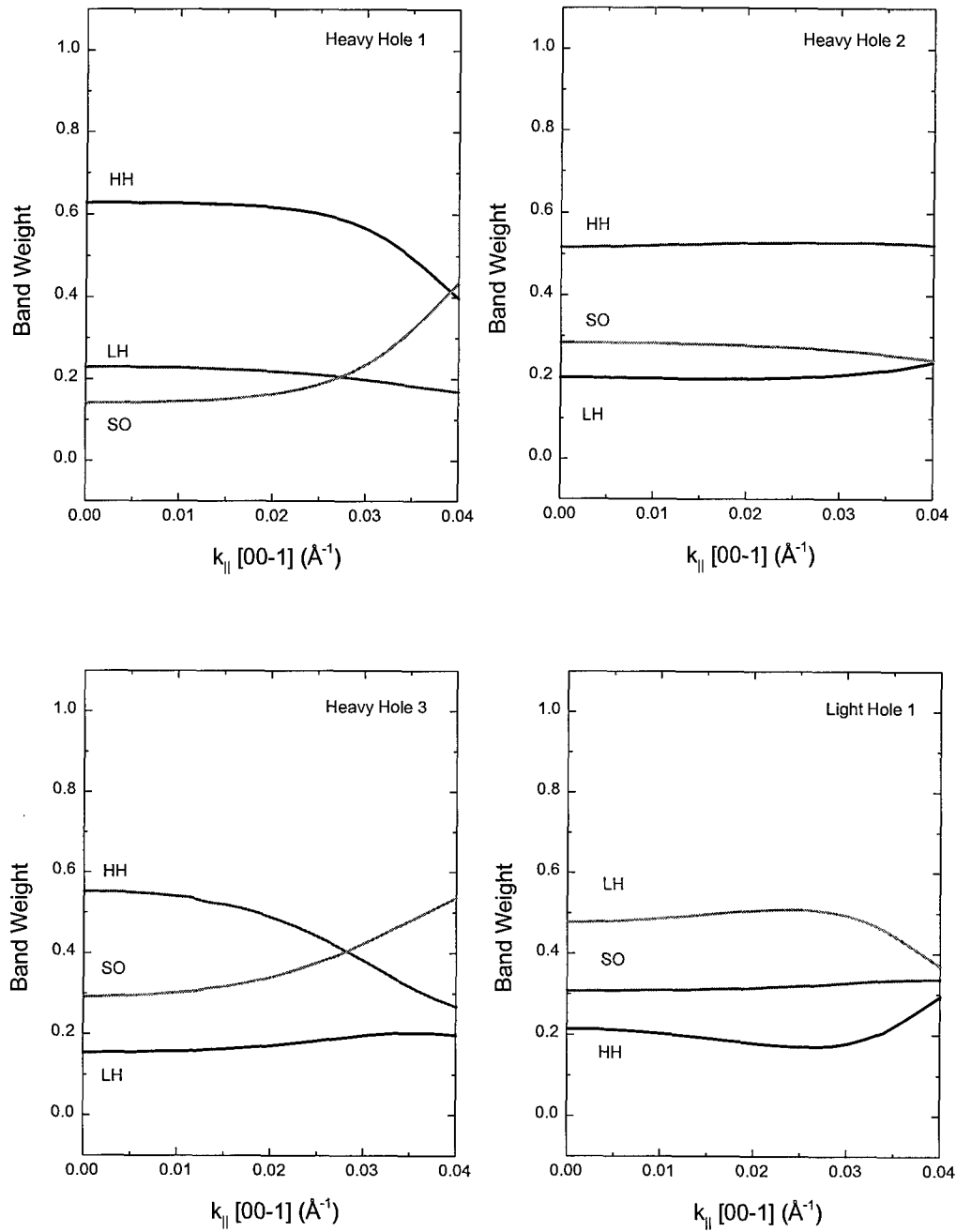


Figure 3-14. Band weights vs. k_{\parallel} [00-1] for a Si[110]/Si_{0.70}Ge_{0.30} MQW with $L=30 \text{ \AA}$. $\pi/a \approx 0.51$.

each band, and that the envelope function penetrates deeper into the barrier for each successively higher (for holes) state. The highest band, LH2, is very near the top of the well, and so the wave function associated with this state is delocalized. This is an ideal state to which to make a transition for detector purposes. The excited carrier would easily surmount the barrier and be swept away by an applied field. Each of these envelope functions is composed of six components, $F_{Njm}(\mathbf{k}_{\parallel}, z)$, given by Eq 3-38. Figure 3-16 shows the envelope function decomposition into these components at two different values of \mathbf{k}_{\parallel} . The top part shows that at zone center, the HH2 band is composed entirely of the $j=3/2, m_j=3/2$ contribution which is associated with the heavy hole band. This is in agreement with the lower left plot in Figure 3-13 which shows a HH2 bandweight of nearly 1 at zone center. However, more mixing occurs with increasing wave vector \mathbf{k}_{\parallel} as shown in the bottom part of Figure 3-16. In this figure there is a substantial contribution from the split-off band ($J=1/2, m_j=-1/2$). This is in agreement with the lower left plot of Figure 3-13 which shows near equal split-off and heavy hole character at $\mathbf{k}_{\parallel}=0.04$. The $F_{Njm}(\mathbf{k}_{\parallel}, z)$ (composition of the envelope function has direct bearing on the amplitude of the transition strength as will be demonstrated later.

The absorption coefficient for a transition from one band to another is directly proportional to the transition strength. By computing the transition strength, the selection rules are obtained, and a quantitative measure on the probability of transition is obtained. The 8x8 formalism of Szmulowicz has been adapted and applied here to the 6 x 6 formalism developed in Section C for the Si/SiGe alloy system. The equation for

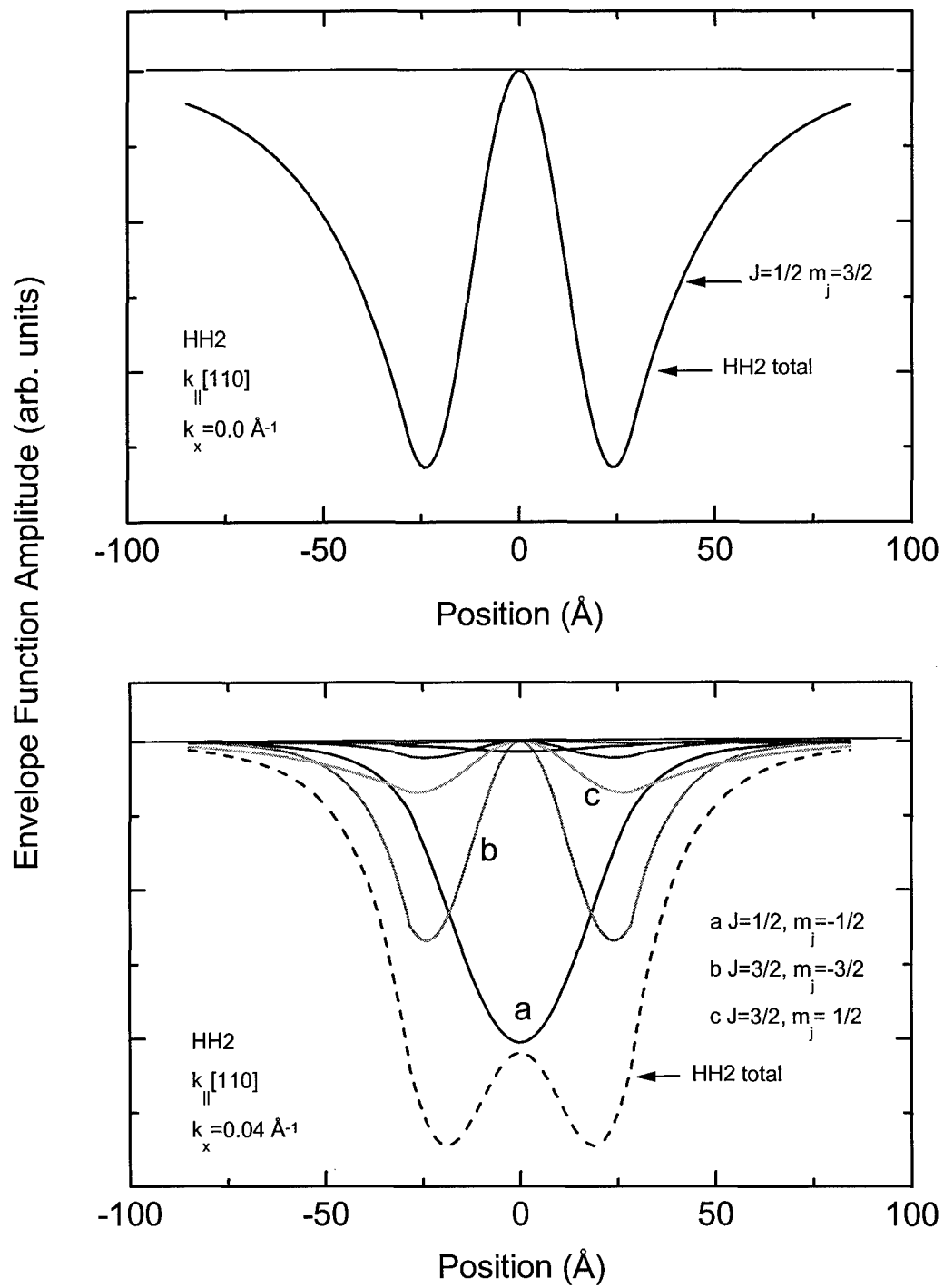


Figure 3-16. Envelope function decomposition for HH2 in a Si[001]/Si_{1-x}Ge_x MQW with $x=0.30$, $L=30 \text{ \AA}$, for two k_{\parallel} values.

transition strength is expressed as follows:

$$T = \frac{2}{m_0(E_N - E_M)} \langle N\mathbf{k}_{\parallel} | \hat{\boldsymbol{\varepsilon}} \cdot \mathbf{p} | M\mathbf{k}_{\parallel} \rangle. \quad (3-56)$$

E_N and E_M represent the energy for the bands in question. From Eq 3-56, it is apparent that the transition strength depends on the polarization of the incident light and the momentum matrix elements between wave functions. The interaction between the cell periodic parts of the zone center Bloch function, $u_{N0}(\mathbf{r})$ are factored out, and the momentum matrix elements are written in a more explicit fashion as

$$\begin{aligned} \langle N\mathbf{k}_{\parallel} | \hat{\boldsymbol{\varepsilon}} \cdot \mathbf{p} | M\mathbf{k}_{\parallel} \rangle = & \hat{\boldsymbol{\varepsilon}} \cdot \sum_{vv'} \left\{ \int dz F_v(N\mathbf{k}_{\parallel}, z)^* P_{vv'}(\mathbf{k}_{\parallel}, z) F_{v'}(M\mathbf{k}_{\parallel}, z) + \right. \\ & \frac{1}{2} \int dz \left[-i \frac{d}{dz} F_v(N\mathbf{k}_{\parallel}, z) \right]^* Q_{vv'}(\mathbf{k}_{\parallel}, z) F_{v'}(M\mathbf{k}_{\parallel}, z) + \\ & \left. \frac{1}{2} \int dz F_v(N\mathbf{k}_{\parallel}, z)^* Q_{vv'}(\mathbf{k}_{\parallel}, z) \left[-i \frac{d}{dz} F_{v'}(M\mathbf{k}_{\parallel}, z) \right] \right\} \end{aligned} \quad (3-57)$$

where the P's and Q's are both polarization and growth direction dependent.⁴⁰ The expressions for P and Q are quite lengthy and are placed in Appendix D. It is important to note that the P and Q matrices for [001] growth are available in the literature, but the matrices for the [110] growth direction were derived for this work. The first term of Eq 3-57 is the overlap integral for direct coupling of subbands with the same symmetry, such as HH-to-HH or LH-to-LH transitions. The second and third terms in the equation are dipole coupling terms for HH-LH transitions. As first pointed out by Chang and James

and later by Szmulowicz, intersubband absorption at normal incidence is possible in p-type quantum wells because of band mixing. In other words, the Ps and Qs will more strongly couple the initial state to the final states together for mixed bands. The strength of the absorption depends also upon the wave vector \mathbf{k}_{\parallel} . The momentum matrix elements along one direction in k-space for Si[001] and Si[110] quantum well structures with $x=0.30$ and $L=30 \text{ \AA}$ are shown in the Figure 3-17 and Figure 3-18. Notice in Figure 3-17 that an HH1-LH1 transition is allowed for xy-polarization in Si[001] based MQWs, but only when carriers populate states away from zone center. (The momentum matrix elements are the same for x or y polarization for [001] MQWs because of symmetry.) Notice also that HH1-HH2 is strongly allowed for z polarization. The behavior of the HH1-LH2 transition is difficult to ascertain from the few data points obtained. Figure 3-18 shows that the momentum matrix elements are much larger for Si[110] based MQWs. In addition, more transitions are possible and all are allowed at relatively small wave vectors. This will make identification of the individual peaks in experimental data difficult because the peaks will tend to overlap. It is important to note that the momentum matrix elements have been shown for only one direction in k-space. Because the [110] material shows such large anisotropies, it is expected that the momentum matrix elements in a different direction in k-space have a different character. Furthermore, to make truly quantifiable predictions on the position and shape of the intersubband transitions, one must calculate matrix elements in all directions in k-space. Such a complete calculation was beyond the scope of this project. The purpose of the theoretical

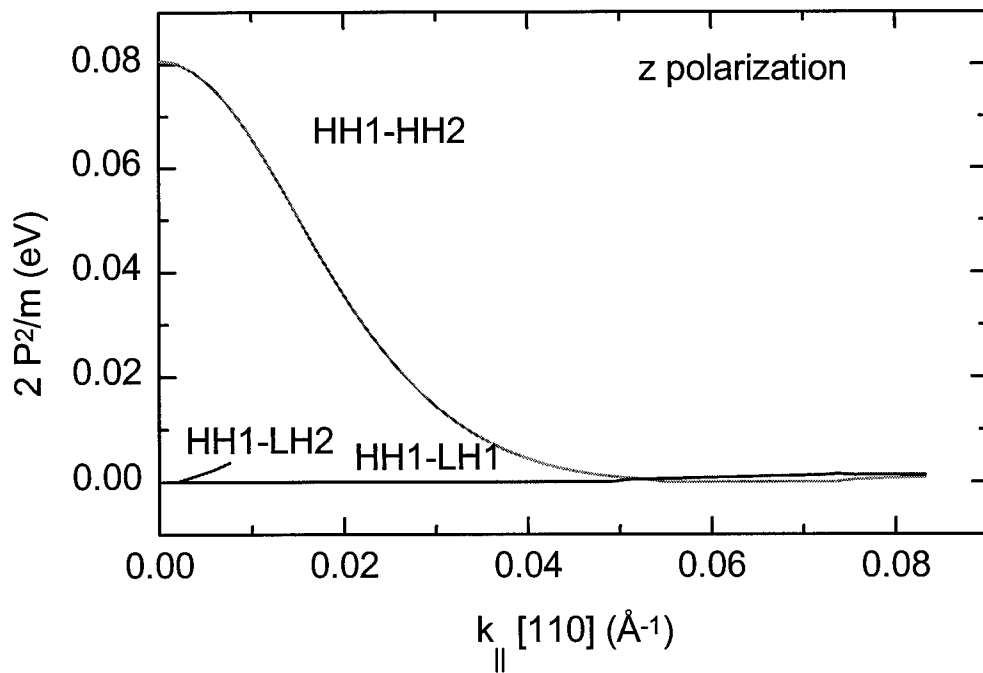
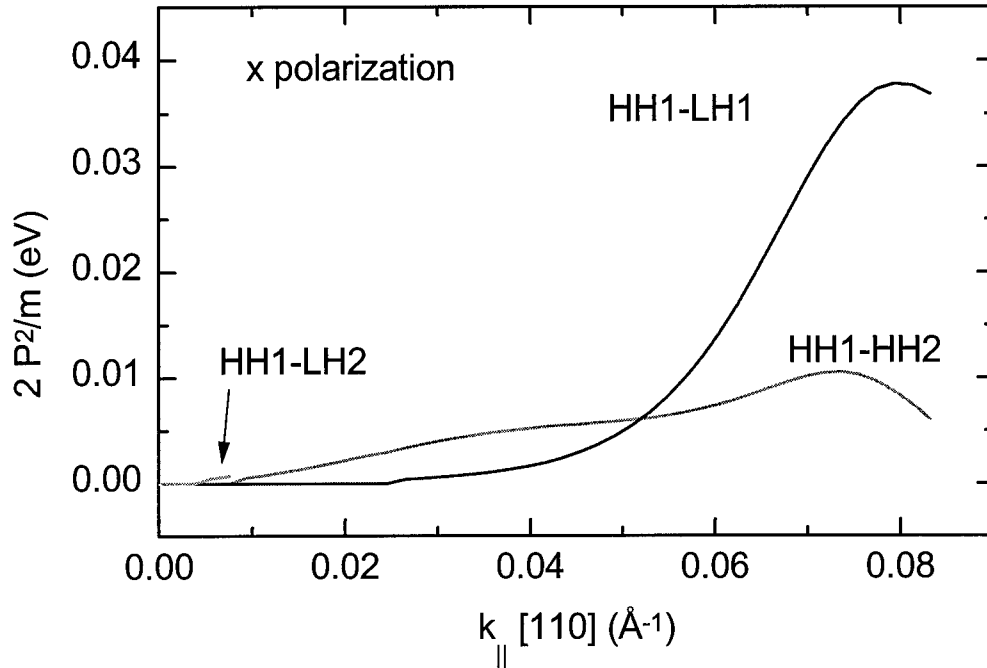


Figure 3-17. Squared momentum matrix elements for two polarization of incident light for a Si[001]/Si_{0.70}Ge_{0.30} MQW with $L=30 \text{ \AA}$.

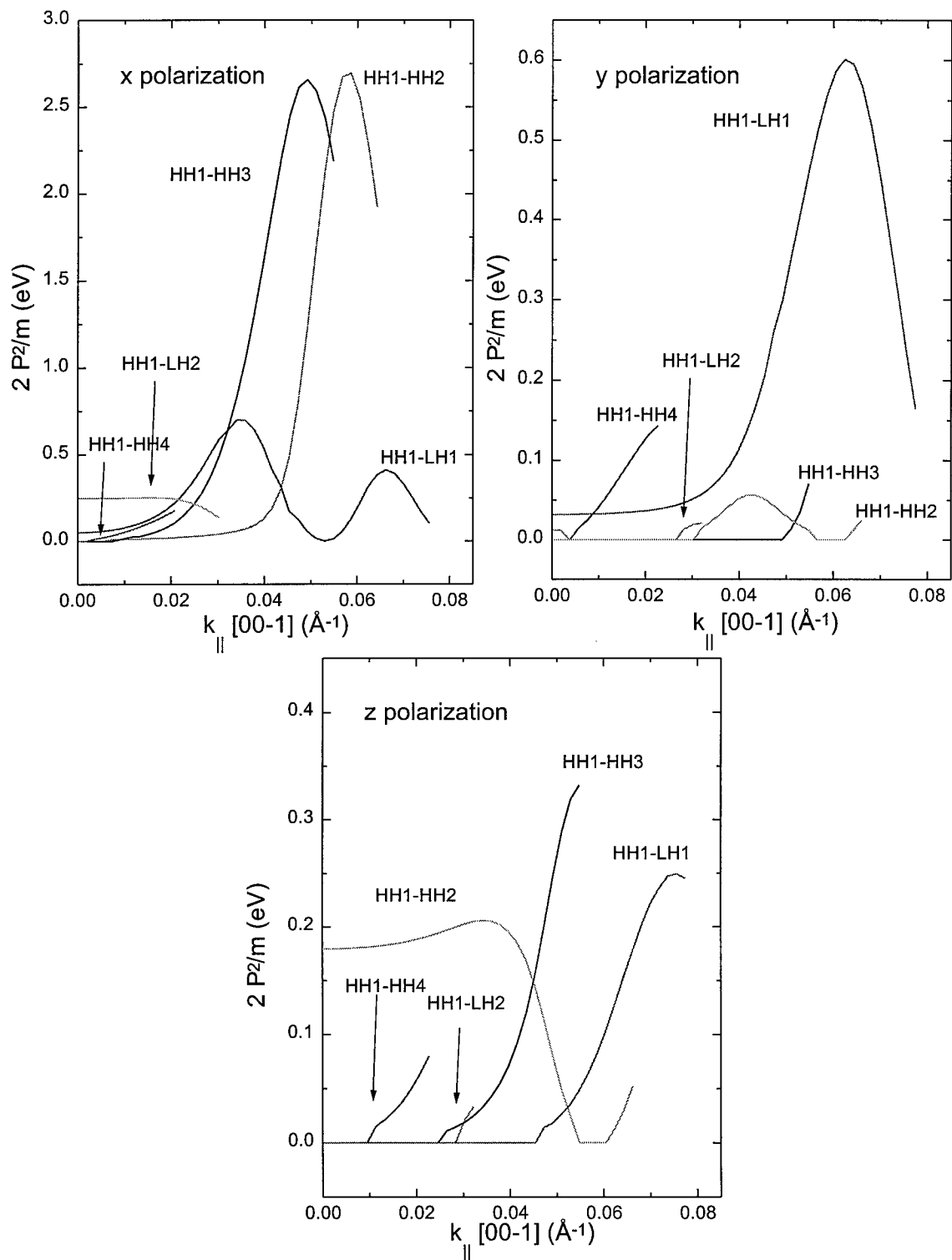


Figure 3-18. Squared momentum matrix elements for a Si[110] MQW with $x=0.30$ and $L=30 \text{ \AA}$ at three different polarizations.

calculations performed was to obtain a qualitative understanding of the experimental results.

G. Fermi Level Approximation.

The position of the Fermi level must be calculated to determine what region of k -space is occupied with holes. To approximate the Fermi energy, the density of states with respect to energy or wave vector must be known together with the total number of carriers occupying the states. A density of states calculation requires knowledge of the dispersion relations $E=E_N(\mathbf{k}_{\parallel})$ obtained using the prescription developed previously in the Section E. For wave vectors very close to zone center, the bands are parabolic and isotropic. However, as more impurities are incorporated into the quantum wells, the holes occupy states where the bands are no longer parabolic or isotropic. The anisotropy is particularly pronounced for the Si[110] MQWs. Figure 3-19 shows constant energy contours for the dispersion relations of identical MQW structures, $x=0.18$, $L=45 \text{ \AA}$, on different orientation substrates. The Si[110] MQW has a pronounced elongation of the constant energy surface along the [-110] direction while Si[001] MQW has elongation along the [010] direction. Because the constant energy surfaces show anisotropies, the density of states can not be calculated by assuming a simple parabolic band in a single direction. It is more appropriate to take an average of the dispersion relations along different projections in k -space. From the average of the bands, the density of states is approximated by the following equation.

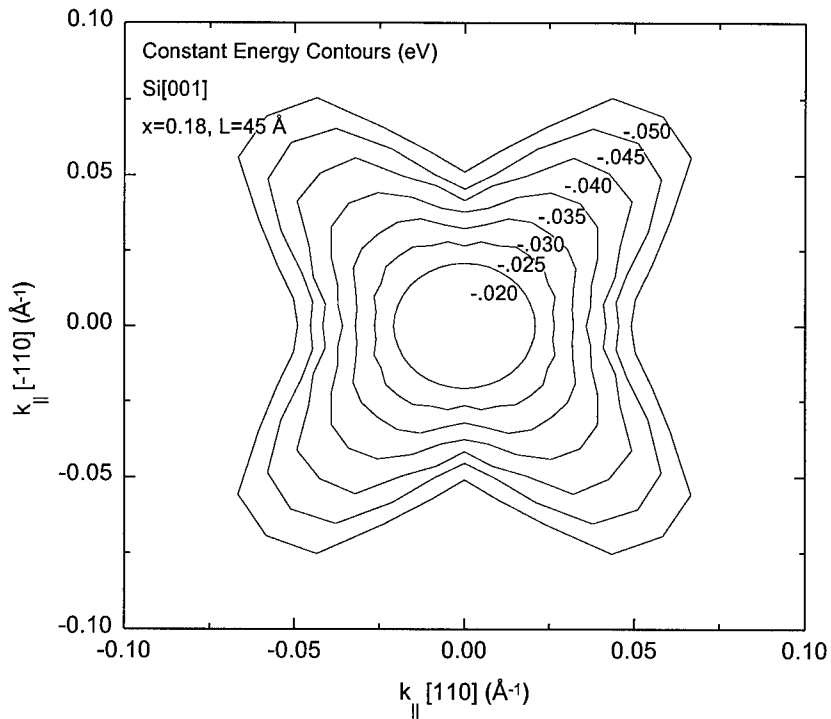
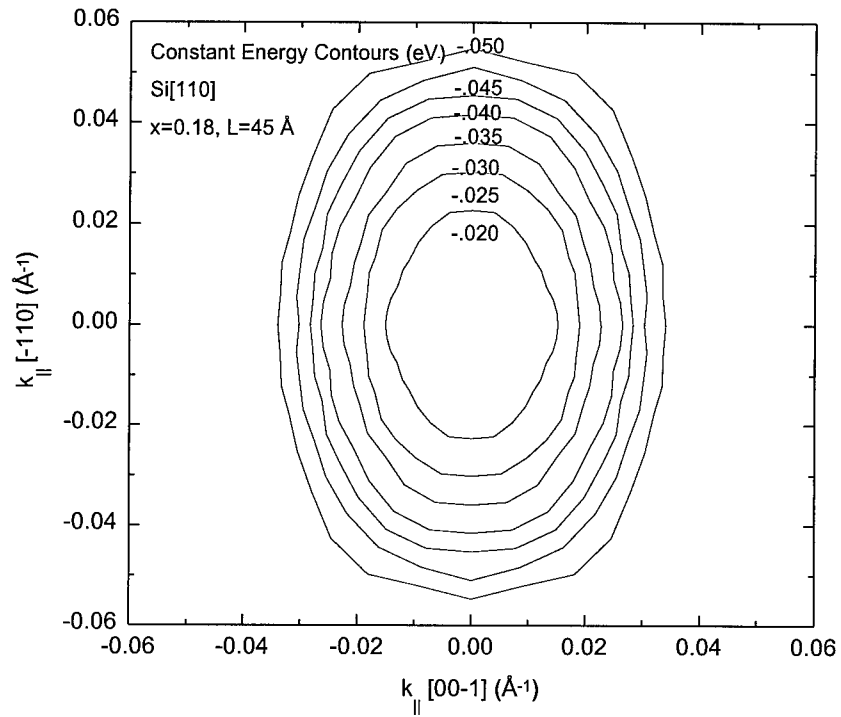


Figure 3-19. Constant energy contours for identical Si[110] (top) and Si[001] (bottom) MQW structures.

$$\begin{aligned}
g(E)dE &= g(k)dk \\
&\text{or} \\
g(E) &= g(k)\left(\frac{dk}{dE}\right) && (3-58) \\
&\text{or} \\
g(E) &= k_0 / \left. \frac{dE}{dk} \right|_{k_0}
\end{aligned}$$

where $g(E)$ is the density of states with respect to energy and k_0 is the k value at which the derivative is taken. The average dispersion curves for the top bands in each of the previous structures, $x=0.18$, $L=45 \text{ \AA}$, are shown in Figure 3-20. The horizontal lines in the figure represent the Fermi level for a given doping level. The Fermi levels are determined by first calculating the density of states as a function of energy as outlined above. Then the total number of states is calculated by integrating the density of states over the desired energy range. The Fermi energy will be the energy where integrated density of states equals the total number of dopant atoms/cm². For this calculation, the assumption is made that all dopant impurities incorporated into the well region are ionized. This assumption is less accurate at high carrier concentrations where a more refined statistical calculation is necessary. Furthermore, as the sample temperature is decreased, less ionization will occur thus changing the number of populated states. The density of states and integrated density of states generated from the average bands in Figure 3-20 are shown in Figure 3-21 and Figure 3-22. Van Hove singularities occur at the onset of an allowed energy band. Since most of the samples were grown for this project before the calculations were complete, the [110] samples were doped to $1 \times$

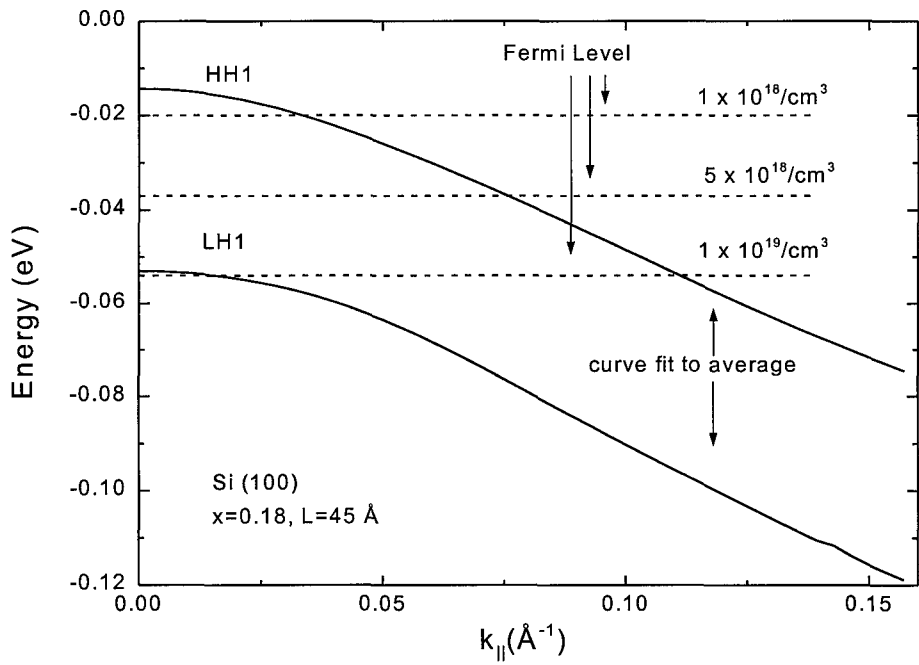
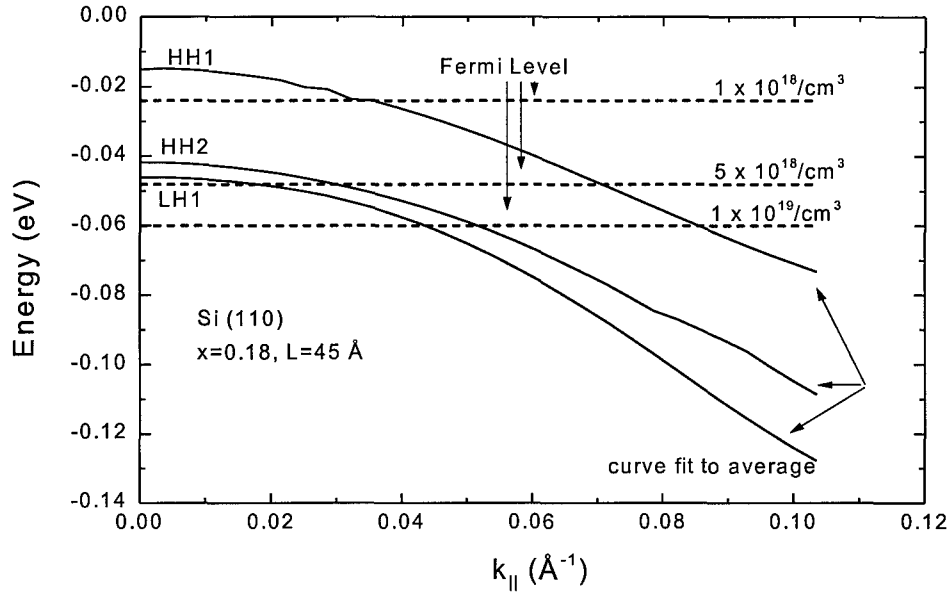


Figure 3-20. Average energy bands and Fermi levels for different doping levels for MQWs grown on Si[110] (top) and Si[001] (bottom).

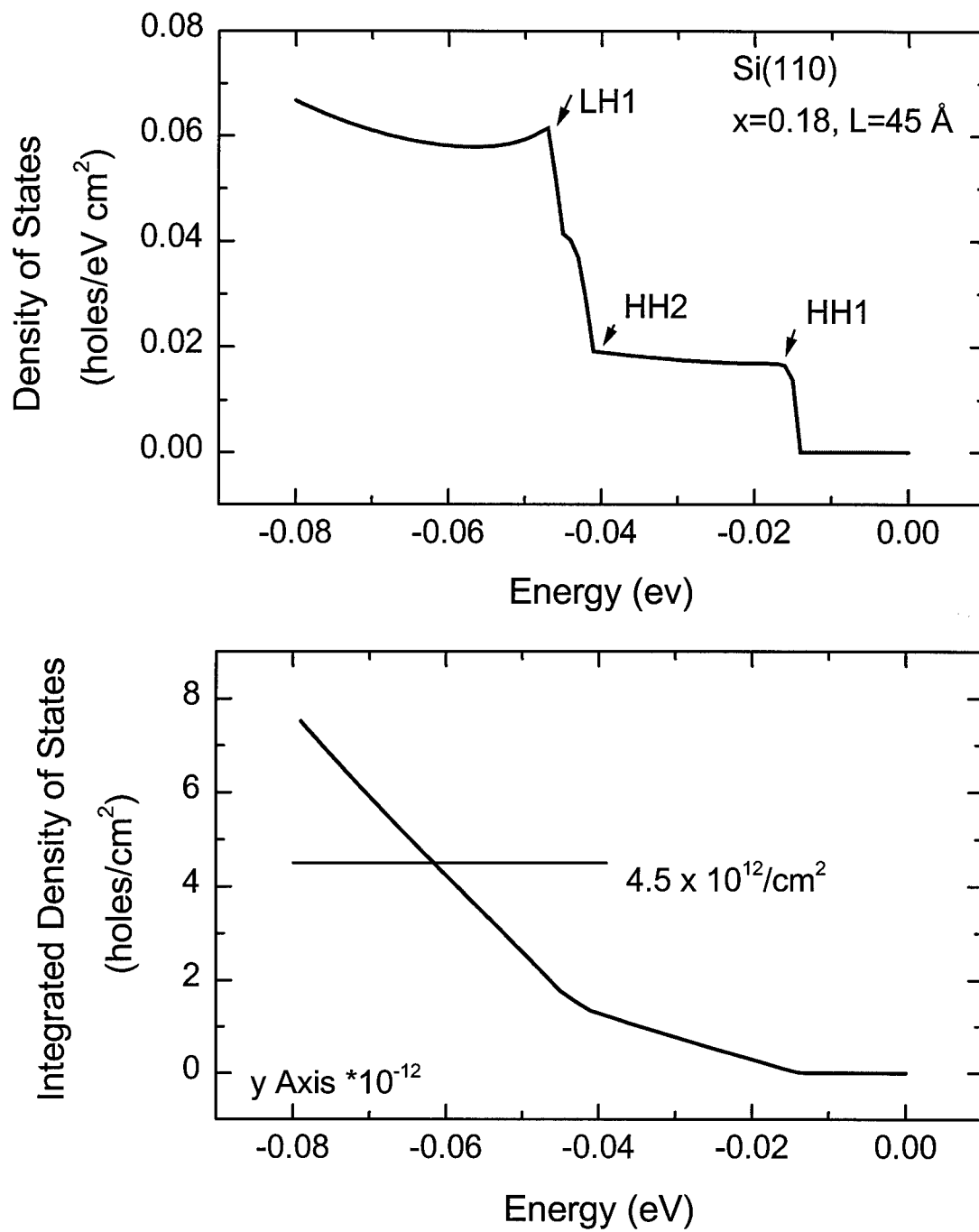


Figure 3-21. Density of states and integrated density of states for averaged energy bands in a Si[110] MQW where $x=0.18$ and $L=45 \text{ \AA}$.

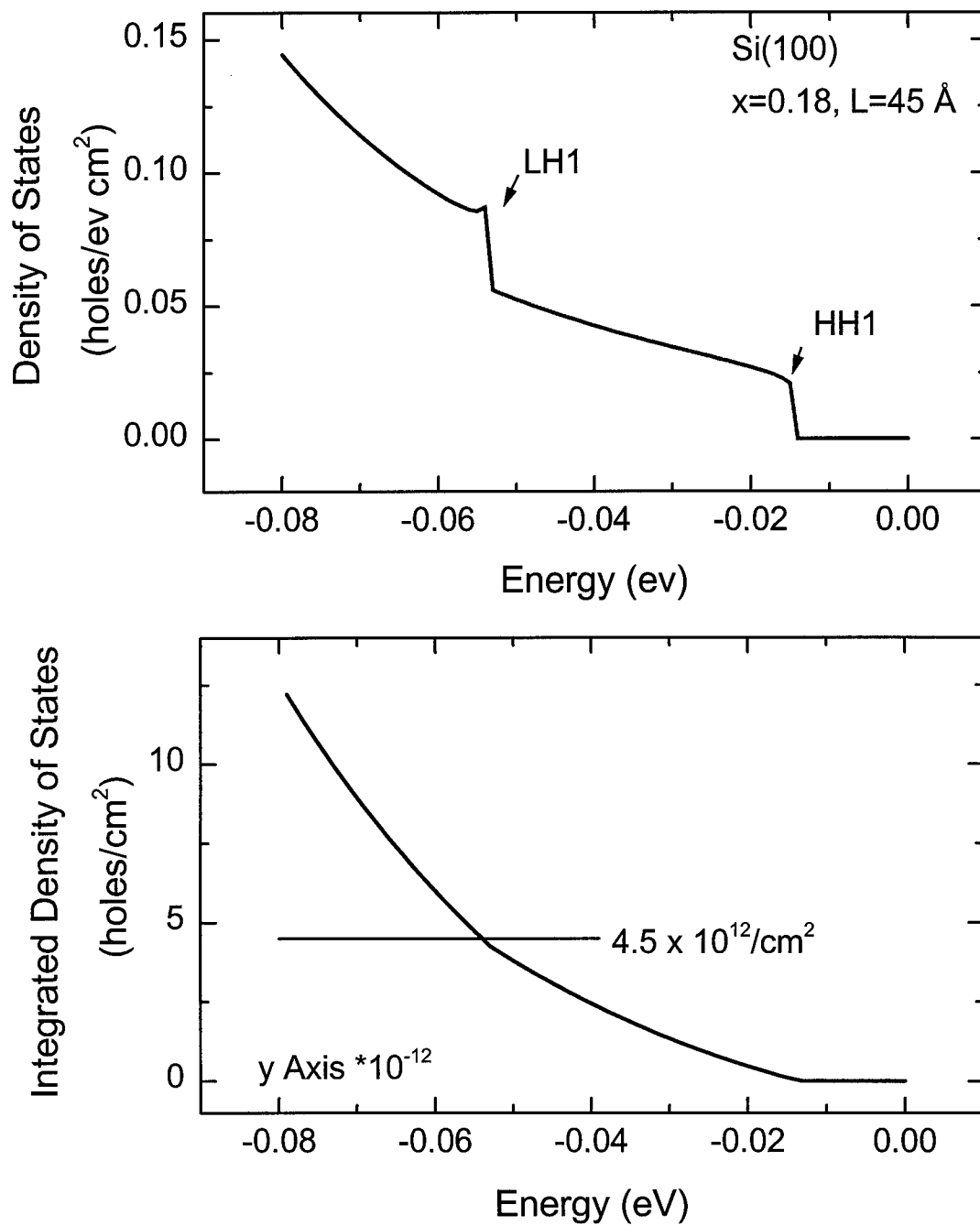


Figure 3-22. Density of states and integrated density of states for averaged energy bands in a Si[001] MQW where $x=0.18$ and $L=45 \text{ \AA}$.

$10^{19}/\text{cm}^3$. Unfortunately, this will push the Fermi level below the second and third bands.

This effect will tend to broaden the peaks in the absorption spectra as will be seen in

Chapter 5. The high doping will also increase the free carrier absorption which occurs

within a band which will further broaden the peaks in the absorption profile.

H. Comparison Between Si/SiGe and GaAs/AlGaAs

Having developed models to calculate the energy bands, transition strengths, etc. for any alloy system if the necessary constants are known, it is worthwhile to make comparisons between alloy systems. The necessary constants include the Luttinger parameters, the deformation potentials (if the material is strained), the spin-orbit splitting, and the band offsets. Since industry, for the most part, has concentrated on developing QWIPs in the GaAs/Al_xGa_{1-x}As system, it is instructive to compare Si/Si_{1-x}Ge_x QWIPs to GaAs/Al_xGa_{1-x}As QWIPs. The comparison is made on the basis of optimized performance in the 10 μm region which requires a well depth of approximately 150 meV and a ground state energy in the 15 meV to 25 meV range. With this criteria in mind, GaAs/Al_{0.30}Ga_{0.70}As and Si/Si_{0.82}Ge_{0.18} compositions have been chosen with well widths of 50 Å and 45 Å respectively. Figure 3-23 through Figure 3-25 show the band structures for these growth parameters. There are seven bound states in the Si[110] structure, compared to four in the Si[001] and GaAs[001] structures. This is in large part due to the heavier effective mass in the growth direction for Si[110]. Both Si structures show significantly more anisotropy in **k**-space which is due to strain effects and reduction in rotational symmetry. For a particular region of **k**-space, the effective masses change sign. This is especially evident in the LH1 band of the GaAs/AlGaAs structure. Using these dispersion relations and the equations of Section E, transition strengths can be computed, and they are presented in Figures 3-26 thru 3-28. For Si[110] MQWs the transition properties are different for the E-field polarized in the y-direction vs. polarized in the x-

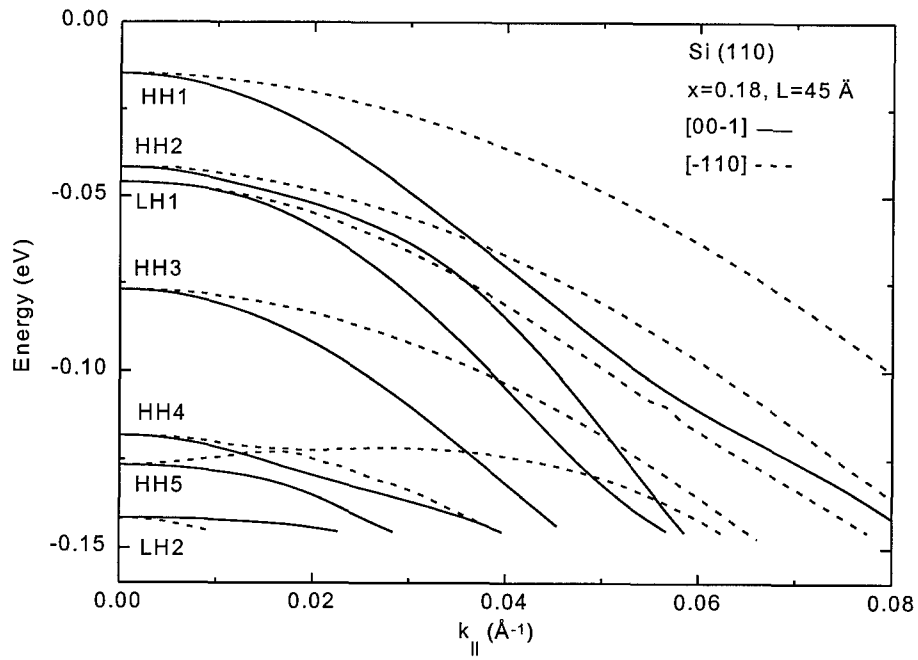


Figure 3-23. Dispersion relations for Si[110]/ $\text{Si}_{0.82}\text{Ge}_{0.18}$ MQW with well width of 45 Å. Solid lines are for the [00-1] direction and the dashed lines are for the [-110] direction.

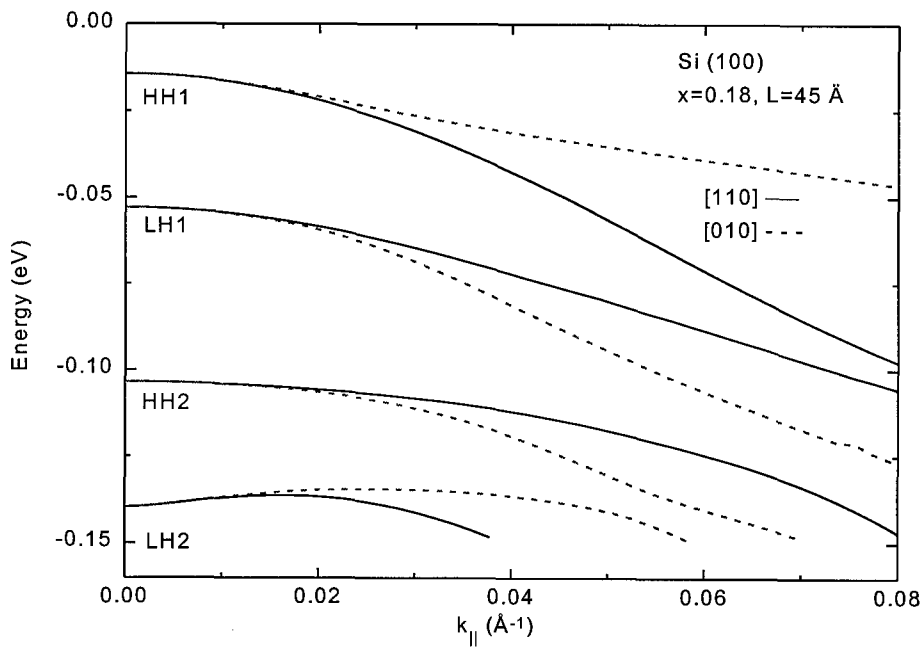


Figure 3-24. Dispersion relations for Si[001]/ $\text{Si}_{0.82}\text{Ge}_{0.18}$ MQW with well width of 45 Å. Solid lines are for the [110] direction and the dashed lines are for the [010] direction.

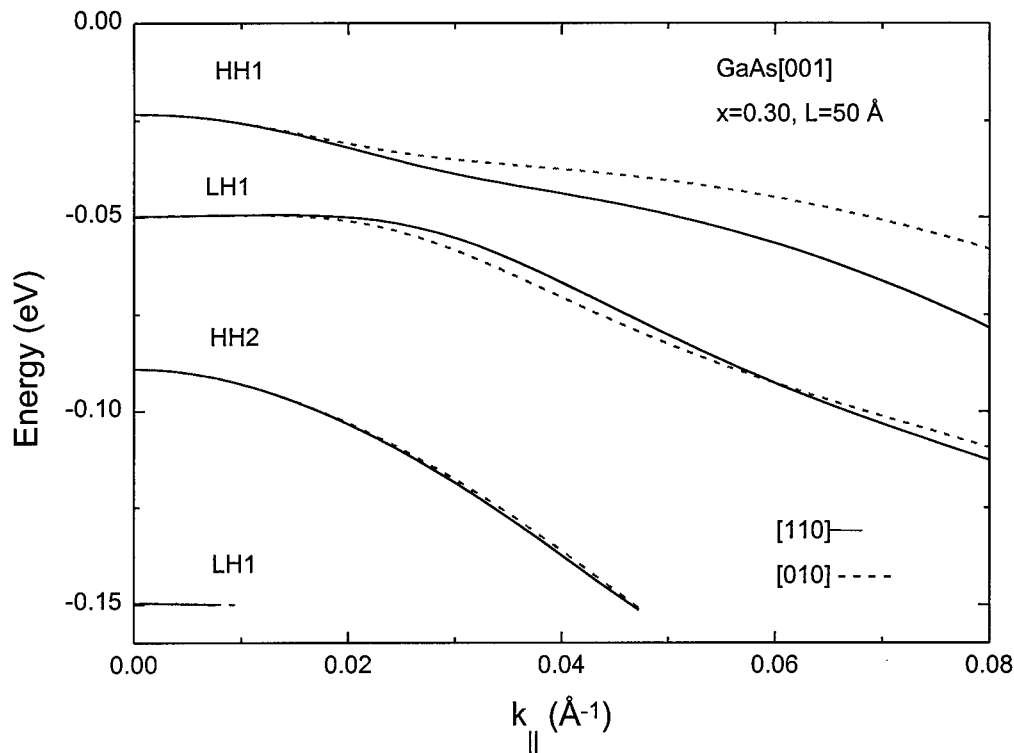


Figure 3-25. Dispersion relations for GaAs[001]/Al_{0.30}Ga_{0.70}As MQW with well width of 50 Å. Solid lines are for the [110] direction and the dashed lines are for the [010] direction.

direction. This phenomena is due to the anisotropic nature of the energy bands. For Si[001] and GaAs(001) MQWs, the band structure is isotropic in the (10) and (01) direction and so the transition properties are the same for both x and y-direction polarization. It is important to note that the selection rules have almost completely broken down for the Si[110] material. Once again, this is due the effects of band mixing. Even though normal incidence absorption should be enhanced near the zone center for the Si[110] material, the momentum matrix elements for the Si[001] material are at least a factor of five stronger farther out in the zone thus indicating that Si[001] MQWs should

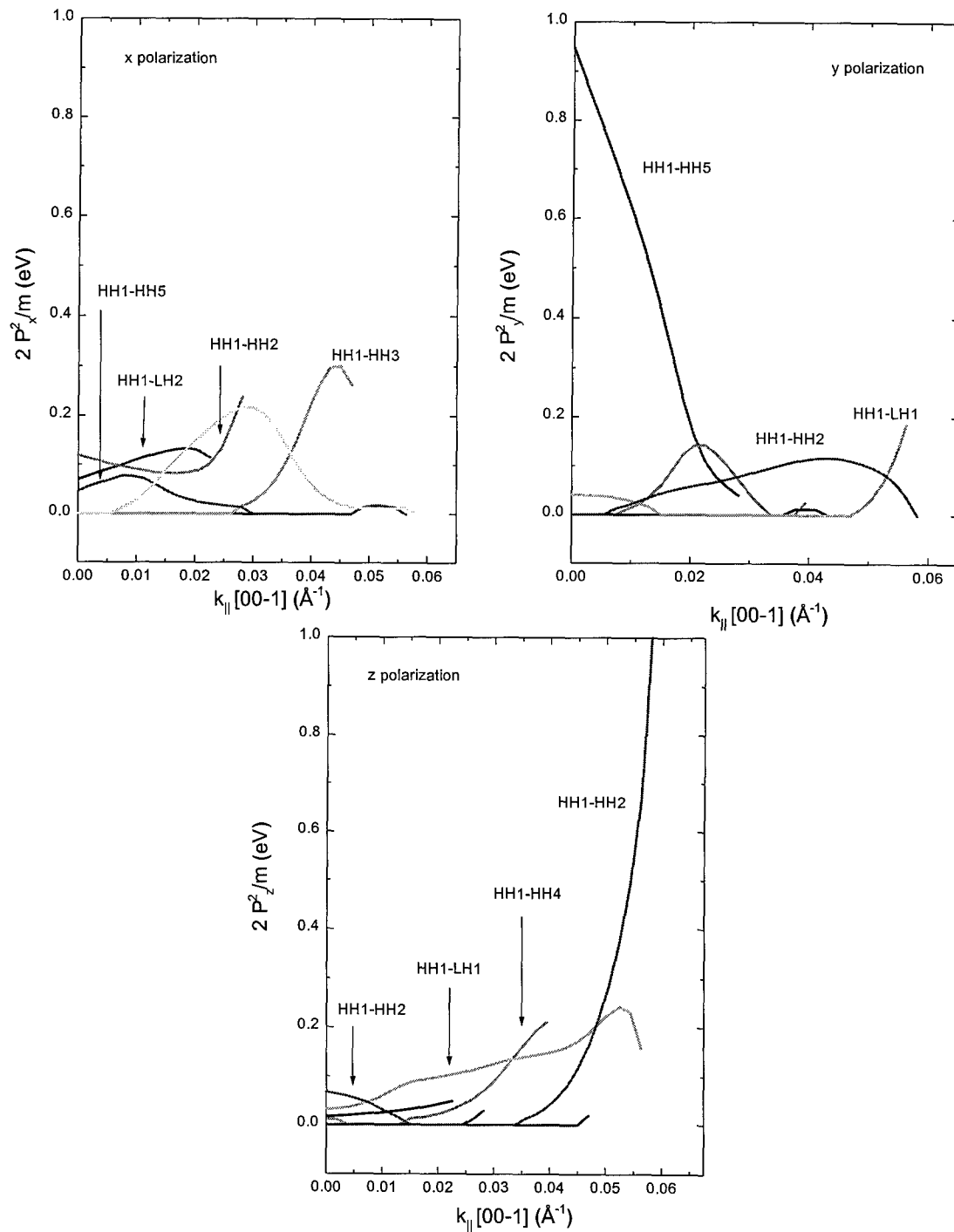


Figure 3-26. Squared momentum matrix elements for three polarizations of incident light for a Si[110]/Si_{0.82}Ge_{0.18} MQW with L=45 Å.

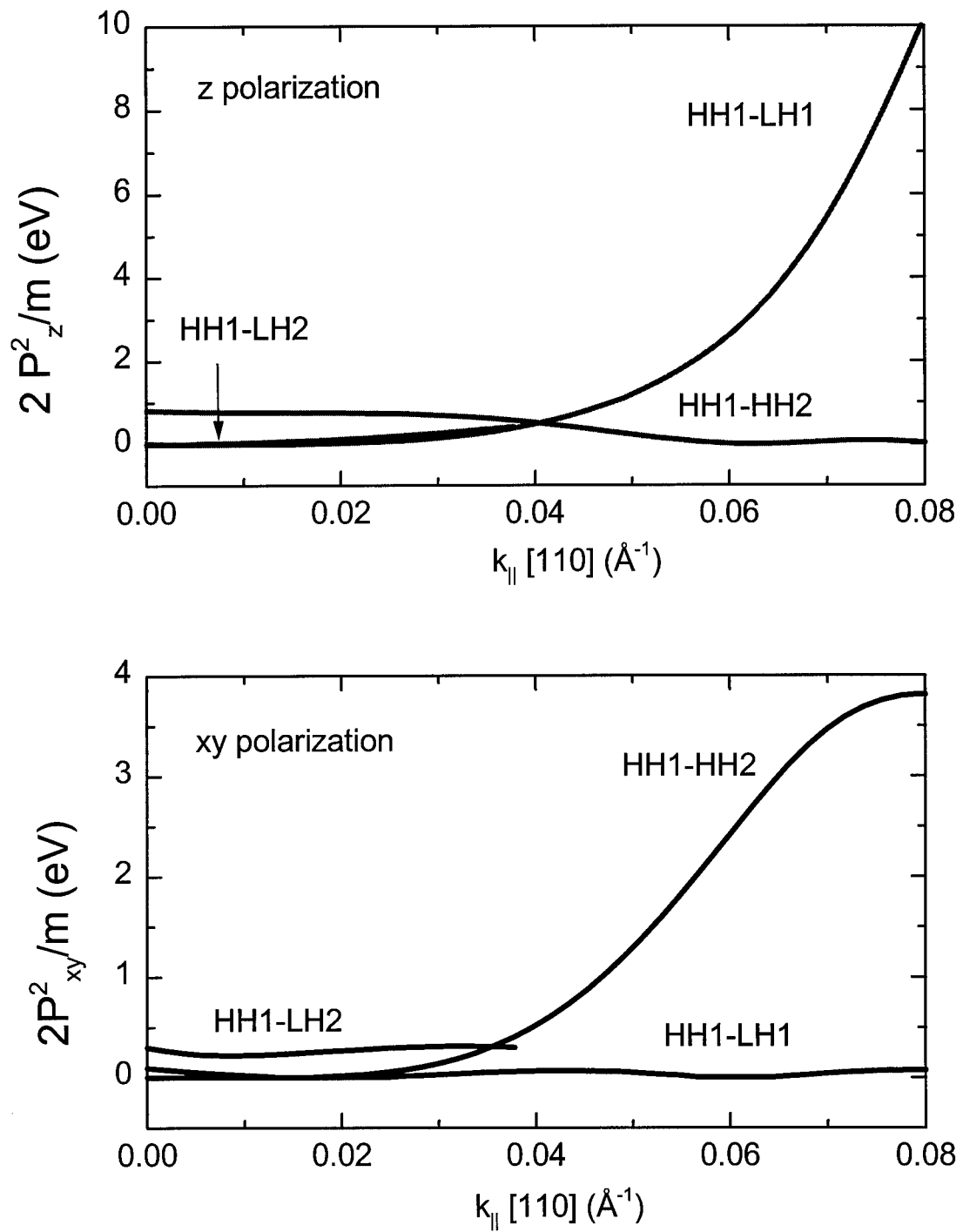


Figure 3-27. Squared momentum matrix elements for two polarizations of incident light for a Si[001]/Si_{0.82}Ge_{0.18} MQW with L=45 Å.

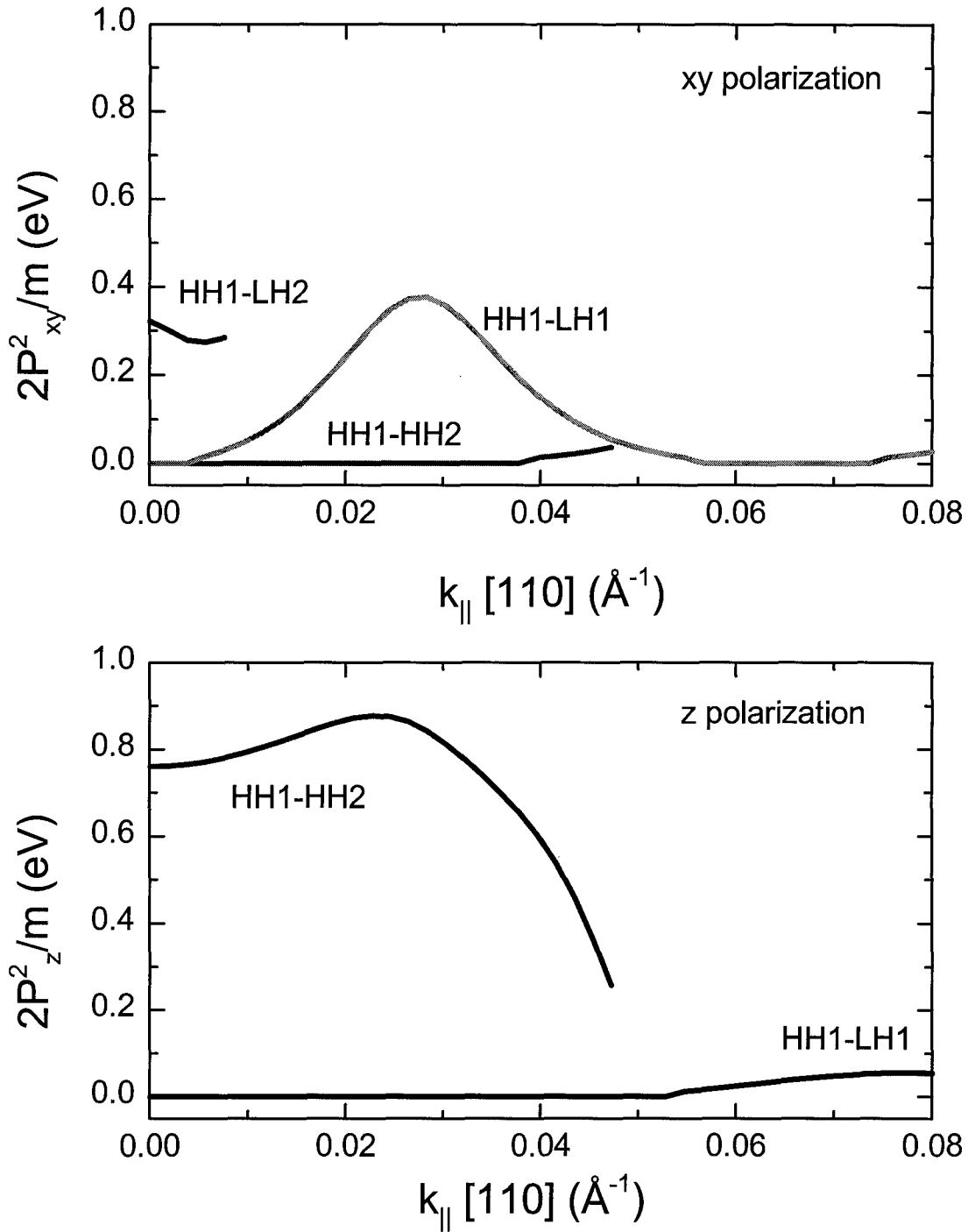


Figure 3-28. Squared momentum matrix elements for two polarizations of incident light for a GaAs(001)/Al_{0.30}Ga_{0.70}As MQW with L=50 Å.

perform better at the high doping levels used in Si/SiGe QWIPs. Both Si structures show significantly larger matrix elements than the GaAs/AlGaAs structure for both polarizations. This data indicates that Si based structures should perform at least comparably to GaAs structures. It must be noted however, that calculations of the absorption coefficients may alter the analysis. The data presented on the GaAs/AlGaAs system compares favorably with the published data of Szmulowicz.⁴⁰ Data obtained on the Si[001]/SiGe system (not presented here) compares favorably with data published by Fromherz⁴⁶ and Liou.⁷⁶

I. Calculated Energy Values

The theory outlined in the previous sections has been used to write a series of computer programs⁴⁴ to find the envelope functions, dispersion relations, transition strengths and Fermi levels for MQW structures. These programs are readily adaptable to any substrate orientation and may be applied to systems other than Si/Si_{1-x}Ge_x if the empirically obtained constants are available. Theoretical and experimental data was available in the literature for the GaAs/AlGaAs system and somewhat less available for the Si[001]/SiGe system. The approach to evaluating the validity of the programs was to write the codes so as to reproduce the data in the literature for the GaAs/AlGaAs. This was done successfully. The next step was to adapt the codes to consider strain in the Si[001]/SiGe system. Once again, the accuracy of the theory and approach was confirmed by comparison against existing data in the literature. The final step was to rewrite the codes to accommodate a [110] growth direction. To the author's knowledge, there is no existing data for Si[110] quantum well structures. Furthermore, explicit matrix elements for the 6 x 6 total Hamiltonian for the [110] growth direction could not be found in the literature and were derived using the same approach used in obtaining the matrix elements for the [001] direction. The validity of the [110] calculations is inferred by the validity of the [001] calculations. All the [110] dispersion relations, band decompositions, transition strengths, density of states calculations represent a new contribution to the field. It is important to note that the absorption coefficient to the continuum energy levels has not been calculated which is necessary to completely

analyze the absorption and photoresponse data. However, with knowledge of the bound states and the Fermi energy, a more than adequate analysis can be performed.

Now that both approximations for obtaining energy levels have been discussed, it is instructive to compare some of the numbers obtained. Table 3-1 lists the data for Si[001] and Table 3-2 list the data for Si[110]. To reiterate the data for the [001] growth direction is confirmed by other calculations in the literature, but the data for the [110] data is new.

Table 3-1. Calculated zone center energies for Si[001]

x	L	HH1	HH2	HH3	LH1	LH2	cont
Ge %	(Å)	(meV)	(meV)	(meV)	(meV)	(meV)	(meV)
uncoupled band approximation							
20	40	38	137		83		164
30	30	64	224		126		246
40	40	48	187		126	278	328
60	40	54	217	458	162	354	491
envelope function approximation							
20	40	39	142		81		164
30	30	68	225		128	243	246
40	40	50	191	308	120	268	328
60	40	55	217	449	154	317	491

Table 3-2. Calculated zone center energies for Si[110]

x	L	HH1	HH2	HH3	LH1	LH2	cont
Ge %	(Å)	(meV)	(meV)	(meV)	(meV)	(meV)	(meV)
uncoupled band approximation							
15	50	15	58	114	66		119
20	40	22	85	159	82	158	159
30	30	39	148		124	241	240
30	40	25	99	206	105	222	241
envelope function approximation							
15	50	11	53	80	57	112	119
20	40	19	50	95	54	144	160
30	30	36	77	169	93	225	241
30	40	13	51	101	60	179	241

The data points out the large discrepancy between the uncoupled band approach and the EFA approach for the Si[110] quantum wells.

Momentum matrix elements, $P_{mn}(k_{\parallel})$, together with subband energy differences, $\Delta E_{mn}(k_{\parallel}) = E_n(k_{\parallel}) - E_m(k_{\parallel})$ can be used to calculate absorption coefficients.⁴⁰ This calculation is computationally intensive as a result of the anisotropic nature of the dispersion relations. However, it is possible to use the zone center EFA energies tabulated above to qualitatively analyze the experimental data. This analysis begins with the

observation that there are many more transitions at zone center for [110] materials as compared to [001] materials. Furthermore, the momentum matrix elements such as those presented in Figure 3-18 indicate that almost all these transitions are allowed. These transitions are broadened to a significant degree by the finite lifetime of the bound states as well as the functional dependence of ΔE_{mn} on k_{\parallel} . However, zone center transitions can give a general indication over which wavelength range transitions are likely to occur in absorption measurements. In addition, a long wavelength, cutoff for the photoresponse can be determined by taking the difference in energy between the zone center HH1 and the continuum level. Remember that the continuum level at zone center is determined by the magnitude of the valence band offset at the heterojunction interface.

4. Experimental Techniques

A. Introduction

This research is based on experimental characterization of MQW material. A theoretical background was developed in the previous chapter to aid the interpretation of experimental results, while techniques necessary to obtain experimental results are explained in this chapter. Three spectroscopic techniques are used to obtain the experimental characterization; photoluminescence, absorption, and photoresponse. A different facet of the overall problem is illuminated with each technique, and ideally they should be consistent. Photoluminescence (PL) measurements are used to determine the crystalline quality. Absorption (AB) measurements are used to determine the position in energy of the bound states in the quantum well and the resonant states above the well and the absorption strength of the transitions between states. Photoresponse (PR) measurements are used to indicate the energy or wavelength range in which the material can be used as a detector. Thus, although photoresponse is a better measure for detector characterization, absorption measurements provide insight into the process by which the detector response can be tuned to a desired wavelength. However, neither measurement can be made successfully unless the material is of sufficiently high quality so as to allow quantum confined effects, an assessment which can be made with PL. Thus all three of the measurements should be complementary.

All the $\text{Si}_{1-x}\text{Ge}_x$ samples used for optical characterization were grown via molecular beam epitaxy (MBE) at the Naval Research Laboratory (NRL) by Dr. Phil

Thompson in a *VG-V80* MBE system. Eagle-Picher silicon and germanium bulk sources with purity levels exceeding 2×10^{21} ppm were evaporated by a Temescal CV-14 electron beam. The details of the particular MBE growth system used there are reported elsewhere.⁷⁷ For an in-depth description of the MBE process, the reader is referred to Herman and Sitter.⁷⁸ The QW structures were grown on commercial 76 mm (100) and (110) substrates. The substrates were undoped with a 10-20 Ω -cm resistivity for the (100) and 20-70 Ω -cm resistivity for the (110). Prior to growth, the substrates were prepared with a modified Shiraki process,⁷⁹ resulting in a hydrogen-terminated surface. The surface hydrogen was subsequently removed prior to growth by heating the sample to 650 °C. Most of the samples used for PL diagnostics were grown at 710 °C while those used for absorption and photoresponse were grown at 550 °C. A Si buffer layer was first grown on the substrates to insure a clean, low-defect growth surface for the quantum wells. Typical buffer layers were grown at 710 °C, at the rate of 0.5 Å/sec for a total thickness of 1000-1700 Å. MQW structures were grown fully strained above the Si buffer layer at temperatures ranging from 550 to 710 °C with a typical SiGe alloy deposition rate of 0.625 Å/sec. The MQW structures consisted of 5 to 50 periods of 300 Å Si barriers followed by $\text{Si}_{1-x}\text{Ge}_x$ wells that varied in width from 20 Å to 50 Å. The $\text{Si}_{1-x}\text{Ge}_x$ alloy wells had germanium compositions, x , ranging from 0.10 to 0.60. The doped samples had boron concentrations ranging from 1×10^{18} atoms/cm³ to 8×10^{19} atoms/cm³. The MQW structures were capped with undoped Si layers ranging in thickness from 500 Å to 2000 Å, grown in the same manner as the buffer layer. Surface morphology was verified using 2×2 low-energy electron diffraction (LEED) and

Nomarski optical microscopy. A complete list of the samples and their growth parameters is presented in Appendix E.

B. Photoluminescence

1. Diagnostic Tool

Photoluminescence (PL) was performed in this research primarily to provide feedback on sample quality to the crystal grower at NRL. Photoluminescence is a standard, nondestructive, diagnostic tool used in the analysis of semiconductor material. It is used to probe the energy levels within the band gap region, by observing the optical transitions between levels, but it can also be used to observe defect levels or impurity levels within the band gap. PL produces a distinct spectrum, rather like a fingerprint, in every semiconductor material. If the crystal is very uniform and defect free, the spectrum will exhibit at least some sharply defined features, otherwise the spectrum exhibits broad and indistinct features. Once a standard spectrum has been obtained for a particular material, it serves as a benchmark for subsequently grown materials of the same composition. All the samples used in this research were grown via MBE. An MBE system is quite complex, and small changes to the system can substantially affect the quality of the material produced. Occasionally control electronics, mechanical feedthroughs, viewport windows, etc. must be repaired or replaced. In addition, the growth chamber must be periodically opened to replace the elemental Si and Ge sources, the B doping source, or to replace the substrate heater tapes. These departures from the norm can create variations in the growth and thus introduce changes which necessitate an extensive re-calibration period. The PL spectrum of the material grown subsequent to system maintenance should reproduce the benchmark spectrum. When used in this

fashion, PL serves a vital role in the production of high quality material, and it has become a standard practice at NRL to grow replicate samples after each substantial system upgrade or source change.

PL is the optical radiation produced when an electron, excited to a higher energy state by the absorption of an incident photon, decays to a lower energy state, thus emitting a photon characteristic of the energy difference between the two states. A diagram of the different decay or recombination processes is shown in Figure 4-1.

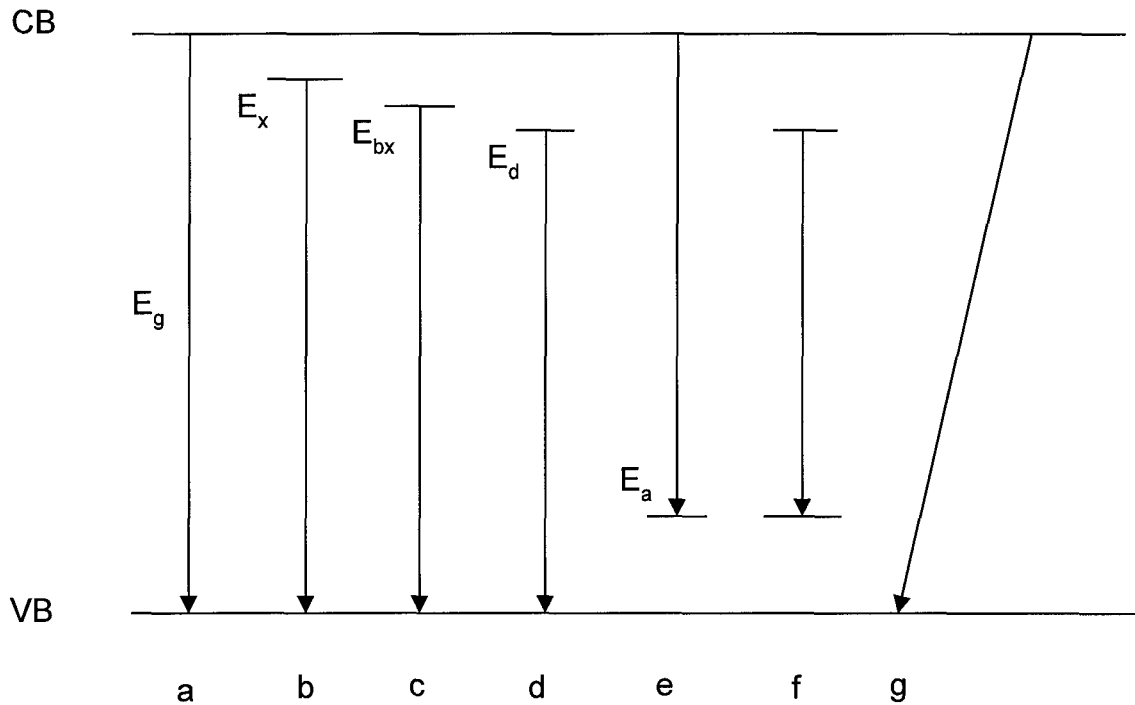


Figure 4-1. Recombination processes of excited electrons in semiconductors. (a) band-to-band; (b) free exciton; (c) bound exciton; (d) donor-to-valence band; (e) conduction band-to-acceptor; (f) donor-acceptor pair; (g) phonon-assisted or indirect.

The incident photons are usually supplied by a laser operating at a wavelength sufficient to excite an electron from the valence band (VB) into the conduction band (CB). The 488 nm line of an Ar ion laser was the primary source of excitation used in this research. Since $E=hc/\lambda$, where E is the photon energy, h is Planck's constant, c is the speed of light, and λ is the wavelength of the source, the laser delivers a photon of energy 2.54 eV. This energy is sufficiently greater than the band gap energy (E_g) of intrinsic Si, approximately 1.1 eV to excite a valence electron into the conduction band. For most of the samples grown for this research, the MQW layers of interest are contained within the top 5000 to 7000 Å. As a result, the penetration depth of the incident photons is a concern. The penetration depth, at which $I(x)/I_0 = 1/e$, is determined through Beer's Law:

$$I(x) = I_0 e^{-\alpha x} \quad (4-1)$$

where $I(x)$ is the intensity of the light as a function of depth, I_0 is the incident intensity, and α is the absorption coefficient of the material. Aspnes and Studna⁸⁰ published a detailed study of dielectric functions of Si and Ge from which the absorption coefficients, as a function of photon energy, can be determined. Table 4-1 lists the absorption coefficients and resulting penetration depths germane to this research.

PL is usually obtained via dispersive spectroscopic techniques which divide the total, multi-frequency, light signal into spatially separated, frequency bands. The light passes through a spectrometer which uses an optical grating to spatially separate bands of intensity as a function of frequency. A detector responds to the signal intensity of each of these bands as the grating/mirror system scans the frequency-selected signal past the

Table 4-1. Absorption coefficients and penetration depths of available laser lines.

wavelength (nm)	photon energy (eV)	absorption (10^3 cm^{-1})	penetration depth(μm)
647.1 (red)	1.92	3.4	2.97
514.5 (green)	2.41	15.0	0.67
488.0 (blue)	2.54	20.6	0.48
350.0 (UV)	3.54	1078.0	0.01

output slit. Other dispersive spectroscopic techniques may also use prisms, etalons, or combinations of these optical components; however, they all share the common function of spatially separating the signal as a function of frequency, scanning the output past a detector, and recording the detector response.

2. PL Experimental Procedures and Apparatus

The MBE samples were usually received from NRL as a section of a quartered 2 inch wafer. A smaller sample, measuring approximately 3 mm by 10 mm, was cleaved from the larger section using a diamond tipped scribe. The samples were affixed to a four sided copper sample holder with a small amount of rubber cement placed between the holder and the lower half of the sample. During data runs, the laser spot would be centered on the upper half of the sample thus minimizing any effects on the luminescence due to strain in the sample. A schematic illustration of the experimental apparatus used for PL is shown in Figure 4-2.

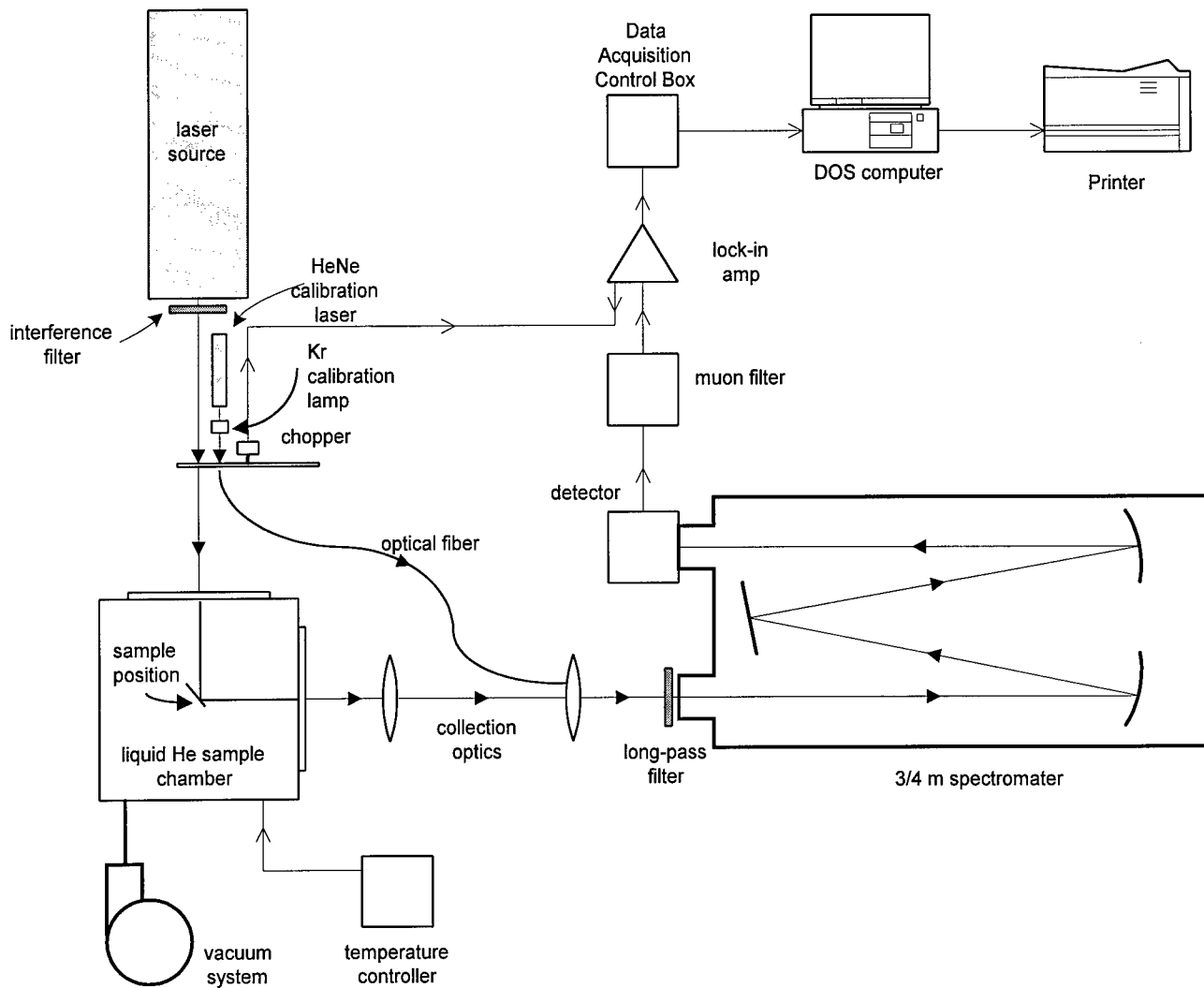


Figure 4-2. Schematic diagram of photoluminescence experimental apparatus.

After mounting the samples and cleaning them with acetone, the sample holder was subsequently mounted inside a *Janis Super VariTemp 10DT* optical dewar. The dewar was evacuated with a mechanical roughing pump to produce better temperature control and allow a minimum temperature of 1.5 K. The sample chamber was cooled to LHe temperatures by opening a throttle valve on the *Janis* dewar which allowed LHe to flow

into the sample chamber. The LHe was allowed to pool in the bottom of the dewar and rise to a level where it just touched the sample. Sample temperature was roughly controlled by adjusting LHe flow with the throttle valve, but more accurate control was obtained with a *Lakeshore 805a* temperature controller utilizing *Lakeshore 100DT* silicon diode temperature sensors and two thermal resistance heater coils. One coil was placed in the bottom of the dewar and the other was wrapped around the sample holder just above the area where the samples were mounted. The PL spectra were collected with a *Spex 750M*, $\frac{3}{4}$ -meter dispersive monochromator. The monochromator utilized a 600 groove/mm grating blazed to 1.25 μm in first order. The input and output slits were usually set to 600 μm . The signal was detected by a LN-cooled, *Applied Detector Corporation 403L* germanium detector responsive from 0.8 to 1.7 μm . The analog signal was filtered by a *North Coast 829B* muon filter and amplified by a *Stanford Research SR850* lock-in amplifier. Laser excitation was provided by a *Spectra Physics 2085* Ar ion laser at power levels between 50 mW and 500 mW. Spontaneous emission lines from the laser tube were filtered at the source with a 5 nm notch filter centered around the 488 nm line of the laser. The portion of the 488 nm line reflected off the sample and extraneous room light was filtered at the monochromator entrance slit with a 1 μm long-pass filter. All the PL data was collected via *Spex Data Acquisition and Control Software*. Parameters such as scan range, wavelength step-size, integration time, etc. were all set through a system of pull-down menus on the 486-class computer used to run the software. To set up a particular sample, the monochromator was set to the wavelength corresponding to the strong bound-exciton line in Si at 1137.5 nm. Next, the sample was

rotated so that the specular reflection of the laser was positioned just *outside* the entrance slit. Finally, the collection optics were adjusted spatially to maximize the detector response. At this point, data was collected via software control. The resulting data was converted to ASCII format, then analyzed and plotted with Microcal Origin™ software. No special data reduction techniques were used to analyze the data.

C. *Fourier Transform Infrared Spectroscopy (FTS)*

1. **Introduction to FTS Techniques**⁸¹

The emphasis of this study was placed on obtaining absorption and photoresponse spectra. For absorption measurements, an input beam passes through a sample and the light transmitted through the sample falls on a detector to generate an electrical signal. Photoresponse is measured in a similar manner except that the *sample itself* serves as the detector. The input beam falls on the sample and generates an electrical signal. Fortunately, both absorption and photoresponse data can be acquired with the same Fourier transform spectrometer. As was mentioned in section B, in any spectroscopic technique, a polychromatic beam of radiation must be acted upon so that each frequency in the spectrum is somehow differentiated from all the other frequencies. The intensity of the radiation of each resolution element, or the effect on the sample of each resolution element, is measured to yield the spectrum. The primary difference between Fourier transform spectroscopy (FTS) and dispersive spectroscopic techniques is that the data in all frequency resolution elements is obtained simultaneously by taking the Fourier transform of an interferogram. An interferogram is the response of a sample, due to an input signal generated by a two-beam interferometer, as a function of mirror position. This is fundamentally different from dispersive spectroscopic techniques such as those used to obtain PL in this study. The primary optical system of the most basic FTIR setup is a Michelson interferometer which consists of two perpendicular plane mirrors at 45° to

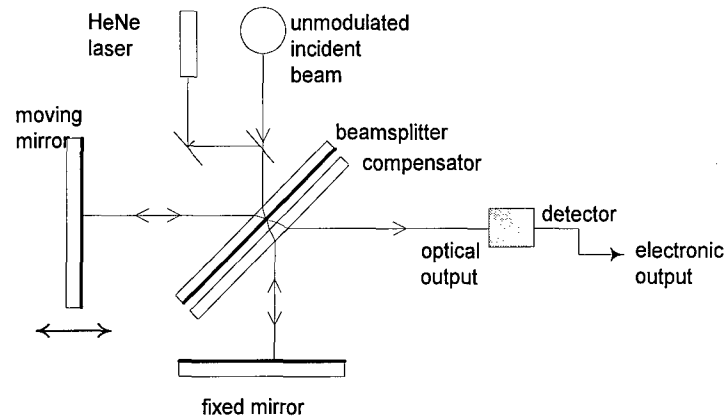


Figure 4-3. Michelson interferometer.

a beamsplitter (see Figure 4-3). One mirror is fixed while the other is moved in a direction perpendicular to its front surface. The beamsplitter divides the incoming light from the source and, ideally, transmits 50% of the light to one mirror while the remaining energy is reflected to the other mirror. A compensator plate is introduced in one leg of the interferometer to keep the optical path length $l = \sum_{i=1}^m n_i s_i$, where n_i is the index of refraction, in the two arms at approximately equal length. Assuming a perfectly monochromatic source input and identical optical path lengths, the two beams will be in phase and constructively interfere when they return to the beamsplitter to create a bright field. If a π phase shift between the two beams occurs, the beams will destructively interfere, and the field will appear dark. If the moving mirror is smoothly translated in a single direction, the field would gradually appear light and dark for each π phase shift and form a perfectly oscillating sinusoidal signal which may be described as

$$I(X) = 0.5H(\nu)I(\nu)\{1 + \cos(2\pi X\nu + \theta_\nu)\} \quad (4-2)$$

where $I(X)$ is the intensity of the output signal as a function of mirror displacement, X , and $I(\nu)$ is the source emission intensity as a function of optical frequency, ν . Note that $I(X)$ is the interferogram, i.e., the mapping of the optical signal intensity the detector senses at each position of the moving mirror. $H(\nu)$ represents the departures from the actual spectral intensity, $I(\nu)$, due to the instrument characteristics and is less than unity, while θ_ν is a phase shift introduced by the beam-splitter and detector. The frequency of the output oscillation depends on 1) the frequency of the incoming electromagnetic radiation, and 2) the velocity with which the mirror is moved:

$$f = \frac{V}{\left(\frac{\lambda}{2}\right)} = 2V\nu \quad (4-3)$$

where f is the frequency of the detected signal, λ is the wavelength of the incident monochromatic light, V is the velocity of the moving mirror, and ν is the frequency of the incident light measured in wavenumbers (cm^{-1}). This relationship allows a very high optical frequency to be encoded in the form of a low-frequency oscillation. For example, if the moving mirror translates at a velocity of 0.16 cm/sec (which is the recommended speed for use with a DTGS detector used in the 2-25 μm region), then a 10 μm (1000 cm^{-1}) source is "down shifted" from an optical frequency of 3×10^{14} Hz to an acoustic frequency of 320 Hz. Magnetic voice coil actuators are used to move the mirror in a continuous or step-scan mode. Most FTS systems use broad-band sources of light to

obtain the widest possible range of frequency information. When a broad-band source is considered, each frequency component is superposed onto each other, and the resulting interferogram looks far from sinusoidal. However, the previous mathematical description is easily extended since each frequency may be considered independently. The resulting interferogram is the summation of all cosine oscillations caused by all of the optical frequencies of the source. When the two interferometer mirrors are equidistant, or have zero path difference, then all the waves are in phase and form a "centerburst." As the moving mirror translates away from the zero position, the independent oscillations rapidly sum out to a steady average value. The resulting ac signal (interferogram) obtained by moving the mirror may be expressed by,

$$I(X) = \int_{-\infty}^{\infty} B(\nu) \cos(2\pi X\nu + \theta_{\nu}) d\nu$$

where (4-4)

$$B(\nu) = 0.5H(\nu)I(\nu),$$

which is the integral of Eq 4-2 of the monochromatic source over the entire frequency domain. Mathematically, this equation is a cosine Fourier transform. The inverse Fourier transform is given by,

$$B(\nu) = \int_{-\infty}^{+\infty} I(X) \cos(2\pi X\nu) dX. \quad (4-5)$$

Equations 4-4 and 4-5 provide a clear relationship between the interferogram $I(X)$ and the spectrum $I(\nu)$. The interferogram is directly measured, while the spectrum may be found

by simply taking the Fourier transform of the interferogram. Note however, that interferograms are seldom symmetric since it is impossible to make a perfectly-compensated interferometer over an extended wavelength range. Imperfect compensation leads to sine components in the interferogram and an asymmetric centerburst. Therefore, the resulting interferogram and spectrum must be related by the following complex Fourier transforms:

$$\begin{aligned} I(X) &= \int_{-\infty}^{+\infty} B(\nu) e^{i2\pi X\nu} d\nu \\ B(\nu) &= \int_{-\infty}^{+\infty} I(X) e^{-i2\pi X\nu} dX, \end{aligned} \tag{4-6}$$

where the exponential term now contains both cosine and sine contributions.

In order to reconstruct the exact spectrum of the source, an interferogram would need to be integrated from $-\infty$ to $+\infty$, which is impossible since this would require infinite mirror travel. Since the interferogram can only be measured over finite mirror translation, the infinite interferogram is, in effect, multiplied by a boxcar, triangular or some other truncation function (i.e. $T(X)=1$ from X_{init} to X_{final} and $T(X)=0$ for all else). The convolution of the initial interferogram, $I(X)$, with the boxcar truncation function, $T(X)$, yields the resolution function, $\sin(x)/x$, which is the Fourier transform of the truncated cosine wave. The central lobe of the resolution function is centered at the frequency of the cosine wave, as before, but now with finite width. This width, usually measured as the full-width-half-maximum (FWHM) of the central lobe, is inversely

related to the maximum extent of the interferogram and the mirror movement. In general, the resolution of an FTS system may be approximated by the following relationship:

$$\text{resolution}(\text{cm}^{-1}) \propto \frac{1}{\text{mirror excursion (cm)}} \quad (4-7)$$

Therefore, as the number of cycles over which the cosine wave is observed increases, i.e. as the mirror moves further from the equidistant position, the width of this resolution function decreases and the resolution improves. It is important to note that the "number of cycles" refers to the number of cosine wave oscillations corresponding to mirror displacement. The resolution function of the interferometer is fundamentally limited by the full travel range of the moving mirror.

FTS has two primary advantages over dispersive spectroscopic techniques. Since information from all frequencies in the spectrum is gathered simultaneously, a given interferogram can be measured in the time it takes to measure one resolution element with a slit spectrometer using the same source, detector and optical throughput. This is called Fellgett's advantage.⁸² In any spectroscopic system, spectral information contained in a narrower bandwidth than the resolution of the system is not observed. Therefore, the number of resolution elements of the spectrum, M , indicates the total amount of information contained in the spectrum and may be defined as the bandwidth, $\lambda_{\text{max}} - \lambda_{\text{min}}$, divided by the resolution $\delta\lambda$. In a dispersive spectrometer, the entire spectrum is observed for only a fraction of the total scanning time, T , divided by the number of resolution elements, M , observed in that time. The signal adds with the time spent

observing it, while the random, white noise from the source adds as the square root of the observation time. Thus, for a dispersive spectrometer, the signal adds as T/M , the noise as $(T/M)^{1/2}$, and the SNR as $(T/M)^{1/2}$. However, in an FTS system, each resolution element is being observed all of the time, i.e., all optical frequencies are multiplexed. Subsequently, the signal adds as T , the noise as $T^{1/2}$, and the SNR as $T^{1/2}$. Comparing the FTS and dispersive techniques on the basis of SNR alone, the multiplex case is superior to the dispersive technique by $M^{1/2}$. In the preceding derivation it was assumed that the noise was independent of signal intensity and, therefore only dependent on measuring time. For the infrared region, the dominant noise constituent is usually detector noise, which is independent of signal strength. However, in the visible wavelength region noise is usually dominated by shot noise which is proportional to the square root of the source intensity thus canceling out Fellgett's advantage.

The other primary advantage of FTS over grating spectrometry is the increased light throughput. This is infrequently referred to as Jacquinot's advantage. While a dispersive spectrometer uses entrance and exit slits to act as aperture stops which filter side-lobe interference, a typical FTS uses a relatively large diameter entrance aperture and turning mirrors. As a result, since optical throughput is the product of the projected area of the limiting optical element and the solid angle subtended by the source, it is on the order of 200 times greater for FTS instruments.⁸³ In addition to having larger apertures, FTS setups are optically more efficient, since there are no reflection or transmission losses from dispersive gratings or prisms. Michelson mirrors and turning flats normally have broad-band, highly-reflective silver coatings. Collection mirrors on

the far side of the sample leading to the detector are normally gold coated with even better broad-band behavior in the far IR than silver. High throughput and efficiency were the most important reasons why initial FTS techniques were developed in broad-band/low-light and narrow-band/high-speed applications. As a general rule, an equivalent spectrum may be measured with FTS in the same time as a grating spectrometer with better SNR or in a shorter time with equivalent SNR.

A secondary advantage of using FTS, Conne's advantage, comes from using the laser, collinear with the input beam, to reference the position of the moving mirror in the interferometer as shown in Figure 4-3. Though it does not give an advantage in SNR over dispersive technique, it can provide an advantage in frequency accuracy.⁸⁴

2. FTS Experimental Apparatus

A diagram of the BioRad 60A Fourier transform spectroscopy (FTS) system used at AFIT is shown in Figure 4-4. The Michelson interferometer shown in the top half of the diagram, is comprised of the source, beam splitter-compensator, translating mirror, and fixed mirror. A Class I HeNe laser is used for system calibration and dynamic alignment of the interferometer. The two sources pictured, Source 1, a ceramic glowbar and Source 2, a tungsten bulb, are used for different wavelength regions. As currently configured, the ceramic glowbar is used to cover the 2 to 25 μm wavelength region while the tungsten bulb covers the visible to 2 μm . A potassium bromide (KBr) beamsplitter is used with the glowbar source, while a quartz beamsplitter is used with the tungsten lamp.

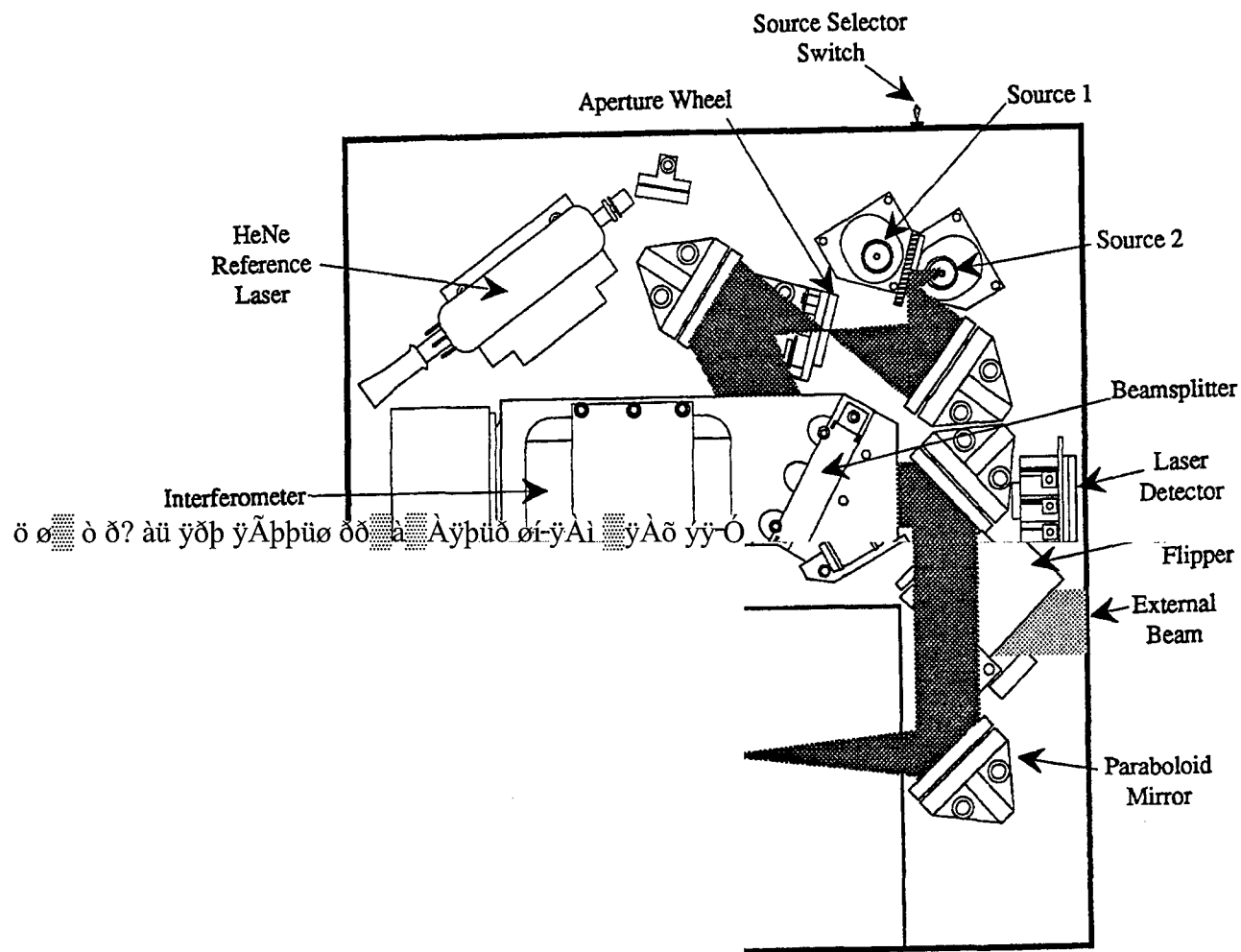


Figure 4-4. Diagram of the BioRad FTS 60A Fourier transform spectroscopy system.⁸¹

Compensators are built into the beamsplitter assembly which is kinematically mounted for easy removal and installation. The beam splitter is actually mounted at approximately 60° to minimize multiple reflections from its front and back surfaces. The moving mirror has air bearings and is translated along the piston axis of the interferometer leg by a

magnetic voice coil. Any errors in system alignment from the moving mirror are corrected by dynamically-controlled piezoelectric transducers mounted on the backside of the fixed mirror. Alignment is initiated through software control. The modulated HeNe signal passes through a small aperture at the first turning mirror and is detected by a 3-point array of Si detectors. The subsequent electronic signal is sent to a digital control circuit for system alignment and to the analog-to-digital converter board as a system timing signal. The modulated light from the broadband source is directed with mirrors into an N₂-purged sample chamber. After passing through the sample the transmitted light is collected by an Au-coated off-axis parabolic mirror attached to the detector assembly and focused onto the face of a DTGS detector for the IR wavelength range. For the visible-2 μ m region, Si and PbSe detectors are used. The DTGS, glowbar, and KBr configuration was used exclusively in this work. Figure 4-5 shows the range of responsivity for this configuration and various windows. The polarizer used in absorption measurements is composed of a wire grid on a KRS5 substrate which will have similar absorption properties as the KRS5 window shown in the figure. ZnSe windows are used in photoresponse measurements and their spectral response is also shown in the figure. The electronic signal from the detector is processed on a hard-wired motherboard built into the interferometer unit, then sent to a 486-class, 50 MHz computer where the data is stored and displayed in a psuedo-Unix operating system, called IDRIS, written by BioRad. After initial examination, selected files are converted to ASCII format for further analysis, storage, and display.

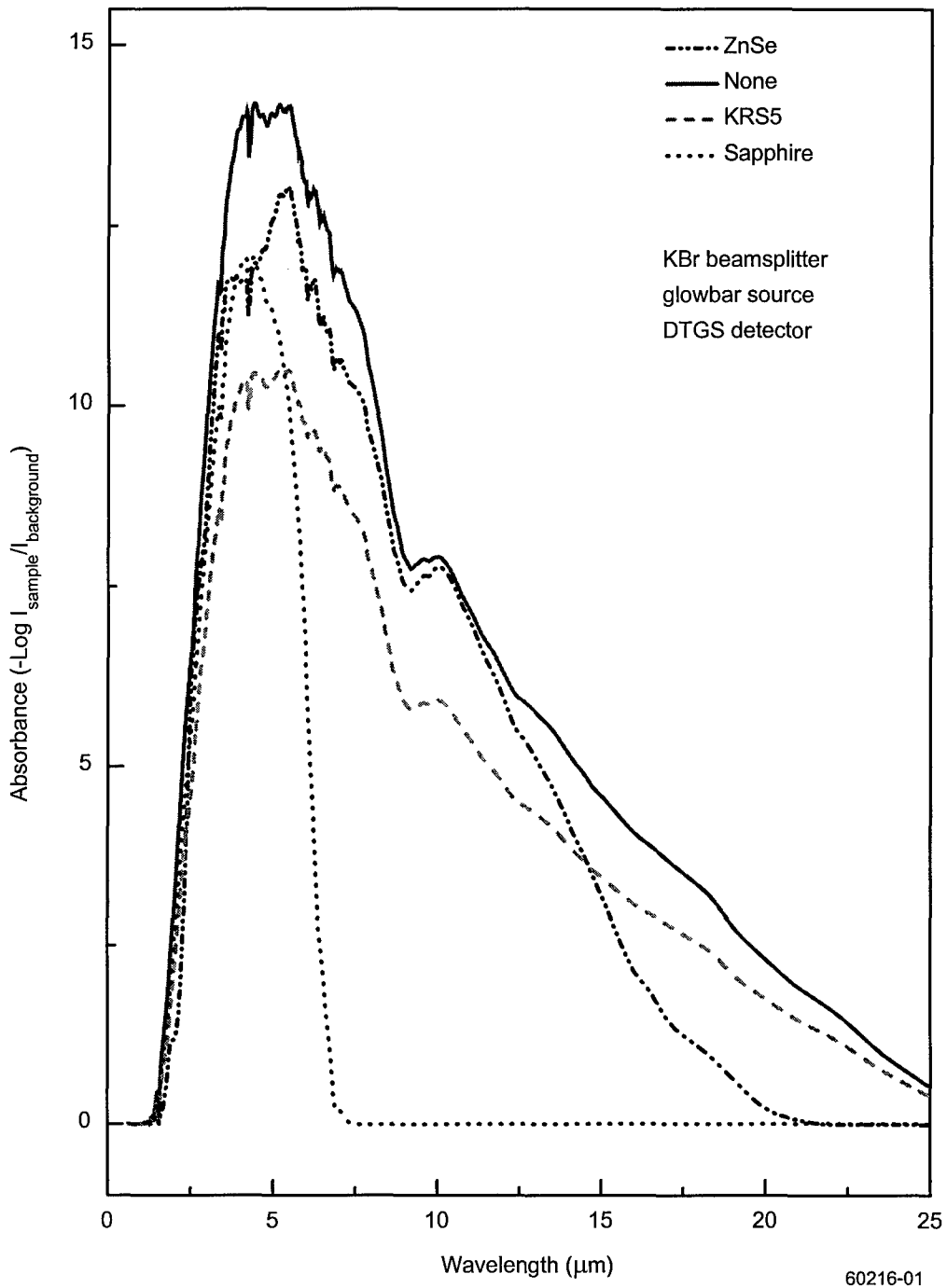


Figure 4-5. Spectral response produced by the combination of the glowbar source, KBr beamsplitter, and DTGS detector through various window materials.

D. Absorption Measurements

1. Absorption measurements on Si/Si_{1-x}Ge_x waveguides

AFIT, in cooperation with NRL, desires to develop Si/Si_{1-x}Ge_x MQW structures for use in IR detectors. Consequently, absorption characteristics of the material must be understood to properly design the detector. Selection rules dictate that the absorption characteristics depend upon the orientation of the electric field with respect to the quantum well planes. In the case of growth on (100) substrates, when the Poynting vector is parallel to the growth axis (normal incidence), intervalence-subband (heavy hole to light hole) and free-carrier transitions are observed. When the Poynting vector is perpendicular to the growth axis, intrasubband transitions heavy hole to heavy hole) and free-carrier transitions are observed. The case of growth on (110) substrates is not as straightforward because the selection rules are partially relaxed. To observe the different transitions experimentally, the E-field must be rotated in and out of the quantum well planes with a polarizer. (see Figure 4-6) As a result, conventional absorption measurement techniques, utilizing a single light pass through the sample at normal incidence, are not useful for exploring different transitions. An alternative to the single pass method is the waveguide approach in which the substrate and MQW structure serve as a cavity and the ambient air serves as a cladding layer.^{85,86} A waveguide allows the incident light to sample the quantum wells many times as it bounces through the cavity. Because the quantum well thickness is so small compared to the thickness of the Si

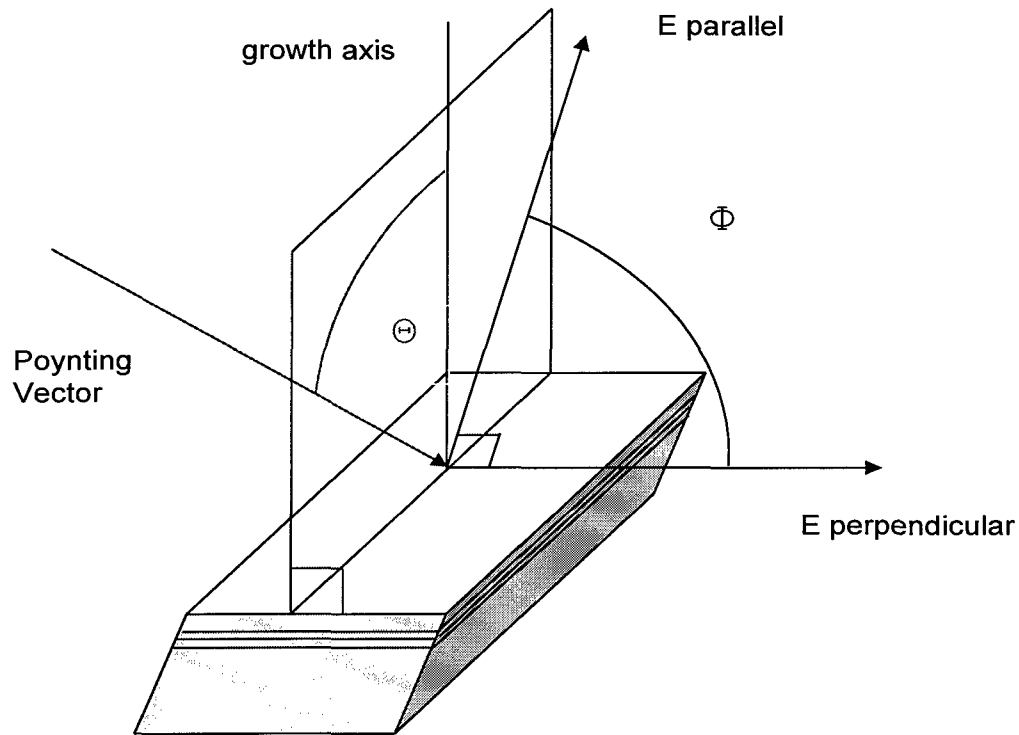


Figure 4-6. Diagram of the quantum well structure, the plane of incidence formed by the incident ray and the surface normal, the Poynting vector, and the electric field vectors.

substrate, the effective index of refraction is approximated to be the index of Si, n_{Si} .

Because it is desirable that the incident light pass through the waveguide, to sample the quantum wells, and not leak out the sides, the experiment must be designed to achieve total internal reflection. To achieve total internal reflection, the light ray must bounce at an angle less than the complementary critical angle. The critical angle for a silicon/air interface, $\Theta_c = \text{ArcSin}\left(\frac{n_{\text{air}}}{n_{\text{Si}}}\right)$, is 17.1 degrees, and therefore the complementary critical angle is 72.9 degrees. After determining the complementary critical angle, (see Figure 4-7) the proper angle of incidence must be determined. The numerical aperture,

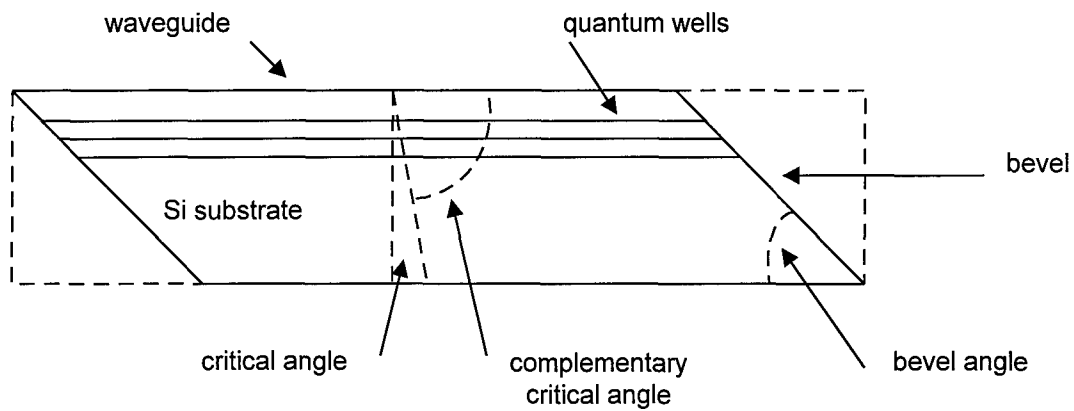


Figure 4-7. Illustration of the critical and complementary critical angles.

$NA \equiv (n_{Si}^2 - n_{air}^2)^{1/2} = \sin(\Theta_i)$, is used to determine the angle of acceptance of the rays entering the waveguide. For a silicon/air interface, any angle between 0 and 90 degrees is allowed. Bevels are ground on the waveguide to create specular surfaces that allow efficient coupling of light in and out of the waveguide as shown in Figure 4-8. Using the constraints of the critical angle and Snell's Law, $n_i \sin(\Theta_i) = n_t \sin(\Theta_t)$, it is determined that the bevel angle must not be smaller than 34 degrees. For a bevel angle of 34 degrees

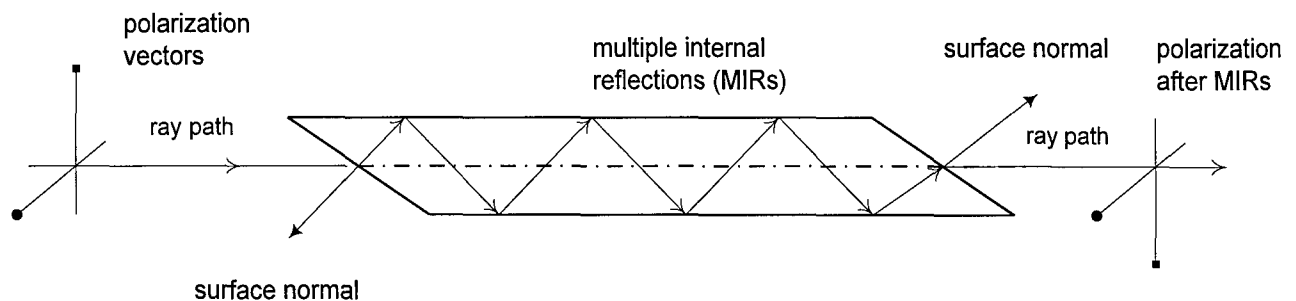


Figure 4-8. Schematic of sample fashioned into an optical waveguide and the light path through the sample.

and an incident angle of 90 degrees, the bounce angle exceeds the complementary critical angle and so total internal reflection is no longer maintained. The transmission coefficients for light incident on the beveled face are shown in Figure 4-9. Once a range of incident angles has been determined, the particular angles that best couple into the mode structure of the waveguide must be selected. In more common waveguide applications, incident light must couple into modes that the cavity will support in order to propagate down the waveguide. The bounce angles are generally discretely spaced. However, for Si/Si_{1-x}Ge_x MQWs, the bounce angle distribution is near continuous because the waveguide is so thick. As a result, great care is not necessary when choosing

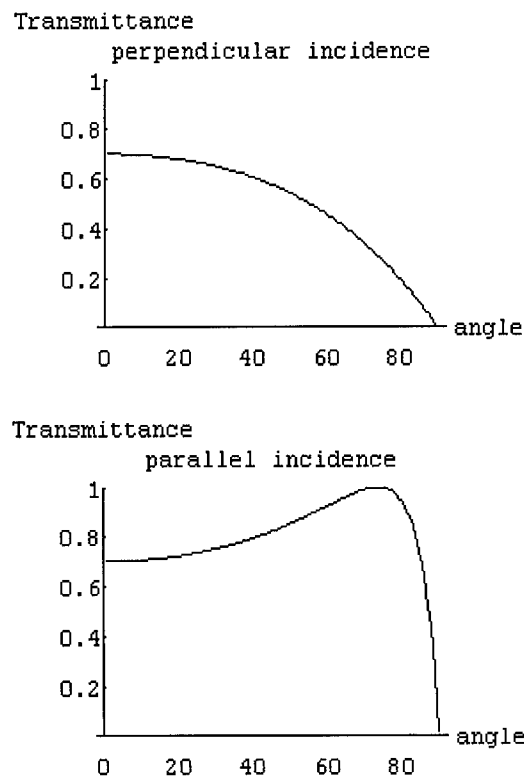


Figure 4-9. Transmission of parallel and normal components as a function of bevel angle.

an angle of incidence for coupling the light into the waveguide. As the bevel angle is decreased, more of the higher order modes are coupled into. The higher order modes make more bounces in the cavity and thus sample the quantum wells more. In more common waveguide applications such as fiber optics, as the bounce angle increases, the light penetrates further into the cladding and is less confined. In the case at hand however, the power confinement factor remains greater than 0.98 for bounce angles between 0 and 72 degrees. The confinement is very good because the difference in index of refraction is relatively large between Si and air. As Figure 4-10 shows, the power confinement factor for an air/ silicon interface is rather high.

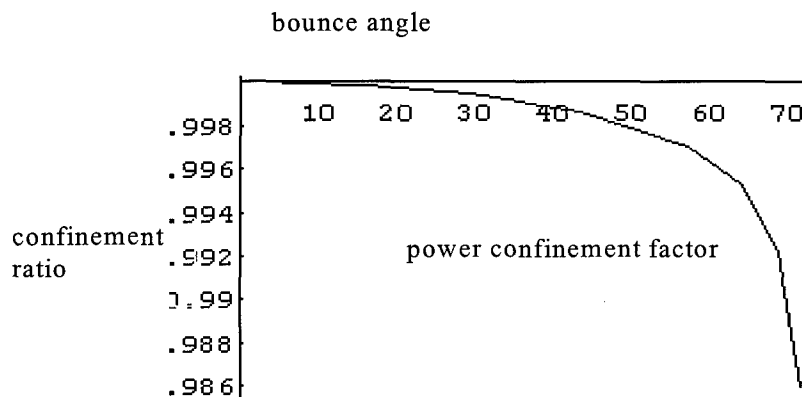


Figure 4-10. The power confinement factor for an air/silicon interface.

Making absorption measurements on waveguide configurations has proven to produce the best results, and so all the absorption data collected in this research was obtained when using the waveguide configuration. An absorption spectrum is obtained

by taking the ratio of the sample response to a background reference response and is usually expressed in one of three ways:

$$\text{absorptance} = 1 - \left(\frac{I_{\text{sample}}}{I_{\text{background}}} \right) \quad (4-8a)$$

$$\text{absorbance} = -\log_{10} \left(\frac{I_{\text{sample}}}{I_{\text{background}}} \right) \quad (4-8b)$$

$$\text{absorption} = \alpha = -\ln \left(\frac{I_{\text{sample}}}{I_{\text{background}}} \right) / l_{\text{effective}} \quad (4-8c)$$

where I_{sample} is the sample single beam response, $I_{\text{background}}$ is the reference single beam, and $l_{\text{effective}}$ is the effective path length through the sample. Spectra reported in the literature are primarily reported in absorbance and absorptance since absorption requires the estimation of the path length. Using the proper background reference signal is paramount to obtaining credible and reproducible spectra. To reference properly, all contributions to the background signals must be accounted for. The spectral response produced by a combination of the glowbar source, KBr beamsplitter, various window materials, and DTGS detector was shown in Figure 4-5. Each of the spectral features shown will appear in the absorption spectra of the samples unless they are perfectly accounted for. The effects of the polarizer used to rotate the electric field of the input beam on the data must also be considered. Since the polarizer is made by evaporating a wire grid on a KRS-5

substrate, it has a similar response as the KRS-5 window. However, failure to account for a partial polarization of the input beam may lead to errors in interpretation of the data. It is apparent from Figure 4-11 that the input beam is partially polarized after passing through the Michelson interferometer. The light intensity, which behaves as

$$I = I_{min} + I_{max} * \text{Cos}(\Theta) \quad (4-9)$$

where I_{max} is the maximum signal intensity and Θ is the rotation angle of the polarizer, exhibits the $\text{Cos}(\Theta)$ intensity dependence of polarized light through an analyzer.

Although the degree of polarization is on the order of 10 percent, it necessitates the use of a correction factor when comparing single beam spectra taken at different polarizations.

Not even the background of an undoped substrate can be properly subtracted without correction factors. Figure 4-12 shows the correction factors vs. wavelength that must be applied to sample data taken at different polarizer settings to account for the partial polarization of the input beam.

2. Reference Techniques

Obtaining a proper reference signal is one of the most important elements in making absorption measurements. Referring to Eqs 4-8, both a sample and background, or reference, signal must be measured. The sample signal, I_{sample} , measures the light intensity on the detector after the input beam has passed through the sample of which the

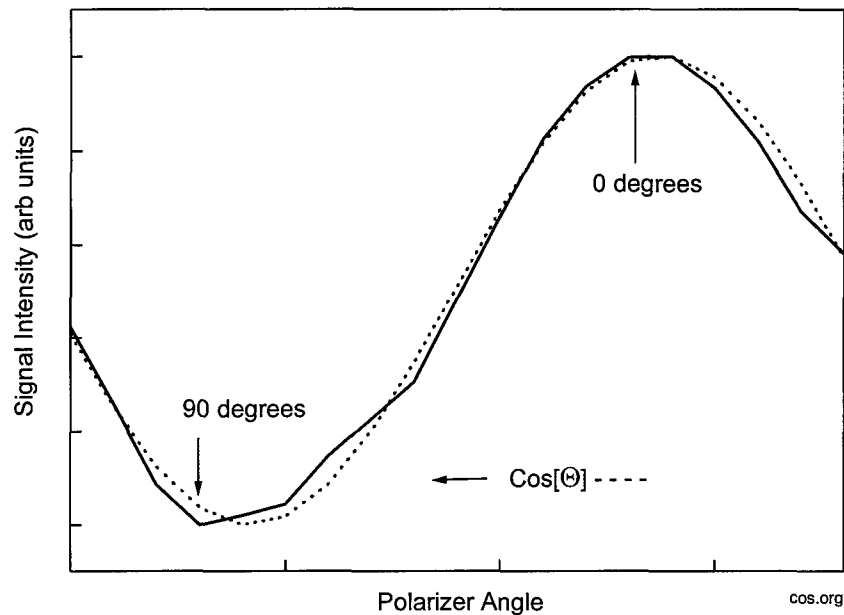


Figure 4-11. Plot showing the $\cos(x)$ dependence of the partial polarized input beam through the polarizer.

absorption characteristics are desired. The background signal, $I_{\text{background}}$, measures the light intensity on the detector after the input beams pass through a specimen with different absorption characteristics than the sample. It is desirable in this study to measure absorption in the sample resulting only from the incorporation of the dopant into the MQW since the holes available for intersubband, intrasubband and free-carrier absorption transitions come from ionized dopant impurities. Therefore the background sample must be identical in every way possible to the actual sample except for the doping. With this in mind, it seems obvious that the best possible reference sample would be a waveguide fashioned from an undoped MQW sample with a structure identical to the doped sample.

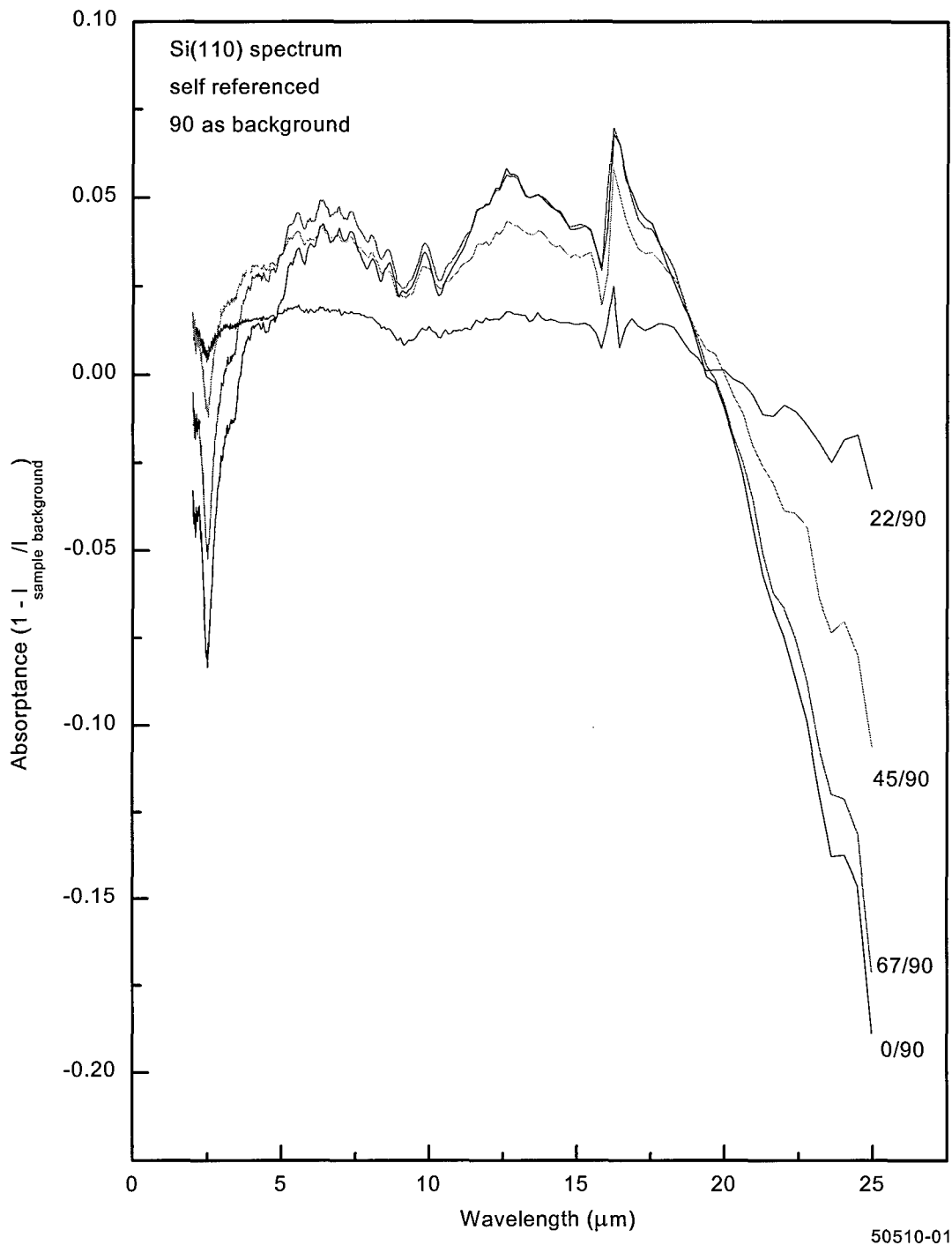


Figure 4-12. Self-reference correction factors taken from an undoped Si (110) substrate generated by dividing spectra at 0,22,45,67 polarizer settings by 90 degree setting.

Unfortunately, it is cost and time prohibitive to grow an undoped sample for every doped sample, and so alternative reference methods must be found. The first alternative is to use an undoped silicon wafer, and consequently this method is referred to as the “substrate reference” technique. For substrate reference, a doped MQW sample and undoped substrate are fashioned into identical waveguides (with the exception of the added thickness due to the MQWs). Remember that waveguides are used to enhance the number of passes the light makes through the quantum well region, and a waveguide allows the possibility of rotating the electric field with respect to the growth axis. The doped sample is mounted into the sample chamber, and a polarizer is rotated to specific settings between 0 and 90 degrees to rotate the electric field vector in and out the quantum well planes. Then a single-beam spectrum is taken at each of the desired polarizer settings and stored as I_{sample} . Next, the substrate waveguide is mounted in precisely the same way into the sample chamber, after which a spectrum is measured at the same polarizer settings as the previous waveguide and stored as $I_{\text{background}}$. Example single beam spectra for both a doped MQW sample and an undoped substrate are shown in Figure 4-13. Remember that a single beam spectra is the plot of the signal intensity vs. wavelength. This relationship is determined through Eq 4-4 and 4-5. Notice that the overall intensity is much smaller for the doped samples marked s00 and s90 to indicate polarizer settings of 0 (or z-polarization) and 90 (or xy-polarization) degrees. For z-polarization, the electric field vector has a component parallel to the growth direction, and for xy-polarization, the electric field vector is parallel to the growth direction. The

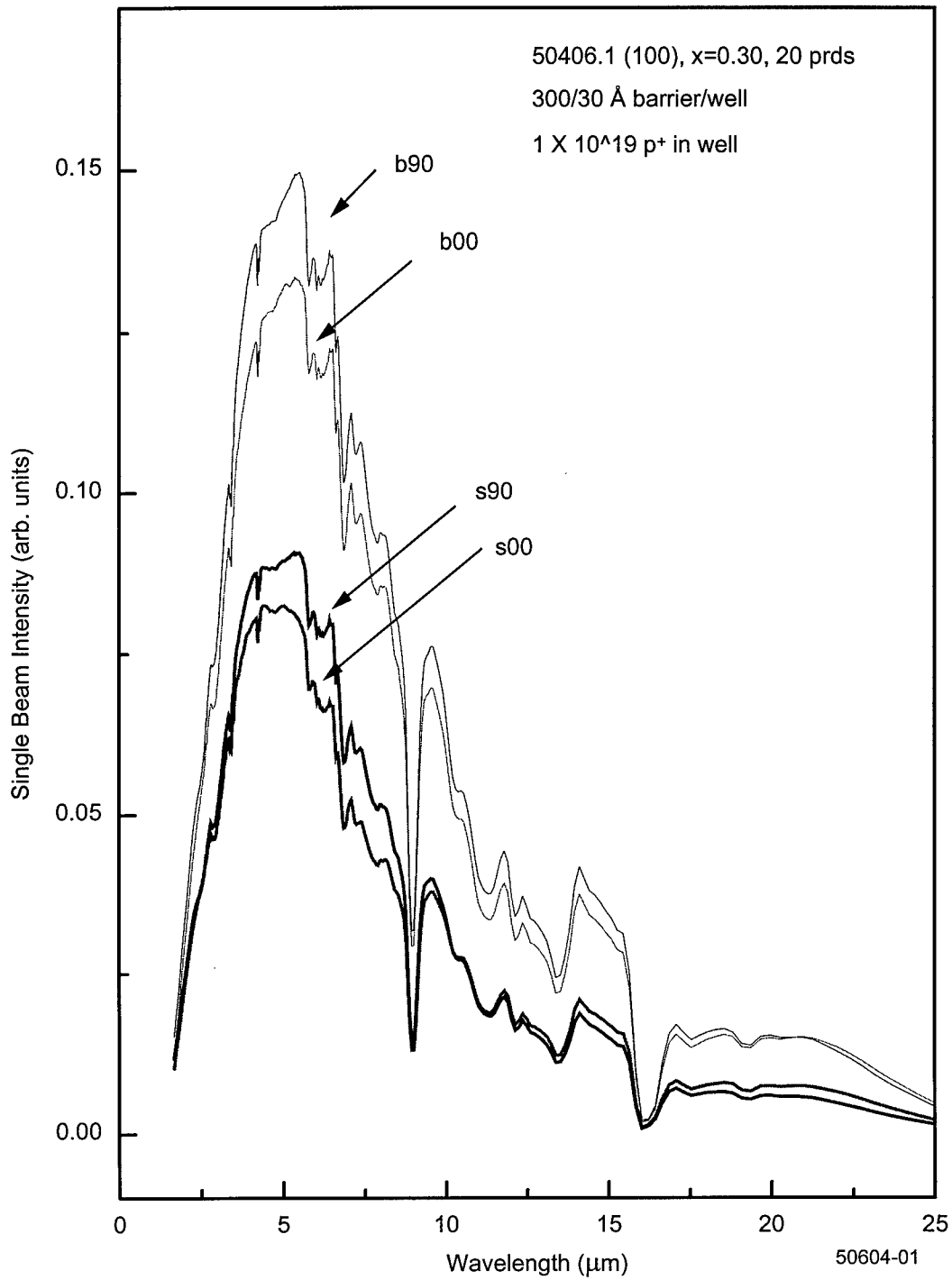


Figure 4-13. Raw single beam data. s00 and s90 represent the signal intensity, I_{sample} , taken at polarizer settings of 0 and 90 degrees. b00 and b90 represent $I_{\text{background}}$ taken at 0 and 90 degrees.

drop in intensity is attributed to intersubband, intrasubband and free-carrier absorption which attenuates overall signal intensity. In theory, the substrate data, indicated by b00 and b90, should be identical. However, as indicated previously, the transmission coefficients for TE and TM modes are slightly different and the input beam is partially polarized. A combination of these effects will cause the difference in intensity shown between b00 and b90. The drawback to the waveguide technique is that the electric field can have, at best, only a projection parallel to the growth axis because the angle of incidence is 45 degrees with respect to the growth axis. Nevertheless, this is sufficient to incite the desired transitions. Because the electric field vector has equal components in the z and xy directions at a polarizer setting of 90, the data is corrected in the following manner. One-half the signal intensity of the xy-polarization single beam data is subtracted from the z-polarized single beam data. The resulting single beam is subsequently multiplied by a factor of two. This algorithm is used to approximate the true intensity of the single beam under total z-polarization conditions. Using data such as this, sample and substrate data are plugged into the absorbance equation (Eq 4-8b) to generate an absorbance spectrum of intensity vs. wavelength as shown in Figure 4-14. 0/0 indicates the z-polarization sample single beam has been referenced by the z-polarization substrate data, and 90/90 indicates the xy-polarization sample single beam has been referenced by the xy-polarization substrate data. The spectral features labeled as Si-O, C-Si and C-O are multi-phonon transitions associated with impurities in the silicon. Unfortunately, as Figure 4-15 shows, Si has many strong absorption lines in the infrared.

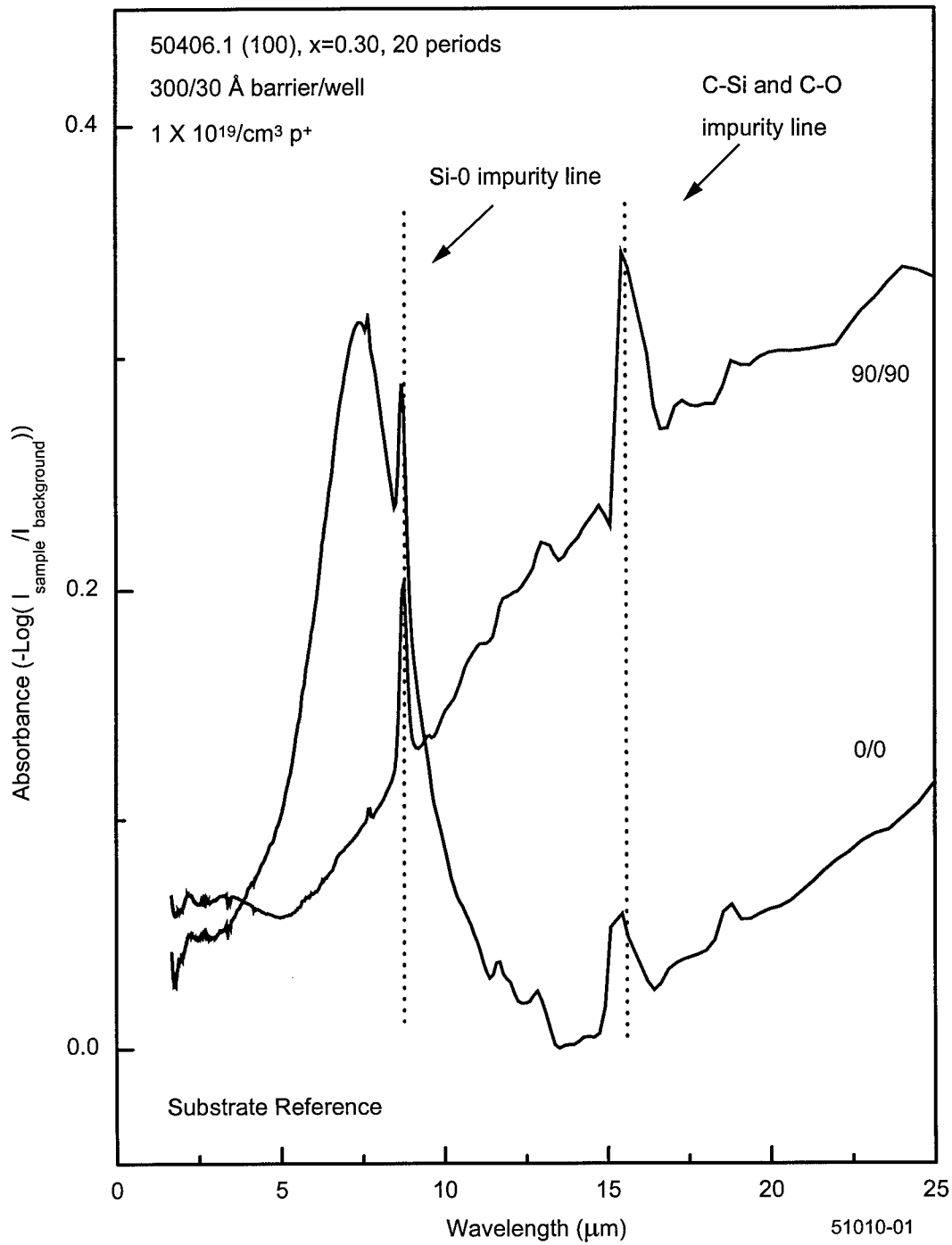


Figure 4-14. Absorbance spectra taken in substrate reference mode. Data for 0 and 90 degree polarizations shown.

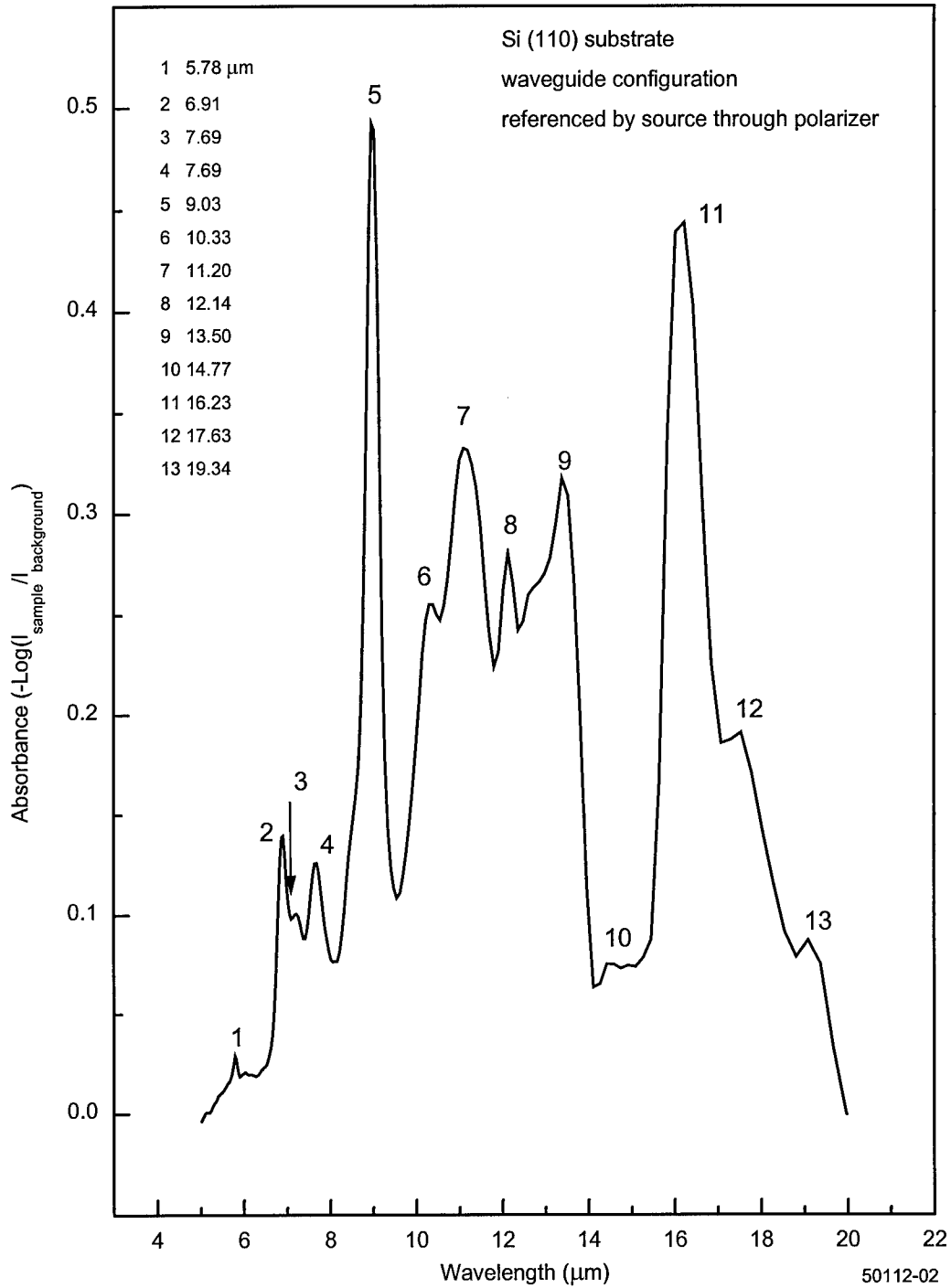


Figure 4-15. Absorbance spectrum a Si(110) substrate measured in the waveguide configuration. Numbered lines indicate multi-phonon transitions associated with impurities in silicon. (see Appendix F).

(Note, see Appendix F for an extensive list of the phonon absorption lines in bulk silicon.) These background lines are very difficult to subtract out entirely through the reference signal, especially the very strong lines at 9.03 μm and 16.41 μm . Since these features are an artifact of imperfect background subtraction, they will be eliminated via software control by replacing the peak with a straight line through the base of the peak as shown in Figure 4-16. This figure also shows the correction factors used to account for free-carrier absorption. Because of the high carrier concentrations in the MQWs, free-carrier absorption is large, especially at longer wavelengths. Free-carrier absorption changes as the electric field vector is rotated in and out of the quantum well planes according to the Drude model⁸⁷ which indicates that free-carrier absorption will be larger under 90 or xy-polarization. This is corroborated by the spectra in the figure. The dashed lines indicate a $\beta\lambda^2$ approximation to the free-carrier absorption where β is a constant prefactor used to fit the curve and λ indicates wavelength.⁸⁸ The correction factor is subtracted from the absorbance data via software control to produce the final form of the data shown in Figure 4-17. The large peak around 7.5 μm indicated by a dashed line in the 0/0 spectrum is the absorption due to a heavy-hole 1 to heavy-hole 2 transition. This transition has selection rules that allow the transition to occur only if the electric field of the incident light has a component parallel to the growth axis (z-polarization). The large hump indicated by a dashed line in the 90/90 spectrum is a heavy-hole 1 to light-hole 1 transition. This transition has selection rules that allow the transition to occur only if the electric field is xy-polarized. Refer to Chapter 3 for a discussion of the selection rules for

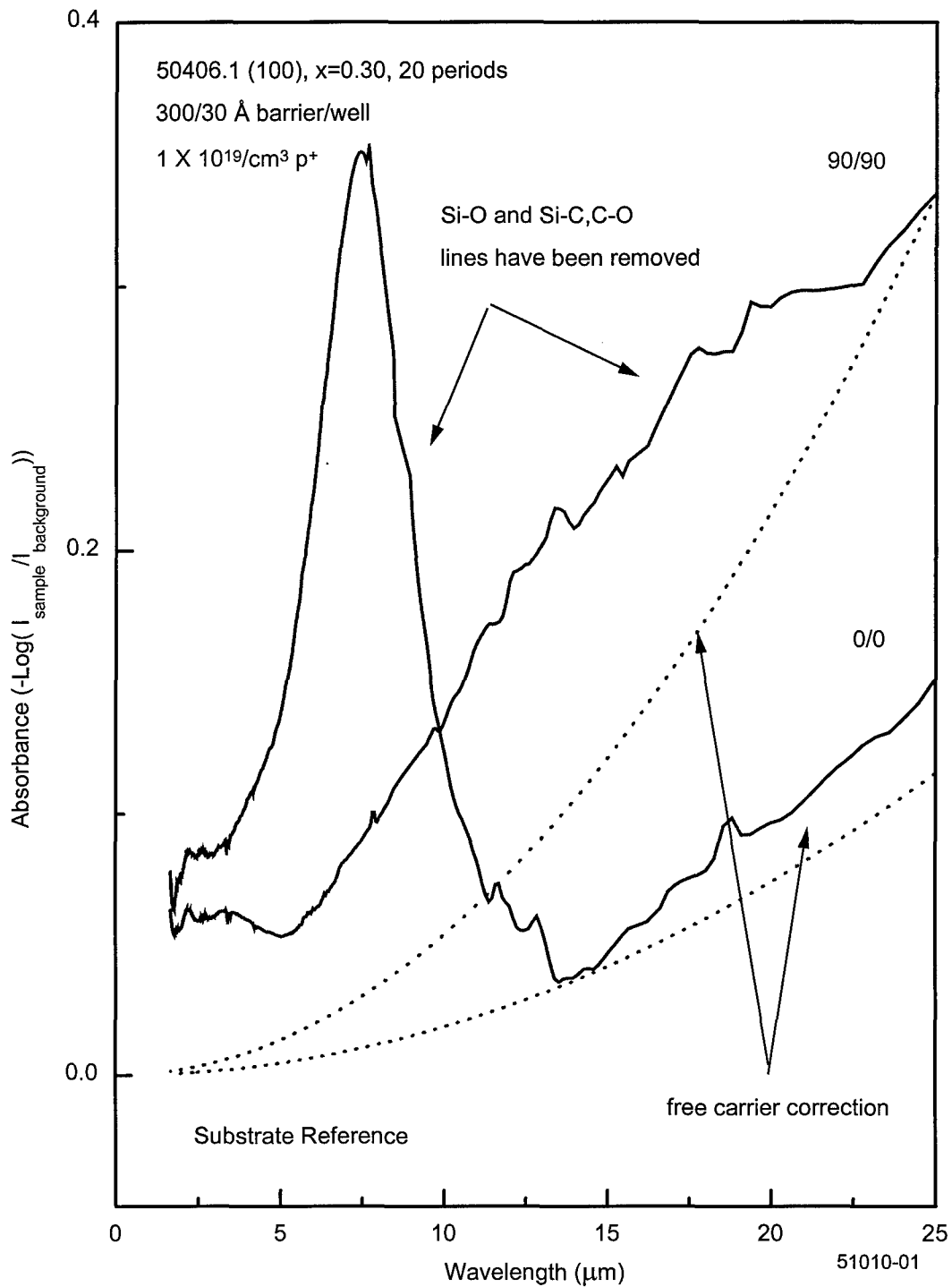


Figure 4-16. Absorbance spectra showing the elimination of absorption peaks associated with multi-phonon transitions in Si and the free carrier correction factors.

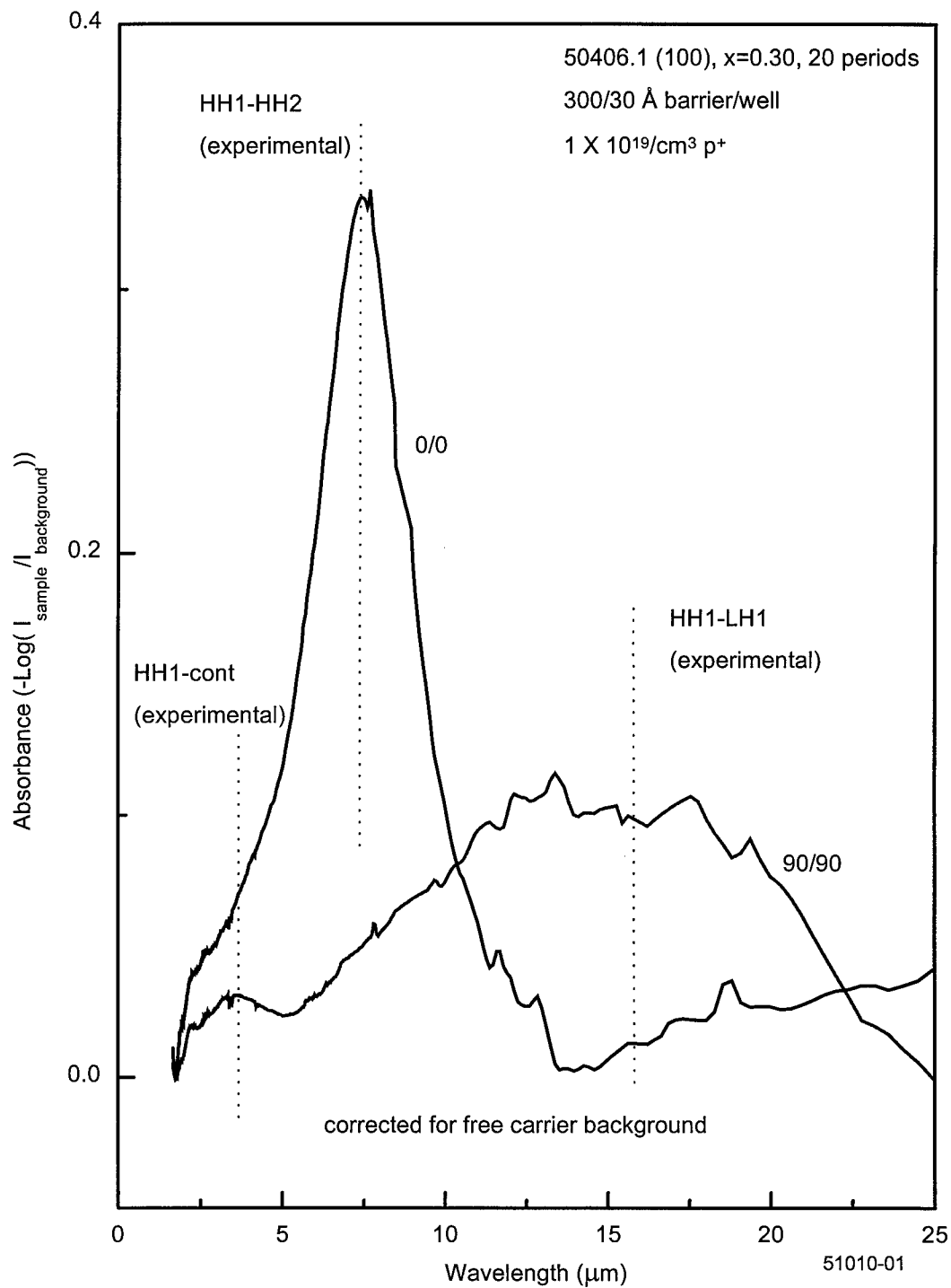


Figure 4-17. Final form of absorbance spectra corrected for Si background peaks and free carrier background absorption.

this particular sample. The third peak indicated by a dashed line represents absorption between the ground state and the continuum levels. Hereafter, all absorption data will be presented in final form, or after corrections for Si absorption peaks and free-carrier absorption have been performed.

A second reference technique is to use the doped sample itself as a reference by using a single beam spectrum taken at a particular polarizer setting as the background. This technique is referred to as the "self-reference" technique. The MQW is mounted as before, and data at sequential polarizer settings are obtained without disturbing the sample. The idea behind the technique is that since silicon and germanium are cubic materials, spectra taken at one polarization should not be different than spectra taken at a different polarizer setting except for the differences attributed to the intersubband and intrasubband transitions. As a result, the only features that remain after a self-reference background subtraction are attributed to the MQWs alone. Unfortunately, this technique does not work as well as might be expected. The MQWs themselves break translational symmetry causing a variation in the absorption with respect to the angle of incidence. In addition, if the selection rules are relaxed to the point where transitions are allowed in any polarization, then this technique will tend to minimize the absorption peaks. Furthermore, if one transition is strongly allowed in only one polarization and a different transition is strongly allowed in another polarization, the self-reference technique will produce a positive absorption peak and a negative absorption peak simultaneously. These factors make data obtained with this technique difficult to interpret and so it will not be used in this study.

Some authors prefer another referencing method referred to as the "normal-incidence, single-pass method." In this case, a single-beam spectrum of a doped MQW sample is referenced to that of an undoped MQW or substrate, but no waveguiding is performed. The angle of incidence is 0 degrees, or the Poynting vector is parallel to the growth direction. This technique does not seem well suited to the study of quantum well phenomena for two reasons. The quantum well region is sampled only once compared to 6-10 times for the waveguides, and since the strong heavy-hole ground state to heavy hole excited state transition is not allowed in this polarization and thus not observed under normal incidence illumination. Some data was collected under these conditions, but the spectra were dominated by the Si background. More spectra were recorded when the angle incidence was near 90 degrees or perpendicular to the growth direction. This data was equally poor and showed no bound-to-bound transitions. As a result, all the absorption data presented in this document were evaluated using substrate reference.

3. Sample Preparation and Mounting

The Si/Si_{1-x}Ge_x multiple quantum well samples arrive from NRL on a quarter-section of a two inch wafer with an unpolished backside. The backside must be polished to increase the reflectivity which will allow more light to traverse the sample in the waveguide configuration. A section of the wafer measuring about 3 cm square is cut off with a scribe and mounted on a polishing chuck with black wax. The wafer is sanded on 1500 grit paper until a shine develops. Then the polishing chuck is placed in *Buehler Minimet 1000*TM lapper, and the wafer is polished to a specular finish using aluminum

oxide powders and Clorox™ Bleach. Such a process takes approximately 2 hours. The wafer is then dismantled and cleaved into 3 mm by 14 mm rectangles(100) or parallelograms(110) with a diamond tipped scribe. Once the sample is sliced to the correct dimensions, it is placed on a stainless steel beveling jig to make the waveguide facets. (see Figure 4-18) Beveled edges are carefully ground on the sample first with 600 grit sandpaper, then with 1500 grit paper. They are subsequently polished to a mirror-finish with the aluminum oxide powder on the mechanical lapper. After finishing one

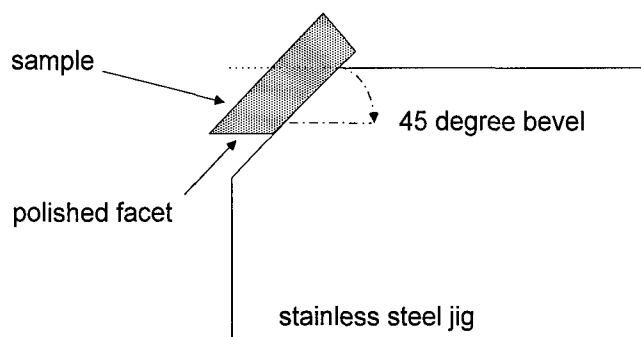


Figure 4-18. Schematic drawing of waveguide polishing jig.

side, the sample must be dismantled and flipped over, not rotated, to put a bevel on the other side. The rotational speed of the lapper must be sufficiently slow to avoid rocking the polishing jig which will cause a rounding of the waveguide facet. It is imperative that the bevel is perfectly flat, not rounded, and the sides must be parallel to each other. If they are not, spurious features appear in the spectra. It has proven beneficial to make both the sample and its reference at the same time on a large chuck designed for this purpose. This insures that both waveguides are the same width. It has also proven beneficial to mark the pair in such a way so that they can be placed in the knife-edge mount with the same spatial orientation. The waveguide must be cleaned thoroughly

after the polishing steps to remove the polishing powder and mounting wax. The cleaning steps are as follows:

1. Place in glass dish filled with 4 ml of TCE then place dish in ultrasonic cleaner for 5 minutes.
2. Rinse in Acetone
3. Rinse in Methanol then immediately blow dry with dry nitrogen.
4. Soak in 25% HF solution for 5 minutes.
5. Rinse in deionized water (DI).
6. When removing the waveguide from the DI, the water should not adhere to or "wet" the sample surface. If the solution does not bead up then it is still dirty and the above steps must be performed again.
7. Blow off any residual DI with dry nitrogen.

The waveguide is now ready to be mounted and placed in the system. The mount to hold the waveguide contains two spring-loaded, stainless steel knife-edges with 45 degree bevels. The sample is mounted so that the waveguide facet is perpendicular to the input beam as shown in Figure 4-19. The sample is mounted in this way to minimize stray light that might leak between the knife-edge and the waveguide. In addition, the sample is placed horizontally because the input beam is slightly oblong and thus more light falls on the sample. The mount is placed into an adjustable stage located in the sample compartment of the FTIR, and adjusted in all three dimensions to maximize signal output. The FTIR was designed so that the input beam comes to a focus at the center of the sample compartment, and after the stage has been positioned for a single waveguide sample, no further adjustment is necessary for subsequent samples. Furthermore, when measuring a doped sample and its undoped reference, it is essential to change as little as

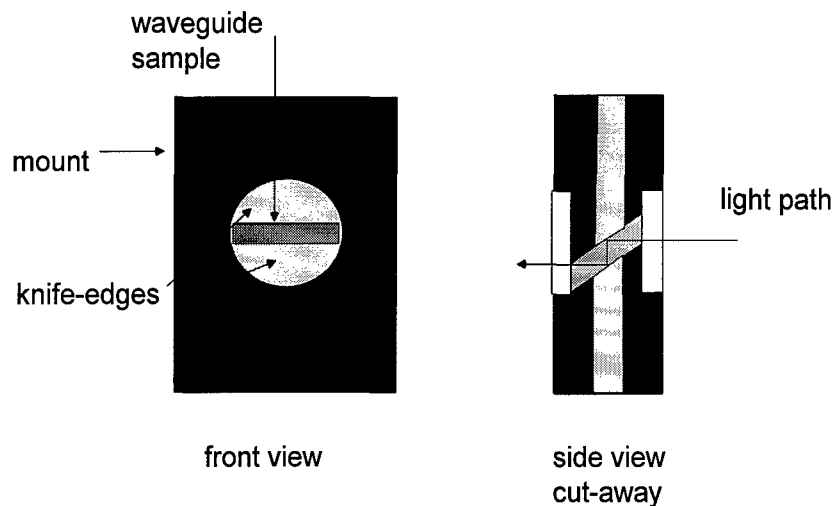


Figure 4-19. Schematic diagram of waveguide mount.

possible to achieve optimum results. Small changes in the angle of incidence or in the rotation of the sample mount can introduce spurious effects into the spectra.

After the waveguide is placed in the sample chamber, the system response must be determined for each optical configuration. Whenever a different filter, lens, window, or sample mount is installed, a new calibration step and centerburst measurement must be accomplished to determine the appropriate combination of detector sensitivity and aperture settings. The BioRad FTS-60A has a self-aligning Michelson interferometer and a software driver which enables both alignment and calibration to be accomplished via function keys on the keyboard. Achieving a centerburst magnitude ranging from -2.5 to -8.0 is necessary to ensure sufficient signal to noise during the actual measurement. A spectrum may be obtained with a centerburst magnitude less than -2.5 but more scans are required to reach an appropriate SNR value. To scan with a centerburst greater than -9.0 usually results in an overload of the A-D converter and is to be avoided. It is important to take the reference data and sample data at the same sensitivity and aperture wheel

settings. Failure to do so will result in spurious peaks in the background data. A spectrum can be taken after a minimum 20 minute purge with dry nitrogen to remove weak H₂O absorption which occurs near 1650 and 3750 cm⁻¹, and CO₂ absorption at 2300 cm⁻¹.

E. Photoresponse Measurements

1. Signal Generation and Data Acquisition Procedures

For photoresponse measurements, the sample itself served as the detector. Light from the source falls on the sample surface and generates excited holes. When the sample is biased, these photogenerated carriers can be swept out of the device and into the signal processing circuit. For this experiment, the photocurrent is input into a pre-amp designed for a MCT detector operating in the photoconductive mode. The amplified signal is subsequently fed to the analog-to-digital (A-D) board of the BioRad system just like the indigenous DTGS or Si detectors. A centerburst can be usually obtained when the sample temperature falls below 100K. Above this temperature, random thermally generated carriers dominate the signal. The amplitude of the centerburst grows with decreasing temperature until it reaches a maximum around 40 K at which time the number of holes introduced by ionized dopant atoms begins to significantly tail off. The sample is positioned in coordinate-space to maximize the centerburst just as in the case of absorption measurements. After aligning and calibrating the FTIR system through software control, data can be collected in the form of a single beam spectra. All the photoresponse measurements were made under normal incidence conditions. The collected data is transformed to ASCII format and analyzed with Microcal Origin™ software. In Figure 4-20, the single beam data and a curve fit are shown. A curve fit is used because the KBr beamsplitter and ZnSe window in the apparatus have an absorption

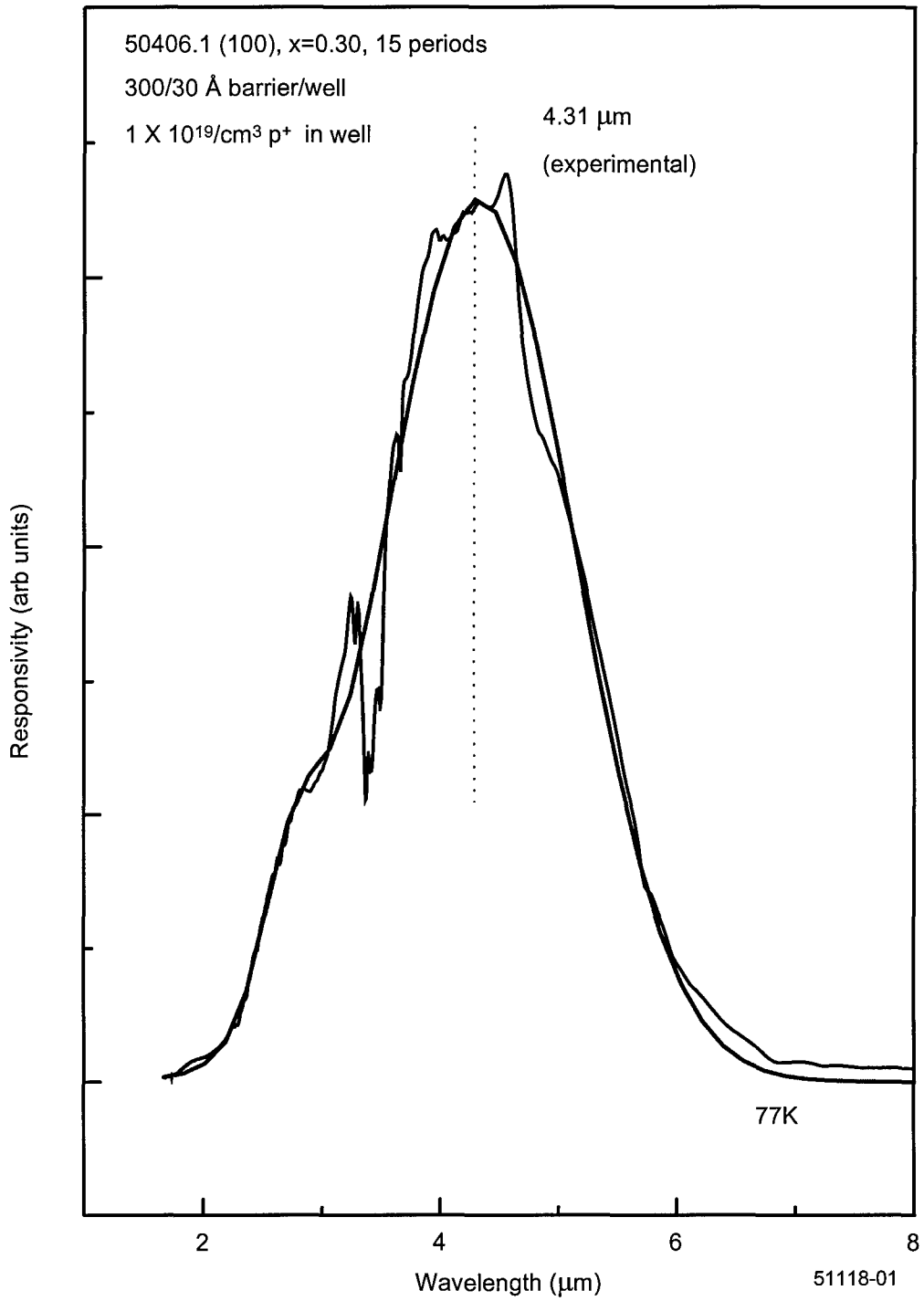


Figure 4-20. Photoresponse spectra taken at 77 K under normal incidence illumination. Raw data and curve fit are shown.

line at the wavelength indicated by the dashed line in the figure. This absorption dip tends to alter the appearance of the data in an erroneous fashion and so a curve fit removes this feature and other spurious lines attributed to absorption in the silicon. Subsequent photoresponse curves will be treated in the same way.

2. Sample Preparation and Experimental Setup

The samples used for photoresponse measurements were fashioned into mesa structures with photolithography and reactive ion etching (RIE). The surface area of the mesas was very large, approximately 4 mm x 4 mm. Material was etched down to the undoped buffer layer grown on top of the substrate. The ultimate mesa height was determined by the thickness of the cap layer and the thickness of the QW layers. Some of the samples were grown with doped cap layers to lower the contact resistance, while others were not. This factor had little effect on the measurements. (See Appendix E for a list of sample parameters.) Electrical contact was made to the sample by soldering a line of indium to the sample surface as shown in Figure 4-21. After the indium was applied to the device, copper wires, approximately one inch long, were soldered to each contact. At this time the sample was glued with rubber cement to a beryllium oxide wafer which was in turn attached to a copper block on the end of the cold finger of a Helitran system manufactured by *Air Products*. The beryllium oxide provided good thermal contact while simultaneously providing electrical isolation from the remainder of the system. (Electrical isolation is necessary to reduce noise due to ground loops in the remainder of

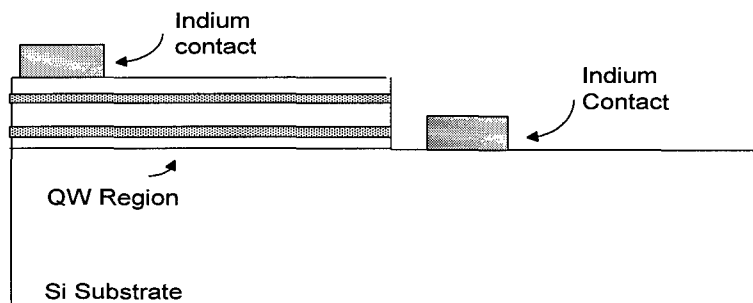


Figure 4-21. Cut-away diagram of mesa structure used in PR measurements.

the system.) Refer to Figure 4-22 for a diagram of the photoresponse system. After soldering the copper wires to contact posts which were embedded in the cold finger and electrically isolated, the contact resistance was tested to make sure that the sample was properly mounted. 1-5 k Ω was the normal value obtained. The cold finger was then placed in a vacuum chamber, with optical ports, that went through the top of the FTIR. The chamber was evacuated to 2×10^{-6} Torr, before a data run commenced, with a diaphragm roughing pump, followed by a drag pump and a turbo-molecular pump. This combination was used to eliminate the introduction of hydrocarbons into the sample chamber, but it had the secondary effect of producing better temperature control. ZnSe windows, with a transmission range of approximately 1-14 μm , were sealed to the vacuum chamber with rubber o-rings. Cryogenic temperatures were reached by forcing LHe through a capillary tube into the cold finger. The LHe flow was controlled with a ball valve. When the LHe comes in contact with the copper block, it boils off, forming a gas over-pressure. As the ball valve is opened to allow the gas to escape more rapidly, more LHe flows through the capillary which in turn allows the copper block to reach a

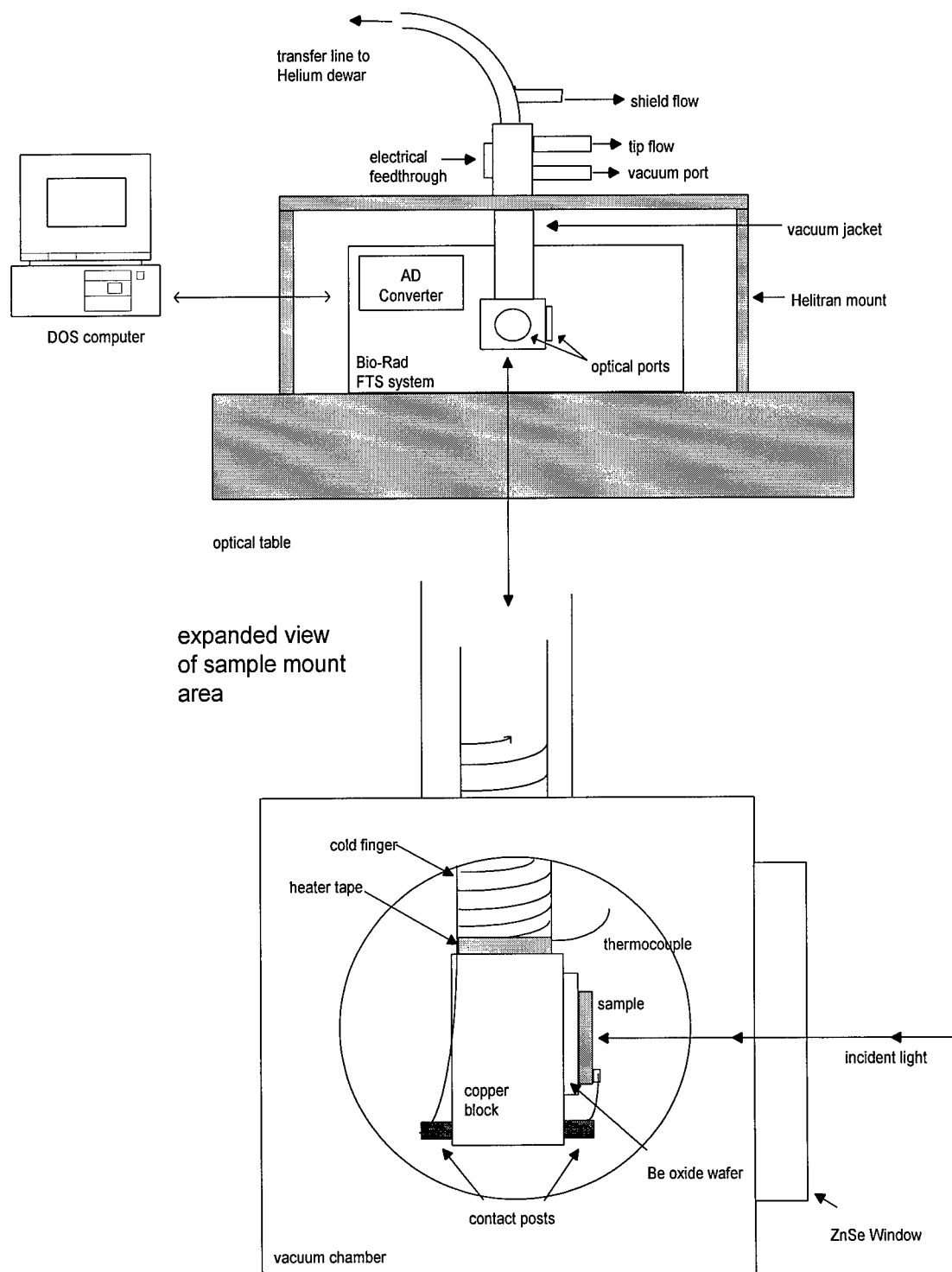


Figure 4-22. Schematic diagram for photoresponse measurements.

lower temperature. A second capillary tube wrapped around the first served as a thermal shield. LHe flow in this tube was controlled in the same way. Fine temperature control was obtained by using a thermal resistance heater wrapped around the cold finger just above the sample in conjunction with an *Air Products* temperature controller. Using this system, measurements could be made at any temperature between 7 K and room temperature.

This chapter was written to describe the experimental equipment and give some detail on the techniques involved to obtain photoluminescence, absorption and photoresponse data. The data is presented and examined in the next chapter.

5. Results and Discussion

A. Introduction

The goal of this research was to determine if the SiGe alloy system was useful for developing QWIP structures that would operate as detectors in the 3-12 μm wavelength range under normal incidence illumination. To make this determination, optical measurements, including photoluminescence, photoresponse, and absorption, were made on Si/Si_{1-x}Ge_x MQWs. Unfortunately, such MQWs are difficult to grow and also difficult to characterize. Many research groups have performed PL measurements, but as outlined in Appendix B, few groups have yet successfully demonstrated absorption or photoresponse measurements for MQWs grown in the more conventional [001] direction, much less for doped quantum well structures on non-conventional substrates such as the [110]. To date, there is *no* data theoretical or experimental, for p-type Si/Si_{1-x}Ge_x MQWs with a [110] growth direction. Many growth issues are not yet fully understood and are currently under investigation. For example, Thompson has recently indicated that boron doping may play a role in germanium segregation out of the well region, and that this effect differs with substrate orientation.⁸⁹ Sunamura⁹⁰ has recently indicated that an upper bound for Ge incorporation into the well material may exist. Transmission electron microscopy (TEM) reveals the emergence of growth islands for germanium compositions above 40 percent. Thompson⁹¹ and Zeindl⁹² are investigating the luminescent properties of the MQWs with respect to growth temperature. Despite the questions that remain about the exact nature of the QW materials, it is desirable to push

the material into device fabrication to justify the time and effort already expended as well as to obtain an indication of the potential for SiGe as a detector material. Unfortunately, a seeming paradox has evolved between photoluminescence measurements and absorption measurements. Historically, PL that showed no-phonon resolved spectral features was taken as an indication of high-quality material with few defects or dislocations. Kriefels *et al.*¹⁶ determined that the growth temperature which produces the *best*, or no-phonon resolved, PL is 710 °C. However, materials grown at this temperature showed little or no intersubband absorption. In contrast, materials grown at 550 °C produced good bound-to-bound absorption but poor PL. To further confuse the issue, photoresponse of near equal magnitude and bandwidth can be obtained from material grown at either temperature. Consequently, the best method to fully characterize the material in question is not obvious at this time and appears to depend on the intended application. In the end, the merit of the Si_{1-x}Ge_x system will be determined by its usefulness in detector structures, whether it is fully characterized or not.

The data presented in this chapter have been obtained by PL, FTIR absorption, and FTIR photoresponse. The PL measurements were made to compare samples as they came from the grower and to provide the grower with data necessary for fashioning future samples. A small portion of this data will be presented here for comparison with other studies. The absorption measurements were made to confirm the theoretical predictions arrived at from the **k·p** calculations in Chapter 3. These measurements provided the most direct test of the predicted energy levels and transition strengths between levels in the well. Finally, the photoresponse measurements provide the key data for assessing the

value of these MQWs for use as detectors. As was stated earlier, that is the principle question posed by this dissertation and it is the photoresponse measurements which provide credence for continued development of these devices.

B. Photoluminescence

Many researchers have performed photoluminescence on Si/Si_{1-x}Ge_x MQWs, especially structures oriented in the (100) direction. Fewer researchers have performed PL on (110) oriented samples, however, the spectra are very similar. As mentioned previously, PL was used in this project to assess the quality of the grown structures in order to provide feedback to the crystal grower. Figure 5-1 shows a representative spectrum for an undoped Si [110] substrate and an undoped standard [110] reference, NRL sample 30528.2, grown at 710 °C. The standard samples were characterized by the following parameters: an initial 1700 Å Si buffer layer, 5 periods composed of alternating layers of 30 Å Si_{0.80}/Ge_{0.20} to form the well region and 300 Å Si to form the barrier region, and a final 2000 Å Si cap layer. (Note: see Appendix E for the composition of each sample.) The Si substrate has one dominant line and four smaller lines, all of which are associated with excitons bound to boron impurities.⁹³ Their identification and energy positions are presented in Table 5-1. (Note: see Appendix G for an extensive list of the PL lines seen in Si.) If more impurities such as antimony, phosphorous, arsenic, etc., are incorporated into the material then the dominant line will develop a fine structure because a slightly different binding energy is associated with each individual dopant species. The standard sample, Si/Si_{0.80}Ge_{0.20}, exhibits other transitions superimposed on the Si substrate spectrum. The large features are due to a no-phonon transition, labeled number 9, and its phonon replicas labeled numbers 7 and 8. The no-phonon line represents a transition from an exciton, bound to a neutral impurity at

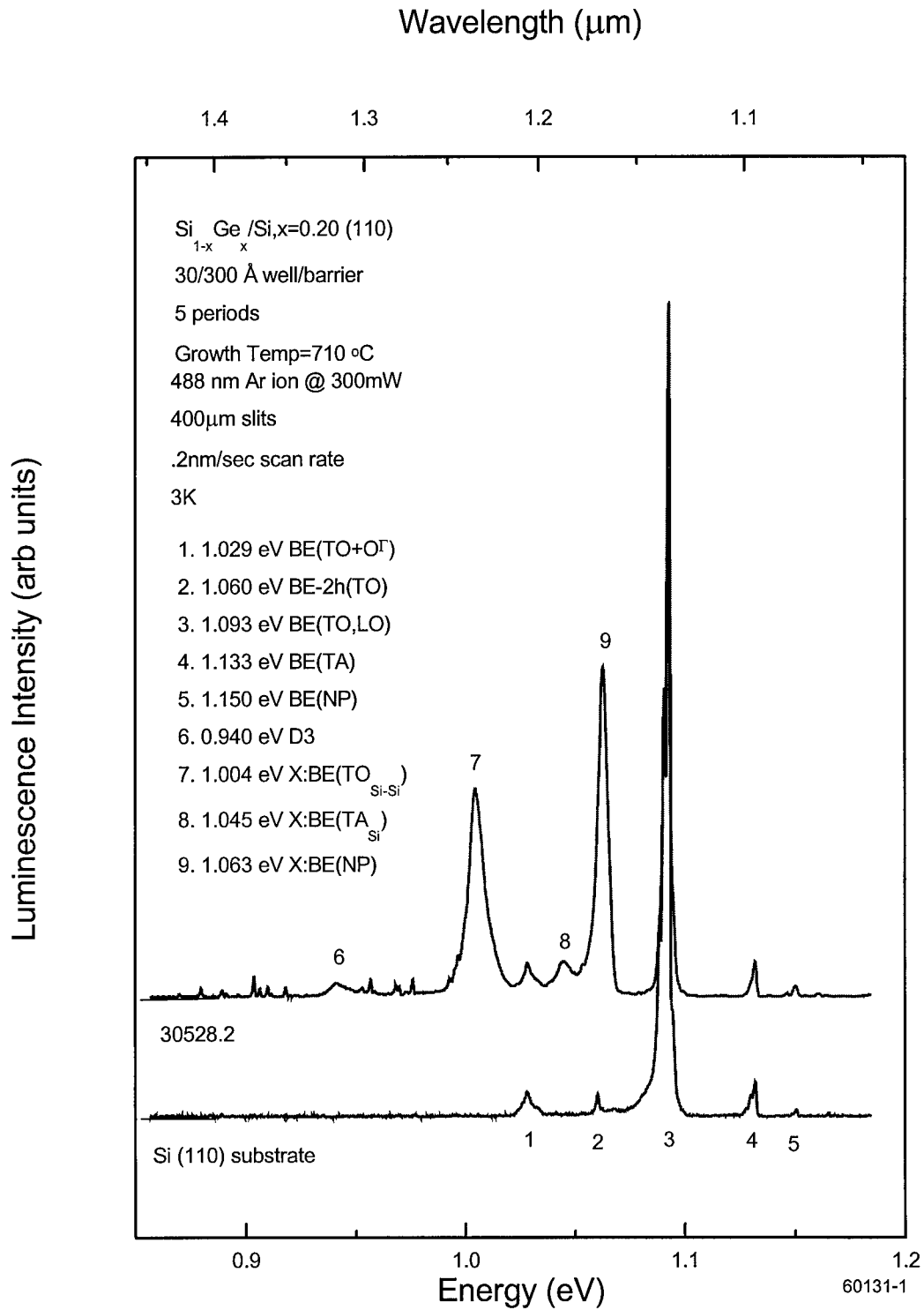


Figure 5-1. PL spectra of a Si[110] substrate and an undoped standard sample 30528.2.

Table 5-1. PL emission peaks associated with boron impurities.

energy (eV)	identification
1.150	BE(NP)
1.133	BE(TA)
1.093	BE(TO,LO)
1.060	BE-2h(TO)
1.029	BE(TO +O ^T)

an energy level near the first conduction band state, to the first heavy-hole energy level in the valence band. The no-phonon transition is allowed because the alloy is somewhat random thus breaking the transitional symmetry and relaxing the requirement of momentum conservation. The appearance of the no-phonon line and its associated phonon replicas has been used previously as an indication of high material quality. As Kriefels determined however, these features are visible only when the growth temperature is above 700 °C. The position of the no-phonon line varies as a function of germanium composition because it depends on the band gap energy in the alloy. Characteristic phonon energies are listed in Table 5-2. The spectrum of sample 30528.2 shows a peak at 0.940 eV which may be a D3 dislocation line.

Whenever a modification of the MBE growth system was performed, a new standard was grown and the resulting PL was compared to previous results to assure system integrity. PL was also taken on samples used in the absorption and photoresponse

Table 5-2. Identified phonons and their energy values.

phonon replica	energy (meV)
TA _{Si}	18
TO _{GeGe}	34
TO _{Si-Ge}	49
TO _{Si-Si}	58

measurements. These samples were grown at 550 °C with varying doping levels. As previously indicated, these materials did not show no-phonon lines but they did have other spectral features. Figure 5-2 shows the spectra of undoped sample 50117.1 grown at 550 °C taken at five different sample temperatures. It is immediately obvious that the no-phonon structure seen in Figure 5-1 has disappeared, and new features have emerged. The five labeled features are associated with carbon-related defects and are summarized in Table 5-3. These structures are non-existent at 1.6 K and begin to diminish above 30 K. The dashed line in the figure indicates the band gap energy in the alloy layer, or the energy difference between the first conduction band state and the first heavy hole state. The broad feature centered at 0.825 eV remains somewhat constant with temperature. This broad feature, approximately 100 meV below the band gap, has not been positively identified in the literature. It does not match the energies or the line shape of the D1-D4 lines (see Appendix G) which are caused by a high density of dislocations.^{96,94,95} Other

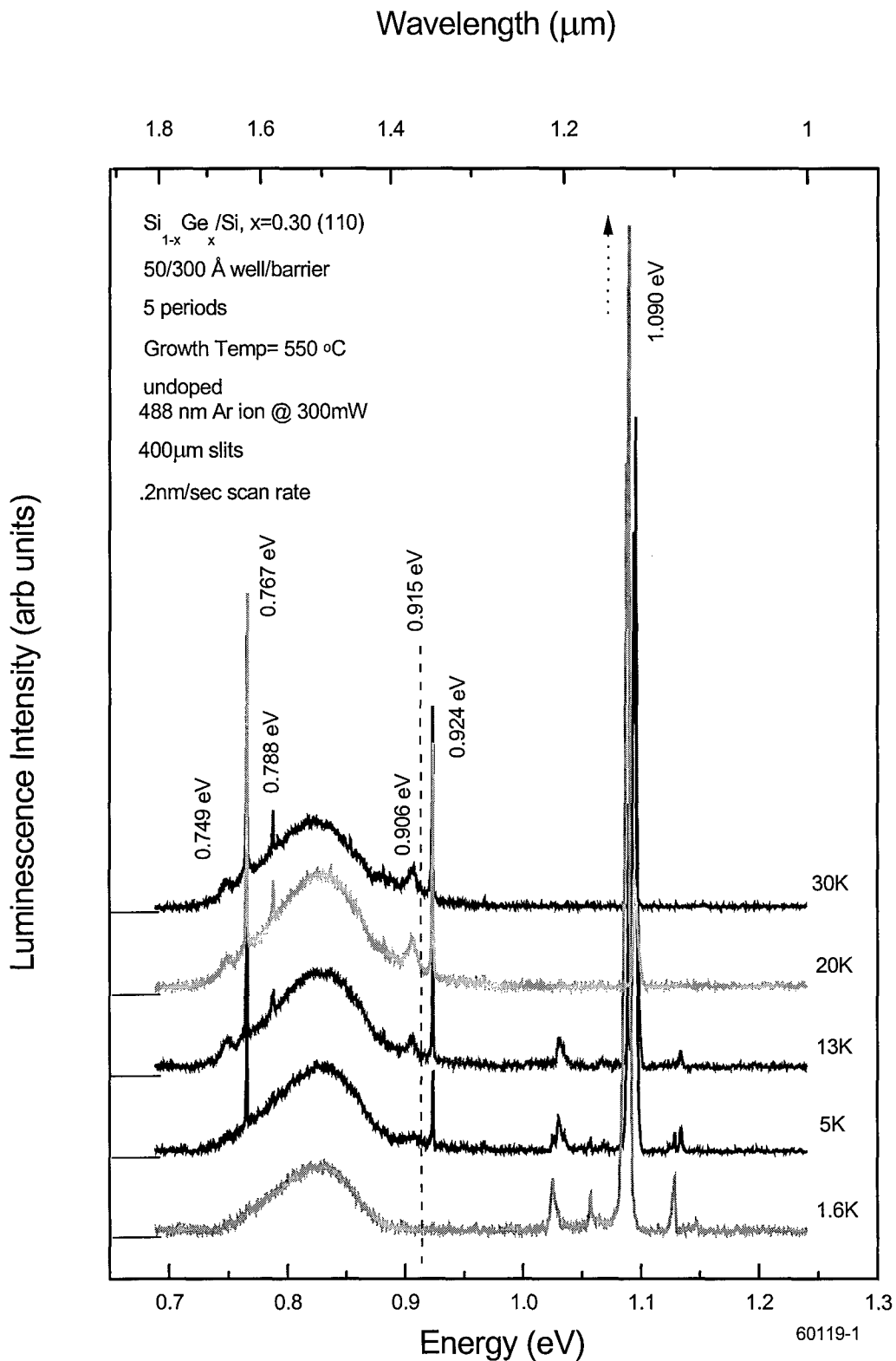


Figure 5-2. PL spectra of sample 50117.1 taken at different temperatures showing broadband and carbon related features

Table 5-3. Photoluminescence peaks due to carbon related defects.

energy (eV)	identification ⁹⁶
0.925	“H” or “K” monoclinic I center with C dependence
0.907	TA _{Si} phonon replica of 0.925 eV
0.788	“C” monoclinic I center with C and O dependence ⁹⁷
0.767	“N ₄ ” or “P” monoclinic I center with C dependence or C and O dependence
0.749	TA _{Si} phonon replica of 0.767 eV

groups associate this broad luminescence with an excitonic mechanism involving isoelectronic centers related to Ge complexes in the alloy layers.^{98,99} The large bound exciton line at approximately 1.090 eV shifts with temperature because the band gap energy, from which the exciton energy is referenced, shifts with energy. The luminescence also changes with the amount of boron doping in the wells as shown in Figure 5-3. The sample parameters, except for the doping level, are identical to sample 50117.1 shown in Figure 5-2. As the doping is increased, the center of the broad band shifts to higher energies and the peak height flattens out. This effect may be associated with band filling. As more holes, due to ionized impurities, populate the valence band, electrons have a wider energy range in which they can make a transition. In addition, since the density of states increases away from the valence band edge, higher energy transitions are more likely. This effect may also occur because, at the high doping levels,

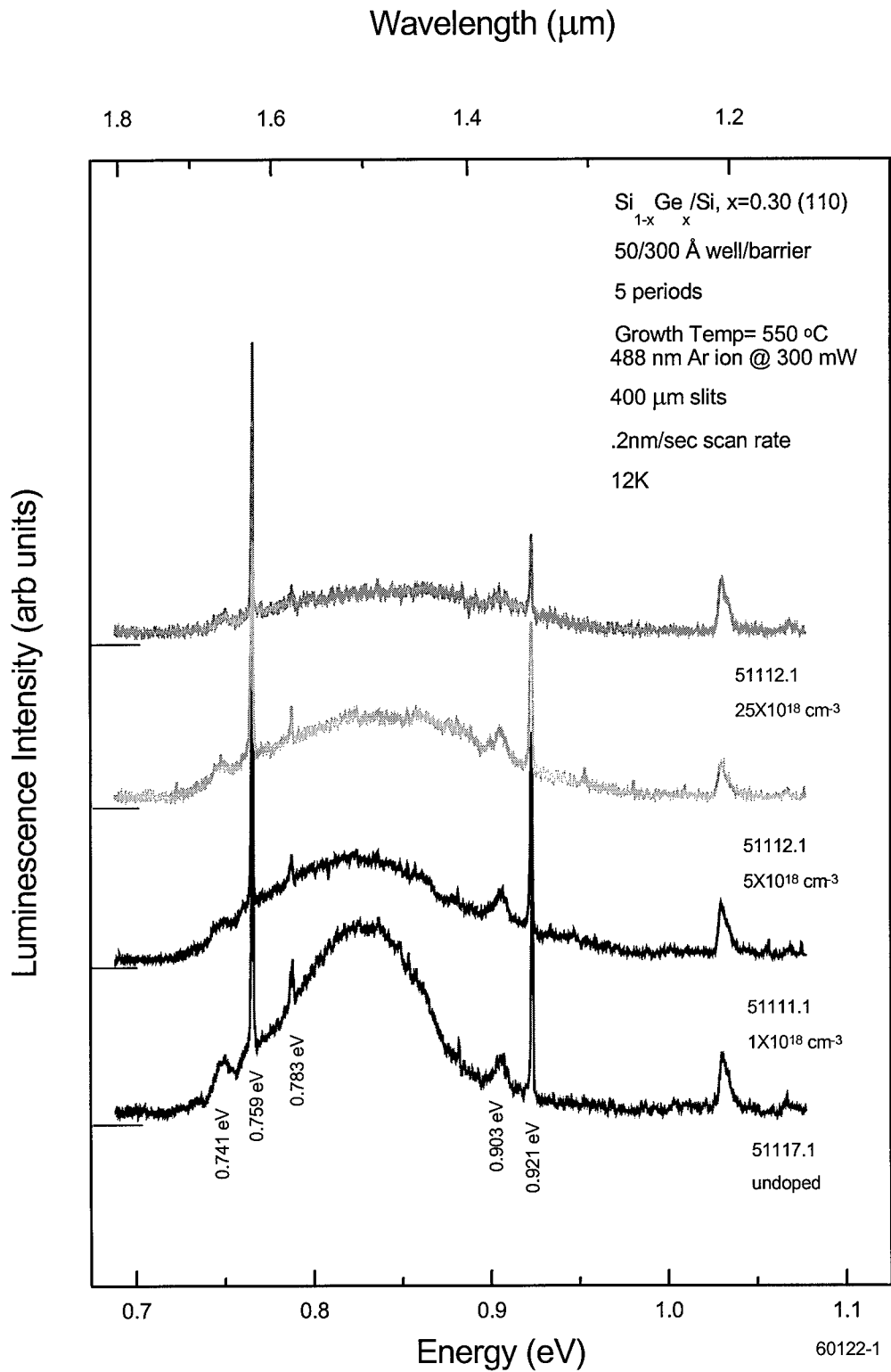


Figure 5-3. PL spectra showing luminescence intensity as a function of boron doping.

the quality of the crystal may be sufficiently degraded that radiative recombination is quenched, and at low growth temperatures the doping related defects are not annealed out. A series of PL spectra were run on the MQW samples grown at 550 °C to determine the quality of the samples to the extent possible. The result of these measurements is shown in Figures 5-4 through 5-10. Figure 5-4 shows the variation in the position of the broadband luminescence with quantum well width. The position of the ground state shifts as the well width changes, and so the band gap changes. Dashed lines are once again placed at the band gap energy. The spectrum of sample 51212.2 shows a D2 peak at 0.873 eV. The broadband shift correlates in direction with the band gap shift but not in the size of the shift. This same phenomena is seen in Figure 5-5 where the Ge percentage is varied while the well width is kept constant. For a constant well width, the energy position of the ground state will drop for increasing well depth which is associated with increasing Ge composition. This indicates that either the broadband feature is not associated with the $\text{Si}_{1-x}\text{Ge}_x$ alloy, or that the actual material composition is not what was intended. The second hypothesis seems to corroborate the conclusion of Sunamura⁹⁰ who determined that there is an upper bound for Ge incorporation into the alloy. What was intended to be 40 or 60 percent germanium may actually be closer to 30 percent. The data presented in Figure 5-6 and Figure 5-7 was collected in an attempt to determine from which layer of the quantum well structure the broadband luminescence originates. Referring to Table 4-1 in Chapter IV, the penetration depth of the incoming photons can be tuned by varying the laser wavelength. Samples 40601.1 and 40602.1 are identical

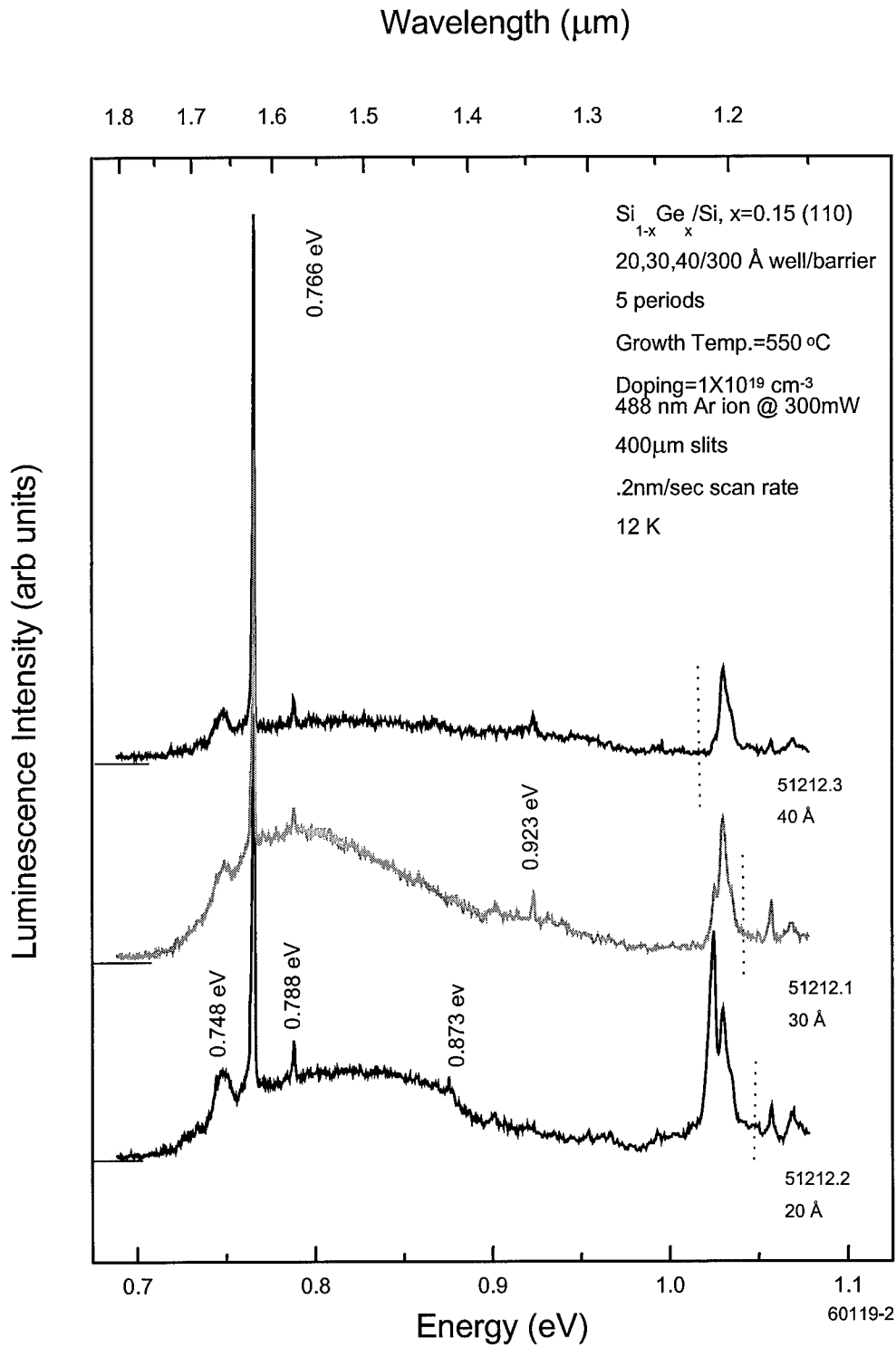


Figure 5-4. PL spectra showing change in peak position with variation in quantum well width and constant Ge composition.

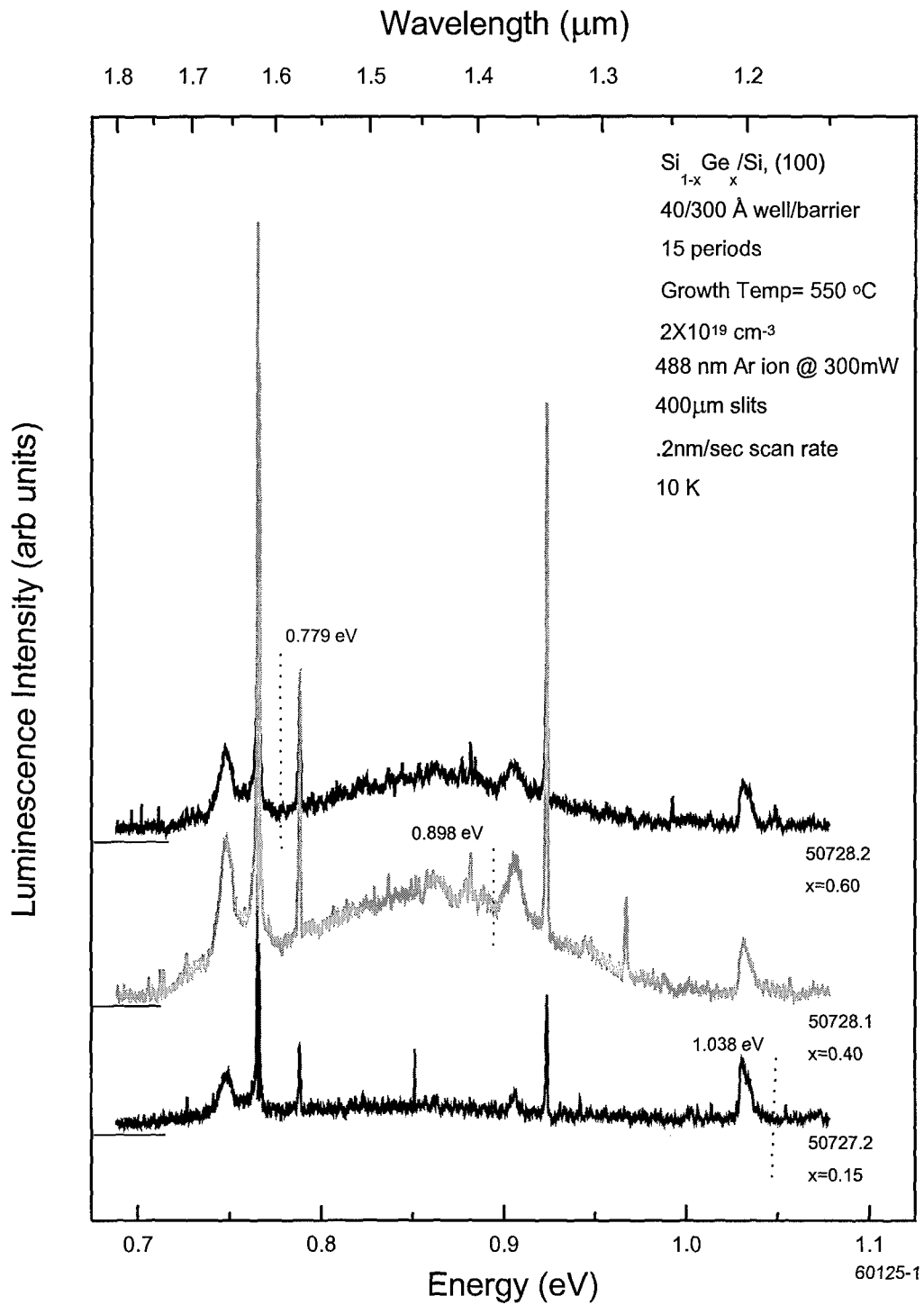


Figure 5-5. PL spectra showing broadband shift with different Ge compositions and a constant well width.

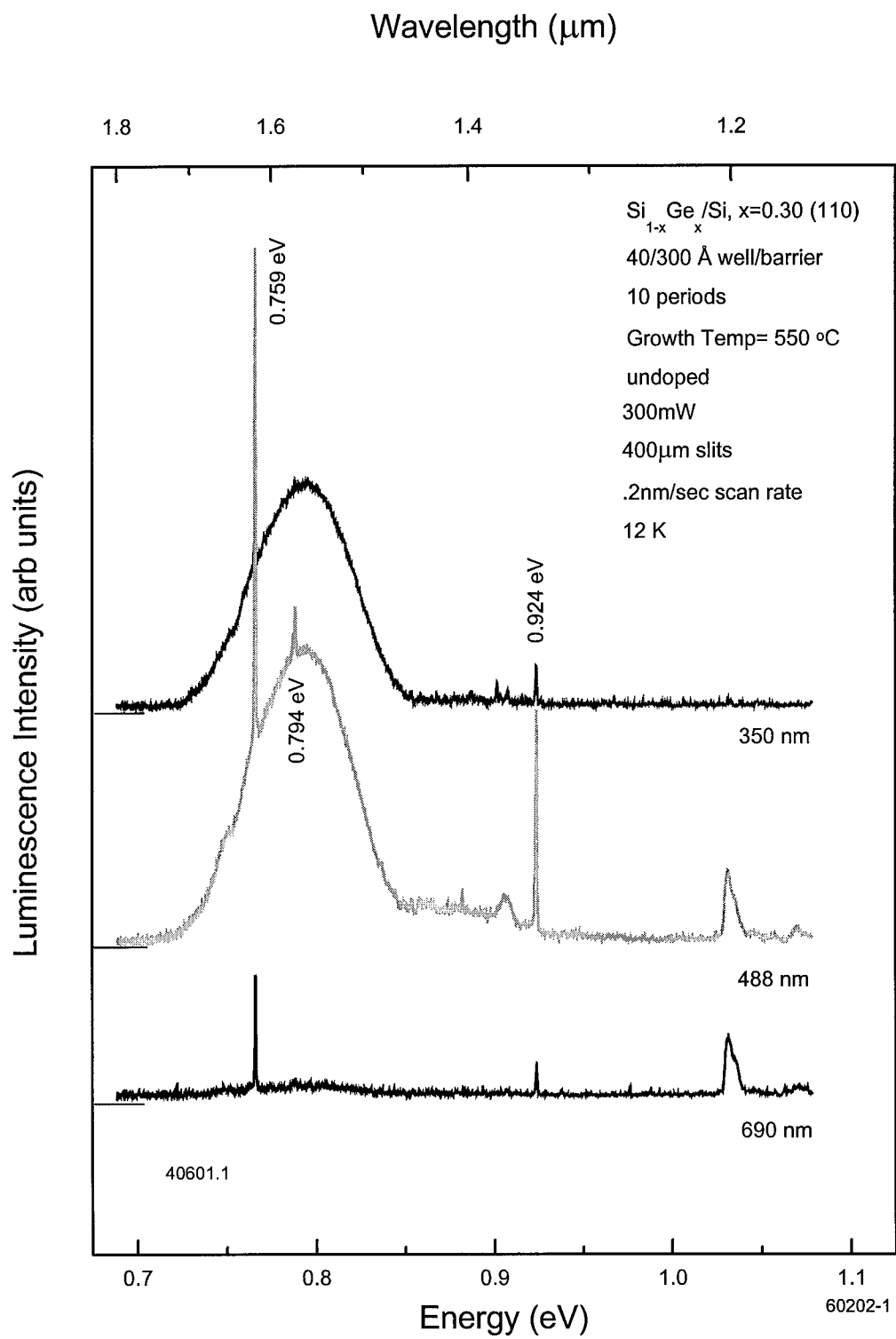


Figure 5-6. PL spectra of an undoped sample showing the penetration depth dependence of the broadband and carbon related features.

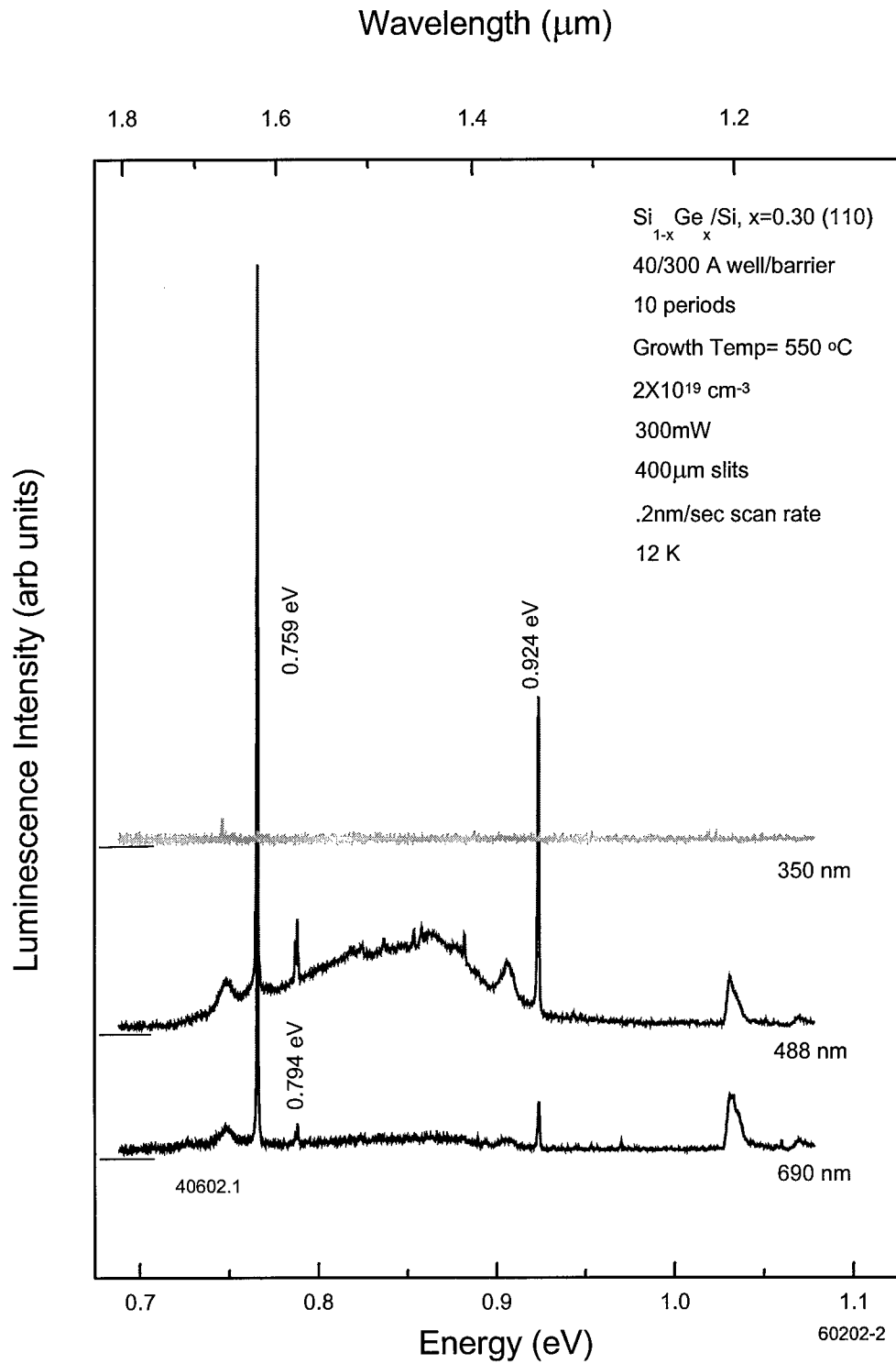


Figure 5-7. PL spectra of a doped sample showing the penetration depth dependence of the broadband and carbon related features

2

samples with the exception that 40602.1 is boron doped to $2 \times 10^{19} \text{ cm}^{-3}$. The UV laser line at 350 nm excited luminescence in the 0.5 nm thick, Si cap layer. The blue 488 nm line excited luminescence in the cap and MQW region, and the red 690 nm line excited through all layers and into the substrate. It is immediately obvious that the source of most of the spectral features due to isoelectronic carbon centers is the MQW region. However, the broadband luminescence has an anomalous behavior. For the undoped sample in Figure 5-6, the broadband originates in the cap layer, while for the doped sample in Figure 5-7, the broadband is confined to the MQW region. The broadband and carbon features are not limited to (110) oriented samples. Figure 5-8 shows a comparison between identical structures grown on (100) and (110) substrates. Sample 50406.1 (100) has a very large "P" center and TA phonon replica. Nevertheless, this particular sample produced the best absorption spectra obtained throughout the study while sample 50501.1 produced nondescript absorption spectra. Figure 5-9 shows a comparison of identical structures grown at different temperatures; 50501.1 grown at 550 °C, and 50912.3 grown at 710 °C. At the high growth temperature, the carbon defects are annealed out, but the broadband remains.

The effects of sample annealing are shown in Figure 5-10. In this figure, PL was taken on a sample grown at 550 °C in the standard configuration. The top line is a spectrum from the "as grown" sample which shows a large broadband feature and the carbon related defects. The middle spectrum represents a sample cut from the same wafer as the previous sample but annealed at 700 °C for twenty minutes in a pure N_2

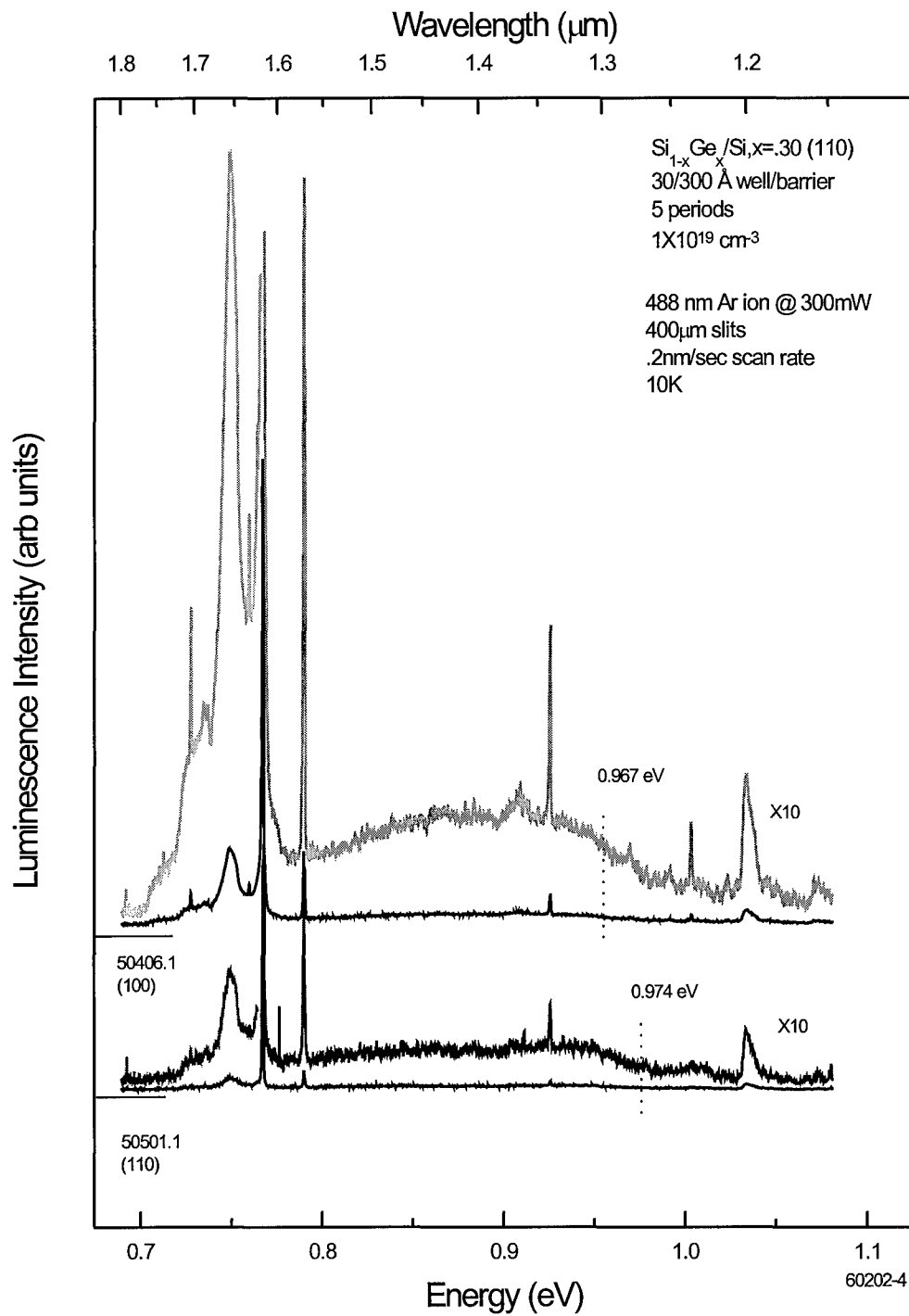


Figure 5-8. PL spectra showing a comparison between identical MQW structures grown on (100) and (110) substrates. Portions of the plots have multiplied by a factor of 10.

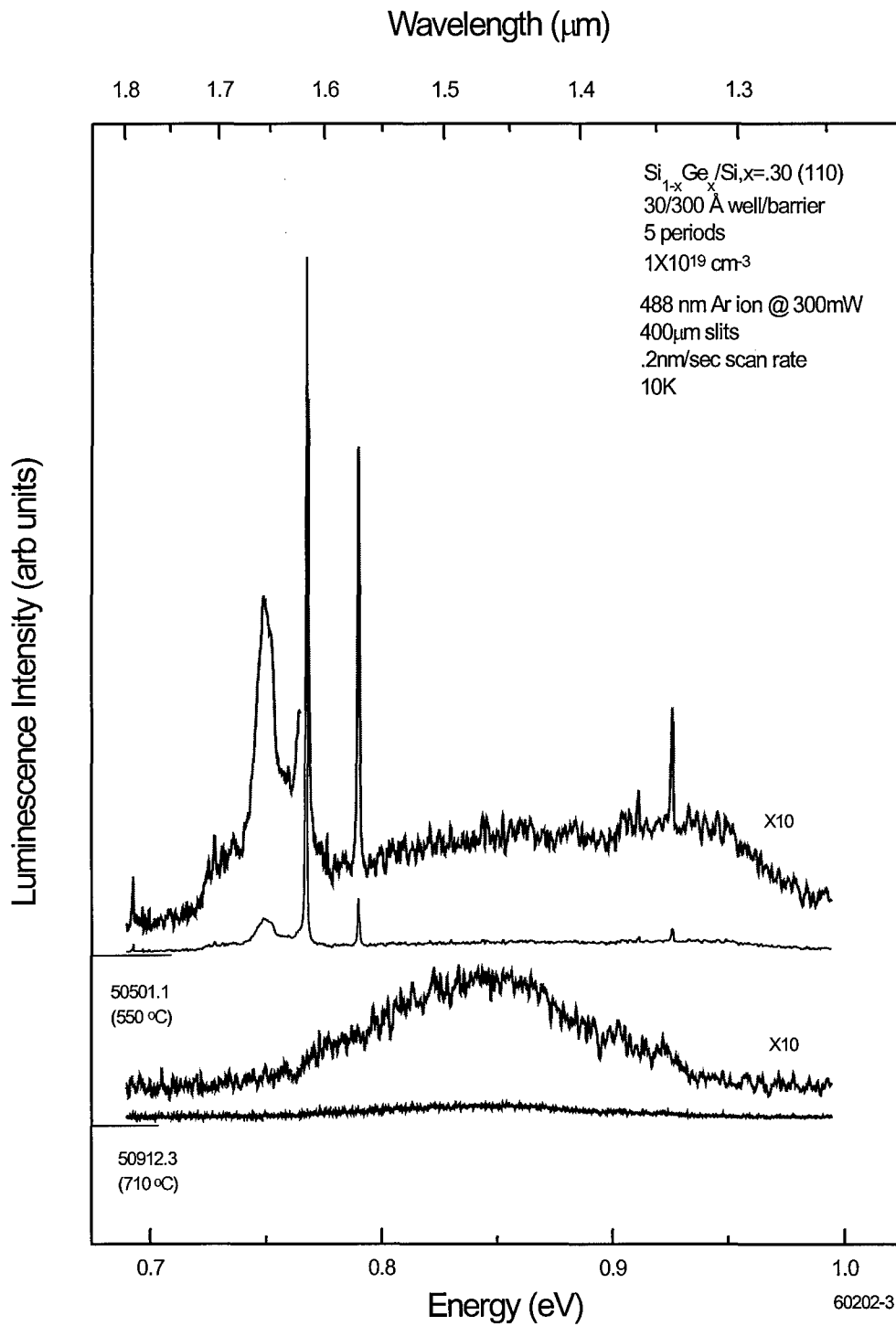


Figure 5-9. PL spectra showing a comparison between identical MQW structures grown at temperatures of 550 °C and 710 °C. Portions of the plots have multiplied by a factor of 10.

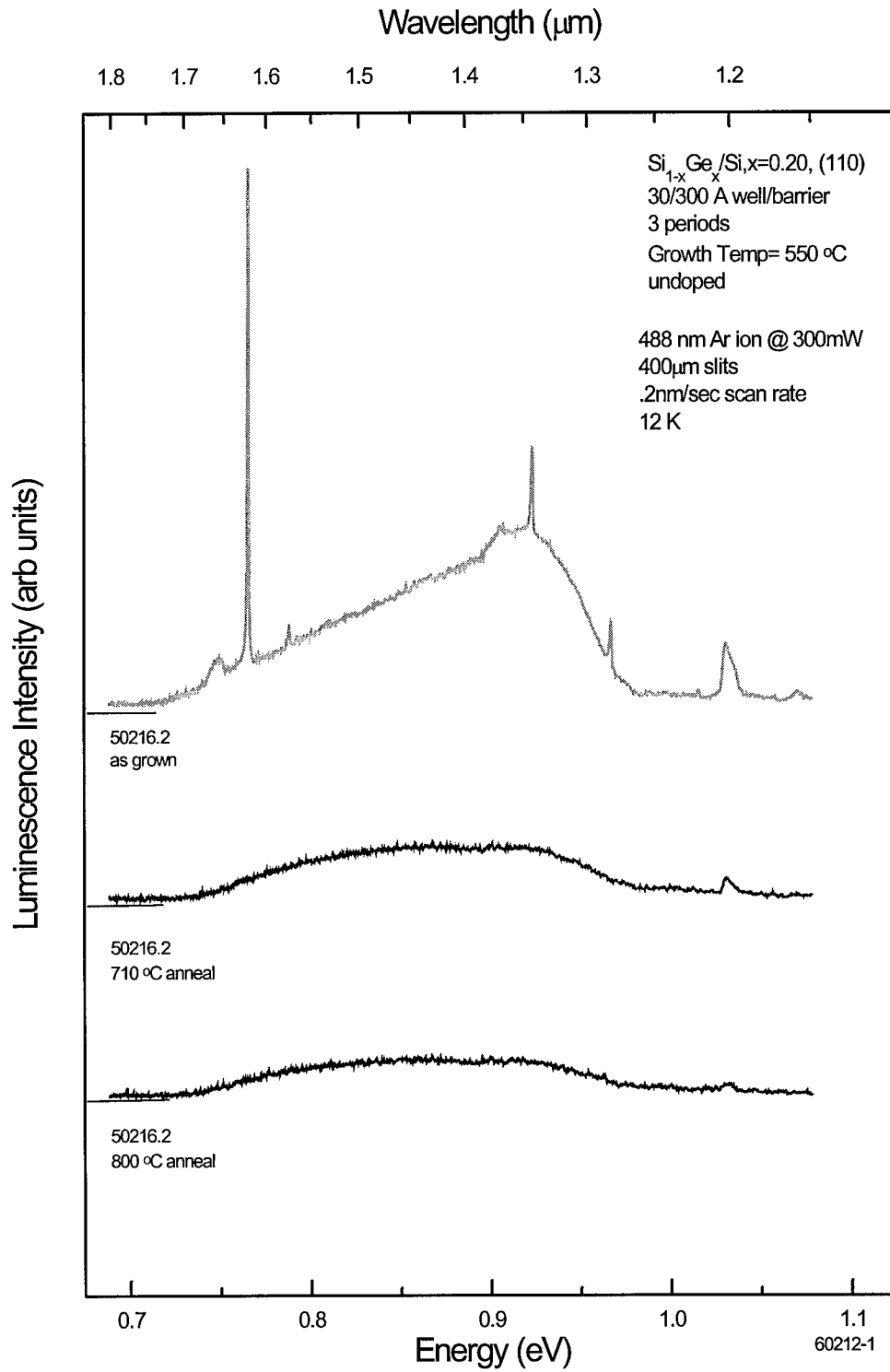


Figure 5-10. PL spectra showing the effects of annealing on the carbon related defects and the broadband luminescence.

environment. The spectral features have been substantially reduced. The bottom spectrum represents a sample annealed at 800 °C for twenty minutes in a pure N₂ environment. Little changes between the 700 and 800 °C anneal. These plots show that some of the defects can be annealed out if a sample is grown at low temperatures. What is not known at this time is the amount of strain relaxation which occurs with the annealing, or if samples grown at 710 °C have more relaxation than samples grown at 550 °C which are subsequently annealed.

The previous paragraphs indicate that PL serves as a good diagnostic tool to determine crystal quality for undoped material grown at 710 °C. However, the use of PL as a measure of the quality of doped materials to be used for photoresponse or absorption measurements appears to be of little use. The PL spectra show that when samples are grown at sufficiently low temperatures to insure a coherently strained structure, defects and dislocations are incorporated into the material. These defects, along with the incorporation of boron impurity atoms, result in non-radiative recombination centers which appear to quench the no-phonon related luminescence. However, the strongest bound exciton line and the broadband luminescence approximately 100 meV below the SiGe alloy bandgap remain. In addition, carbon isoelectronic centers cause very strong PL lines along with phonon replicas. Shiraki has shown that the intensity of the no-phonon line and its phonon replicas increase with increasing growth temperature.¹⁰⁰ This happens because the atoms have more energy to move around on the surface at higher temperatures, and defects, which may quench luminescence, are subsequently eliminated. However, surface segregation is enhanced with higher growth temperature. Surface

segregation will cause the Ge and B concentration to be lower in the well than expected, which appears to significantly alter the absorption properties. It is also possible that the strain is relaxed at high growth temperatures which would also significantly alter the absorption and photoresponse properties. It may well be that annealing, which reduces the broadband luminescence and the carbon defects in low growth temperature samples, may enhance the absorption and photoresponse. However this line of inquiry was not pursued.

C. Absorption

1. Introduction

As was stated in the introduction to this chapter, absorption measurements are essential to test the predictions of the $\mathbf{k}\cdot\mathbf{p}$ theory. They allow confirmation of both energy levels and transition energies as a function of quantum well width, quantum well depth, and Ge concentration. Unfortunately, intersubband, or intrasubband absorption is very difficult to measure in the SiGe alloy system for many reasons, and very few researchers have reported such data.^{41,45} In fact, *no* absorption data has yet been presented in the literature for structures grown on Si[110]. Absorption measurements are difficult to make because a reference signal must be obtained and then subtracted out of the sample spectrum. Referring to Figure 4-15, Si has many strong absorption lines in the infrared region of interest. These strong background lines are very difficult to subtract out when performing referencing operations. Quoting Kriefels, "Consider that for a typical superlattice sample, only 150-200 Å of SiGe alloy is the "active" absorption region grown on 0.3 mm of Si substrate. Assuming an atomic spacing of 2 Å, then a clean FTIR absorption measurement becomes an attempt to discriminate the photo-absorption properties of approximately 80 atoms against a background of 1,500,000 atoms!"¹⁶ Furthermore, the total number of quantum well periods must be kept rather small, 5-20 periods, to keep the alloy below the critical thickness so as to minimize dislocations. This will, however, keep the absorption signal from the MQW to a minimum. By contrast, the GaAs/AlGaAs system does not have such strong, sharp absorption lines

making correction for substrate absorption relatively easy, and the total number of quantum well periods that are used for the lattice-matched material can be as high as 50. Finally, the waveguide technique, as outlined in the previous chapter, must be used to observe intersubband transitions with particular polarization selection rules. Making waveguides has proven to be a "black art," and the proper method was obtained through trial and error.

It also important to mention again that the best absorption spectra were obtained on samples grown at 550 °C. This is counter-intuitive when one considers that the best PL was obtained at 710 °C, but with further thought and investigation a plausible explanation is obtained. As mentioned in the PL section, growth at high temperatures tends to be self-annealing which will reduce the non-radiative recombination centers associated with the high doping levels and crystal defects. However, at high temperatures, segregation of boron and germanium becomes problematic, and it may be that segregation effects will cause the sharp interface between the well and barrier regions to become diffuse. When you consider that the well regions are on the order of four to eight monolayers, a one or two monolayer graded region could have significant impact on the quantum confined effects and thus significantly affect the absorption spectra. It is also possible that growth at high temperatures will cause the strain to relax which would have significant impact on the position of the energy levels.

2. [001] Absorption Data.

For MQW material grown at 550 °C, intersubband absorption on Si[001] samples was relatively easy to obtain when measured in the waveguide configuration. (Refer to the previous chapter for a discussion of referencing schemes.) The data was obtained as function of electric field polarization in order to probe the selection rules. Features of a typical spectra, shown in Figure 5-11, can be qualitatively explained using zone center energy levels and transition strengths obtained from EFA models developed in Chapter 3. Zone center energy levels such as those indicated in Figure 5-12 are based on EFA calculations. It is important to note that zone center energies provide only a general indication of where the labeled transition may occur. In fact, the predicted energy difference between two levels will change as a function of parallel momentum. In addition, the transition strengths change as a function of polarization and direction in k-space. Because of the higher degree of symmetry and the fewer number of bands in the [001] materials, it is somewhat easier to identify a particular peak with a particular transition. However, this is impossible to do for the [110] materials unless a full absorption calculation is performed which considers all directions in k-space. Such a calculation was beyond the scope of this work. For [001] materials, the heavy-hole 1 (HH1) to heavy-hole 2 (HH2) transition was usually the dominant feature observed, but it was observable only with a component of the input beam polarized for parallel incidence (component of the Poynting vector perpendicular to growth axis). In Figure 5-11, normal incidence (xy-polarization) is indicated by the 90/90 curve and parallel

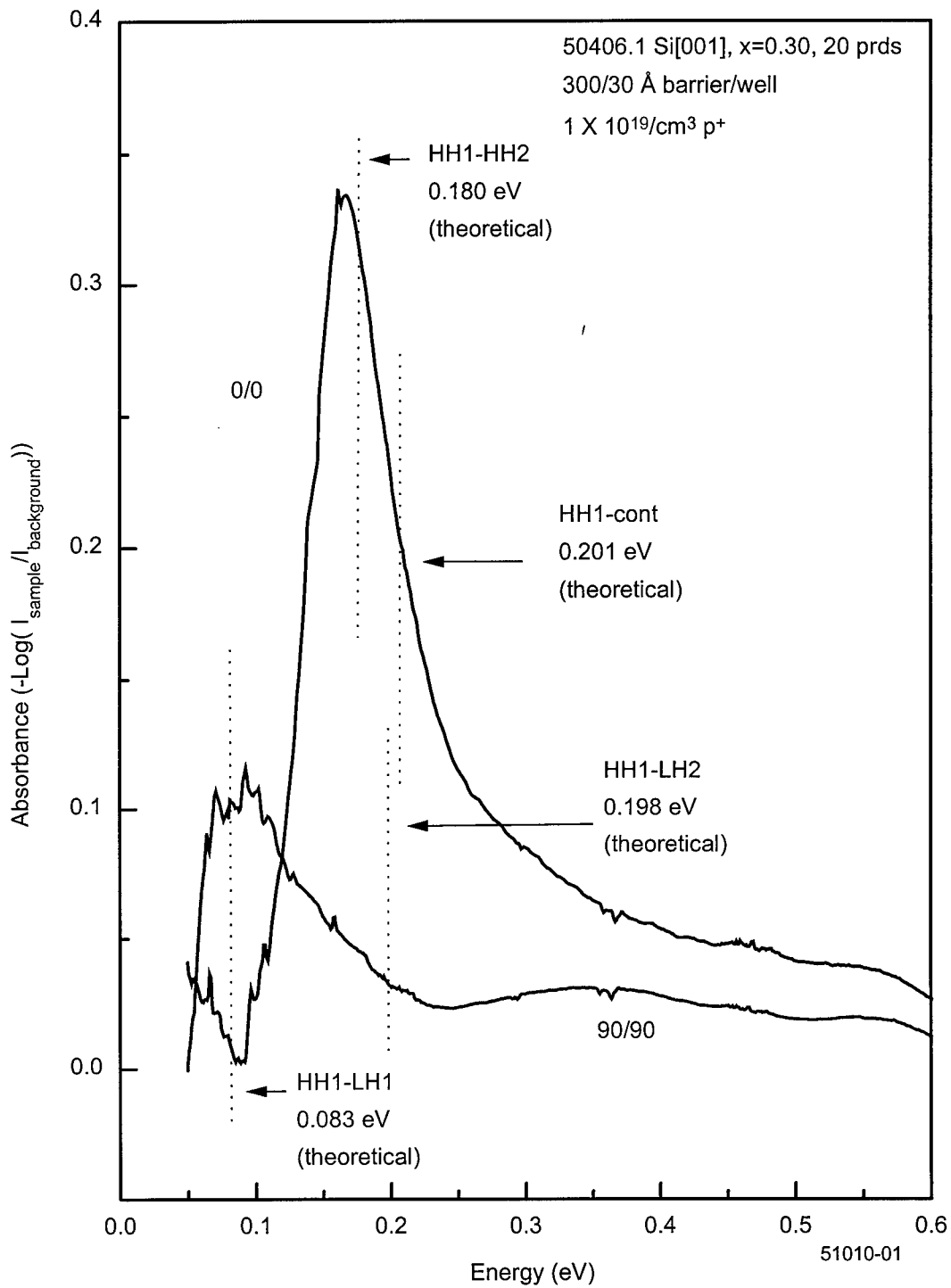


Figure 5-11. Absorbance spectra of NRL sample 50406.1 using substrate referencing background subtraction.

$x=0.30, L = 30 \text{ \AA}$.

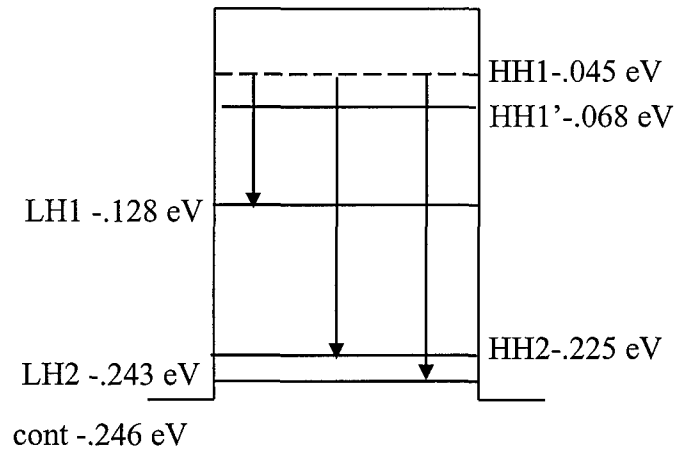


Figure 5-12. Schematic drawing showing the EFA zone center energies and possible transitions for a Si[001]/Si_{0.70}Ge_{0.30}, 30 Å well MQW structure. The shifted position of HH1 due to the exchange interaction effect is indicated by the dashed line.

incidence (z-polarization) is indicated by the 0/0 curve. The peaked feature observable at 0.170 eV in the 0/0 spectrum is the HH1-HH2 transition. The EFA calculation at zone center predicts a peak at 0.160 eV as indicated by the energy differences between the two levels in Figure 5-12. However, because the doping level is high at $1 \times 10^{19}/\text{cm}^3$, the exchange effect lowering of the ground state must be considered. (This effect will be considered phenomenologically. The theory of exchange interaction is beyond the scope of this work and so this effect will be calculated numerically using the method of Choe *et al.*¹⁰¹) Using a numerical routine, a 0.023 eV shift of the ground state is calculated for this sample which pushes the predicted peak position for HH1-HH2 to 0.180 eV. The peaked feature at 0.080 eV in the 90/90 spectra is labeled as a HH1-LH1 transition. Using the exchange interaction correction, the predicted peak positions are

very good. The strength of these transitions and their polarization selection rules were accurately predicted by the calculations performed in Chapter 3 (see Figure 3-17) which indicate that under parallel incidence (z-polarization) conditions, HH1-HH2 is a strong transition, and under normal incidence (xy-polarization) conditions, HH1-LH1 is allowed provided states sufficiently out in the zone are occupied. For NRL sample 50406.1, k-space is occupied out to approximately 0.06 \AA^{-1} , which is far enough to ensure that some of these transitions take place as evidenced by the spectra in Figure 5-11. The dashed line designated by the label, HH1-cont, represents the EFA zone center energy difference between the ground state and the edge of the quantum well. Below this energy, one would expect bound-to-bound transitions, and above this energy, one would expect free-to-bound transitions. To further confirm that these are intersubband transitions, the HH1-HH2 transition was probed with different electric field polarizations. Figure 5-13 shows how the absorbance changes when rotating the Poynting vector in and out of the quantum well planes. This angular dependence confirms the valence band selection rules for the absorption strength of the HH1-HH2 transition which should show a $\text{Cos}^2(\phi)$ dependence according to the following equation,

$$I = \rho_s N_T \frac{e^2 \eta}{8\pi c \epsilon_0 n_r m^*} f \frac{\cos^2 \Theta}{\sin \Theta} \cos^2 \Phi \quad (5-1)$$

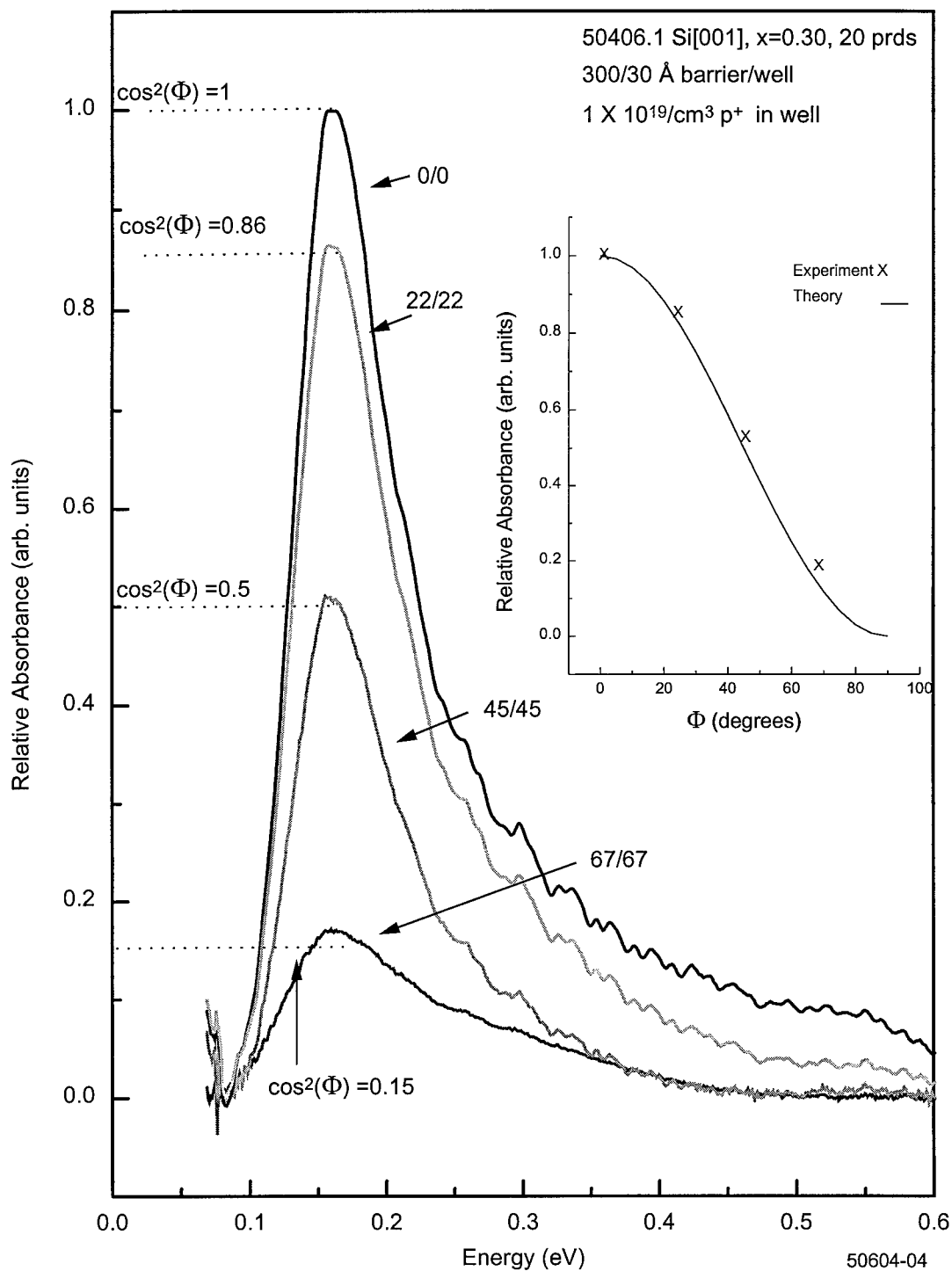


Figure 5-13. Absorbance spectra of NRL sample 50406.1 showing the effects of rotating the Poynting vector perpendicular and parallel to the quantum well planes. Data has been normalized.

where I is the absorption strength, ρ_s is the two-dimensional density of holes, N_T is the total number of quantum wells that the beam passes through due to multiple reflections, n_r is the refractive index, m^* is the effective mass along the growth direction, f is the transition strength, Θ is the angle of incidence, and Φ is the polarizer angle.¹⁰²

Figure 5-14 shows absorbance spectra for NRL sample 50728.1 which was also grown on Si[001] and has a germanium concentration of 40 percent and a well width of 40 Å. The dashed lines are the theoretically predicted transitions at zone center as calculated by EFA, and corrected for exchange. The small peak at 0.360 eV is similar to the peak structure found in GaAs/AlGaAs structures which is attributed to a HH1 to split-off band transition. (see page 299 of Yu and Cardona)¹⁰³ However this energy is 0.130 eV greater than the transition calculated by the decoupled band method and the EFA method was not used to calculate energies above the HH and LH continuum level. This sample is doped to $2 \times 10^{19} \text{ cm}^{-3}$ which results in an exchange interaction lowering of the ground state by 0.030 eV as shown in Figure 5-15.

A number of other samples were grown on Si[001] substrates and then examined experimentally. They produced results very similar to the samples just presented. Since the purpose of growing and examining Si[001] samples was to gain confidence in the growth and experimental techniques before moving on to Si[110] samples no further Si[001] data will be presented here.

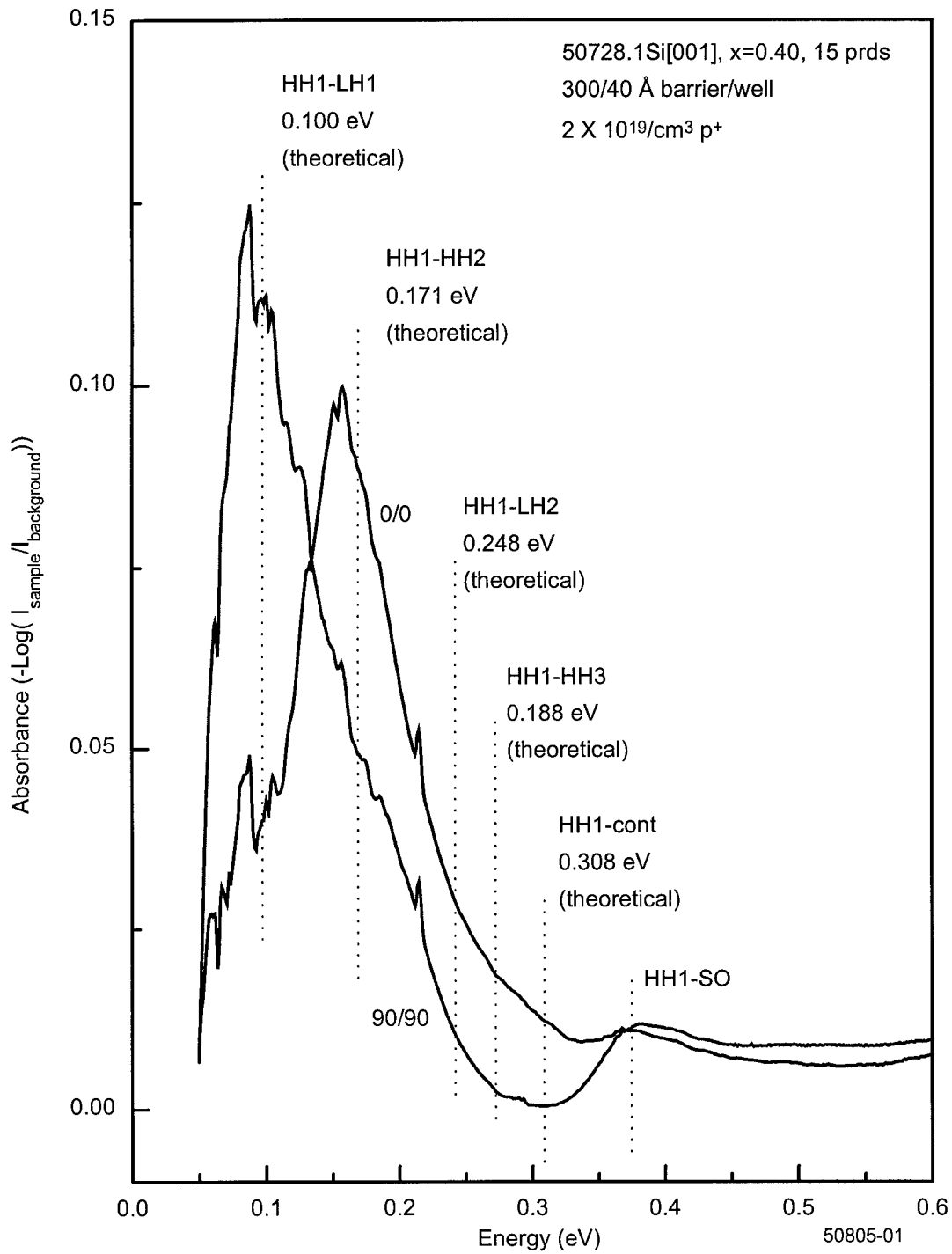


Figure 5-14. Absorbance spectra of NRL sample 50728.1 using substrate referencing background subtraction.

$x=0.40, L = 40 \text{ \AA}$.

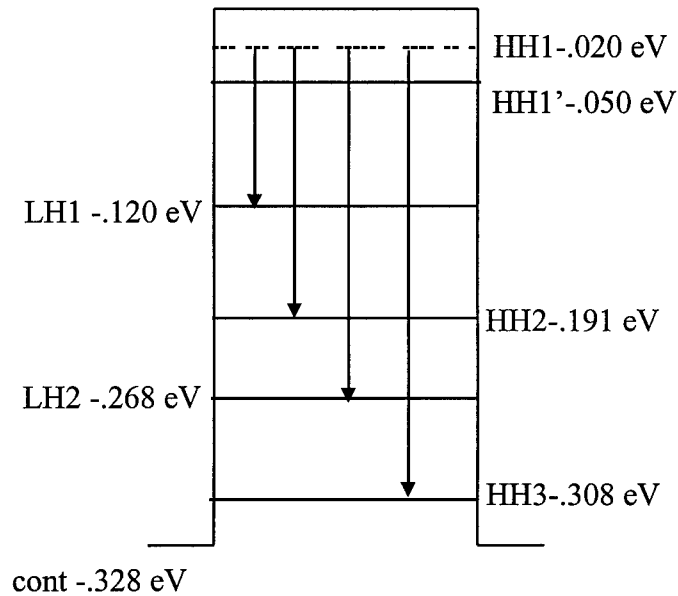


Figure 5-15. Schematic drawing showing the EFA zone center energies and possible transitions for a Si[001]/Si_{0.60}Ge_{0.40}, 40 Å well MQW structure. The shifted position of HH1 due to the exchange interaction effect is indicated by the dashed line.

3. [110] Absorption Data

The waveguide fabrication and measurement process for Si[110] samples was carried out in a manner identical to that used for the Si[001] samples. However, absorption measurements on MQWs grown on Si[110] substrates have been more difficult to interpret. Because of the nature of the band structure for [110] material, the HH1-HH2 transition which was very strong for Si[001] MQWs, generally occurs at wavelengths greater than 12 μm for the [110] samples studied in this research. At this wavelength, the transition is usually buried under the free-carrier absorption. (see Figure

4-14) It is also true, as indicated by the theoretical results, that for materials grown in the [110] direction, many more bound states exist in the well due to the increased heavy hole effective mass, and so the absorption might occur between many closely spaced bands with no single peak dominating as is the case with the [001] materials. As stated previously in Chapter 3, most all transitions are allowed because the selection rules break down in Si[110] due to the band mixing (see Figure 3-18), thus making identification of individual peaks very difficult. Figure 5-16 shows the absorbance spectra for a Si[110]/Si_{0.70}Ge_{0.30}, 30 Å well MQW sample where as many as seven transitions are allowed compared to three for a structure with identical parameters grown on a Si[001] substrate. The dashed lines in Figure 5-16 and the schematic diagram in Figure 5-17 indicate EFA calculated values at zone center. As mentioned previously, the zone center energies only indicate the general energy position of a transition. Due to anisotropies in k -space, the difference between energy levels changes as a function of $k_{||}$. The actual absorption spectrum is a superposition of many broadened transitions. Because the doping level is so high at $2 \times 10^{19}/\text{cm}^3$, the next highest bands, which are LH1 and HH2, are partially populated, thus also allowing transitions from these states. The population of this state is determined by the position of the Fermi energy which in this case is around 100 meV using the approximation method discussed in Chapter 3. Since LH1 and HH2 are only partially populated, it is assumed that the exchange lowering effects are minimal. A qualitative analysis of this spectrum points out the absolute necessity of performing the EFA theoretical calculations. Without them the correct number of bound states would be

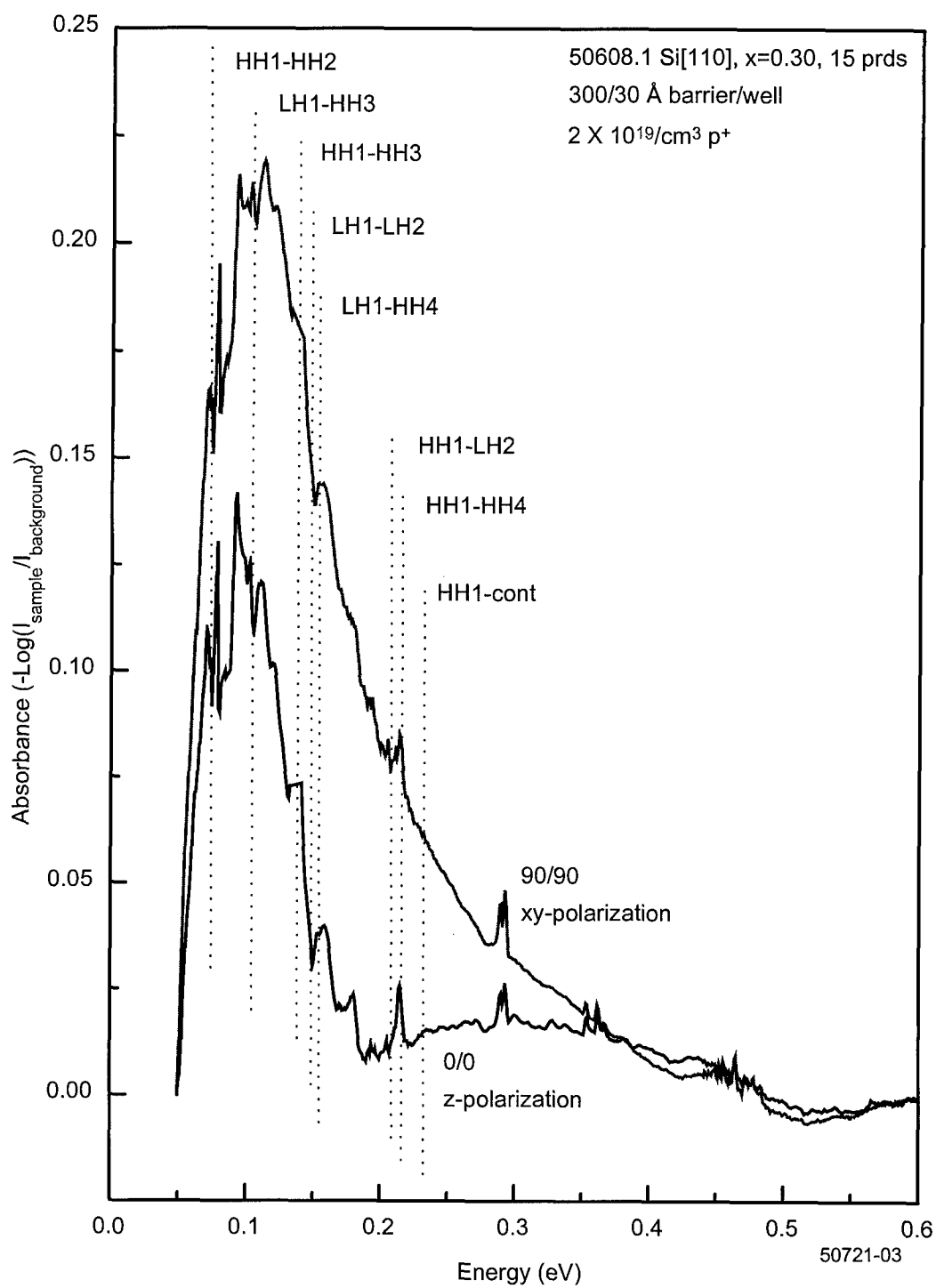


Figure 5-16. Absorbance spectra for a Si[110]/Si_{0.70}Ge_{0.30}, 30 Å well MQW structure with 15 periods. Sample grown via MBE at 550 °C.

$x=0.30, L = 30 \text{ \AA}$.

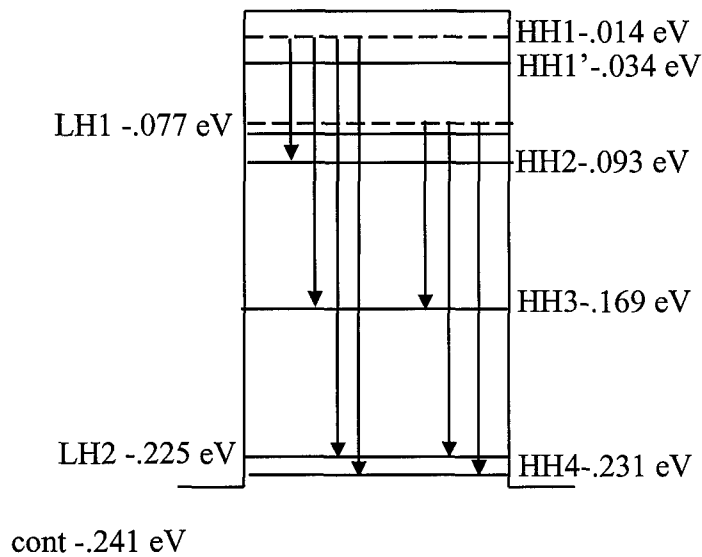


Figure 5-17. Schematic drawing showing the zone center band energies and possible transitions for a Si[110]/Si_{0.70}Ge_{0.30}, 30 Å well MQW structure. The shifted position of HH1 due to the exchange interaction effect is indicated by the dashed line.

underestimated. From the model one learns that a large number of possible transitions are allowed. Furthermore, the transition energy changes with parallel momentum and the transitions themselves are broadened. The effect of the heavy doping which causes LH1 and HH2 to can be approximated because the Fermi level can be estimated. In Figure 3-18 the plots of the momentum matrix elements show that in general, xy-polarized light should induce greater absorption. In particular the higher energy transitions, HH1-HH4 and HH1-LH2, are larger which is why the 90/90 absorption curve is broader on the high energy side.

Figure 5-18 and Figure 5-19 show a similar set of spectra and schematic diagram for a Si[110]/Si_{0.70}Ge_{0.30}, 20 Å well MQW structure with 20 periods. X-ray analysis of the 20 Å sample performed at NRL indicates the sample growth parameters were as intended.¹⁰⁴ This sample is doped at $1 \times 10^{19}/\text{cm}^3$ which puts the Fermi energy around 100 meV. Once again, the effect of band mixing is to cause the selection rules, to break down, and so almost all transitions are allowed to varying degrees for both normal and parallel incidence. Even though the well depth is the same as for the previous sample, the smaller well width causes the ground state to be more than 40 meV higher in the well. As a result the absorption should occur over a smaller range of energies. In particular, the 20 Å sample should not have the same response at shorter wavelengths or higher energies. This is confirmed by the experimental data shown in Figure 5-20. This figure shows the 90/90 (xy-polarization) data from the previous two plots where the FWHM for the 30 Å sample is approximately 50 meV wider than the 20 Å sample on the high energy side.

Many other absorption spectra have been taken for MQWs grown on Si[001] and Si[110] with results similar to those just presented. Generally, Si[001] MQWs exhibit a dominant HH1-HH2 transition under z-polarization and a weaker HH1-LH1 transition under xy-polarization. This occurs because the selection rules are more rigid and fewer bound states exist when compared to Si[110] structures. In contrast, the spectra for the Si[110] MQWs show few dominant features. This happens for many reasons. Because the selection rules are relaxed, more transitions are allowed. The high doping levels present in these samples caused higher energy states to become occupied

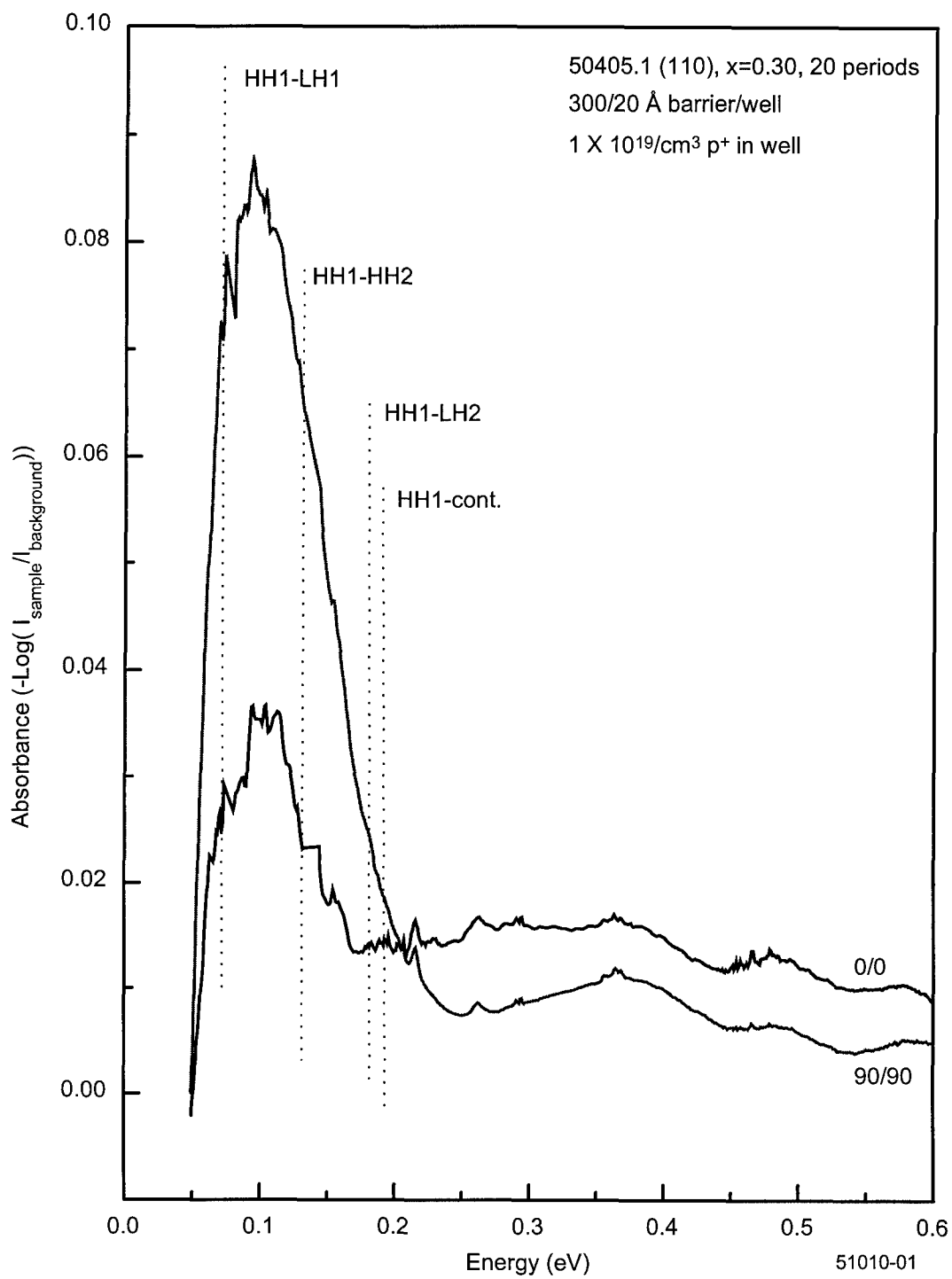


Figure 5-18. Absorbance spectra for a Si[110]/Si_{0.70}Ge_{0.30}, 20 Å well MQW structure with 20 periods. Sample grown via MBE at 550 °C.

$x=0.30, L = 20 \text{ \AA}$.

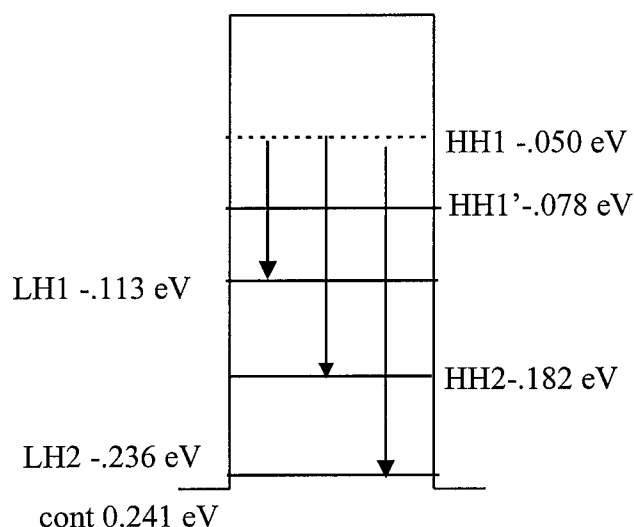


Figure 5-19. Schematic drawing showing the band structure and possible transitions for a Si[110]/Si_{0.70}Ge_{0.70}, 20 Å well MQW structure. The shifted position of HH1 due to the exchange interaction effect is indicated by the dashed line.

from which transitions can then occur. In addition, at the high doping levels, states farther out in the zone are occupied. The band structure farther out in the zone is highly non-parabolic and anisotropic. Such factors can lead to more allowed transitions and higher probabilities. The combined effect is to produce broad spectra with many overlapping peaks that cannot be resolved. For many months it was assumed that the Si[110] samples were poor or the measurement technique was inadequate because a broad featureless peak appeared in contrast to the single dominant peak that appeared under z-polarization in the Si[001] samples. This was clarified by the $\mathbf{k}\cdot\mathbf{p}$ calculations on the [110] material.

Whereas theory would predict a dominant transition for [001] material, such is not

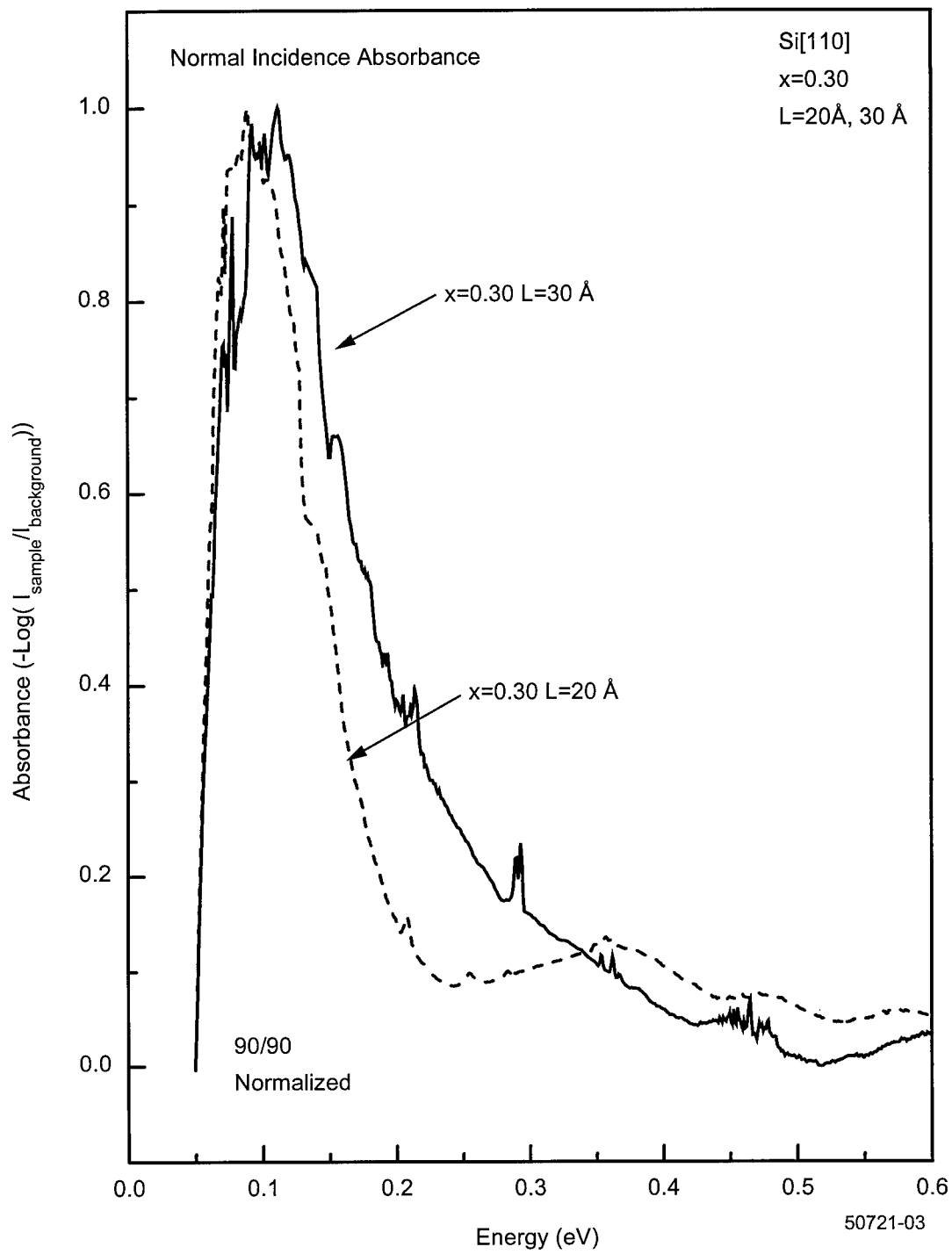


Figure 5-20 Normalized absorbance spectra for two samples with a constant germanium composition of 30 percent and well widths of 20 Å and 30 Å.

necessarily true for [110] material, and in fact, is probably not to be expected. The result is an absorption behavior of Si[001] samples and Si[110] samples which is dramatically different.

Since the ultimate goal of this research was not absorption measurements, but to determine if a silicon based QWIP was feasible, it is important to consider photoresponse at this point. Further absorption data will be presented along with the photoresponse data.

D. Photoresponse

1. Shifting the responsivity range

Although for detectors, it is desirable to obtain a detectivity or D^* measurement, photoresponse is one of the primary measurements for determining the usefulness of SiGe MQWs as a detector. To that end, a wide parameter space (see Appendix E), for MQWs grown on both Si[001] and Si[110] substrates, has been explored through photoresponse to find a structure responsive in the 3-12 μm range. To reiterate, photoresponse represents the current created by photo-excited holes. The holes are excited from an occupied state in the quantum well to a state just at the well edge or a state in the 2-D continuum of unbound levels out of the quantum well. They are subsequently swept away when the quantum wells are biased. Photoresponse can occur only to the extent that absorption occurs to excite the holes, and thus the photoresponse and absorption measurements should be consistent with each other.

One of the primary motivating factors for developing QWIPs over other device designs is that QWIPs allow the frequency response range to be tuned by varying the quantum well depth *and* width. The response frequency for HIP structures can also be tuned by varying the band offset which is similar to changing the well depth. However, because HIPs are generally fabricated with a single heterojunction, the frequency response cannot be tuned by changing the epilayer thickness. Therefore QWIP structures have much more flexibility to tune over a desired response range. Just as in the case of absorption, calculations based on the theoretical models developed in Chapter 3 (EFA

approximation) can be used to predict how the photoresponse will shift with different growth parameters. In particular, the calculations as they presently exist are used to predict the energy at which the onset of photoresponse will occur. The peak position and the FWHM can be estimated from experimental data with a semiempirical calculation. Unfortunately, the exact shape of the photoresponse curve and the peak position can only be predicted if the continuum wave functions are known. However, as was stated in Chapter 3, at the present time they have not been calculated because they were beyond the scope of this project.

It is desirable to operate detectors at LN temperatures, around 77 K, to avoid the great cost and complexity of operating at lower temperatures with special cryogenic equipment. Therefore most of the experimental photoresponse data in this research was taken at 77 K. All the photoresponse data was taken under the condition of normally incident, unpolarized light, and a 1 volt bias was used unless otherwise indicated. Unfortunately, large absorption lines from the KBr beamsplitter in the FTS system and the ZnSe window mounted on the Helitran vacuum chamber assembly are present and are visible in the photoresponse data as narrow dips..

To verify the photoresponse experimental technique described in Chapter 4, a measurement was performed on a GaAs/AlGaAs MQW sample, provided by Dr. Gail Brown of the Wright Laboratory, on which data was published in the literature.¹⁰⁵ The spectrum shown in Figure 5-21 was produced by that sample, and it agrees very well with

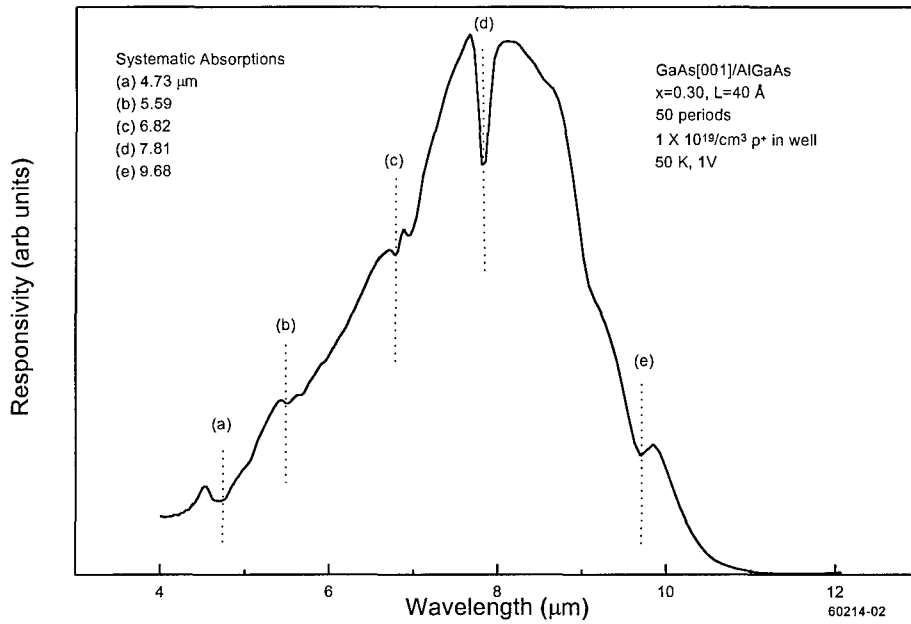


Figure 5-21. Photoreponse spectrum of a GaAs/Al_{0.30}Ga_{0.70}As MQW with a well width of 40 Å taken at 50 K. Used to verify experimental technique.

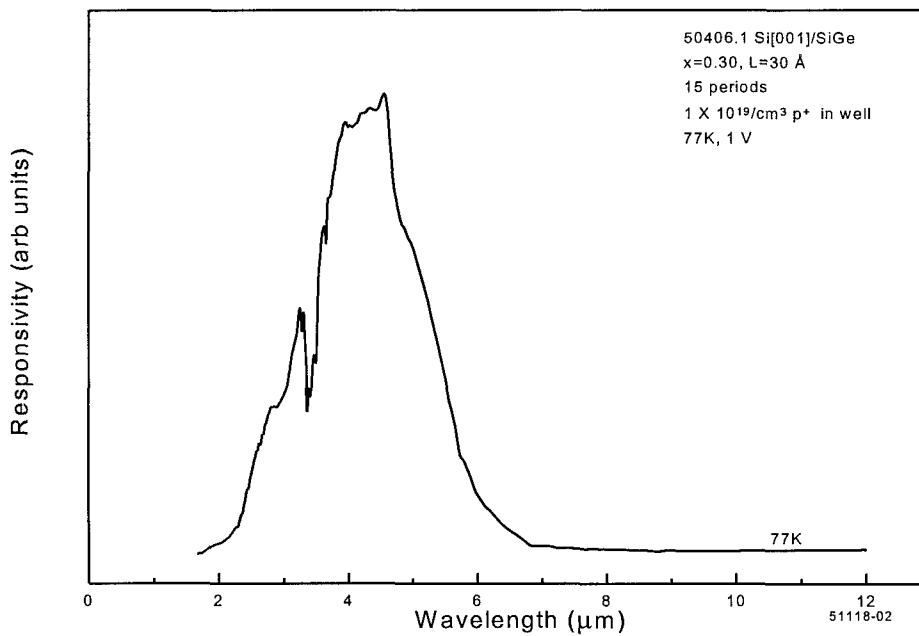
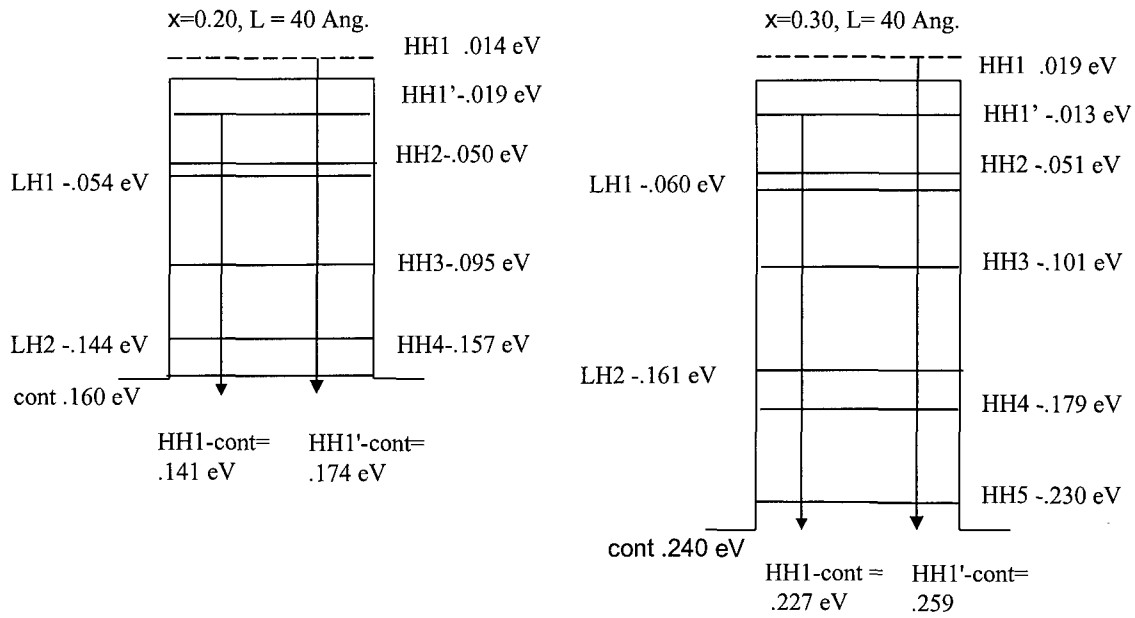


Figure 5-22. Typical photoreponse spectrum of a Si[001]Si_{0.70}Ge_{0.30} MQW with a well width of 30 Å taken at 77 K under normal incidence illumination.

the published data which indicates a proper measurement technique. The data was collected under normal incidence illumination at 50 K with a 1 volt bias across the MQWs. (Refer to Figure 4-5.) Figure 5-22 shows a typical photoresponse spectrum for a Si[001]/Si_{0.70}Ge_{0.30} sample taken at 77 K under normal incidence. The details of the experimental technique are found in Chapter 4. Once again, the sharp dip at 3.5 μm is due to large absorption lines from the KBr beamsplitter in the FTS system and the ZnSe window mounted on the Helitran vacuum chamber assembly.

The ability to tune the photoresponse has been a prime consideration of this research. One way to tune the response is to vary the quantum well depth. This will shift the position of the ground state with respect to the continuum level which will in turn shift the long wavelength cutoff. Schematic diagrams showing the zone center energy positions for varying well depths at a constant well width of 40 \AA are shown in Figure 5-23. Remember that a higher Ge concentration results in a larger valence band offset which means a deeper well. Figure 5-24 shows a combined absorbance and photoresponse plot for a 20 percent sample with a 40 \AA well width. The bound to bound transitions as predicted by the theoretical calculations using zone center EFA energy values (including exchange interaction effects) are indicated by the dotted lines. The experimental absorption spectrum represents both bound-to-bound transitions as well as free-to-bound transitions. It is rather broad and shows no distinguishing details. The photoresponse curve represents only free-to-bound transitions. As mentioned previously, the photoresponse curve should overlap the absorption curve for transitions out of the



(110) Si substrate

Figure 5-23. Schematic diagram for position of zone center energy levels in a Si[110]/SiGe QW with a constant well width of 40 Å and Ge concentration of 20 and 30 percent.

well because photoresponse cannot occur unless absorption takes place to continuum levels. As shown, the photoresponse curve has been magnified to show more detail. The dotted curve is the actual data, the solid curve is a numerical fit. This fit is done since many of the dips in the photoresponse spectrum are associated with absorption peaks in the beamsplitter and ZnSe window and are therefore systematic. As a result a two-Gaussian curve fit was performed to eliminate the dips. The fit works well except at the onset of the photoresponse where it overestimates. Using the schematic diagram in Figure 5-23 as a reference, the photoresponse for the 20 percent sample should begin to appear at 0.141 eV, i.e. at the point at which the photon energy equals the energy difference between the populated ground state and the zone center continuum level.

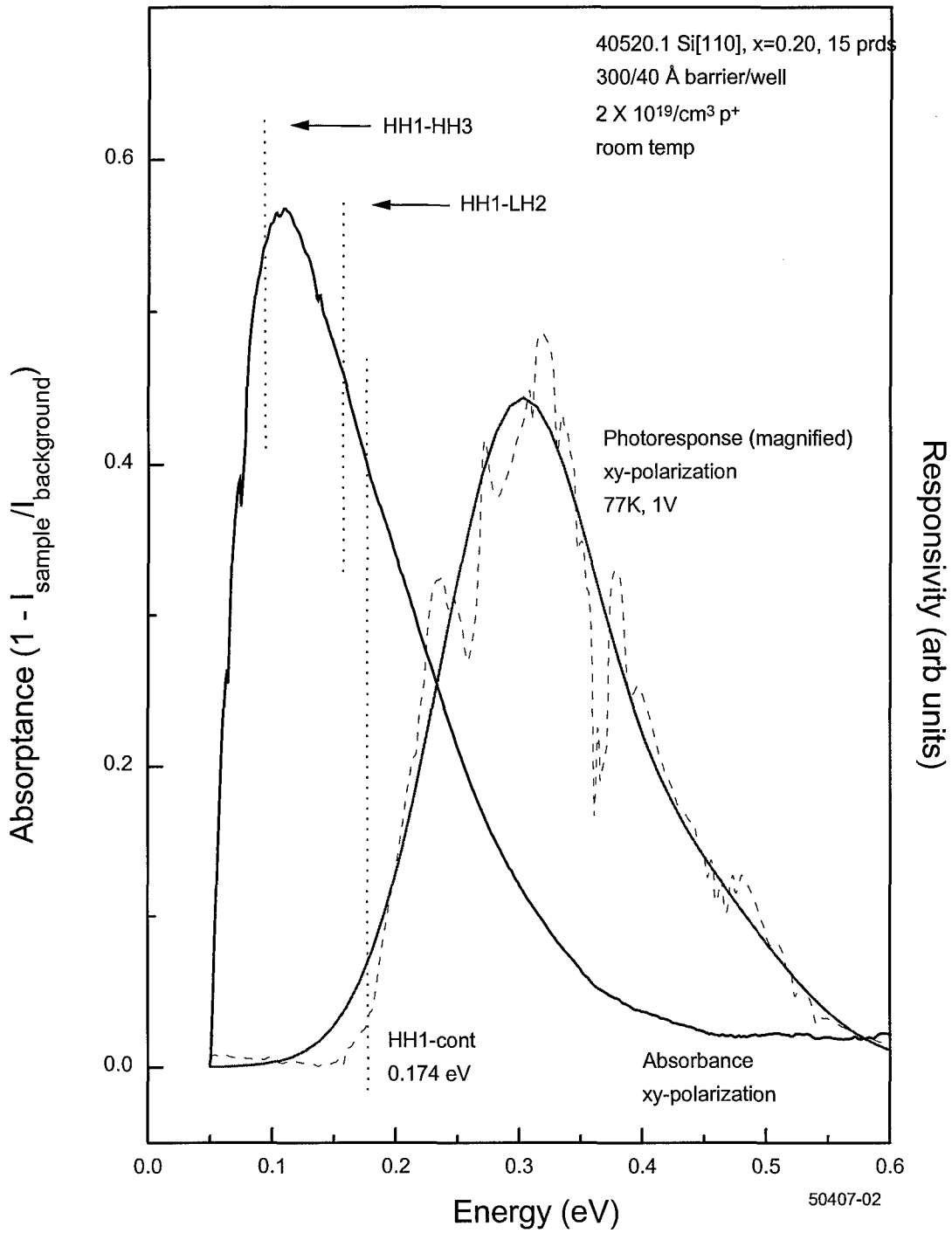


Figure 5-24. Combined absorbance and photoresponse spectra for a Si[110]/Si_{0.80}Ge_{0.20} MQW with 40 Å well width. The photoresponse has been enlarged to show detail.

Holes making transitions to levels significantly below this energy will not be excited out of the well and therefore will not contribute to the photocurrent. Looking at the experimental data in Figure 5-24, it is obvious that the prediction is close but not close enough. Because the doping level in the sample is very high at $2 \times 10^{19}/\text{cm}^3$, it is again imperative to make a correction for the exchange interaction on the ground state which causes a shift in the band. The exchange interaction can be calculated numerically using the method of Choe *et al.*,¹⁰¹ as was done for the absorption measurements. The new position of the ground state is indicated on the schematic diagram as HH1. Looking at the experimental data, the intensity begins to rise at the energy designated at the dotted line as the HH1-cont.

Using a similar analysis, the photoresponse for a Si[110]/Si_{0.70}Ge_{0.30} MQW with a 40 Å well width should begin to appear at 0.259 eV. Looking at Figure 5-25 which shows spectra for such a sample, this prediction is very accurate. Because this sample has a deeper well, it should have a shorter wavelength or higher energy response than the 20 percent sample which is shown in the previous figure. The photoresponse spectrum has a shoulder on the high energy side, the reason for which is not known. It is possible that the shoulder represents transitions to a resonant state in the continuum.

Figure 5-26 shows the combined photoresponse plots for the previous two samples. The FWHM for the 20 percent sample is 0.189 eV and the peak position is 0.129 eV from the continuum edge. For the 30 percent sample, the FWHM is 0.186 eV and the peak position is 0.146 eV from the continuum edge. The data in this figure

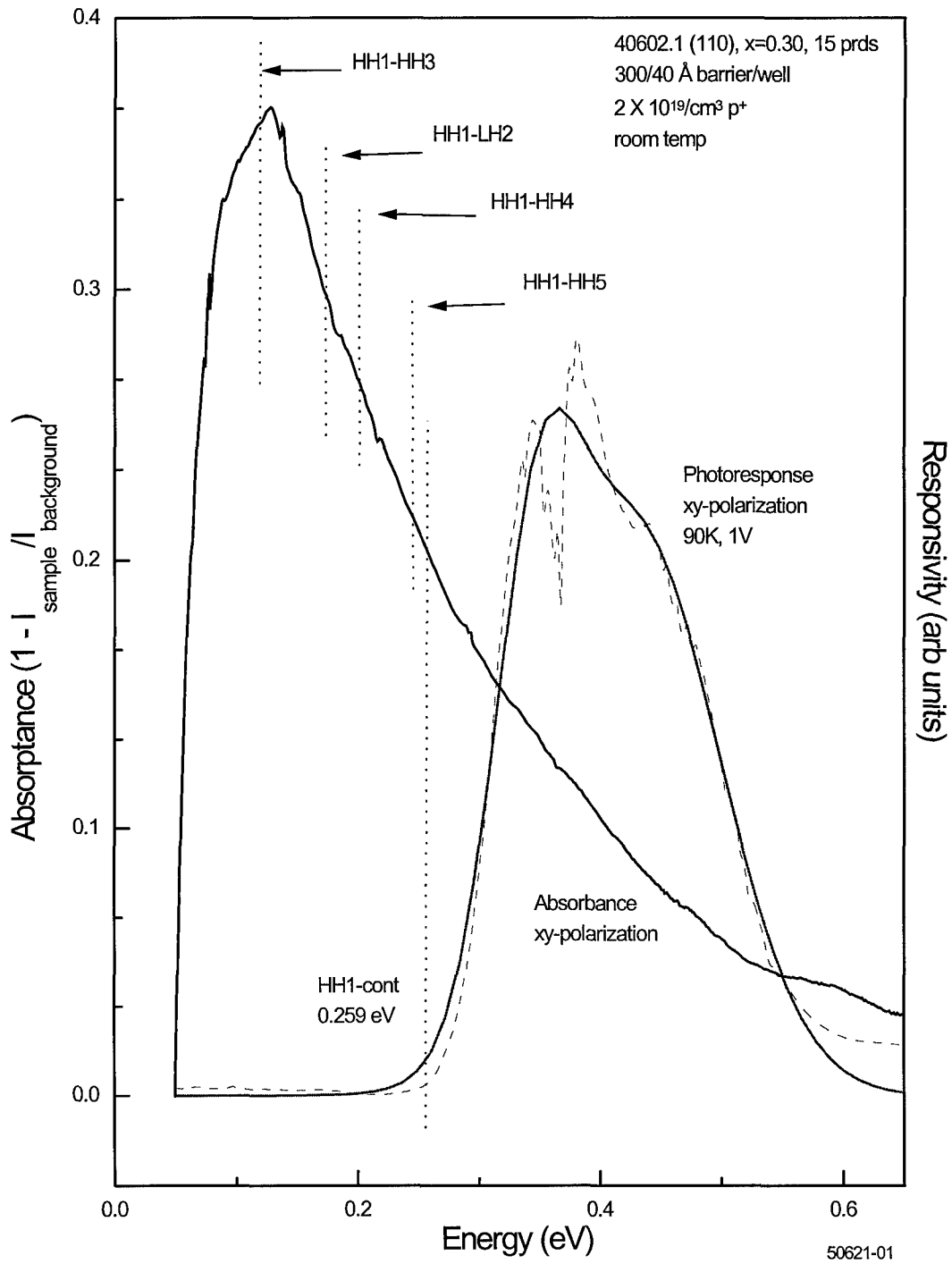


Figure 5-25. Combined absorbance and photoresponse spectra for a Si[110]/Si_{0.70}Ge_{0.30} MQW with 40 Å well width. The photoresponse has been enlarged to show detail.

confirms that the response range can be tuned by varying the well depth. When changing the Ge concentration from 20 percent to 30 percent, the peak position shifts 0.1 eV or moves the peak response from 4 μm to 3 μm .

The range of responsivity can be similarly varied by changing the well width for a constant well depth. The schematic diagrams in Figure 5-27 show that for a given constant well depth, the position of the ground state will fall deeper in the well with the increasing well width, and more bound states will exist. Using the zone center energies depicted in the diagram, photoresponse should begin to rise at 0.191 eV, 0.235 eV, and 0.259 eV for the 20 Å, 30 Å, and 40 Å well widths respectively after exchange interaction correction. The theoretical predictions for the onset of the photoresponse thus show excellent agreement with the experimental data shown in Figure 5-28, Figure 5-29, and Figure 5-30. These figures show absorption and photoresponse for samples identical in every way except for well width and sheet carrier concentration. Consider again the schematic energy diagrams for these samples. Because the ground state is deeper in the well for increasing well width, higher energy transitions are possible. As a result, the absorption will be larger on the high energy side for increasing well width. This is confirmed in the combination plot shown in Figure 5-31. Not only does the width increase, but the overall absorption strength increases. This may be because the sheet carrier density decreases from $8 \times 10^{12}/\text{cm}^2$ to $6 \times 10^{12}/\text{cm}^2$ and to $4 \times 10^{12}/\text{cm}^2$ for 40 Å, 30 Å, and 20 Å respectively. The photoresponse should show an identical shift with well width for the same reason the absorption shifts, as seen in Figure 5-32. Just as expected,

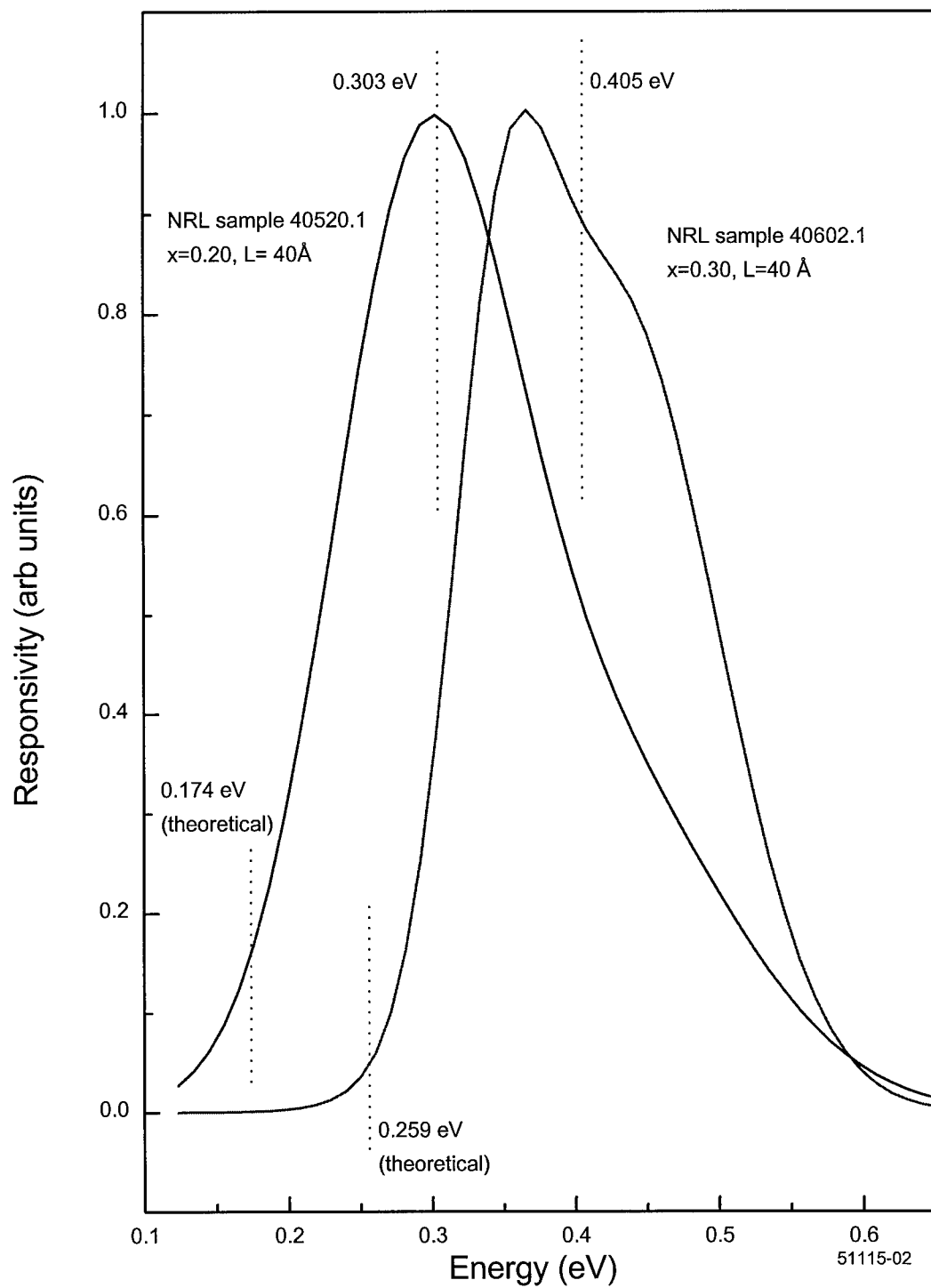


Figure 5-26. Photoresponse spectra (normalized) of 2 (110) Si/SiGe MQW samples with constant well width of 40 Å and Ge compositions of 0.20, and 0.30. Data was taken at normal incidence at 77 K, 1 V bias.

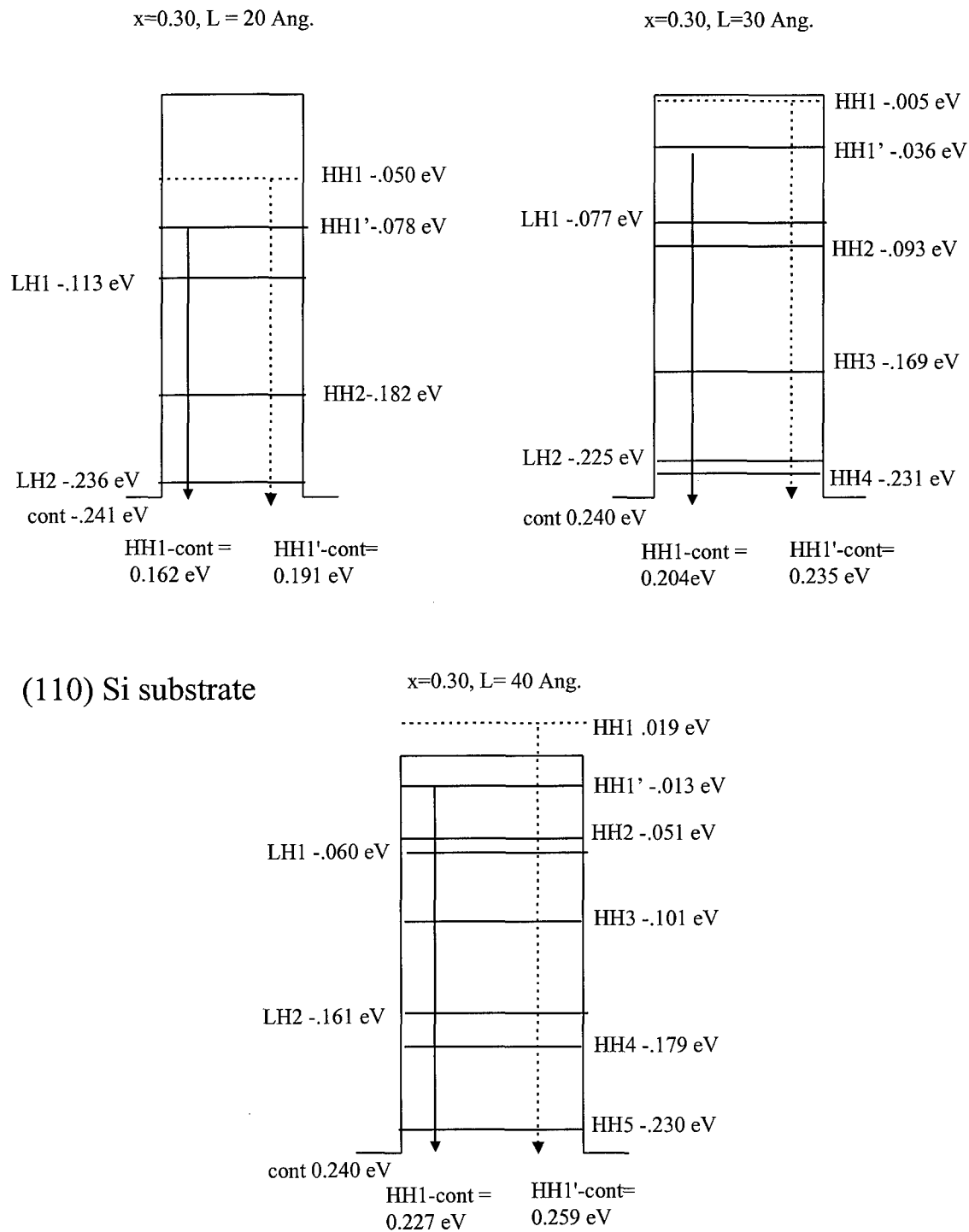


Figure 5-27. Schematic diagram for position of the EFA zone center energy levels in a Si[110]/SiGe QW with a constant Ge percentage of 30 percent and well widths of 20 Å, 30 Å and 40 Å.

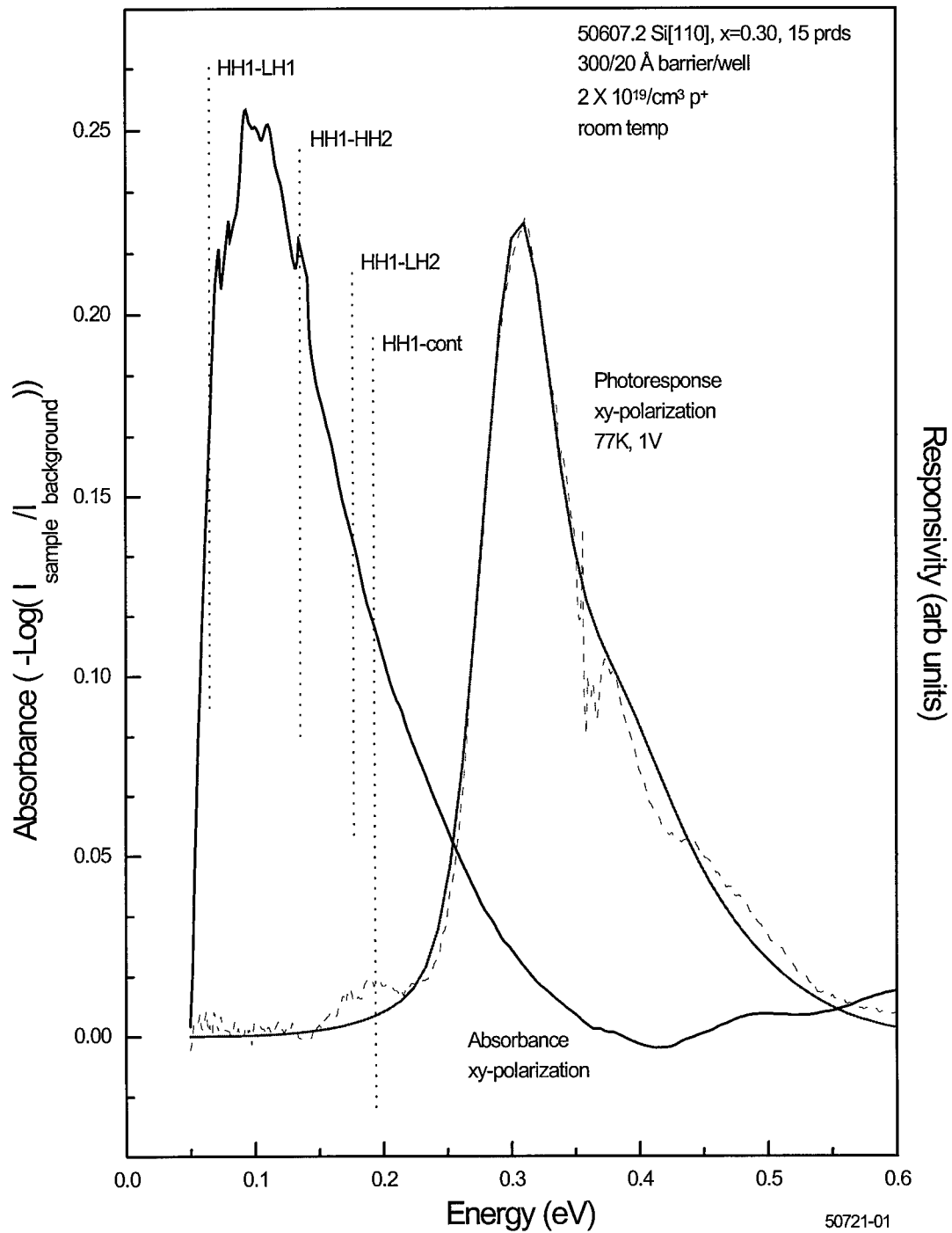


Figure 5-28. Combined absorbance and photoresponse spectra for a Si[110]/Si_{0.70}Ge_{0.30} MQW with 20 Å well width. The photoresponse has been enlarged to show detail.

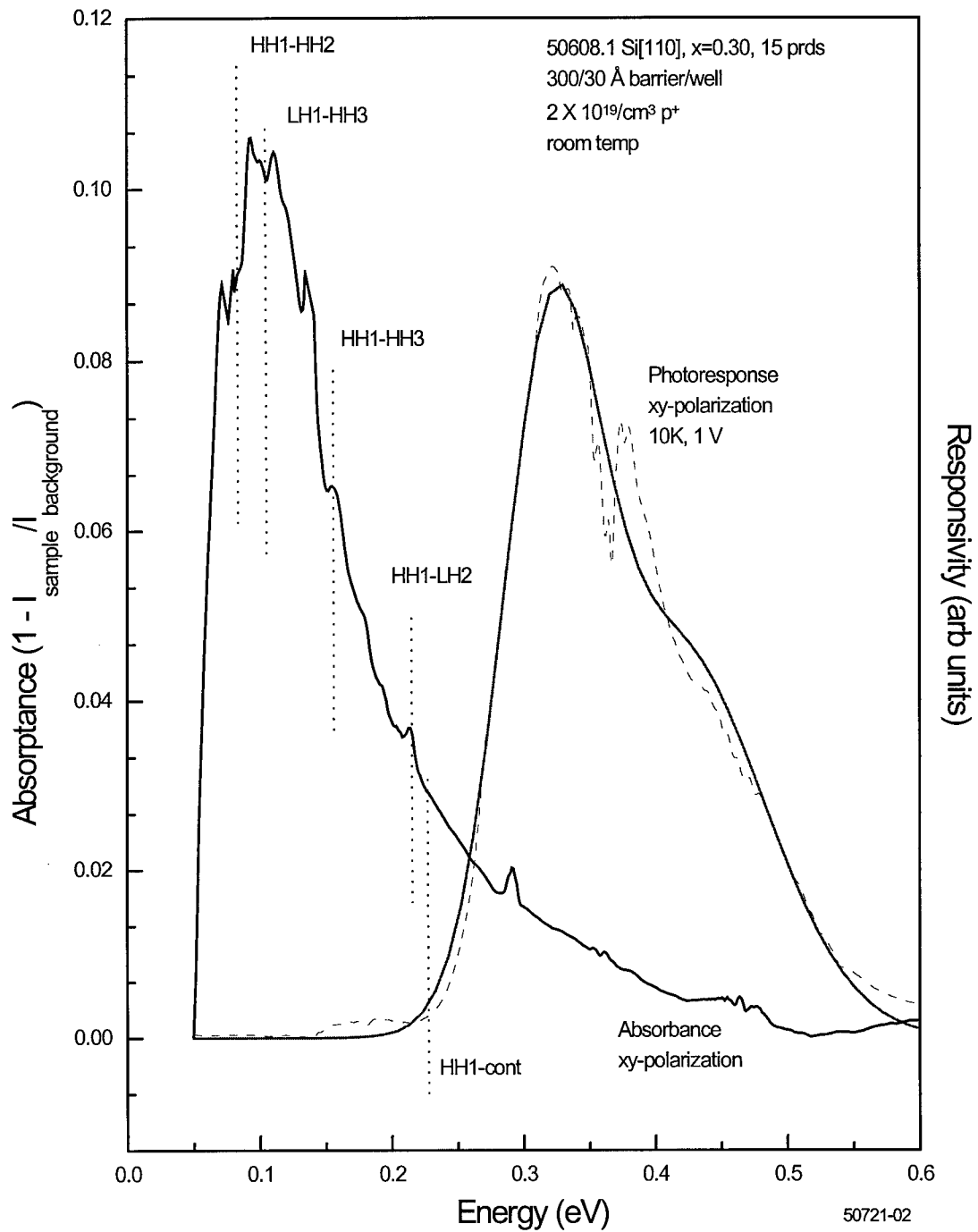


Figure 5-29. Combined absorbance and photoresponse spectra for a Si[110]/Si_{0.70}Ge_{0.30} MQW with 30 Å well width. The photoresponse has been enlarged to show detail.

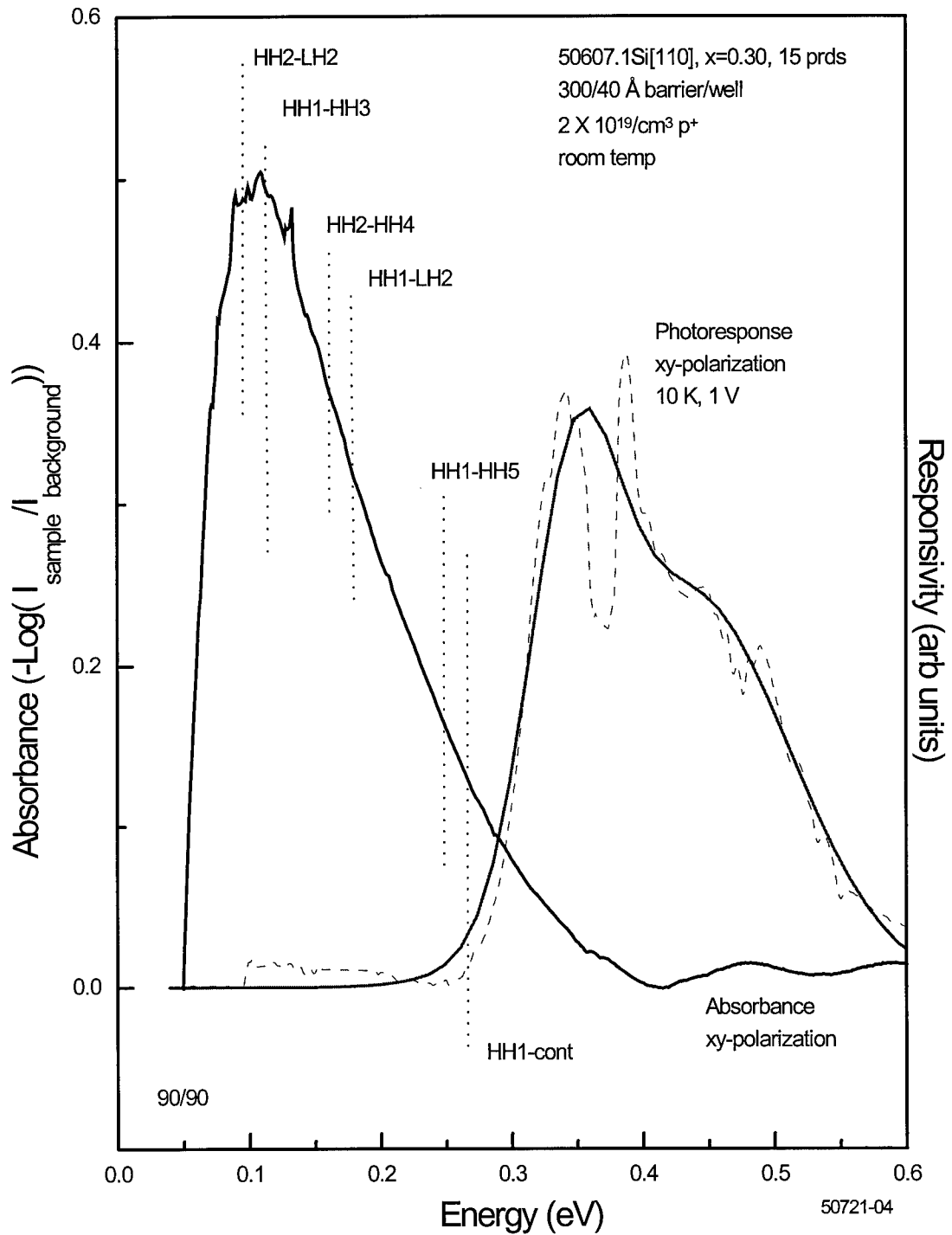


Figure 5-30. Combined absorbance and photoresponse spectra for a Si[110]/Si_{0.70}Ge_{0.30} MQW with 40 Å well width. The photoresponse has been enlarged to show detail.

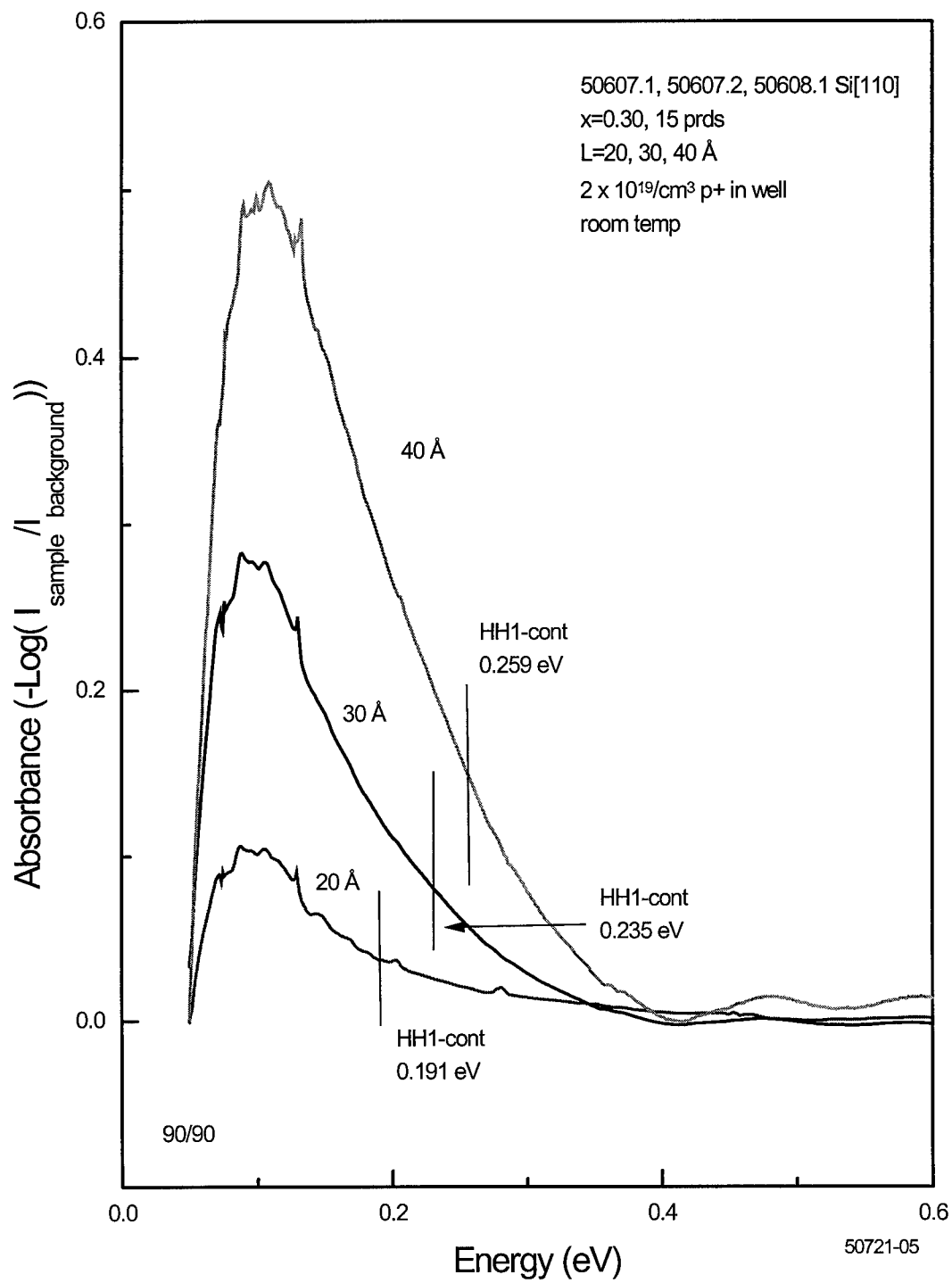


Figure 5-31. Absorbance spectra of 3(110) Si/SiGe MQW samples with a constant well depth and well widths of 20, 30, & 40 Å. Data taken in waveguide configuration, substrate referenced.

the photoresponse shifts to higher energies with increasing well width. In addition, a shoulder on the high energy side grows with increasing well width. The FWHM is 0.152 eV, 0.171 eV, and 0.176 eV for 20 Å, 30 Å, and 40 Å respectively. The peak position is 0.122 eV, 0.146 eV and 0.139 eV from the predicted HH1 to continuum energy. Using the data from the five previous samples considered, the FWHM is approximately 0.175 eV with a standard deviation of 0.013 eV, and the peak position is 0.138 eV from the continuum edge with a standard deviation of 0.009 eV. This is admittedly a small sample set, but the semiempirical model is useful to make rough predictions. From this plot it is also demonstrated that the frequency response can be tuned as a function of well width.

A third way to vary the responsivity range is to change the doping level. The ground state energy band is filled with holes to a greater degree with increasing doping thus increasing the energy range or the k_{\parallel} range of the populated hole states as illustrated in Figure 5-33. Holes occupying higher states in the band are excited into the continuum by lower energies photons. Another by-product of higher doping is the possible population of the next highest states as indicated in the diagram. Holes in these states are also excited into the continuum by lower energy photons. As a result, higher doping will introduce an increase in the spectral band of response on the long wavelength side as shown in Figure 5-34. The short wavelength side will be minimally affected, the difference being due to many-body and exchange correlation effects.

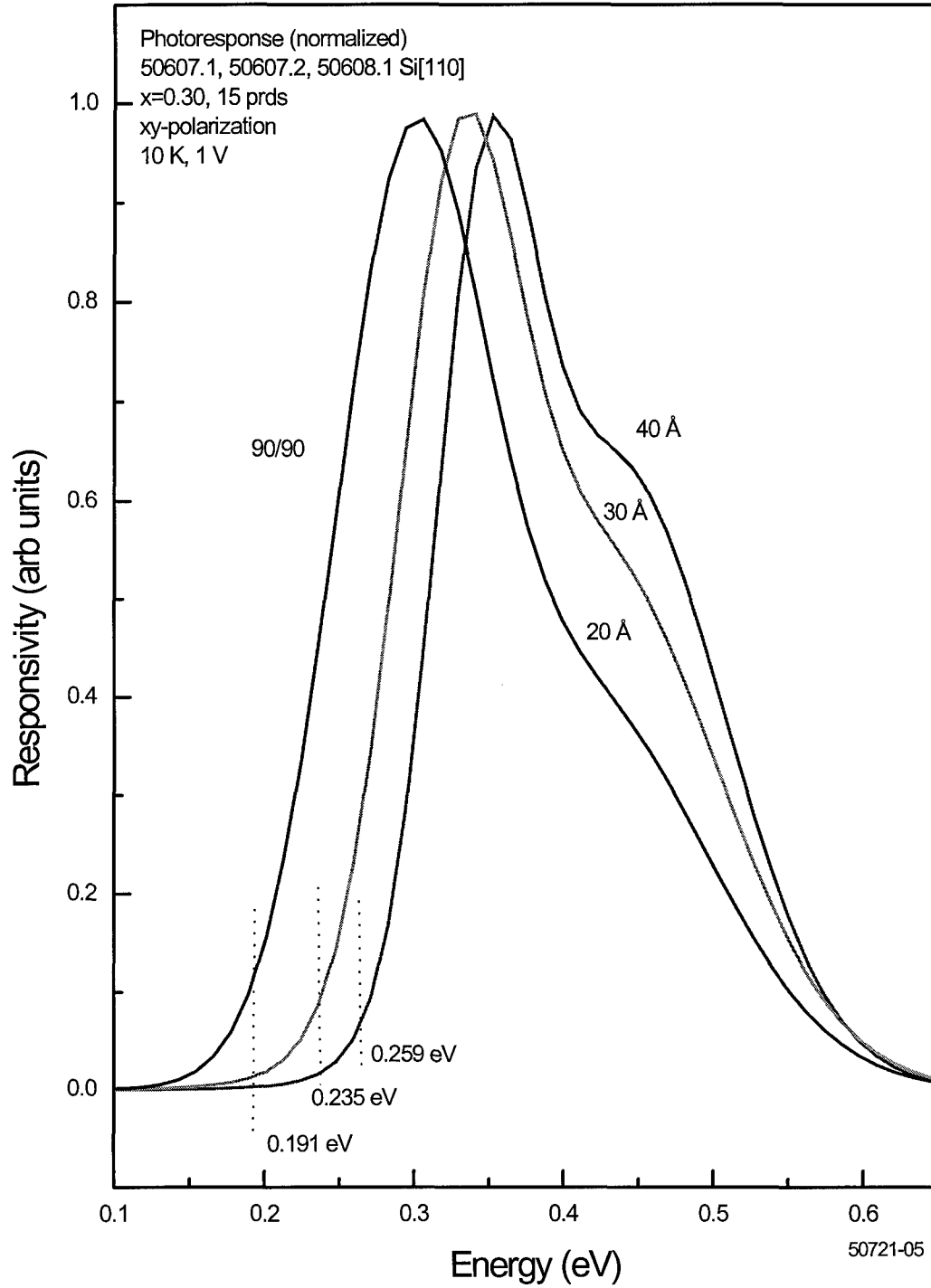


Figure 5-32. Photoresponse spectra (normalized) of 3(110) Si/SiGe MQW samples with a constant well depth and well widths of 20, 30, & 40 Å. Data taken at normal incidence at 77 K and 1 V bias.

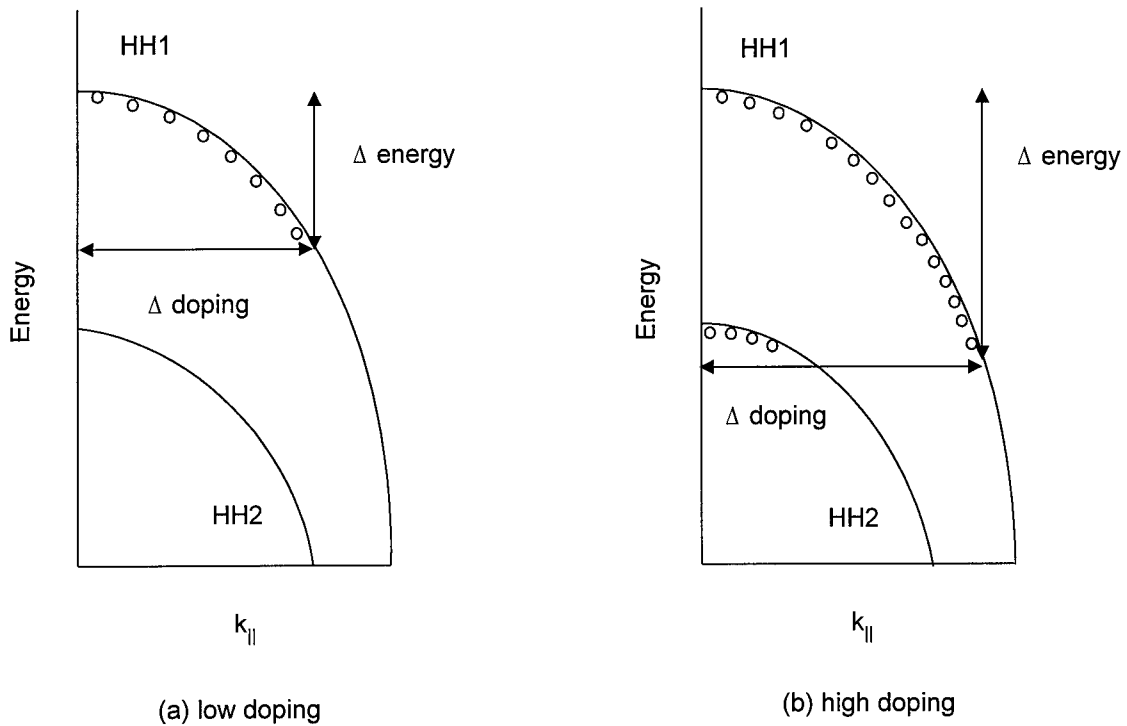


Figure 5-33. Schematic drawing show effect of doping level on energy range of holes.

2. Phenomenological Effects

a) *Variation of photoresponse with sample temperature*

The remainder of this chapter is devoted to exploring the effects of various parameters on the photoresponse in a phenomenological way. These parameters were explored to determine the optimum operating conditions for such a detector and to determine the best way to grow SiGe MQWs for use in detectors.

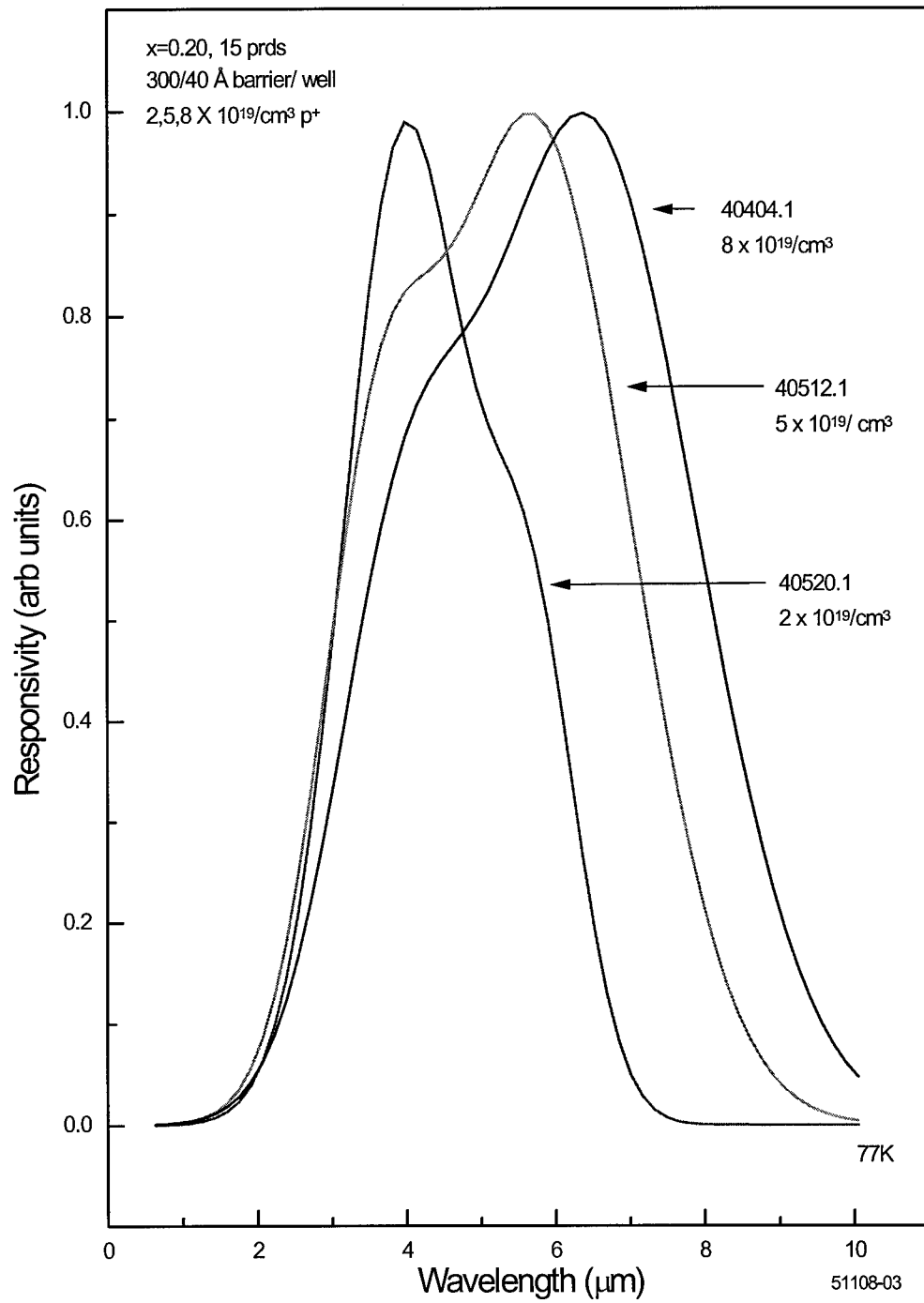


Figure 5-34. Photoresponse spectra (normalized) of 3(110) Si/SiGe MQW samples with $x=0.20$ and $L=40 \text{ \AA}$ and 3 doping levels. Data taken at normal incidence at 77 K.

As stated previously, it is desirable to operate detectors at LN temperatures around 77 K to avoid the great cost and complexity of operating at lower temperatures. So the majority of the photoresponse measurements were taken at 77 K, but photoresponse dependence on sample temperature was measured for many samples. Typical spectra for Ge composition greater than 0.15 are shown in Figure 5-35 where the response was measured on NRL sample 50405.1, ($x=0.30$, $L=20 \text{ \AA}$) at four different temperatures. Generally, only marginal signal gain is realized for temperatures below 60 K. For samples with shallow wells, or Ge composition less than 0.15, the temperature dependence is more evident. Figure 5-36 shows the temperature dependence for NRL sample 51213.2, ($x=0.10$, $L=30 \text{ \AA}$) at 20 K and 77 K. At this shallow well depth, approximately 80 meV, the holes can more easily obtain enough thermal energy at 77 K to be randomly excited out of the well, thus substantially reducing the number of carriers that can be excited optically. This dependence of the responsivity on temperature can be explained by considering a series of equations.¹⁰⁶ First, the peak responsivity can be expressed as

$$R = \frac{e}{h\nu} \eta p_e g \quad (5-2)$$

where η is the quantum efficiency, p_e is the escape probability and g is the optical gain.

The optical gain can be determined from the equation

$$g = \frac{i_n^2}{4eI_d \Delta f} \quad (5-3)$$

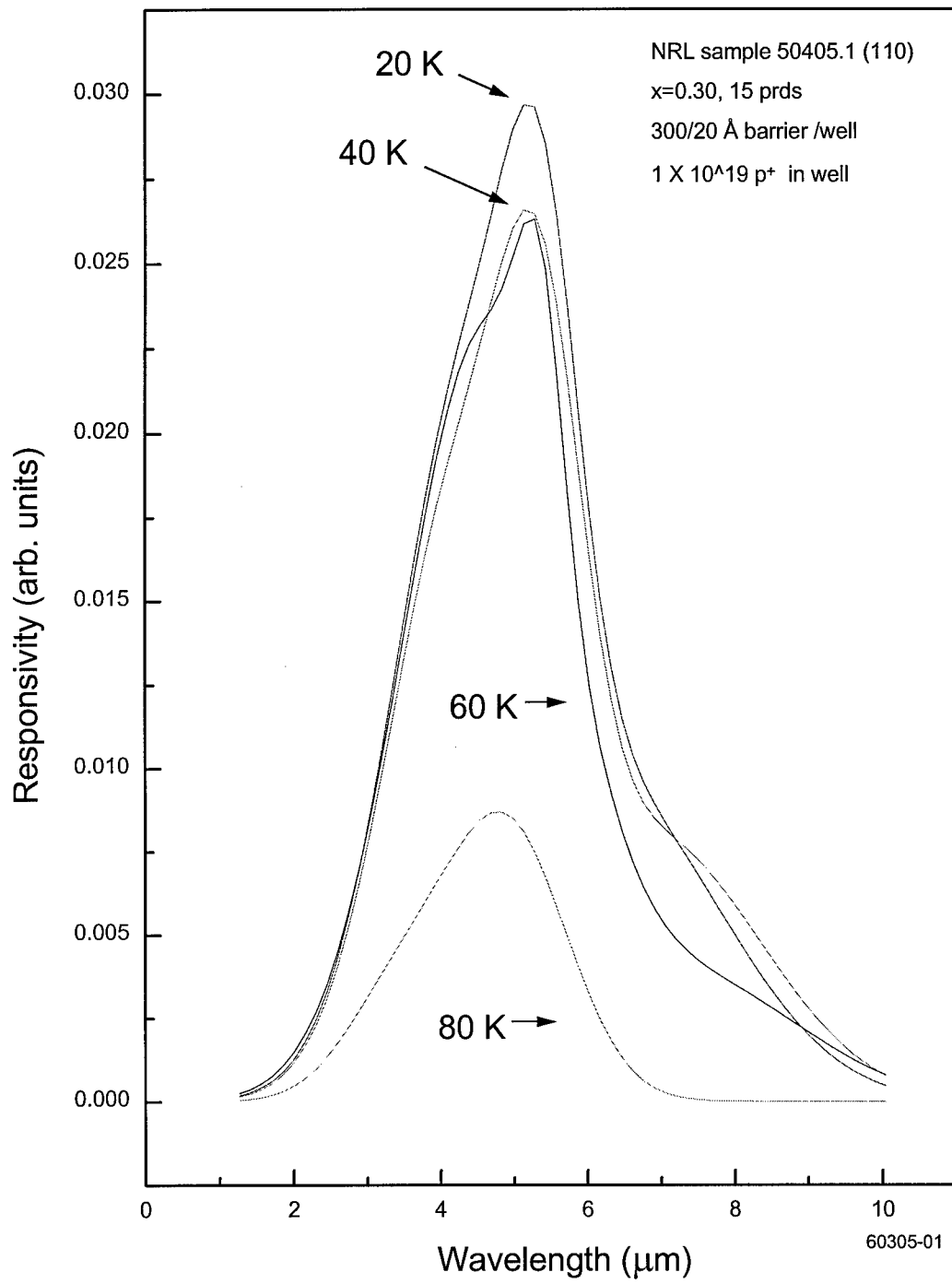


Figure 5-35. Photoresponse spectra of a (110) Si/SiGe MQW samples with $x=0.30$ and $L=20 \text{ \AA}$ at 4 different temperatures. Data taken at normal incidence.

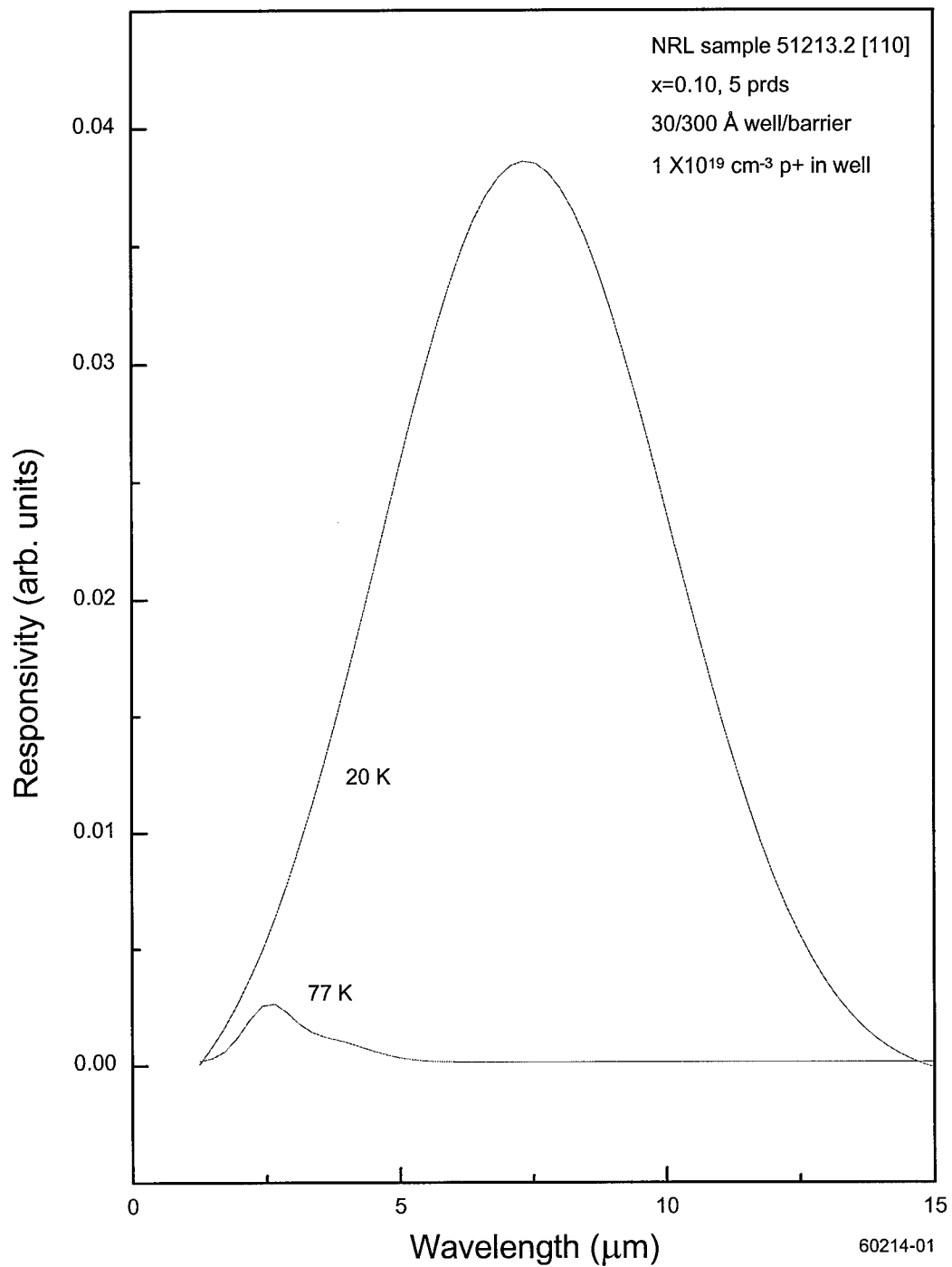


Figure 5-36. Photoresponse spectra of a (110) Si/SiGe MQW samples with $x=0.10$ and $L=30 \text{ \AA}$ at 2 different temperatures. Data taken at normal incidence.

where i_n^2 is the photoconductor current shot noise, I_d is the dark current, and Δf is the band width. Next, the dark current can be expressed as

$$I_d = n^* e v A \quad (5-4)$$

where n^* is the number of thermally generated carriers, v is the average transport velocity, and A is the device area. Finally, an expression for the number of thermally generated carriers can be written as follows;

$$n^* = \left(\frac{m^*}{\pi \eta^2 L_p} \right) \int_{E_1}^{\infty} f(E) T(E, V) dE \quad (5-5)$$

where m^* is the effective mass, L_p is quantum well period, $T(E, V)$ is the bias-dependent tunneling current transmission factor for a single barrier, and $f(E)$ is the familiar Fermi factor

$$f(E) = \left[1 + \exp(E - E_1 - E_F) / kT \right]^{-1}. \quad (5-6)$$

E_1 is the bound ground state, and E_F is the two-dimensional Fermi level. Combining these equations, one sees that the responsivity is inversely proportional to the number of thermally generated carriers which increases with temperature according to Fermi-Dirac statistics. The responsivity is more strongly affected by temperature with the shallower well precisely because it does not take much energy to create thermal carriers and so the dark current is rather high.

b) Variation of photoresponse with bias voltage

To enhance the number of optically-excited carriers collected by the device, several different voltages were placed across the mesa. (The bulk of the data was collected with a 1 volt bias from the top to the bottom of the mesa.) Figure 5-37 shows the change in photoresponse with respect to bias voltage. Only small differences were observed when the polarity was switched. The increase in intensity with increasing voltage is linear (see the inset in Figure 5-37). These results are in good agreement with the published results of Karunasiri.¹⁰⁷ If the expression for the optical gain in Eq 5-3 is written as

$$g = \left(\frac{v\tau}{l} \right) \quad (5-7)$$

where $v=v(E)$ is the drift velocity, τ is the transit time and l is the mean free path, the responsivity will scale linearly with the drift velocity until the drift velocity begins to saturate. The drift velocity scales according to the following

$$v(E) = \mu E / (1 + \mu E / v_s) \quad (5-8)$$

where μ is the mobility, E is the amplitude of the electric field and v_s is the saturated drift velocity.

c) Other Observations

Many other experimental parameters were explored with the result that

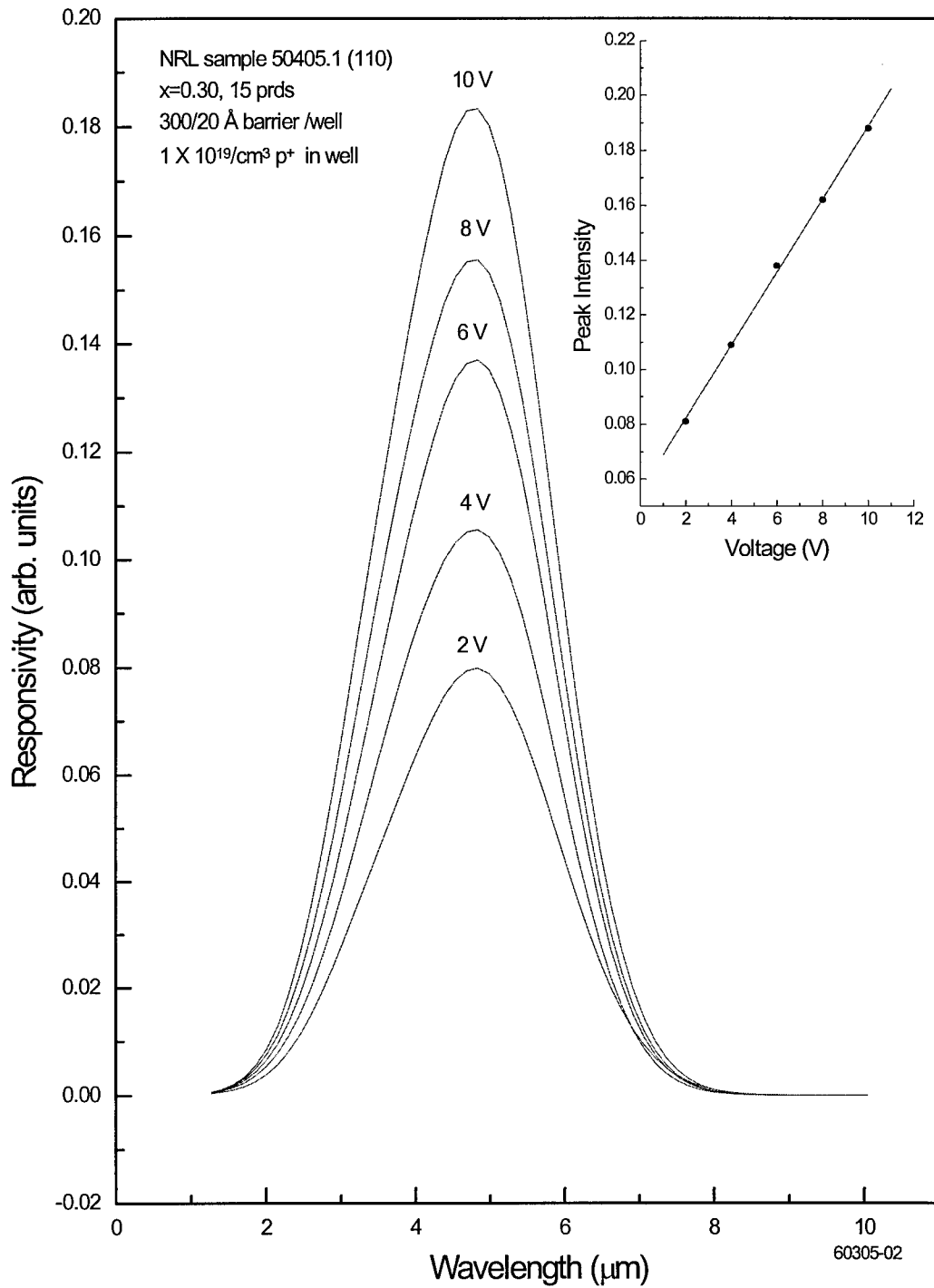


Figure 5-37. Photoreponse spectra of a Si[110]/SiGe MQW samples with $x=0.30$ and $L=20$ Å at 5 different voltages. Data taken at normal incidence. Inset shows dependence of peak intensity on bias voltage.

photoresponse was obtained on almost every sample grown. Samples with 5, 10, 15, 20 and 50 periods were observed to produce photoresponse with nearly the same intensity. This result was totally unexpected and a cogent argument is not yet forthcoming.

Absorption measurements could not be obtained from samples grown at 710 °C. This may be due to the segregation effects and strain relaxation as discussed in section C.

However as Figure 5-38 attests, similar photoresponse was obtained on samples grown at 550 °C and 710 °C. Once again, this result was unexpected and requires further research.

In general, MQWs grown at 550 °C had higher peak intensities. It was also postulated that MQWs grown on Si[110] would show better normal incidence response than MQWs grown on Si[001]. Figure 5-39 shows that for two identical structures grown at 710 °C there is little difference in peak intensity. However the MQWs on Si[110] are narrower and usually shifted toward lower wavelengths. This result is confirmed by theoretical calculations in which the ground state of a Si[110] MQW is always lower in energy than a Si[001] sample of identical composition. The width of the peak may be a result of the different segregation coefficients for boron for the two different growth directions.

Recent work by Thompson⁹¹ has shown that there is substantial boron segregation for growth on Si[110] when the growth temperature is elevated to 710 °C. As a result of less boron in the wells, the energy bands will be less occupied away from zone center which will reduce longer wavelength transitions. This is the same effect of that shown in Figure 5-34.

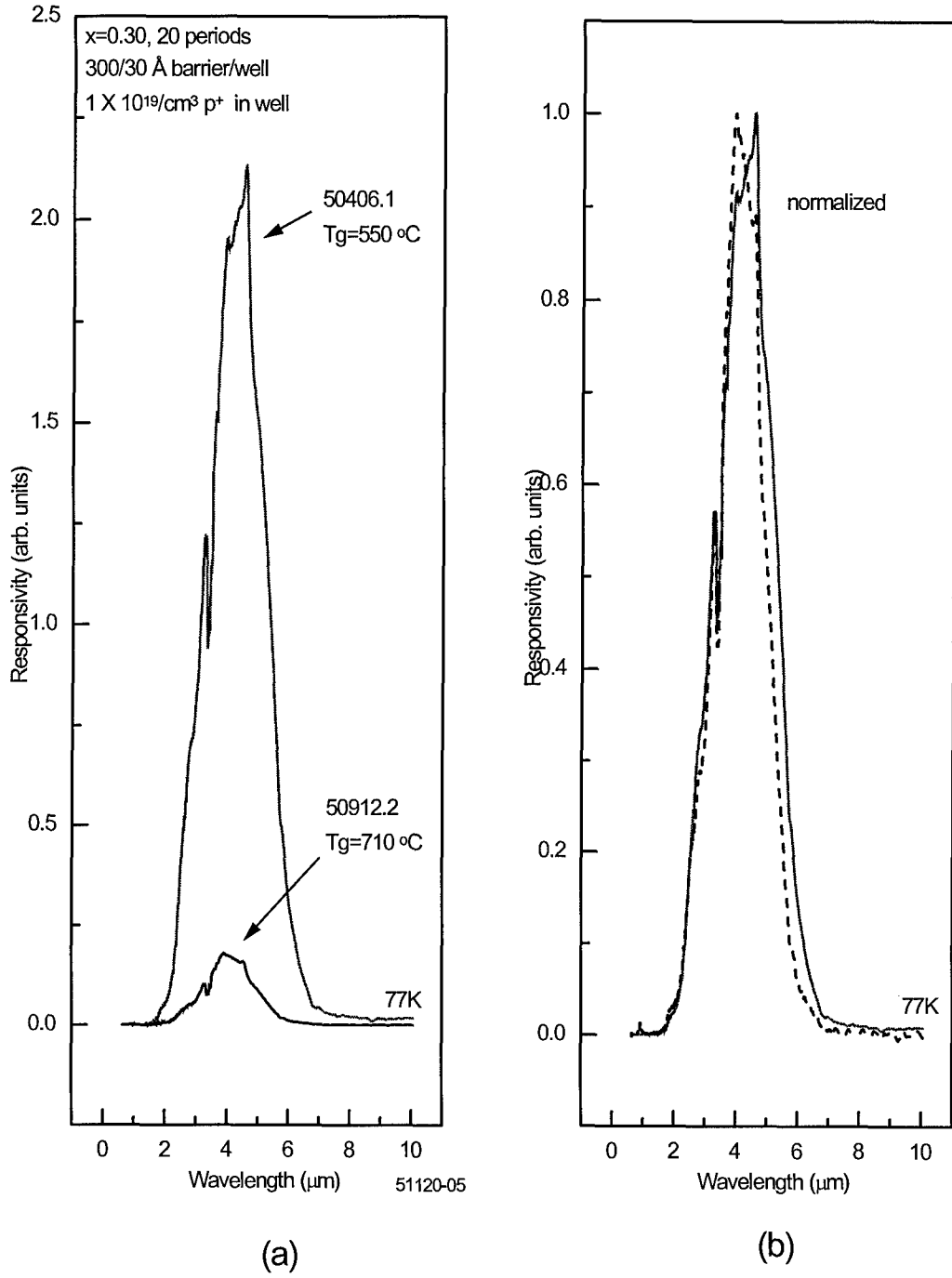


Figure 5-38. (a) Photoresponse spectra of a Si[001]/SiGe MQW sample with $x=0.30$ and $L=30 \text{ \AA}$ at 2 different growth temperatures. Data taken at normal incidence. (b) Normalized spectra

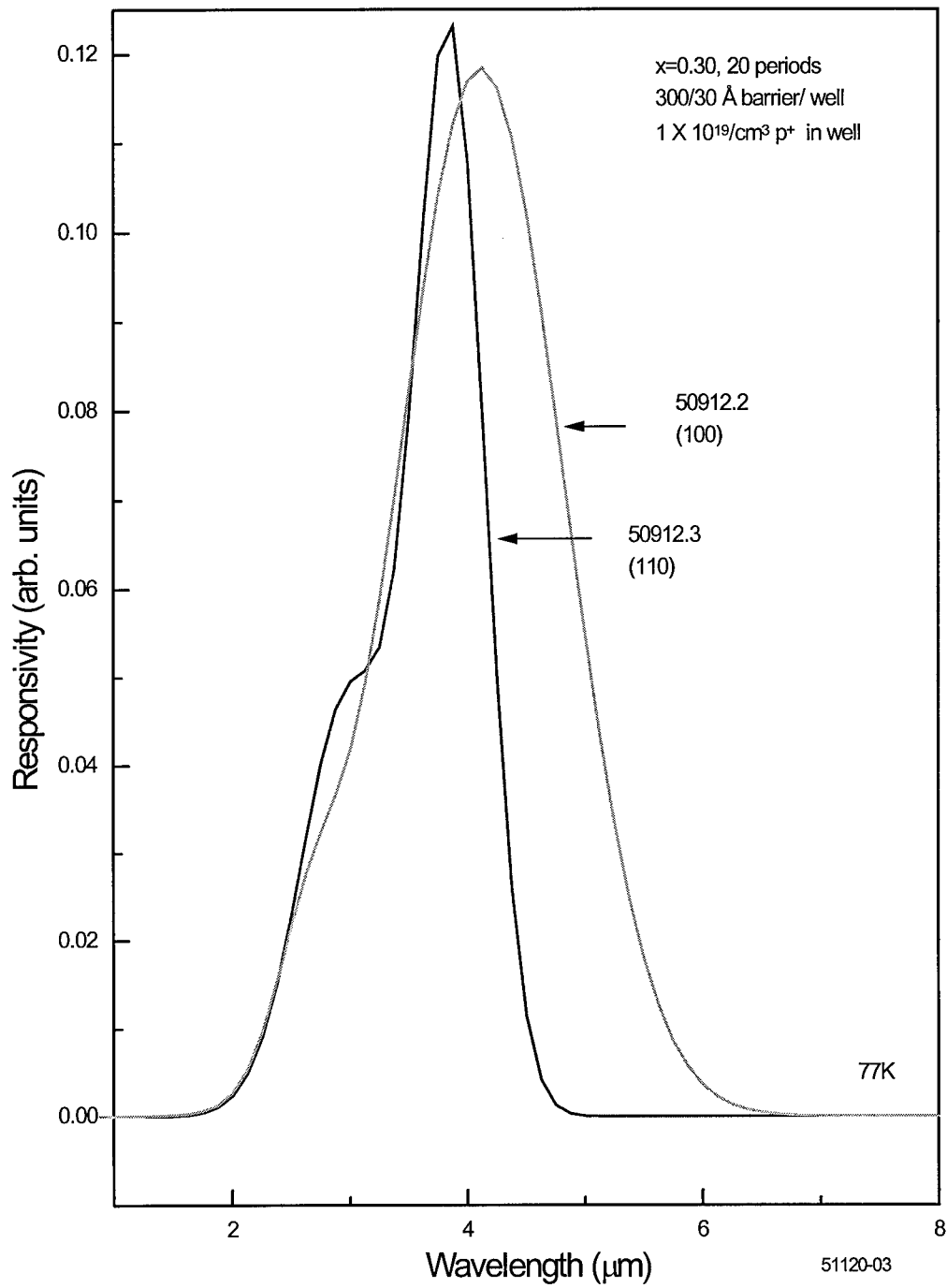


Figure 5-39. Photoresponse spectra of a [001] and [110] Si/SiGe MQW sample with $x=0.30$ and $L=30 \text{ \AA}$. Data taken at normal incidence at 77 K. Growth temperature = 710 °C.

3. SiGe Alloys used in QWIPs

The stated goal of this research was to characterize the properties of Si based QWIPs using SiGe alloys to determine their usefulness as IR detectors. The data presented thus far in the chapter strongly indicates considerable potential for SiGe MQW IR detectors. Several earlier spectra are combined in Figure 5-40 showing that Si based QWIPs can be used to obtain photoresponse over the 2-12 μm region, through the use of three different MQW samples, in the normal incidence mode by varying the well depth for a constant well width. Furthermore, these devices are operable at 77 K and have a responsivity comparable to GaAs/AlGaAs structures. The long wavelength cutoffs can be accurately predicted by EFA calculations, and the peak positions can be predicted semi-empirically. It has thus been demonstrated here that SiGe alloys can be used to make QWIPs. Furthermore, AFIT and NRL, have developed multi-color structures that allow normal incidence detection in the 2-10 μm region using a single device. NRL samples 60425.1 and 60425.2 were grown at 550 $^{\circ}\text{C}$ and had two distinct MQW regions, one grown on top of the other. Sample 60425.1 was grown on a [001] Si substrate. The first region was composed of five periods with a 300 \AA Si barrier and a 45 \AA $\text{Si}_{0.85}\text{Ge}_{0.15}$ well. The second region was composed of five periods with a 300 \AA Si barrier and a 45 \AA $\text{Si}_{0.55}\text{Ge}_{0.45}$ well. Figure 5-41 shows the photoresponse measured on this sample. The spectrum show two distinct regions and a very large temperature dependence. The strong temperature dependence of the long wavelength region is expected because this photoresponse comes from the MQWs with the shallow well. In this region, the carriers

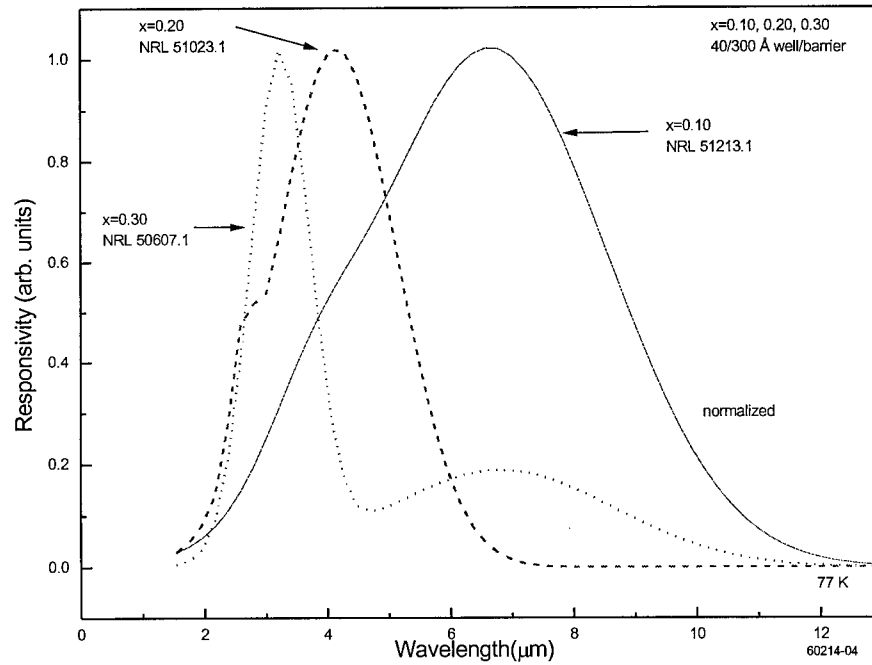
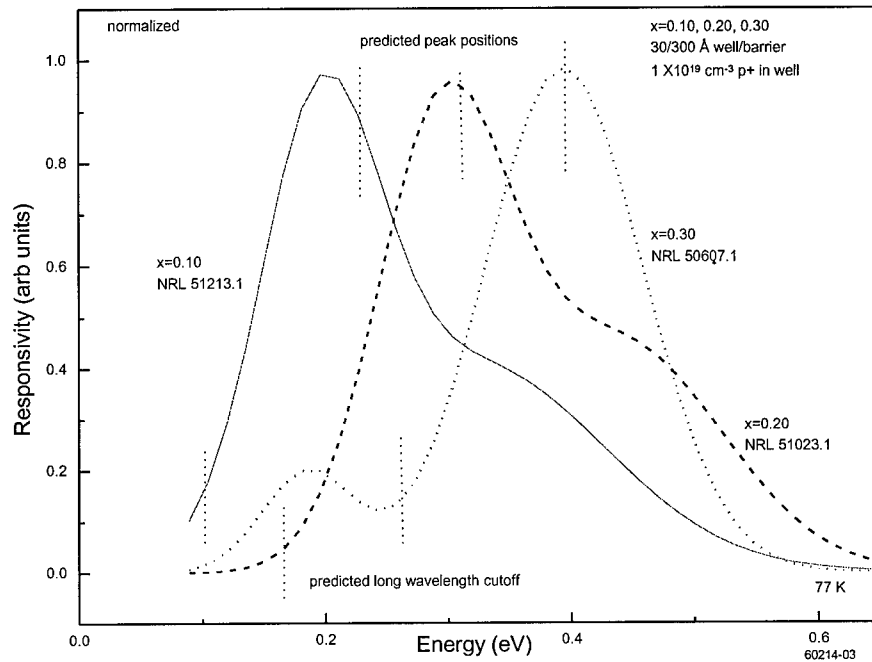


Figure 5-40. Spectra that show the photoresponse can be tuned to cover the 3 to 12 μm wavelength range. The top curve is plotted vs. energy and shows the predicted values for the long wavelength cutoff and peak position. The bottom curve is plotted vs. wavelength and shows the tuning effect with change in Ge composition.

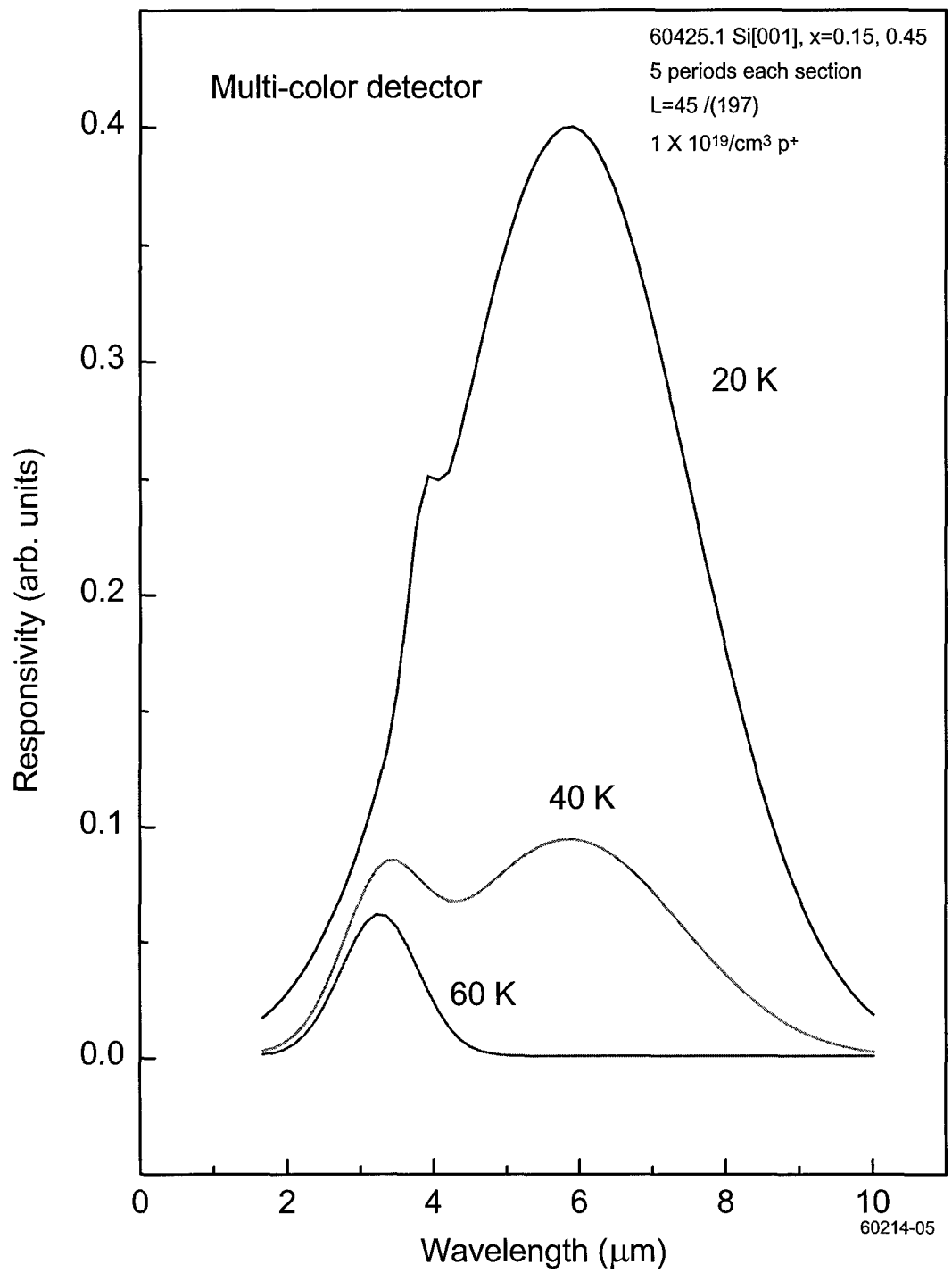


Figure 5-41. Photoresponse spectra of multi-color detector #1 taken at three different temperatures under normal incidence and 1 V bias.

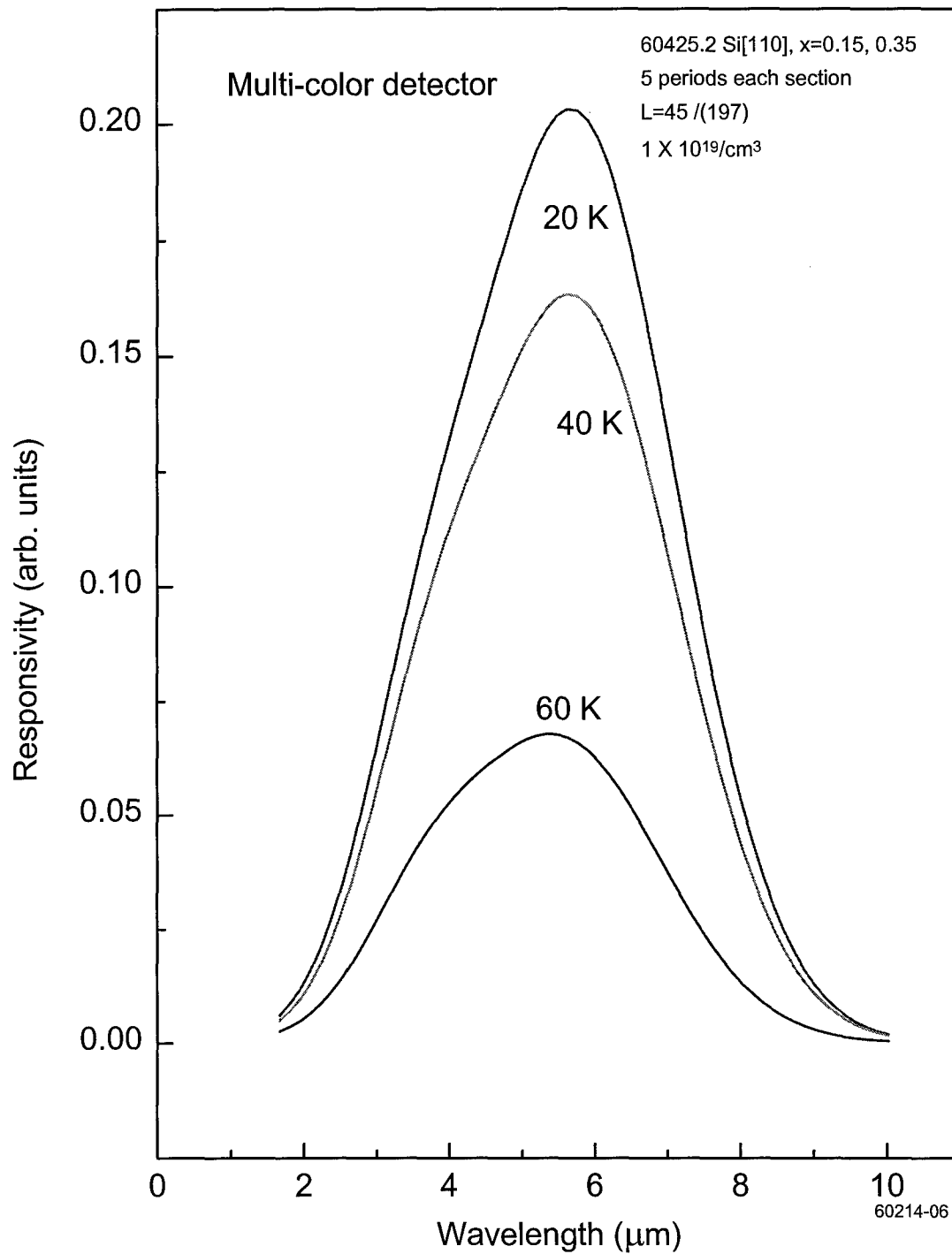


Figure 5-42. Photoresponse spectra of multi-color detector #2 taken at three different temperatures under normal incidence and 1 V bias.

are easily excited over the small barrier, and so a large photoresponse is difficult to get above 50 K. A similar structure, sample 60425.2, was grown on a [110] Si substrate. The first region was composed of five periods with a 300 Å Si barrier and a 45 Å $\text{Si}_{0.85}\text{Ge}_{0.15}$ well. The second region was composed of five periods with a 300 Å Si barrier and a $\text{Si}_{0.65}\text{Ge}_{0.35}$ well. This sample showed the same temperature dependence as the Si[001] sample. Figure 5-42 shows the photoresponse for this sample where the peaks in the regions are broader and have thus overlapped. Only a shoulder is seen instead of two distinct regions. This sample does appear to have a better long wavelength response at the higher temperature than does the [001] sample. It is not immediately obvious why this happens. A larger study on similar structures is necessary to achieve a better understanding. Conceivably, this concept of multi-color detection can be expanded to include a third or even fourth MQW region to tailor the photoresponse to the specific need.

The data presented in Figures 5-43, 5-44, and 5-45 clearly show the potential for SiGe MQWs as IR detectors. Such a Si compatible detector has not been previously demonstrated and the results indicated here demonstrate the power of the theory in predictably designing such a detector. Band width and wavelength responsivity can clearly be varied as desired.

6. *Conclusions and Recommendations*

A. *Conclusions*

The goal of this research was to explore the Si/Si_{1-x}Ge_x alloy system for possible applications in infrared detection. More specifically the intent was to determine if this alloy system could be used to make quantum well infrared photodetectors (QWIPs) that would operate under normal incidence illumination at 77 K. The research included both extensive calculations and experiment.

The calculations were based on the $\mathbf{k} \cdot \mathbf{p}$ formalism extended into the envelope function approximation (EFA). At the beginning of this study, the 6 x 6 $\mathbf{k} \cdot \mathbf{p}$ Hamiltonian for growth along the [110] direction, which is essential to the theoretical calculation, was not in the literature and therefore had to be derived. Using the computer programs developed from this theory, energy bands, band decompositions, transition strengths and Fermi levels were obtained for bound states in Si[001]/Si_{1-x}Ge_x, Si[110]/Si_{1-x}Ge_x, and GaAs/AlGaAs QWIPs. The results for the Si[110] MQWs are new and represent a contribution to the field. Results from EFA indicate that the zone center energy levels obtained from a simple, decoupled-well picture and often used in previous studies for Si[001] MQWs, are poor approximations, especially for Si[110]/Si_{1-x}Ge_x, where the bands are heavily mixed. Such band mixing leads to a relaxation of the zone center selection rules. Because of the band mixing, transition strengths are stronger in Si[110]/Si_{1-x}Ge_x, near zone center, but comparable to Si[100]/Si_{1-x}Ge_x and GaAs/AlGaAs farther out in the zone. The models were used to compare Si[110]/Si_{1-x}Ge_x, Si[100]/Si_{1-x}Ge_x and GaAs/AlGaAs structures designed for a long

wavelength cutoff at 10 μm . Both of the Si structures indicated that they should have superior absorption properties to the GaAs based structure. Furthermore, the Si[110] sample is predicted to produce better results under low doping conditions but is comparable to the Si[001] results under high doping conditions. The theory developed was limited to bound state transitions and did not include calculation of continuum energy levels and, as a result, bound-to-continuum transition energies or calculation of absorption coefficients. The development was however, sufficient to provide the information necessary for the MBE grower to fabricate highly credible detector structures as well as the computational results required for initial validation of the experimental data.

Experimental data was obtained using photoluminescence, absorption, and photoresponse. A large parameter space of doped Si[110]/Si_{1-x}Ge_x and Si[001]/Si_{1-x}Ge_x samples were studied with photoluminescence. The results indicate that an upper bound on the amount of Ge incorporation into the MQW structures exists. Furthermore, the photoluminescence showed large amounts of carbon impurities in addition to the broad photoluminescence associated with other impurity centers. However, this did not correlate with poor absorption or photoresponse. Unfortunately, the paradox of good photoluminescence and poor absorption was not completely resolved. However when considering recent articles in the literature, it seems most likely that defects are not annealed out at low temperatures which would produce poor PL, and segregation effects are large at higher growth temperatures which would produce poor absorption. Samples with poor luminescence have good absorption characteristics and visa versa.

It has been determined that absorption measurements must be made in the waveguide configuration to properly probe normal and parallel incidence effects. The substrate reference technique has proven to be the most reliable method for background subtraction. For the most part, absorption measurements for SiGe MQWs must be very carefully performed and thus have proven to be exceedingly difficult to make and interpret. Si[110]/Si_{1-x}Ge_x spectra are particularly difficult to interpret because of the abundance of bound states and the anisotropy of the energy bands. While it is good for detector purposes to have many strong transitions, this makes detailed analysis and comparison to theoretical predictions difficult to make. Nevertheless, good absorption data has been obtained on a wide variety of samples. This data can be qualitatively correlated with both theory and photoresponse data. Absorption on the Si[110] MQWs generally covers a broader wavelength range and is larger than absorption in Si[001] MQWs for any electric field polarization.

Although the absorption measurements proved difficult to make, photoresponse measurements were somewhat easier to make. The photoresponse results provided strong indication that a silicon based QWIP structure can operate in the normal incidence mode at 77 K. In addition, the response can be tailored over the 3-12 micron range by varying well width, well depth and doping level. Comparable responsivity was obtained for both Si[110]/Si_{1-x}Ge_x and Si[001]/Si_{1-x}Ge_x samples and for the single GaAs/AlGaAs sample examined. The small edge in absorption strength obtained in the [110] orientation is probably minimized because Si signal processing circuits are by and large fabricated on [001] substrates. However, the multi-color Si[110] device had better high temperature performance which is a critical factor in detector performance. Nevertheless, adequate data has been

obtained to make a strong argument that Si based QWIPs should be further explored for use in IR detectors.

The significant contributions produced by this work are in both the results of the calculations and the experiments. Extensive development of existing theory now allows the researcher to perform calculations on strained SiGe alloys grown along the [110] direction. In fact the tools are now in place to consider strained growth along any growth direction. All the experimental data on the Si[110] MQWs is new. In particular, the absorption and photoresponse data are sufficient to conclude that a Si based QWIP can be made that will operate under normal incidence at 77 K, and that the photoresponse can be tuned over the 2-12 μm wavelength region.

To make a final conclusion on the viability of the SiGe alloys for IR detectors, measurements such as detectivity, absolute responsivity, dark current, etc. must be made. However, the results of the current work provide strong support for making such measurements.

B. Recommendations

The most pressing issue in need of further work is the performance of true D^* detectivity measurements to compare to other material systems. In close connection with the D^* measurements are the measurements to obtain dark current, drift velocity, and mean free path. Once a particular range in the IR is chosen a full optimization on the growth conditions and parameters can be performed. In particular, the following experiments should be performed: 1) Growth temperature should be varied to obtain optimum photoresponse instead of optimum photoluminescence or absorption. 2) The number of periods should be maximized. 3) A more in depth and exacting study is necessary to determine the scaling factor with the number of quantum well periods. 4) A more rigorous doping study should be performed to better quantify exchange interaction effects and include many body effects. 5) Lower doping, particularly on the Si[110] MQWs may bring out a finer structure on the absorption and photoresponse measurements. 6) More device structures should be tried in which two or more regions of 5-10 periods of MQWs with different compositions are grown successively.

In addition to the experimental work, a large amount of work on the theoretical calculations can be done. For example, 1) it would be beneficial to calculate the continuum resonances and the absorption coefficients. 2) The $6 \times 6 \mathbf{k} \cdot \mathbf{p}$ formalism should be extended to an 8×8 to make a more accurate comparison with the GaAs/AlGaAs system. 3) The Si(111)/ $\text{Si}_{1-x}\text{Ge}_x$ system can be easily explored by modifying the current programs. 4) It may prove beneficial to convert the programs developed in Mathematica into Fortran codes to speed up the calculations.

Appendix A. Properties of Intrinsic Silicon and Germanium¹⁰⁸

PROPERTIES	UNITS	Silicon (Si)	Germanium (Ge)
Atomic number	-	14	32
Atomic weight	(based on ¹² C)	28.086	72.59
Periodic classification	-	IV A	IV A
Atomic volume	cm ³ /g·atom	12.07	13.5
Atomic radius	Å	1.18	1.22
Ionic radius	Å	0.41 (Si ⁴⁺)	0.53 (Ge ⁴⁺)
Density	g/cm ³	2.33	5.323
Lattice type	-	FCC, diamond	FCC, diamond
Lattice constant, a	Å	5.417	5.658
Valence electrons	-	3s ² 3p ²	4s ² 4p ²
Melting point	°C	1412	934
Boiling point	°C	2480	2827
Critical temperature	K	4920	5642
Linear thermal expansion coefficient	10 ⁻⁶ cm/cm/°C	4.2	5.75
Specific heat	cal/g/°C	0.162	0.074
Electronic specific heat	10 ⁻⁴ cal/mole/°C ²	0.050	0
Thermal conductivity	cal/cm ² /cm/sec/°C	0.20	0.15
Latent heat of fusion	kcal/mole	12.0	7.6
Latent heat of vaporization at B.P.	kcal/mole	71	79.9
Heat of combustion	kcal/mole	191 (to SiO ₂)	
Heat of sublimation	kcal/mole	108.4	89.5
Heat capacity at constant pressure	cal/°C/mole	4.64	5.47
Heat content at M.P.	kcal/mole	8.07	5.81
Entropy	cal/°C/mole	4.50	7.43
Longitudinal sound velocity	m/sec	9101	4914 (001)
Electrical resistivity	microhm·cm	2.3x10 ⁵	47x10 ⁶
Photoelectric work function	eV	4.1	4.56
First ionization potential	eV	8.151 (Si ⁺)	7.899 (Ge ⁺)
Oxidation potential	V	1.2 (acid, Si/SiO ₂)	0.0 (Ge ²⁺)
Electrochemical equivalent	mg/Coulomb	0.07269 (Si ⁴⁺)	0.1881 (Ge ⁺)
Magnetic susceptibility	c.g.s. units	-0.13x10 ⁻⁶	-0.10x10 ⁻⁶
Refractive index	-	3.45 (at 2 μm)	4.10 (at 2 μm)
Young's modulus of elasticity	10 ⁻⁶ kg/cm ²	1.05	1.01
Shear modulus	10 ⁻⁶ kg/cm ²	0.405	0.40
Bulk modulus	10 ⁻⁶ kg/cm ²	1.008	0.7874
Poisson's ratio	-	0.44	0.27
Spin orbit splitting	eV	0.44	0.290
Luttinger parameter γ ₁	-	4.22	13.4
Luttinger parameter γ ₂	-	0.39	4.25
Luttinger parameter γ ₃	-	1.44	5.69
valence hydrostatic potential a _v	eV	2.46	1.24
conduction hydrostatic potential	eV	1.5	-4.5
valence uniaxial potential (100) Du	eV	3.15	4.29

valence uniaxial potential (111) Du'	eV	4.20	4.59
conduction uniaxial potential Ξ_d	eV	9.2	16.2
elastic constant C11	dyn/cm ²	1.675	1.315
elastic constant C12	dyn/cm ²	0.650	0.494
elastic constant C44	dyn/cm ²	0.801	0.684

Appendix B. Chronological Review of the Development of Si/Si_{1-x}Ge_x Heterostructures

1975

- Kasper *et al.* grow the first pseudomorphic (coherently strained) Si_{1-x}Ge_x epilayers on silicon.¹⁰⁹

1984

- Luryi *et al.* fabricate a Ge p-i-n diode on a silicon substrate via MBE. The structure consisted of the Ge p-i-n layers grown on top of a compositionally graded (Si_{1-x}Ge_x) buffer layer on top of a silicon wafer.¹¹⁰
- Bean *et al.* demonstrate that high quality epitaxial layers can be grown provided that the temperature of growth is kept within a certain range and, the layers do not exceed a critical thickness.¹¹¹
- Coon and Karunasiri propose the use of quantum wells, where absorption occurs between the ground state in the well and an excited state above the barriers, for IR detectors.¹¹²

1985

- Pearsall *et al.* fabricate a modulation doped, Si_{1-x}Ge_x p-channel field effect transistor (FET). This device did not exhibit outstanding performance but did show that the strained layer alloys could withstand conventional device processing such as ion implantation, activation anneals, reactive ion etching and CVD oxide deposition.¹¹³
- Lang *et al.* measure bandgaps on strained Si_{1-x}Ge_x alloys using photocurrent spectroscopy.¹¹⁴
- People develops theoretical calculation of the indirect bandgap on coherently strained Si_{1-x}Ge_x alloys on Si (100) substrates.¹¹⁵
- West and Eglash report the first observation, via infrared absorption, of a direct intraconduction band transition between square quantum well states in an GaAs/AlGaAs system.¹¹⁶

1986

- The development of structures for detector applications that used Si_{1-x}Ge_x alloy layers as an integral part of the device came in 1986 when Temkin *et al.* fabricated a strained layer waveguide photodetector (PIN structure) operating near 1.3 μm. In an effort to boost quantum efficiency, Temkin selects the strained layer as the absorbing region.

¹¹⁷

- Pearsall *et al.* fabricate the first avalanche multiplication photodetector. IR absorption occurs in the strained Si/ Si_{1-x} Ge_x layer while avalanche multiplication takes place in one of the Si-cladding layers.¹¹⁸
- Bevk *et al.* produce the first ordered Si/Ge strained superlattice. They made a structure with one dimensional periodicity of one unit cell (GeGeSiSi). They also grew a superlattice composed of sublayers of pure Si and alternating bilayers of Ge and Si.¹¹⁹
- Van de Walle and Martin determine valence band offset for pseudomorphic Si_{1-x} Ge_x interfaces using a pseudopotential calculation.¹²⁰

1987

- Iyer *et al.* fabricate the first heterojunction bipolar transistor with a Si_{1-x} Ge_x base, but the performance was much less than expected indicating that growth issues must be resolved.¹²¹
- Levine *et al.* report the first demonstration of an infrared detector based on intersubband absorption and sequential resonant tunneling in doped GaAs/AlGaAs quantum well superlattices.¹²²

1988

- Rhee *et al.* report on resonant tunneling of holes through an unstrained Si_{1-x} Ge_x well between two strained Si barriers on a relaxed Si_{1-y} Ge_y buffer layer. The demonstration of resonant tunneling in the Ge_x Si_{1-x}/Si heterostructures indicates that the interfaces are sufficiently smooth for the fabrication of quantum devices.¹²³
- Yang and Pan are the first to propose and calculate intersubband absorption of n-type multiple Si_{1-x} Ge_x quantum wells (MQWs) at 10 μm for [100], [110], [111] Si crystal orientations. They determine that for the [110] and [111] growth directions, normal incidence absorption is allowed due to the anisotropic effective mass in Si.¹³

1989

- Chang and James develop the theory for intersubband transitions in p-type quantum wells.¹²⁴
- King *et al.* fabricate an npn HBT which showed superior performance. This is an important development because unlike FETs, HBTs are minority carrier devices and require low-defect density to function successfully.¹²⁵

1990

- Karunasiri *et al.* observe intersubband IR absorption of holes in a Si/Ge superlattice for the first time. The different minibands of the superlattice are populated with holes using an external bias across the device and, an enhanced photoresponse is observed when the emitter Fermi level is aligned with one of the minibands.¹²⁶
- Karunasiri *et al.* observe intersubband IR absorption of holes in Si/ Si_{1-x} Ge_x MQWs using room temperature FTIR. In this experiment, the IR absorption is measured as a function of polarization using a waveguide geometry. The polarization dependent spectra agrees with the selection rules for the intersubband transition.¹²⁷
- Lin and Maserjian report on the first Si_{1-x}Ge_x/Si heterojunction internal photoemission (HIP) detector responsive out to 10 μm.⁹

1991

- Hertle *et al.* observe intersubband IR absorption of conduction band electrons in Ge_x Si_{1-x}/Si MQWs at 8 K using FTIR. They note absorption peaks at 38 and 60 μm due to transitions between the ground state and first excited state.¹²⁸
- Karunasiri *et al.* observe intersubband IR absorption in δ-doped p-type Si MQWs. Near 100% absorption is measured by FTIR using waveguides. Absorption peaks range from 3 to 7 μm and can be tuned by varying the doping concentration in the δ-doped layer. Polarization-dependent spectra show good agreement with the intersubband selection rules and suggests that that transitions occur between the first two heavy hole subbands.¹²⁹
- Karunasiri *et al.* demonstrate a long-wavelength infrared detector (LWIR) using Si/ Si_{1-x} Ge_x MQWs. A broad peak in photoresponse is observed near 9 μm with a FWHM of 80 meV. A peak responsivity of 0.3 A/W and detectivity of D*=1 X 10⁹ cm √Hz/W at 77K are measured.¹³⁰

1992

- People *et al.* report the fabrication of a broadband (8-14 μm), normal incidence, p-type Si/ Si_{1-x} Ge_x strained-layer IR photodetector. A detectivity of D*=3.3 X 10⁹ cm √Hz/W at 77K is observed.¹³¹
- Park, Karunasiri and Wang also report normal incidence absorption in p-type Si/ Si_{1-x} Ge_x MQWs but only for germanium concentrations above 30%.¹³²
- Lee and Wang report strong electron intersubband IR absorption near 10 μm in Sb in δ-doped Si MQWs grown on (100) Si substrates. The peak absorption can be shifted by changing the doping concentration in the wells.¹³³

- Lee and Wang report electron intersubband IR Absorption for Sb δ -doped Si/ Si_{1-x} Ge_x MQWs grown on (110) Si substrates. The intersubband absorption is shown to be allowed for both the optical field components perpendicular and parallel to the quantum wells due to the anisotropic effective mass.¹³⁴

1994

- Lee and Wang grow a Ge/Si_{1-x} Ge_x MQW structure on a Si (100) substrate and observe electron intersubband absorption. The absorption is shown to be allowed for the optical field components both perpendicular and parallel to the quantum wells.¹³⁵
- Corbin, Wong, and Jaros report on theoretical calculations for p-type, strained (100) Si/Si_{1-x} Ge_x MQWs. They discuss normal and parallel incidence transitions. Their theory is based on pseudopotential calculations.¹³⁶
- Fromherz et al. discuss hole energy levels and intersubband absorption in modulation doped (100) Si/Si_{1-x} Ge_x MQWs. Their theoretical approach is based on a 6 X 6 Luttinger-Kohn Hamiltonian. They report that intersubband transitions are allowed for parallel and normal incidence due to the mixing of the heavy-hole, light-hole and split-off valence bands due to a confining potential and strain.¹³⁷

1995

- Bernard-Hofer et al. fabricate Si/Si_{1-x} Ge_x structures on a Si (110) substrate for use as waveguides coupling into a PIN structure.¹³⁸
- Robbins et al. report normal incidence absorption in p-type (100) Si/Si_{1-x} Ge_x MQWs. However they attribute the normal incidence response to free carrier absorption.¹³⁹
- Zanier, et al. report on free carrier and intersubband absorption in p-type (100) Si/Si_{1-x} Ge_x MQWs. They include a discussion of a Drude model use to calculate the free carrier absorption.¹⁴⁰

Appendix C. Zone Center Energies

(100) Zone Center Energies

%Ge	L	HH1	HH2	HH3	LH1	LH2	SO	cont	hh1- hh2	hh1- hh3	hh1- lh2	hh1- cnt	hh1- so	lh1- lh2	lh1- cnt	lh1- so
x	Å	meV	meV	meV	meV	meV	meV	meV	μm	μm	μm	μm	μm	μm	μm	μm
0.60	40	54	217	458	162	354	415	491	7.63	3.07	4.13	2.83	3.43	6.46	3.76	4.90
0.40	40	48	187		126	278	297	328	8.93		5.40	4.42	4.99	8.18	6.13	7.26
	30	71	264		150	326	305	328	6.43		4.86	4.82	5.3	7.06	6.96	8.02
	20	115			192		318	328				5.80	6.09		9.08	9.81
0.35	40	46	177		116	255	267	287	9.45		5.94	5.14	5.62	8.96	7.25	8.25
	30	68	245		139		274	287	6.98			5.64	6.00		8.33	9.14
	20	108			176		287	287				6.90	6.93		11.13	11.21
0.30	40	44	166		106	229	236	246	10.12		6.69	6.12	6.44	10.07	8.83	9.53
	30	64	224		126		243	246	7.75			6.78	6.90		10.31	10.59
	20	100			159		254	246				8.47	8.03		14.16	12.97
0.25	40	41	153		95		205	205	11.07			7.55	7.55		11.24	11.23
	30	60	197		113		212	205	8.98			8.48	8.12		13.38	12.50
	20	91			140		222	205				10.85	9.49		19.03	15.20
0.20	40	38	137		83		175	164	12.54			9.81	9.09		15.27	13.58
	30	54	164		98		180	164	11.25			11.22	9.82		18.65	15.07
	20	81			120		189	164				14.85	11.52		27.72	18.00
0.15	50	25	94		61	121	139									
	40	34	115		70		143	123	15.31			13.90	11.36		23.11	16.85
	30	48			81		148	123				16.31	12.31		29.28	18.50
	20	68			96		155	123				22.60	14.41		46.03	21.34
0.10	40	29			53		112	82				23.21	14.96		43.04	21.28
	30	39			61		115	82				28.38	16.18		57.55	22.75
	20	52			70		120	82				42.19	18.60		97.60	24.82

(110) Zone center energies

%Ge	L	HH1	HH2	HH3	LH1	LH2	SO	cont	hh1- hh2	hh1- hh3	hh1- -lh2	hh1- cnt	hh1- so	lh1- lh2	lh1- cnt	lh1- so
x	Å	meV	meV	meV	meV	meV	meV	meV	μm	μm	μm	μm	μm	μm	μm	μm
0.40	40	28	110	236	126	265	294	325	15.10	5.95	5.23	4.18	4.66	8.87	6.22	7.35
	30	44	169	322	149	317	304	325	9.95	4.45	4.54	4.41	4.77	7.41	7.06	8.01
	20	77	273		190		314	325	6.36			5.02	5.25		9.25	10.08
0.35	40	27	105	222	115	244	257	283	15.90	6.34	5.71	4.84	5.40	9.66	7.40	8.78
	30	42	159		137		265	283	10.60			5.14	5.55		8.50	9.69
	20	73	250		174		274	283	7.01			5.90	6.18		11.39	12.46
0.30	50	17	70	153	99	199		241								
	40	25	99	206	105	220	219	241	16.84	6.85	6.37	5.74	6.40	10.78	9.09	10.86
	35	32	121	235	125	238	239	241	13.85	6.07	6.01	5.91	5.95	11.0	10.67	10.82
	30	39	148		124	241	226	241	11.41		6.14	6.14	6.63		10.60	12.15
	20	68	224		156		234	241	7.93			7.15	7.48		14.58	16.05
0.25	40	24	93	187	94	192	182	200	18.00	7.59	7.35	7.04	7.85	12.57	11.69	14.09
	35	30	113		112	200	207	200	14.88		7.29	7.28	6.98	14.16	14.14	13.04
	30	37	136		111		188	200	12.47			7.59	8.20		13.90	16.08
	20	62	195		137		194	200	9.35			9.00	9.42		19.77	21.96
0.20	40	22	85	159	82	158	145	159	19.57	9.06	9.08	9.07	10.12	16.14	16.09	19.73
	35	28	103		98		175	159	16.36			9.45	8.42		20.28	16.05
	30	34	122		96		150	159	14.03			9.89	10.70		19.66	23.12
	20	56			117		154	159				12.02	12.60		29.24	33.00
0.15	40	21	77		69		108	119	21.97			12.64	14.14		24.90	31.51
	30	30	104		80		112	119	16.76			14.04	15.22		31.67	38.38
	20	49			94		115	119				17.69	18.61		50.08	58.24
0.10	40	18	64		53		72	79	26.87			20.48	23.04		48.50	65.85
	30	26			60		74	79				23.50	25.62		65.69	85.38
	20	39			68		77	79				31.44	33.27		113.3 2	141.4 0

Appendix D. P's and Q's for Momentum Matrix Elements

The matrices P and Q necessary for determining the momentum matrix elements are obtained by taking derivatives of the Hamiltonian $H_{k,p}$. Since the Hamiltonian is different for different crystal orientations, the P's and Q's are also different. Using the following set of equations, the subsequent matrices are derived (in Mathematica format) where the w subscript denotes the well region. Similar matrices are derived for the barrier region with the substitution of the barrier Luttinger parameters for the well Luttinger parameters.

$$P_x = \frac{\partial^2 H}{\partial x \partial x} k_x + \frac{\partial^2 H}{\partial x \partial y} k_y$$

$$P_y = \frac{\partial^2 H}{\partial y \partial y} k_y + \frac{\partial^2 H}{\partial y \partial x} k_x$$

$$P_z = \frac{\partial^2 H}{\partial z \partial x} k_x + \frac{\partial^2 H}{\partial z \partial y} k_y$$

$$Q_x = \frac{\partial^2 H}{\partial z \partial x} \left(-i \frac{d}{dz} \right)$$

$$Q_y = \frac{\partial^2 H}{\partial z \partial y} \left(-i \frac{d}{dz} \right)$$

$$Q_z = \frac{\partial^2 H}{\partial z \partial z} \left(-i \frac{d}{dz} \right)$$

(100) case

$$P_{xw} = \{ \{ -(k_x*(y1w + y2w)), 0, I^{3/2}*(I*k_x*y2w + k_y*y3w), 0, 0, \\ 6^{1/2}*(I*k_x*y2w + k_y*y3w) \}, \\ \{ 0, k_x*(-y1w + y2w), 0, I^{3/2}*(I*k_x*y2w + k_y*y3w), I^{2/2}*k_x*y2w, 0 \}, \\ \{ -I^{3/2}*(-I*k_x*y2w + k_y*y3w), 0, k_x*(-y1w + y2w), 0, 0, \\ I^{2/2}*k_x*y2w \}, \\ \{ 0, -I^{3/2}*(-I*k_x*y2w + k_y*y3w), 0, -(k_x*(y1w + y2w)), \\ -(6^{1/2}*(-I*k_x*y2w + k_y*y3w)), 0 \},$$

$$\{6^{(1/2)}*(-I*kx*y2w + ky*y3w), 0, -I*2^{(1/2)}*kx*y2w, 0, 0, -(kx*y1w)\};$$

$$\begin{aligned} P_{yw} = & \{ -(ky*(y1w + y2w)), 0, \\ & 3^{(1/2)}*(ky*y2w + I*kx*y3w), 0, 0, \\ & 6^{(1/2)}*(-I*ky*y2w + kx*y3w)\}, \\ & \{0, ky*(-y1w + y2w), 0, \\ & 3^{(1/2)}*(ky*y2w + I*kx*y3w), I*2^{(1/2)}*ky*y2w, \\ & 0\}, \{3^{(1/2)}*(ky*y2w - I*kx*y3w), 0, \\ & ky*(-y1w + y2w), 0, 0, I*2^{(1/2)}*ky*y2w\}, \\ & \{0, 3^{(1/2)}*(ky*y2w - I*kx*y3w), 0, \\ & -(ky*(y1w + y2w)), \\ & -(6^{(1/2)}*(I*ky*y2w + kx*y3w)), 0\}, \\ & \{0, -I*2^{(1/2)}*ky*y2w, 0, \\ & -(6^{(1/2)}*(-I*ky*y2w + kx*y3w)), -(ky*y1w), 0\}, \\ & \{6^{(1/2)}*(I*ky*y2w + kx*y3w), 0, \\ & -I*2^{(1/2)}*ky*y2w, 0, 0, -(ky*y1w)\}; \end{aligned}$$

$$\begin{aligned} P_{zw} = & \{0, 3^{(1/2)}*(I*kx + ky)*y3w, 0, 0, \\ & I*(3/2)^{(1/2)}*(I*kx + ky)*y3w, 0\}, \\ & \{3^{(1/2)}*(-I*kx + ky)*y3w, 0, 0, 0, 0, \\ & (3*I*(I*kx + ky)*y3w)/2^{(1/2)}\}, \\ & \{0, 0, 0, -(3^{(1/2)}*(I*kx + ky)*y3w), \\ & (-3*I*(-I*kx + ky)*y3w)/2^{(1/2)}, 0\}, \\ & \{0, 0, -(3^{(1/2)}*(-I*kx + ky)*y3w), 0, 0, \\ & -I*(3/2)^{(1/2)}*(-I*kx + ky)*y3w\}, \\ & \{-I*(3/2)^{(1/2)}*(-I*kx + ky)*y3w, 0, \\ & (3*I*(I*kx + ky)*y3w)/2^{(1/2)}, 0, 0, 0\}, \\ & \{0, (-3*I*(-I*kx + ky)*y3w)/2^{(1/2)}, 0, \\ & I*(3/2)^{(1/2)}*(I*kx + ky)*y3w, 0, 0\}; \end{aligned}$$

$$\begin{aligned} Q_{xw} = & \{0, I*3^{(1/2)}*y3w, 0, 0, -((3/2)^{(1/2)}*y3w), 0\}, \\ & \{-I*3^{(1/2)}*y3w, 0, 0, 0, 0, (-3*y3w)/2^{(1/2)}\}, \\ & \{0, 0, 0, -I*3^{(1/2)}*y3w, (-3*y3w)/2^{(1/2)}, 0\}, \\ & \{0, 0, I*3^{(1/2)}*y3w, 0, 0, -((3/2)^{(1/2)}*y3w)\}, \\ & \{-((3/2)^{(1/2)}*y3w), 0, (-3*y3w)/2^{(1/2)}, 0, 0, \\ & 0\}, \{0, (-3*y3w)/2^{(1/2)}, 0, \\ & -((3/2)^{(1/2)}*y3w), 0, 0\}; \end{aligned}$$

$$\begin{aligned}
Qyw = \{ & \{0, 3^{1/2}y3w, 0, 0, I(3/2)^{1/2}y3w, 0\}, \\
& \{3^{1/2}y3w, 0, 0, 0, 0, (3Iy3w)/2^{1/2}\}, \\
& \{0, 0, 0, -(3^{1/2}y3w), (-3Iy3w)/2^{1/2}, \\
& 0\}, \{0, 0, -(3^{1/2}y3w), 0, 0, \\
& -I(3/2)^{1/2}y3w\}, \\
& \{-I(3/2)^{1/2}y3w, 0, (3Iy3w)/2^{1/2}, 0, \\
& 0, 0\}, \{0, (-3Iy3w)/2^{1/2}, 0, \\
& I(3/2)^{1/2}y3w, 0, 0\};
\end{aligned}$$

$$\begin{aligned}
Qzw = \{ & \{-y1w + 2y2w, 0, 0, 0, 0, 0\}, \\
& \{0, -y1w - 2y2w, 0, 0, -2I2^{1/2}y2w, 0\}, \\
& \{0, 0, -y1w - 2y2w, 0, 0, -2I2^{1/2}y2w\}, \\
& \{0, 0, 0, -y1w + 2y2w, 0, 0\}, \\
& \{0, 2I2^{1/2}y2w, 0, 0, -y1w, 0\}, \\
& \{0, 0, 2I2^{1/2}y2w, 0, 0, -y1w\};
\end{aligned}$$

(110) case

$$\begin{aligned}
Pwx = \{ & \{(kx*(-2y1w + y2w - 3y3w))/2, 0, \\
& -(3^{1/2}*(kx*y2w + kx*y3w - 2Iky*y3w))/2, \\
& 0, 0, (3/2)^{1/2}* \\
& (I*kx*y2w + I*kx*y3w + 2*ky*y3w)\}, \\
& \{0, -(kx*(2y1w + y2w - 3y3w))/2, 0, \\
& -(3^{1/2}*(kx*y2w + kx*y3w - 2Iky*y3w))/2, \\
& (I*kx*(-y2w + 3y3w))/2^{1/2}, 0\}, \\
& \{-(3^{1/2}*(kx*y2w + kx*y3w + 2Iky*y3w))/2, \\
& 0, -(kx*(2y1w + y2w - 3y3w))/2, 0, 0, \\
& (I*kx*(-y2w + 3y3w))/2^{1/2}\}, \\
& \{0, -(3^{1/2}*(kx*y2w + kx*y3w + 2Iky*y3w))/ \\
& 2, 0, (kx*(-2y1w + y2w - 3y3w))/2, \\
& I(3/2)^{1/2}*(kx*y2w + kx*y3w + 2Iky*y3w), \\
& 0\}, \{0, (-I*kx*(-y2w + 3y3w))/2^{1/2}, 0, \\
& -I(3/2)^{1/2}*(kx*y2w + kx*y3w - 2Iky*y3w), \\
& -(kx*y1w), 0\}, \{(3/2)^{1/2}* \\
& (-I*kx*y2w - I*kx*y3w + 2*ky*y3w), 0, \\
& (-I*kx*(-y2w + 3y3w))/2^{1/2}, 0, 0, -(kx*y1w)\} \\
& \};
\end{aligned}$$

$$\begin{aligned}
Pyw = \{ & \{ -(ky*(y1w + y2w)), 0, \\
& 3^{(1/2)}*(ky*y2w + I*kx*y3w), 0, 0, \\
& 6^{(1/2)}*(-I*ky*y2w + kx*y3w) \}, \\
& \{ 0, ky*(-y1w + y2w), 0, \\
& 3^{(1/2)}*(ky*y2w + I*kx*y3w), I*2^{(1/2)}*ky*y2w, \\
& 0 \}, \{ 3^{(1/2)}*(ky*y2w - I*kx*y3w), 0, \\
& ky*(-y1w + y2w), 0, 0, I*2^{(1/2)}*ky*y2w \}, \\
& \{ 0, 3^{(1/2)}*(ky*y2w - I*kx*y3w), 0, \\
& -(ky*(y1w + y2w)), \\
& -(6^{(1/2)}*(I*ky*y2w + kx*y3w)), 0 \}, \\
& \{ 0, -I*2^{(1/2)}*ky*y2w, 0, \\
& -(6^{(1/2)}*(-I*ky*y2w + kx*y3w)), -(ky*y1w), 0 \}, \\
& \{ 6^{(1/2)}*(I*ky*y2w + kx*y3w), 0, \\
& -I*2^{(1/2)}*ky*y2w, 0, 0, -(ky*y1w) \} \};
\end{aligned}$$

$$\begin{aligned}
Pzw = \{ & \{ 0, 3^{(1/2)}*(I*kx*y2w + ky*y3w), 0, 0, \\
& I*(3/2)^{(1/2)}*(I*kx*y2w + ky*y3w), 0 \}, \\
& \{ 3^{(1/2)}*(-I*kx*y2w + ky*y3w), 0, 0, 0, 0, \\
& (3*I*(I*kx*y2w + ky*y3w))/2^{(1/2)} \}, \\
& \{ 0, 0, 0, -(3^{(1/2)}*(I*kx*y2w + ky*y3w)), \\
& (-3*I*(-I*kx*y2w + ky*y3w))/2^{(1/2)}, 0 \}, \\
& \{ 0, 0, -(3^{(1/2)}*(-I*kx*y2w + ky*y3w)), 0, 0, \\
& -I*(3/2)^{(1/2)}*(-I*kx*y2w + ky*y3w) \}, \\
& \{ -I*(3/2)^{(1/2)}*(-I*kx*y2w + ky*y3w), 0, \\
& (3*I*(I*kx*y2w + ky*y3w))/2^{(1/2)}, 0, 0, 0 \}, \\
& \{ 0, (-3*I*(-I*kx*y2w + ky*y3w))/2^{(1/2)}, 0, \\
& I*(3/2)^{(1/2)}*(I*kx*y2w + ky*y3w), 0, 0 \} \};
\end{aligned}$$

$$\begin{aligned}
Qxw = \{ & \{ 0, I*3^{(1/2)}*y2w, 0, 0, -((3/2)^{(1/2)}*y2w), 0 \}, \\
& \{ -I*3^{(1/2)}*y2w, 0, 0, 0, 0, (-3*y2w)/2^{(1/2)} \}, \\
& \{ 0, 0, 0, -I*3^{(1/2)}*y2w, (-3*y2w)/2^{(1/2)}, 0 \}, \\
& \{ 0, 0, I*3^{(1/2)}*y2w, 0, 0, -((3/2)^{(1/2)}*y2w) \}, \\
& \{ -((3/2)^{(1/2)}*y2w), 0, (-3*y2w)/2^{(1/2)}, 0, 0, \\
& 0 \}, \{ 0, (-3*y2w)/2^{(1/2)}, 0, \\
& -((3/2)^{(1/2)}*y2w), 0, 0 \} \};
\end{aligned}$$

$$\begin{aligned}
Qyw = \{ & \{ 0, 3^{(1/2)}*y3w, 0, 0, I*(3/2)^{(1/2)}*y3w, 0 \}, \\
& \{ 3^{(1/2)}*y3w, 0, 0, 0, 0, (3*I*y3w)/2^{(1/2)} \}, \\
& \{ 0, 0, 0, -(3^{(1/2)}*y3w), (-3*I*y3w)/2^{(1/2)}, \\
& 0 \} \};
\end{aligned}$$

$0\}, \{0, 0, -(3^{1/2})y_3w, 0, 0,$
 $-I(3/2)^{1/2}y_3w\},$
 $\{-I(3/2)^{1/2}y_3w, 0, (3Iy_3w)/2^{1/2}, 0,$
 $0, 0\}, \{0, (-3Iy_3w)/2^{1/2}, 0,$
 $I(3/2)^{1/2}y_3w, 0, 0\}\};$

$Q_{zw}=\{\{(-2y_1w + y_2w + 3y_3w)/2, 0,$
 $-(3^{1/2})(y_2w - y_3w)/2, 0, 0,$
 $I(3/2)^{1/2}(y_2w - y_3w)\},$
 $\{0, -y_1w - y_2w/2 - (3y_3w)/2, 0,$
 $-(3^{1/2})(y_2w - y_3w)/2,$
 $(-I(y_2w + 3y_3w))/2^{1/2}, 0\},$
 $\{-(3^{1/2})(y_2w - y_3w)/2, 0,$
 $-y_1w - y_2w/2 - (3y_3w)/2, 0, 0,$
 $(-I(y_2w + 3y_3w))/2^{1/2}\},$
 $\{0, -(3^{1/2})(y_2w - y_3w)/2, 0,$
 $(-2y_1w + y_2w + 3y_3w)/2,$
 $I(3/2)^{1/2}(y_2w - y_3w), 0\},$
 $\{0, (I(y_2w + 3y_3w))/2^{1/2}, 0,$
 $-I(3/2)^{1/2}(y_2w - y_3w), -y_1w, 0\},$
 $\{-I(3/2)^{1/2}(y_2w - y_3w), 0,$
 $(I(y_2w + 3y_3w))/2^{1/2}, 0, 0, -y_1w\}\}\};$

Appendix E. Sample List

SAMPLE	SUBSTR.	BUFFER	Ge	WELL	WELL	BARRIER	CAP	PRDS.	GROWTH	
ID	ORIENT.	ANG.	X	DOPING	WIDTH	ANG.	ANG.	#	TEMP	
				CM-3	ANG.				C	
40404.1		110	1700	0.2	8E19	40	300	2000	10	550
40512.1		110	500	0.2	5E19	40	300	500	15	550
40520.1		110	500	0.2	2E19	40	300	500	15	550
40602.1		110	500	0.3	2E19	40	300	500	15	550
40831.1	PL	100	1700	0.2		30	300	500	5	710
40927.1	PL	110	500	0.2		40	300	500	15	625
40928.1	PL	110	500	0.2		40	300	500	15	710
50111.1		110	2500	0.3	1.E18	50	300	500	5	550
50111.2		110	2500	0.3	5.E18	50	300	500	5	550
50112.1		110	2500	0.3	2.5E19	50	300	500	5	550
50117.1		110	2500	0.3		50	300	500	5	550
50201.1	PL	100	Q Dot							
50216.1	PL	110	1000	0.2		30	300	1000	3	710
50216.2		110	1000	0.2		30	300	1000	3	550
50223.1		110	2500	0.3	1.E18	50	300	500	5	710
50223.2		110	2500	0.3	1.E18	50	300	500	5	550
50331.1	PL	100	1700	0.2		30	300	2000	5	710
50403.1	PL	110	1700	0.2		30	300	2000	5	710
50405.1		110	2000	0.3	1.E19	20	300	2000	20	550
50406.1		100	2000	0.3	1.E19	30	300	2000	20	550
50407.1	PL	100	1700	0.2		30	300	2300	5	710
50407.2	PL	100	1700	0.2		30	300	2300	5	710
50426.1	PL	110	1700	0.2		30	300	2300	5	710
50428.2	PL	110	1700	0.2		30	300	2300	5	710
50501.1		110	2000	0.3	1.E19	30	300	2000	5	550
50607.1		110	500	0.3	2.E19	40	300	500	15	550
50607.2		110	500	0.3	2.E19	20	300	500	15	550
50608.1		110	500	0.3	2.E19	30	300	500	15	550
50620.2	PL	100	1700	0.2		30	300	2000	5	710
50727.2		100	500	0.15	2.E19	40	300	500	15	550
50728.1		100	500	0.4	2.E19	40	300	500	15	550
50728.2		100	500	0.6	2.E19	40	300	500	15	550
50807.1	PL	100	1700	0.2		30	300	2000	5	710
50807.2	PL	100	1700	0.2		30	300	2000	5	710
50808.1	PL	100	1700	0.2		30	300	2000	5	710
50808.2	PL	100	1700	0.2		30	300	2000	5	710
50808.3	PL	100	1700	0.2		30	300	2000	5	710
50911.1		110	500	0.3	1.E19	30	200	500	50	550
50912.2		100	500	0.3	1.E19	30	300	500	20	710
50912.3		110	500	0.3	1.E19	30	300	500	20	710
51023.1		110	1000	0.2	1.E19	40	300	2000	15	550
51024.2		110	1000	0.2	5.E18	40	300	2000	15	550

51103.1	PL	100	1700	0.2		30	300	2000	5	710
51103.2	PL	100	1700	0.2		30	300	2000	5	710
51103.3	PL	100	1700	0.2		30	300	2000	5	710
51104.1	PL	100	1700	0.2		30	300	200	5	710
51104.2	PL	100	1700	0.2		30	300	200	5	710
51105.1	PL	100	1700	0.2		30	300	200	5	710
51206.3	PL	100	1700	0.2		30	300	2000	5	710
51206.4	PL	100	1700	0.2		30	300	2000	5	710
51207.2	PL	100	1700	0.2		30	300	2000	5	710
51212.1		110	1000	0.15	1.E19	30	300	500	5	550
51212.2		110	1000	0.15	1.E19	20	300	500	5	550
51212.3		110	1000	0.15	1.E19	40	300	500	5	550
51213.1		110	1000	0.1	1.E19	40	300	500	5	550
51213.2		110	1000	0.1	1.E19	30	300	500	5	550
51213.3		110	1000	0.1	1.E19	20	300	500	5	550

Appendix F. Multi-phonon transition peaks for bulk
Si^{144,145,146,147,16}

Theoretical Values (cm ⁻¹)	assignment	comments	reported experimental values (cm ⁻¹)	experimental values (μm)
		strong Si-H complex	2210	4.52
		Si-H complex, (Ox related)	2191	4.56
		Si-H complex, (Ox related)	2123	4.71
		Si-H complex	2178	4.59
		Si-H complex	2048	4.88
		Si-H complex	1994	5.02
		Si-H complex	1950	5.13
		strong Si-H complex	1946	5.14
1726	LTO(Γ) + LO(L) + TO(X) + LA(L)		1724	5.80
1443	2 LTO(Γ) + TO(X)		1444	6.93
1397	2 TO(X) + LTO(Γ)		1385	7.22
1300	2 TO(X) + LA(X)		1300	7.69
		O _i	1226	8.16
		Si-O stretching	1207	8.29
1104	2 TO(Γ) + TA(L)	Si-O sym stretch Si ₂ O asym stretch strong O impurity line	1107	9.03
		C-O complex	1093.6	9.14
		C-O complex	1047.5	9.55
		O _i	1059	9.44
		O _i	1013	9.87
968	LA(L) + TA(L) + TO(Γ)		968	10.33
		N impurity	963	10.38
888	TO(Γ) + LO(L)		887	11.27
849.6	TO(X) + LO(X)		839	11.92
		Si-H bending	812	12.32
		Si-H wagging	791	12.64
		N impurity	766	13.05
787	TA(X) + TO(Γ)		790	12.66
741.6	2 TA(X) + TO(X)		739	13.53
676.6	LO(L) + TA(L) + TA(X)	C-O complex	680	14.70
		N impurity	653	15.31
		C-O complex	636.7	15.70
614	TO(L) + TA(X)	strong "two-phonon" band, strong C impurity line inc., C-Si and C-O complexes	609.5	16.41
		C-O complex	586.2	17.05

562	2 TA(X) + TO(X)	O _i	567	17.63
		Si ₂ O bending Si ₂ O sym stretch, O _i	513	19.49

Appendix G. Energies of Si PL Lines⁹⁹

Energy (meV)	Phonons	Description
1170.0		Band gap at 0 K.
1155.7	TO	Free exciton (FE) no phonon (NP) line.
1152.5		"1F" NP emission.
1152		"2F" NP emission.
1150.7	TO	Boron (B) BE NP line.
1150.1	TO	Antimony (Sb) BE NP line.
1150.1	TO	Phosphorus (P) BE NP line. Multiexciton lines at 1146.3, 1143.7, 1141.7, 1140.5, and 1139.3, for m = 2-6.
1149.6	TO	Aluminum (Al) BE NP line. Multiexciton lines at 1146.3, 1147.7, 1141.5, and 1140.3 for m = 2-5.
1149.2	TO	Arsenic (As) BE NP line.
1149.0	TO	Gallium (Ga) BE NP line.
1148.8		"a1" and "a2" NP emission from P donor.
1146.9		Bismuth (Bi) BE NP line.
1143		"TD" produced in CZ Si by heating to 450 C.
1142.2		H ⁺ implantation and anneal 450-600 C.
1141.0		Indium (In) BE NP line.
1137.3	TA	FE with TA emission.
1132.6	TA	Li BE line with TA emission.
1131		"Y"; radiation damage in Si:Li.
1129.9		Multiexciton line involving two excitons bound to Li donor. Similar lines at 1127.8, 1125.9, 1124.5, and 1123.2 for m = 3-6.
1126		"Z"; radiation damage in Si:Li.
1122.3		"A"; Line in MBE Si associated with N + Al (Alt 1985, Lightowlers 1989b).

1122		"ABC"; Trigonal isoelectronic centre involving N + Al.
1117.6		"01"; one of a series including 1115.6, 1113.7, and 1111.8, 02-04. Thermally induced in CZ silicon. Possibly bound to free or strain broadening.
1117.5		"PQR"; In related, associated lines at 1115.9 and 1108.5.
1117		"X"; radiation damage of Si:Li.
1117		Isoelectronic center involving BE + C.
1116.9		"NL1"; associated lines at 1116.1 and 1119.3. Observed after B implantation and 10 in anneal at 450 C.
1108.3		"S"; associated lines at 1104.5, 1100.5, 1092.7, 1090.5, 1088.1, 1085.5, 1070.4, 1067.2, 1060.8, 1034.2, 1023.4, 1014.4, formed in CZ Si by 100 h at 500 C.
1108.1		Produced in CZ Si by neutron irradiation and anneal at 250 C.
1107.2		PL from Si after laser annealing. Associated lines at 1108.2, 1108.7, and 1109.
1106.16		"k"; identified in MBE Si grown at 550 C (Lightowers 1989b).
1100.6		Radiation damage center produced by He ⁺ , H ₂ , or proton bombardment.
1099.5		FE with LO emission.
1097.7		FE with TO emission.
1095	TO	"3F"; Exciton bound to modified 1094.5 F center. Multiexciton emission at 1092, 1090, and 1088.5 for m = 2-4.
1094.5	TO	"F"; Emission of exciton bound to center formed in CZ Si with [C]>5x10 ¹⁶ cm ⁻³ . Multiexciton emission at 1092.5, 1090, 1088.5, and 1087 for m = 2-5.
1093.2	TO	Li BE with TO emission.
1092.7	TO	B BE with TO emission. Multiexciton lines at 1090.4, 1088.1, and 1086.5 for m = 2-4.
1091.9	TO	Sb BE with TO emission.
1091.8	TO	P BE with TO emission. Multiexciton lines at 1088.2, 1085.6, and 1083.7 for m = 2-4.
1091	TO	As BE with TO emission.
1090.0	TO	Multi-BE with 2 excitons + TO. Similar lines at 1088.5, 1086.8, 1085, 1083.8, 1082.5, 1081.1, for m = 3-8.

1086.9		T1 related lines at T<20K. Associated lines at 1081.5 and 1080.4.
1082		Radiation damage of Si:(C+Li); similar to "S" at 1045.
1081.1		Observed in B implanted Si after 400 C anneal.
1080		"I2"; Monoclinic I center produced by B implant or electron irradiation of Si:B, involves 2 B atoms.
1076		Si:BE isoelectronic center.
1074.7	TO+IV	FE with TO + IV(a) emission
1067.2		One of S series; see 1108.3
1066.7		Associated with FE-B pairs in MBE Si
1062.5		Produced by n irradiation and 300 C anneal of CZ Si.
1060		Radiation damage at 100K in high C, O.
1052		"O1"; one of series of 3 lines produced by heating CZ Si for 130 h at 500 C; 02 1048; 03 at 1042.
1051.7	TO+IV	FE with TO + IV(b) emission.
1050.2		"Ga-2"; Ge-related radiation damage center; associated line at 1047.2.
1050.1		"T1 PQR"; T1 related lines for T>15, other lines at 1048, 1042.7.
1049		Radiation damage of Si:Ga and anneal at 250 C.
1045		"Q"; Radiation damage of Si:Li; associated lines at 1044 and 1048.
1039.8		"I3" or "X"; ion implantation, neutron damage and anneal at 500 to 800 K. Also seen in ion beam doped Si:As grown by MBE.
1037		Produced by ion bombardment.
1034.2		One of the S series; see 1108.3 line.
1033.2	TO+G	FE with TO + G emission.
1025		Produced in electron irradiated FZ Si:Li and anneal at 450 C.
1023.4		One of the S series; see 1108.3 line.
1018.9		"I1" or "W"; Ion implantation or similar damage line. Trigonal center.

		Also seen in low temp MBE Si _(1-x) Ge _(x) .
1014.8		Like 1018.9 W but produced with Ne implantation.
1014.7		"Cu"; Cu-related trigonal center.
1014.4		One of the S series; see 1108.3 line.
1012.6		"D6" dislocation related band.
1012		Line like 1018.3 W, but produced by He implantation.
1011.7	TO+G+IV	FE with TO+G+IV emission.
1010.3		Au related center.
1009.7		Line like 1018.3 W, but produced by Ar implantation.
1004.8		Line like 1018.3 W, but produced by Kr implantation.
1003.7		Rhombic I center produced by neutron irradiation and 400 C anneal.
1000		Produced by Xe implantation.
997		"D4" dislocation related center.
990+/-10		Ion implantation damage and hydrogenation.
996.8		Produced by neutron irradiation and anneal at 150 C.
991.37		"j"; Observed in MBE Si grown at 550 C; anneals out at 300 C .
988.8		Produced by neutron irradiation and anneal at 375 C.
977.8		Observed in Si:S.
969.5		"G"; Monoclinic I involving 2 C and one Si atom.
968.7	TO+G+G	FE with TO+2G emission .
967.4		Produced by neutron irradiation and anneal at 150 C.
965.2		"I"; Produced by 450 C heating of CZ Si.
957		Produced in CZ Si by 180 H at 450 C or by irradiation damage below 200 C.
956.9		Perturbed form of 969 G.
953.9		Perturbed form of 969 G.

953		Perturbed form of 969 G.
953		"D5" dislocation related band.
951.2		Perturbed form of 969 G.
949.9		"F"; C-related radiation damage center; monoclinic I symmetry.
947		Produced by radiation damage and 450 C anneal.
945.8		See 944.8.
944.8		Observed in Mn + Zn-doped Si; luminescence from excited state at 945.8.
943.7		"Cu*"; Observed after Cu diffusion; similar to 1014.7 Cu center; trigonal center.
939		"D3" dislocation related center.
935.2		Produced by radiation damage at 20K in C-doped FZ Si.
935.1		"T"; Rhombic I center involving C produced by radiation damage and anneal at 450 C.
929.1		C-related radiation damage center.
929		"Ga3".
926		Radiation damage and anneal at 250 of Si:Ga.
925.5		"H" or "K"; Radiation damage and anneal at 450 C in CZ Si; monoclinic I center with C dependence.
922.3		Produced by high temperature anneal involving possibly C + Al.
919.8		Radiation damage center involving C.
903		"9"; Produced by 300-400 h at 450 C in CZ Si; monoclinic I center.
900		"D5" dislocation related band.
897.9		Produced by radiation damage of CZ Si and anneal at 350 C.
878		Produced by radiation damage and anneal at 100 C of Si:Li.
875		"Ga1"; Radiation damage of Si:Ga involving C in a rhombic I center.
874		"D2" dislocation related tetragonal center: associated lines at 807, 939, and 997.

868.7		Seen in MBE Si:As .
862.17		"i"; Found in MBE Si grown at 550 C. Possibly C-N-H related. Removed with 700 C anneal.
861.68		"h"; Found in MBE Si grown at 550 C. Possibly C-N-H related. Removed with 700 C anneal.
856		Rhombic I radiation damage center produced in Si:C at T < 300 K; thermally destroyed at T > 300 K.
844		Observed after Cr diffusion into Si:B.
836		"Al 1"; Rhombic I radiation damage center produced in Si:Al.
829.8		Au-related center.
812.91		"g"; found in MBE Si grown at 550 C. Possibly C-N-H related.
812.30		"f"; found in MBE Si grown at 550 C. Possible C-N-H related.
811.1		Rhombic I center produced by Pt diffusion at 1150 C.
810.5		See 811.1.
807		"D1"; dislocation related tetragonal center.
805.4		Tetrahedral center produced by Pt diffusion at 1050 C.
793.4		Au-related.
793.0		See 793.4.
792.8		See 793.4.
791.9		See 793.4.
789.4		"C"; Monoclinic I radiation damage center involving C and O. Also seen in Si _(1-x) Ge _(x) layers grown by low temp MBE.
785		Produced by radiation damage and 300 C anneal of Si:Li.
778.53		"e"; Found in MBE Si grown at 550 C. Possibly C-N-H related.
775.1		Room temp irradiation product in Si:Al.
772.4		"N5"; see 745.6.
768.6		C-related radiation damage center.
767.4		"N4"; see 745.6. Seen in MBE Si grown at 550 C .

767.3		"P"; Monoclinic I C-related center produced by radiation damage and annealing at 450 C in CZ Si.
766.7		Produced by neutron irradiation and annealing at 375 C in CZ Si.
761.5		"N3"; see 745.6.
760.6		"M"; Radiation damage center involving C.
758		"N2"; see 745.6. Seen in MBE Si.
745.6		"N1"; Monoclinic I or trigonal center involving N and C atoms. Seen in MBE Si.
744.9		Seen in MBE Si after irradiation with 2 MeV electrons.
737.6		Observed after FE diffusion.
735.1		See 737.6. Seen in MBE Si.
734.7		See 737.6. Seen in MBE Si.
707		Au-related center.
698	TA	"a"; Trigonal center in MBE Si.
677		Observed after Cr diffusion into Si:Ga
567.9		See 564.7.
566.1		See 564.7.
565.7		See 564.7.
564.7		Mn-related tetrahedral center.
488		Monoclinic I radiation damage center involving C and O.

Bibliography

- ¹ B.E.A. Saleh and M.C. Teich, Fundamentals of Photonics, John Wiley and Sons, New York, (1991).
- ² S.M. Sze, Physics of Semiconductor Devices, John Wiley and Sons, New York, (1981).
- ³ M.O. Manasreh and G.J. Brown, Semiconductor Quantum Wells and Superlattices for Long-Wavelength Infrared Detectors, M.O. Manesereh ed., Artech House, Boston, (1993).
- ⁴ A. Roglaski, *Optical Engineering* **43**, 1395 (1994).
- ⁵ F.D. Shepherd, *Proc. SPIE* **1735**, 250 (1992).
- ⁶ M. Kimata, N. Yutani, and N. Tsubouchi, *Proc. SPIE* **1656**, 151 (1992).
- ⁷ B.-Y. Tsaur, *IEEE Electron Device Lett.* **12**, 293 (1991).
- ⁸ F.D Shepherd and A.C. Yang, *Tech. Digest IEDM*, 310 (1973).
- ⁹ T.L. Lin and J. Maserjian, *Appl. Phys. Lett.* **57**, 1422 (1990).
- ¹⁰ R. Misra, D.W. Greve, and T.E. Schlesinger, *Appl. Phys. Lett.* **67**, 1995).
- ¹¹ L. Esaki and R. Tsu, *IBM J. Res Develop.* **14**, 61 (1970).
- ¹² L. Esaki, Molecular Beam Epitaxy and Heterostructures, ed. L.L. Chang and K. Ploog, Martinus Nijhoff, Dordrecht, 1 (1985).
- ¹³ R. People, J.C. Bean, and D.V. Lang, A.M. Sergent, H.L. Stormer, K.W. Wecht, R.T. Lynch, and K. Baldwin, *Appl. Phys. Lett.* **45** 1231 (1984).
- ¹⁴ C.-I Yang, and D.-S. Pan, *J. Appl. Phys.* **64**, 1573 (1988).
- ¹⁵ V.D. Shadrin, V.T. Coon and F.L. Serzhenko, *J. Appl. Phys.* **73**, 7747 (1993).
- ¹⁶ F. Szmulowicz and G.J. Brown, *Phys. Rev B*, **51** 13203 (1994).

- ¹⁷ E.R. Johnson and S.M. Christian, *Phys. Rev.* **95** 560 (1954).
- ¹⁸ A. Levitas, C.C. Wang, and B.H. Alexander, *Phys. Rev.* **95** 846 (1954).
- ¹⁹ R. Braunstein, A.R. Moore, and F. Herman, *Phys. Rev.* **109**, 695 (1958).
- ²⁰ W. Paul and D.M. Warschauer, *J. Phys. Chem. Solids* **6**, 6 (1959).
- ²¹ J.C. Hensel and G. Feher, *Phys. Rev.* **129**, 1041 (1963).
- ²² K. Maurase, K. Enjouji, and J. Otsuka, *J. Phys. Soc. Jpn.*, **29**, 1248 (1970).
- ²³ Q.M. Ma, K.L. Wang, and J.L. Schulman, *Phys. Rev. B.* **47**, 1936 (1993).
- ²⁴ J.M. Luttinger and W. Kohn, *Phys. Rev.* **97**, 869 (1955).
- ²⁵ E.O. Kane, *J. Phys. Chem. Sol.* **1**, 249 (1957).
- ²⁶ G. Dresselhaus, A. Kip, and C. Kittel, *Phys. Rev.* **98**, 368 (1955).
- ²⁷ H. Hasegawa, *Phys. Rev.* **129**, 1029 (1963).
- ²⁸ J.C. Hensel and G. Feher, *Phys. Rev.* **129**, 1041 (1963).
- ²⁹ M. Cardona and F. Pollak, *Phys. Rev.* **142**, 530, (1966).
- ³⁰ Q.M. Ma, K.L. Wang, and J.N. Schulman, *Phys. Rev. B*, **47**, 1936 (1993).
- ³¹ Y.C. Chang and J.N. Schulman, *Phys. Rev. B* **31**, 2069 (1985).
- ³² D.L. Smith and C. Mailhot, *Phys. Rev. B* **33**, 8345 (1986).
- ³³ S.R. White and L.J. Sham, *Phys. Rev. Lett.* **47**, 879 (1981).
- ³⁴ M. Altarelli, *Phys. Rev. B* **28**, 842 (1983).
- ³⁵ M.F.H. Schuurmans and G.W.'t Hooft, *Phys. Rev. B* **31**, 8041 (1985).
- ³⁶ G. Bastard, *Phys. Rev. B* **24**, 5693 (1981).
- ³⁷ G. Bastard, *Phys. Rev. B* **25**, 7584 (1982).
- ³⁸ R. Eppenga, M.F.H. Schuurmans and S. Colak, *Phys. Rev. B.* **36**, 1554, (1987).

- ³⁹ Y.C. Chang and J.N. Schulman, *Phys. Rev. B* **31**, 2069 (1985).
- ⁴⁰ F. Szmulowicz and G. Brown, *Phys. Rev. B* **51**, 13203 (1995).
- ⁴¹ F. Seitz, Modern Theory of Solids, p. 352, McGraw-Hill, New York, (1940).
- ⁴² W. Shockley, *Phys. Rev.* **78**, 173 (1950).
- ⁴³ J.M. Luttinger, *Phys. Rev.* **102**, 1030 (1956).
- ⁴⁴ M.R. Gregg, Dissertation Supplement, Mathematica Programs, AFIT, (1996).
- ⁴⁵ R. People and S.A. Jackson, Semiconductors and Semimetals **32**, T.P. Pearsall vol. ed. Academic Press, New York, (1990).
- ⁴⁶ T. Fromherz, et al., *Phys. Rev. B.* **50**, 15073, (1994).
- ⁴⁷ Z. Ikonic, V. Milanovic, D. Tjapkin, *Phys. Rev. B.* **46**, 4285 (1993).
- ⁴⁸ H. Brooks, Advances in Electronics and Electron Physics **8**, L. Marton ed., Academic Press, New York, (1955).
- ⁴⁹ C. Herring and E. Vogt, *Phys. Rev.* **101**, 933 (1956).
- ⁵⁰ W.H. Kleiner and L.M. Roth, *Phys. Rev. Lett.* **2**, 334 (1959).
- ⁵¹ E.O. Kane, Semiconductors and Semimetals **1**, R.K. Willardson and A.C. Beer eds., Academic Press, New York (1972).
- ⁵² I. Balsev, Semiconductors and Semimetals **9**, R.K. Willardson and A.C. Beer eds., Academic Press, New York (1972).
- ⁵³ F.H. Pollak, *Surface Science* **37**, 863 (1973).
- ⁵⁴ G.L. Bir and G.E. Pikus, Symmetry and Strain-Induced Effects in Semiconductors, John Wiley, New York, (1974).
- ⁵⁵ J.H. Van der Merwe, *J. Appl. Phys.* **34**, 123 (1963).
- ⁵⁶ W.A. Jesser and D. Khulmann-Wilsdorf, *Phys. Status Solidi* **56**, 365 (1967).
- ⁵⁷ J.C. Bean, L.C. Feldman, A.T. Fiory, S Nakahara, and I.K. Robinson, *J. Vac. Sci.*

- Technol.* **A2**,436 (1984).
- ⁵⁸ C.H. Chern, K.L. Wang, G. Bai, and M.-A. Nicolet, *Mat. Res. Soc. Symp. Proc.* **220**, 175 (1991).
- ⁵⁹ J.W. Matthews and A.E. Blakeslee, *J. Cryst. Growth* **32**, 265 (1976).
- ⁶⁰ R. People, and J.C. Bean, *Appl. Phys. Lett.* **46**, 538 (1986).
- ⁶¹ R.H.M. Van der Leur, A.J. Schellingerhout, F. Tuinstra, and J.E. Mooij, *J. of Appl. Phys.* **64**, 3043 (1988).
- ⁶² F.H. Pollak, Semiconductors and Semimetals **32**, T.P. Pearsall vol. ed., Academic Press, Boston, (1990).
- ⁶³ A. Kahan, M. Chi, and L. Friedman, *J. Appl. Phys.* **75**, 8012 (1994).
- ⁶⁴ R.P.G. Karunasiri, J.S. Park, K.L. Wang, and S.K. Chun, *Optical Engineering* **33**, 1468 (1994).
- ⁶⁵ S.M. Sze, Physics of Semiconductor Devices, John Wiley & Sons, New York, (1981).
- ⁶⁶ G.C. Messenger and M.S. Ash, The Effects of Radiation on Electronic Systems, Van Nostrand Reinhold, New York, (1992).
- ⁶⁷ W-X Ni and G.V. Hansson, *Phys. Rev. B* **42**, 3030 (1990).
- ⁶⁸ C.G. Van de Walle and R.M. Martin, *Phys. Rev. B* **35**, 8154 (1987).
- ⁶⁹ R. People, *Phys. Rev. B* **32**, 1405 (1985).
- ⁷⁰ C. Van De Walle, *Phys. Rev. B* **39**, 1871 (1989).
- ⁷¹ E. Anderson, Modern Physics and Quantum Mechanics, W.B. Saunders, Philadelphia, (1971).
- ⁷² R.P.G. Karunasiri, J.S. Park, Y.J. Mii, and K.L. Wang, *Appl. Phys. Lett.* **57**, 2585 (1990).
- ⁷³ R. People, J.C. Bean, C.G. Bethea, S.K. Sputz, and L.J. Peticolas, *Appl. Phys. Lett.* **61**, 1122 (1992).
- ⁷⁴ L.J. Sham and M. Nakayama, *Phys. Rev. B* **20**, 734 (1979).

- ⁷⁵ M. Alterelli, Heterojunctions and Semiconductor Superlattices, Springer-Verlag, Berlin, (1986).
- ⁷⁶ T. Liou, T. Wang, and C. Chang, *J. Appl. Phys.* **12**, 6646, (1995).
- ⁷⁷ P.E. Thompson, *Thin Solid Films*, **192**, 287 (1990).
- ⁷⁸ M.A. Herman and H. Sitter, Molecular Beam Epitaxy, Fundamentals and Current Status, Springer-Verlag, Berlin, (1989).
- ⁷⁹ A. Ishizaka and Y. Shiraki, *J. Electrochem. Soc.* **133**, 666 (1986).
- ⁸⁰ D.E. Aspnes and A.A. Studna, *Phys. Rev. B* **27**, 985 (1983).
- ⁸¹ FTS 40A/60A Getting Started Manual 091-0622B, BioRad, Cambridge, (1992).
- ⁸² P.B. Fellgett, *J. Phys. Radium* **19**, 187 (1958).
- ⁸³ R.J. Bell, Introductory Fourier Transform Spectroscopy, Academic Press, New York, (1972).
- ⁸⁴ J. Connes and P. Connes, *J. O. S. A.* **56**, 896 (1966).
- ⁸⁵ B.F. Levine, K.K. Choi, C.G. Bethea, J. Walker, and R.J. Malik, *Appl. Phys. Lett.* **50**, 1092 (1987).
- ⁸⁶ R.P.G. Karunasiri, J.S. Park, Y.J. Mii, and K.L. Wang, *Appl. Phys. Lett.* **57**, 2585 (1990).
- ⁸⁷ S. Zanier, J.M. Berroir, Y. Guldner, J.P. Vieren, I. Sagnes, F. Glowacki, Y. Campidelli, and P.A. Badoz, *Phys. Rev. B*, **51**, (1995).
- ⁸⁸ S.C. Jain, A. Nathan, D.R. Briglio, D.J. Roulston, C.R. Selvakumar, and T. Yang, *J. Appl. Phys.* **69**, 3687 (1991).
- ⁸⁹ P.E. Thompson, K. Hobart, D. Simons, M. Gregg, T. Kreifels, R. Hengehold, and Y.K. Yeo, To Be Published.
- ⁹⁰ H. Sunamura, Y. Shiraki, S. Fukatsu, *Appl. Phys. Lett.* **66**, 953 (1995).
- ⁹¹ P.E. Thompson, T.L. Kreifels, M. Gregg, R.L. Hengehold, Y.K. Yeo, D.S. Simons, M.E. Twigg, M. Fatemi, and K.D. Hobart, *J. Crystal Growth* **157**, 21 (1995).

- ⁹² H.P. Zeindl and S. Nilsson, *J. Appl. Phys.* **77**, 1753 (1995).
- ⁹³ P.J. Dean, J.R. Haynes, and W.F. Flood, *Phys. Rev.* **161**, 711 (1967).
- ⁹⁴ R. Sauer, J. Weber, and J. Stolz, *Appl. Phys. A* **36**, 1 (1985).
- ⁹⁵ D.J. Robbins, R.A.A. Kubiak, and E.H.C. Parker, *J. Vac. Sci. Technol. B* **3**, 588 (1985).
- ⁹⁶ E.C. Lightowers, and G. Davies, *Solid State Communications* **53**, 1055 (1985).
- ⁹⁷ J.P. Noel, N.L. Rowell, D.C. Houghton, and D.D. Perovic, *Appl. Phys. Lett.* **57**, 1037 (1990).
- ⁹⁸ E.R. Glaser, T.A. Kennedy, D.J. Godbey, P.E. Thompson, K.L. Wang and C.H. Chern, *Phys. Rev. B* **47**, 1305 (1993).
- ⁹⁹ T.D. Steiner, R.L. Hengehold, Y.K. Yeo, D.J. Godbey, P.E. Thompson, and G.S. Pomrenke, *J. Vac. Sci. Technol. B* **10**, 924 (1992).
- ¹⁰⁰ Y. Shiraki and S. Fukatsu, 1588 (1995).
- ¹⁰¹ J.-W. Choe, B. O, K.M.S.V. Bandara, and D.D. Coon, *Appl. Phys. Lett.* **56**, 1679 (1990).
- ¹⁰² R.P.G. Karunasiri, J.S. Park, Y.J. Mii, and K.L. Wang, *Appl. Phys. Lett.* **57**, 2585 (1990).
- ¹⁰³ P.Y. Yu and M. Cardona, Fundamentals of Semiconductors, Springer, Berlin, 1996.
- ¹⁰⁴ M. Fatemi, to be published.
- ¹⁰⁵ F. Szmulowicz and G.J. Brown, *Appl. Phys. Lett.* **66**, 1659 (1995).
- ¹⁰⁶ B.F. Levine, *J. Appl. Phys.* **74**, R1 (1993).
- ¹⁰⁷ R.P.G. Karunasiri, J.S. Park, K.L. Wang, S.K. Chun, *Optical Engineering* **33**, 1468 (1994).
- ¹⁰⁸ A.J. Moses, The Practicing Scientists's Handbook, Von Nostrand Reinhold Co. 614, 662 (1978).
- ¹⁰⁹ E. Kasper, H.J. Herzog, and H. Kibbel, *Appl. Phys.* **8**, 199 (1975).

- ¹¹⁰ S. Luryi, A. Kataliski, and J.C. Bean *IEEE Trans. Electron. Devices* **ED-31**, 1135 (1984).
- ¹¹¹ J.C. Bean, L.C. Feldman, A.T. Fiory, S. nakahara, and I.K. Robinson, *J. Vac. Sci. Technol.* **A2**,436 (1984).
- ¹¹² D.D. Coon and R.P.G. Karunasiri, *Appl. Phys. Lett.* **45**, 649 (1984).
- ¹¹³ T.P. Pearsall, J.C. Bean, R. People, and T.A. Fiory, *Proc. 1st Int. Symp. Silicon Molecular Beam Epitaxy*, 366 (1985).
- ¹¹⁴ D.V. Lang, R. People, J.C. Bean, and A.M. Sergent, *Appl. Phys. Lett.* **47**, 1333 (1985).
- ¹¹⁵ R. People, *Phys. Rev. B* **32**, 1405 (1985).
- ¹¹⁶ L.C. West and S.J. Eglash, *Appl. Phys. Lett.* **46**, 1156 (1985).
- ¹¹⁷ H. Temkin, J.C. Bean, T.P. Pearsall, N.A. Olsson, and D.V. Lang, *Appl. Phys. Lett.* **49**, 155 (1986).
- ¹¹⁸ T.P. Pearsall, H. Temkin, J.C. Bean, and S. Luryi, *IEEE Electron Dev. Lett.* **EDL-7**, 330 (1986).
- ¹¹⁹ J. Bevk, J.P. Mannaerts, L.C. Feldman, and B.A. Davidson, *Appl. Phys. Lett.* **49**, 286 (1986).
- ¹²⁰ C.G. Van de Walle and R.M. Martin, *Phys. Rev. B* **34**, 5621 (1986).
- ¹²¹ S.S. Iyer, et al., *Appl. Phys. Lett.* **54**, 220 (1989).
- ¹²² B.F. Levine, K.K. Choi, C.G. Bethea, J. Walker, and R.J. Malik, *Appl. Phys. Lett.* **50**, 1092 (1987).
- ¹²³ S.S. Rhee, J.S. Park, R.P.G. Karunasiri, Q. Ye, and K.L. Wang, *Appl. Phys. Lett.* **53**, 204 (1988).
- ¹²⁴ Y.-C. Chang and R.B. James, *Phys. Rev B* **39**, 12672 (1989).
- ¹²⁵ C.A. King, J.L. Hoyt, C.M. Gronet, J.F. gibbons, M.P. Scott, and J. Turner, *IEEE Electron Device Lett.* **10**, 52 (1989).
- ¹²⁶ R.P.G. Karunasiri, J.S. Park, and K.L. Wang, *Appl. Phys. Lett.* **56**, 1342 (1990).

- ¹²⁷ R.P.G. Karunasiri, J.S. Park, Y.J. Mii, and K.L. Wang, *Appl. Phys. Lett.* **57**, 2585 (1990).
- ¹²⁸ H. Hertle, G. Schuberth, E. Gornik, G. Abstreiter, and F. Schaffler, *Appl. Phys. Lett.* **59**, 2977 (1991).
- ¹²⁹ R.P.G. Karunasiri, J.S. Park, Y.J. Mii, and K.L. Wang, *Appl. Phys. Lett.* **58**, 1083 (1991).
- ¹³⁰ R.P.G. Karunasiri, J.S. Park, and K.L. Wang, *Appl. Phys. Lett.* **59**, 2588 (1991).
- ¹³¹ R. People, J.C. Bean, C.G. Bethea, S.K. Sputz, and L.J. Peticolas, *Appl. Phys. Lett.* **61**, 1122 (1992).
- ¹³² J.S. Park, R.P.G. Karunasiri, and K.L. Wang, *Appl. Phys. Lett.* **61**, 681 (1992).
- ¹³³ C. Lee and K.L. Wang, *J. Vac. Sci. Technol. B* **10**, 992 (1992).
- ¹³⁴ C. Lee and K.L. Wang, *Appl. Phys. Lett.* **60**, 2264 (1992).
- ¹³⁵ C. Lee and K.L. Wang, *Appl. Phys. Lett.* **64**, 1256 (1994).
- ¹³⁶ E. Corbin, K.B. Wong, and M. Jaros, *Phys. Rev. B* **50**, 2339 (1994).
- ¹³⁷ T. Fromherz, E. Koppensteiner, M. Helm, and G. Bauer, *Phys. Rev. B* **50**, 15073 (1994).
- ¹³⁸ K. Bernhard-Hofer, a. Zrenner, J. Brunner, and G. Abstreiter, *Appl. Phys. Lett.* **66**, 2226 (1995).
- ¹³⁹ D.J. Robbins, M.B. Stanaway, W.Y. Leong, R.T. Carline, and N.T. Gordon, *Appl. Phys. Lett.* **66**, 1512, (1995).
- ¹⁴⁰ S. Zanier, J.M. Berroir, Y. Guldner, and J.P. Vieren, *Phys. Rev. B* **51** (1995).
- ¹⁴¹ M.M. Pradhan, R.K. Garg, and M. Arora, *Infrared Phys.* **27**, 207 (1987).
- ¹⁴² J. Ihm, M.T. Yin, and M.L. Cohen, *Solid State Comm.* **37**, 491 (1981).
- ¹⁴³ M.T. Yin and M.L. Cohen, *Phys. Rev. Lett.* **45**, 1004 (1980).
- ¹⁴⁴ M.T. Yin, and M.L. Cohen, *Phys. Rev. B* **26**, 3259 (1982).

Vita

Captain Michael R. Gregg [REDACTED] in teaching, [REDACTED]. He graduated from T.C. Roberson High School in Skyland, North Carolina in 1983. He obtained a Junior Fellowship at the National Climatic Data Center and worked there while attending Wake Forest University in Winston-Salem, North Carolina. After graduating cum laude with a B.A. in Physics and minor in Mathematics in 1987, he was commissioned through Officer Training School in 1988. Capt. Gregg was assigned to the Rome Air Development Center (Rome Laboratory) where he developed a liquid phase epitaxy system for growing InP/InGaAsP laser structures. In addition, he co-developed a CVD system for depositing SiO₂ on InP. Capt. Gregg was accepted into AFIT, School of Engineering to pursue a Master of Engineering Physics degree in May 1991, and was extended into the Ph.D program in January 1993. Capt. Gregg is married to the former Teresa L. Griffin of Asheville, North Carolina; they have one daughter, Amy. He is a member of Sigma Pi Sigma, Tau Beta Pi, and the American Physical Society. After completing his studies, Capt. Gregg will be assigned to the Phillips Laboratory, Albuquerque, New Mexico.

Permanent Address: Captain Michael Gregg
[REDACTED]
[REDACTED]

REPORT DOCUMENTATION PAGE

Form Approved
OMB No. 0704-0188

Public reporting burden for this collection of information is estimated to average 1 hour per response, including the time for reviewing instructions, searching existing data sources, gathering and maintaining the data needed, and completing and reviewing the collection of information. Send comments regarding this burden estimate or any other aspect of this collection of information, including suggestions for reducing this burden, to Washington Headquarters Services, Directorate for Information Operations and Reports, 1215 Jefferson Davis Highway, Suite 1204, Arlington, VA 22202-4302, and to the Office of Management and Budget, Paperwork Reduction Project (0704-0188), Washington, DC 20503.

1. AGENCY USE ONLY (Leave blank) 2. REPORT DATE **18 Oct 96** 3. REPORT TYPE AND DATES COVERED

4. TITLE AND SUBTITLE 5. FUNDING NUMBERS
**Optical Detection Properties Of
Silicon Germanium Quantum Well Structures**

6. AUTHOR(S)
Michael R. Gregg, Capt, USAF

7. PERFORMING ORGANIZATION NAME(S) AND ADDRESS(ES) 8. PERFORMING ORGANIZATION REPORT NUMBER
**Air Force Institute of Technology
2950 P Street
WPAFB, OH 45433-7765**

9. SPONSORING, MONITORING AGENCY NAME(S) AND ADDRESS(ES) 10. SPONSORING, MONITORING AGENCY REPORT NUMBER
**AFOSR/NE (Lt Col Pomrenke)
110 Duncan Ave, Suite B 115
Bolling AFB, DC 20332-8080**

11. SUPPLEMENTARY NOTES

12a. DISTRIBUTION/AVAILABILITY STATEMENT 12b. DISTRIBUTION CODE
unlimited

13. ABSTRACT (Maximum 200 words)
A study has been carried out on Si/SiGe multi-quantum well structures to determine their applicability as normal incidence infrared detectors in the spectral range of 2-12 μm . The research effort was primarily experimental, however, extensive calculations were performed to initially explain the experimental data and then used to design subsequent structures. Multiple quantum well structures grown on both Si[001] and Si[110] substrates via molecular beam epitaxy were studied by photoluminescence, absorption, and photoresponse measurements over a wide parameter space. Variables included quantum well depth and width, well doping, number of wells and growth temperature. Well widths were varied from 20Å to 50Å, Ge composition from 10% to 60%, boron doping from $1 \times 10^{18} \text{ cm}^{-3}$ to $8 \times 10^{19} \text{ cm}^{-3}$, number of wells from 5 to 30 and growth temperature from 550°C to 710°C.
Calculations using $k \cdot p$ theory and the envelope function approximation were performed to determine the position of the bound states in the wells, the amount of band mixing and the transition strengths for bound-to-bound transitions for Si[001]/Si_{1-x}Ge_x, Si[110]/Si_{1-x}Ge_x and GaAs/AlGaAs quantum well structures. The Si[110] structures have more allowed energy bands which are significantly mixed. A comparison was made between Si[001]/Si_{1-x}Ge_x, Si[110]/Si_{1-x}Ge_x and GaAs/AlGaAs quantum well structures designed to operate in the 8-12 μm region, and all three showed comparable momentum matrix elements.

14. SUBJECT TERMS 15. NUMBER OF PAGES
Infrared Detectors, Silicon-Germanium, SiGe, Quantum Wells, QWIP **283**

16. PRICE CODE 17. DISTRIBUTION STATEMENT
unclassified **unclassified** **unclassified**